EELS investigations of stoichiometric niobium oxides and niobium-based capacitors

Zur Erlangung des akademischen Grades eines
DOKTORS DER NATURWISSENSCHAFTEN
von der Fakultät für Physik
der Universität Karlsruhe (TH)

genehmigte

DISSERTATION

von

Dipl.-Phys. David Bach
aus Mulhouse (France)

Tag der mündlichen Prüfung: 05.06.2009
Referentin: Prof. Dr. Dagmar Gerthsen
Korreferentin: Prof. Dr. Ute Kaiser

Contents

1. Introduction 1

2. The niobium-oxygen system and niobium-based solid electrolyte capacitors 4

2.1 The niobium-oxygen system 4

2.1.1 Niobium (Nb) 6

2.1.2 The lower oxides of niobium: NbO_x with $0 < x \leq 2$ 13

2.1.3 Niobium pentoxide (Nb_2O_5) and the oxides Nb_2O_{5-y} with $0 < y < 1$ 15

2.1.4 Summary 19

2.2 Nb-based solid electrolyte capacitors 20

2.2.1 Fabrication process 20

2.2.2 Advantages of Nb over Ta 21

2.2.3 Problems and solutions 22

2.3 Investigated materials 24

2.3.1 Stoichiometric reference materials 24

2.3.2 Nb-based capacitor structures 25

3. Electron energy-loss spectroscopy in a transmission electron microscope 28

3.1 Basics of TEM 29

3.1.1 The image and diffraction modes in TEM 30

3.1.2 Scanning Transmission Electron Microscopy (STEM) 32

3.2 Basics of EELS 33

3.2.1 The EEL spectrum 33

3.2.2 Experimental aspects 36

3.2.3 Physical fundamentals 39

3.2.4 Determination of the sample thickness 40

3.2.5 Spectra post-acquisition processing 42

3.2.6 Energy loss near-edge structure (ELNES) 45

3.2.7 Quantitative EELS analysis 48

3.3 EELS investigation of niobium and niobium oxides 49

3.3.1 Literature data 49

3.3.2 Experimental setup of the present work 50

4. EELS investigations of reference niobium oxides *53*

4.1 Structural characterization of the reference materials **53**

4.2 Low-loss fingerprinting and ELNES results **56**

4.2.1 Low-loss fingerprinting 57

4.2.2 Nb-$N_{2,3}$ ELNES 59

4.2.3 Nb-$M_{4,5}$ ELNES 60

4.2.4 Nb-$M_{2,3}$ ELNES 62

4.2.5 Nb-M_1 ELNES 66

4.2.6 O-K ELNES 67

4.2.7 Nb-$L_{2,3}$ ELNES 72

4.3 Quantitative EELS results **76**

4.3.1 Choice of the ionization edges for quantification 76

4.3.2 Determination of intensity ratios and *k*-factors 77

4.3.3 Choice of the integration window 83

4.3.4 Quantification tests: NbO_2 85

4.3.5 Influence of the specimen thickness on quantitative EELS 87

4.3.6 Compilation of *k*-factors for different experimental parameters 90

4.3.7 First application: investigation of the native oxide layer grown on Nb 93

4.4 Discussion **98**

4.4.1 Influence of the experimental parameters on the ELNES results 98

4.4.2 O-K ELNES of the reference niobium oxides 103

4.4.3 Chemical-shift measurements 105

4.4.4 Normalized white-line intensities 110

4.4.5 Influence of the specimen thickness on quantitative EELS 111

4.4.6 Precision of quantitative EELS 113

4.4.7 Accuracy of quantitative EELS 120

4.4.8 The use of the experimentally determined *k*-factors for the quantification of unknown niobium oxide phases 127

5. Application of the results obtained from the reference materials: EELS investigations of Nb-based capacitor structures *130*

5.1 Low-loss fingerprinting and ELNES results **131**

5.1.1 Low-loss fingerprinting 131

5.1.2 Nb-$N_{2,3}$ ELNES 132

5.1.3 Nb-$M_{4,5}$ ELNES 133

5.1.4 Nb-$M_{2,3}$ ELNES 134

5.1.5 O-K ELNES 137

5.1.6 Nb-$L_{2,3}$ ELNES 139

5.2 Quantitative EELS results 141
5.2.1 Influence of the specimen thickness on the quantitative EELS results 142
5.2.2 Determination of C_{Nb}/C_O atomic concentration ratios at the LEO microscope 144
5.2.3 Determination of C_{Nb}/C_O atomic concentration ratios at the VG microscope 148

5.3 The nanochemistry of capacitor structures 153
5.3.1 Stoichiometry gradients and inhomogeneities within the capacitor oxide layers 155
5.3.2 The nanochemistry of the interface between Nb anode and oxide layer 159
5.3.3 Crystallites at the An-OL interface of $Cap_{350°C\text{-}1h}$ 162

5.4 Discussion 166
5.4.1 Low-loss fingerprinting and ELNES 166
5.4.2 Quantitative EELS 168
5.4.3 Quantitative efficiency vs. structure differences (amorphous/crystalline) 171
5.4.4 Quantitative efficiency vs. argon contamination 172
5.4.5 Quantitative efficiency vs. homogeneity ranges of the reference materials 174
5.4.6 Nb-based capacitor structures 178

6. Summary *186*

6.1 Plasmons and ELNES of reference niobium oxides 186

6.2 Quantitative EELS analysis of reference niobium oxides 187

6.3 EELS investigations of Nb-based capacitor structures 188

6.4 General aspects of the applied EELS analysis procedures 189

References *191*

Danksagung *203*

Chapter 1

Introduction

The 4d transition metal niobium (Nb) in combination with oxygen is a key material system for a wide range of applications. In the niobium-oxygen system, Nb occurs in formal oxidation states of 0 in metallic Nb, +2 in niobium monoxide (NbO), +4 in niobium dioxide (NbO_2), and +5 in niobium pentoxide (Nb_2O_5) with different electrical properties ranging from conducting (Nb and NbO) over semiconducting (NbO_2) to insulating (Nb_2O_5). Of particular interest is Nb_2O_5 which is studied intensively in context with applications as, e.g., catalysis (Tanabe, 2003; Hanada et al., 2007), sensors (Hoydo et al., 2006), dielectric nanolayers in microelectronic devices (Kim et al., 2005; Matsui et al., 2005), biomimetic implant coating (Eisenbarth et al., 2007), or coating for antireflection camera lenses (Leitel et al., 2006). A high technological potential has recently been attributed to Nb-based solid electrolyte capacitors with Nb_2O_5 dielectric layers formed by anodic oxidation on Nb or NbO (Zillgen et al., 2002; Zednicek et al., 2005). Moreover, niobium may form a complex native oxide layer which affects e.g. the properties of superconducting Nb-cavities for particle accelerators (Delheusy et al., 2008).

However, the physical properties of the Nb-oxides strongly depend on the exact composition. For instance, even a small oxygen deficiency in Nb_2O_5 leads to the transition from insulating to n-type semiconducting behavior (Gmelin, 1970), which can hamper the application as dielectric material. In addition, many applications involve Nb-based heterostructures on a nanometer scale. Hence, for analyzing these structures a technique is required with high spatial resolution and the ability to distinguish between different oxidation states or, preferably, to determine the composition in a quantitative manner. Electron energy-loss spectroscopy (EELS) investigations in a transmission electron microscope are well suited for this analysis task (see, e.g., Brydson, 2000; Keast et al., 2001; Sigle, 2005).

In a transmission electron microscope a thin sample is traversed by a beam of fast electrons. The incident electrons can lose some of their energy by interacting with the material of the sample (*inelastic scattering*). EELS studies reveal the distribution of the transmitted electrons as a function of their energy loss. It results in a so-called *EEL spectrum* showing features such as *plasmon peaks* or *ionization edges* that are characteristic for the investigated material. A specific ionization edge may present some fine structure (energy loss near-edge structure / ELNES) which can serve as “fingerprint” of changes of the oxidation state, chemical bonding,

and atomic environment as shown e.g. for 3d transition-metal oxides by Paterson & Krivanek (1990*a*, 1990*b*), Kurata et al. (1993), and Mitterbauer et al. (2003). In addition, the intensities under appropriate edges enable elemental quantification e.g. by means of experimentally determined sensitivity-factors, the so-called *k-factors* (Malis & Titchmarsh, 1986). These investigations are possible on a sub-nanometer spatial resolution and can be combined with further transmission electron microscopy (TEM) analyses like transmission imaging, electron diffraction, and X-ray emission spectroscopy, making EELS a more and more important technique for studying the physics and chemistry of materials (Egerton, 2009).

The present thesis focuses on the application and optimization of EELS for the specific analysis of niobium-oxide compounds. It has two successive main aims.
Firstly, a prerequisite for the accurate characterization of an unknown niobium-oxide phase by means of ELNES fingerprints and quantitative EELS is the existence of EELS reference data for niobium oxides of known structure and composition. Thus, owing to the lack of a complete set of reference data in the literature, the first aim of the present work is the systematic analysis of four crystalline stoichiometric reference materials - namely Nb metal and all its three stable oxides NbO, NbO_2, and Nb_2O_5 – with respect to plasmons and all the relevant ionization edges accessible to EELS (viz. the so-called *Nb-*$N_{2,3}$, *Nb-*$M_{4,5}$, *Nb-*$M_{2,3}$, *Nb-*M_1, *Nb-*$L_{2,3}$, and *O-K* edges). In addition to the recording of qualitative phase fingerprints, the ability of EELS to characterize the composition of niobium oxides in a quantitative manner should be checked and optimized. Moreover, owing to the large number of reference materials and characteristic EELS features, the investigation of the Nb-O system is also of interest from a methodological point of view, allowing to illustrate, test, and further develop different EELS analysis procedures.
Secondly, the reference results are applied to the investigation of a particular Nb-based technological system, namely solid-electrolyte capacitors containing approximately 130 nm thick amorphous niobium-oxide dielectric layers anodically grown on porous sintered Nb anodes. Since only stoichiometric Nb_2O_5 provides the desired dielectric properties, local oxygen deficiencies in the dielectric layer can strongly affect the capacitor performance. In addition, the capacitors undergo several annealing steps during their complete fabrication process which may yield composition gradients at the interface between the dielectric layer and the anode material (Qiu et al., 2002). Hence, for a better understanding of the electrical properties of the capacitor, the second main aim of the present work is the nanoscale determination of the oxide-layer stoichiometry in various capacitor structures prepared without annealing and with different annealing steps.

This thesis is mainly organized as follows.
Chapter 2 presents the investigated materials. The complex Nb-O system is detailed in terms of physical properties and practical applications. Particularly, the issues related to the use of Nb and Nb-oxides to produce solid-electrolyte capacitors are addressed.
In the 3rd chapter, some basics of TEM and EELS are introduced, providing a brief insight into the most important experimental aspects as well as into the underlying physic. In particular, the origin of the ELNES is described and the *k*-factor method for quantitative

composition analysis is explained. Furthermore, the experimental setups used in the present study are also presented here.

The most significant parts of this thesis are chapters 4 and 5 which present and discuss the original results of the work.

In more detail, chapter 4 deals with the EELS investigations of stoichiometric Nb, NbO, NbO_2, and Nb_2O_5. Plasmon fingerprints and the ELNES of all the relevant ionization edges are systematically analyzed so as to reveal characteristic EELS features which can be used to distinguish between the different oxidation states. Experimental *k*-factors are determined from the quantitative analyses of different combinations of ionization edges (either Nb-$M_{2,3}$ and O-K or Nb-$M_{4,5}$ and O-K) and are optimized in terms of quantification efficiency by taking different systematic and random errors into consideration. The results are discussed with respect to the influence of various experimental parameters on the ELNES details and on the precision and accuracy of EELS quantification. All along chapter 4, the different EELS procedures used to analyze the reference materials are described in detail since they could be of interest for the investigation of other material systems.

In chapter 5, the results gained from the reference materials are applied to the characterization of several Nb-based solid-electrolyte capacitor structures differing in the annealing procedure endured. Plasmons and ELNES features from the capacitor structures are systematically analyzed with respect to the reference data. Experimental *k*-factors are used to determine the composition of the oxide layers. Also the homogeneity of the oxide layers and the interfaces between anodes and oxide layers are investigated on a nanometer scale. Here again, the impact of different factors on the efficiency of ELNES and quantitative EELS analyses is discussed. The results are also discussed in relation to the influence of annealing and are confronted with appropriate data of electrical measurements from the literature.

Finally, chapter 6 summarizes the most relevant findings of the present work.

Chapter 2

The niobium-oxygen system and niobium-based solid electrolyte capacitors

2.1 The niobium-oxygen system

The niobium-oxygen system is particularly complex. Since the fundamental work of Brauer (1940, 1941), it has been extensively investigated (see, e.g., Elliott, 1960; Brauer et al., 1962; Norman, 1962; Cox & Johnston, 1963; Gatehouse & Wadsley, 1964; Andersson & Wadsley, 1966; Fromm, 1966; Niebuhr, 1966; Schäfer et al., 1966; Schäfer et al., 1969; Kimura, 1973; Lindau & Spicer, 1974; Ann McConnell et al., 1976; Cheetham & Rao, 1976; Meyer & Gruehn, 1982*a*, 1982*b*; Pialoux et al., 1982; Halbritter, 1987; Rosenfeld et al., 1994; Nowak & Ziolek, 1999; Kurmaev et al., 2002; Venkataraj et al., 2002; Brayner & Bozon-Verduraz, 2003). Nevertheless, many questions remain open. Thus, the formation and the chemical and physical behavior of niobium oxides call steadily for new investigations owing to the partly contradictory results of the existing studies and the numerous technological applications of niobium and its oxides (see, e.g., Lira-Cantu et al., 2006; Masse et al., 2006; Naka et al., 2006; Hanada et al., 2007; Royon et al., 2007; Delheusy et al., 2008; Helali et al., 2008; Olszta & Dickey, 2008; Sasaki et al., 2008; Störmer et al., 2009). Indeed, niobium forms a large variety of oxides with a wide range of interesting physical properties. Fig. 2.1.1 gives an overview of the main oxides (whose existence is nowadays widely accepted) and their electrical properties as a function of the formal niobium-oxidation state. In addition to three stable oxides, namely, niobium monoxide (NbO, conductor), niobium dioxide (NbO_2, semiconductor), and niobium pentoxide (Nb_2O_5, insulator), the Nb-O system is complicated by the presence of numerous metastable oxides NbO_x with $0 < x < 1$ and $2.0 < x < 2.5$ as well as by the existence of a multitude of Nb_2O_5 polymorphic modifications. Some characteristics and applications of niobium and its oxides are presented in the following sections.

The existence range of the different niobium oxide phases is quite confusing. Elliott (1960) indicates in his phase equilibrium study of the Nb-O system that NbO and NbO_2 are thermodynamically stable within narrow single-phase fields with negligible deviations from the exact stoichiometry. Nevertheless, later on, several authors observed very narrow but

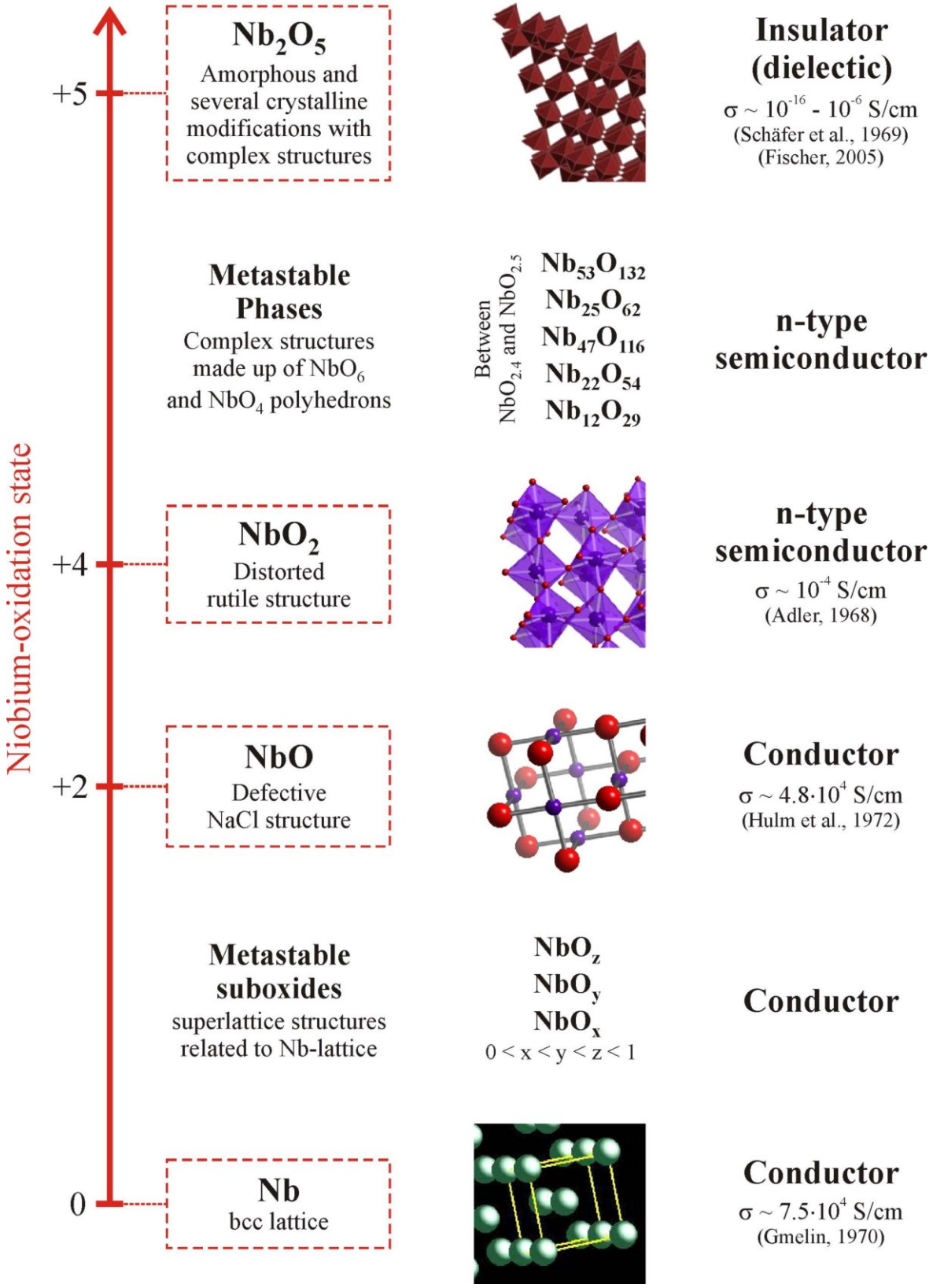

Fig. 2.1.1. The niobium-oxygen system: main oxides and some of their structural and electrical properties (conductivity σ given at ~ 0°-25°C) as a function of the formal Nb-oxidation state (Brauer et al., 1962; Norman, 1962; Gatehouse & Wadsley, 1964; Niebuhr, 1966; Schäfer et al., 1966; Adler, 1968; Gmelin, 1970; Hulm et al., 1972; Kimura, 1973; Cheetham & Rao, 1976; Pialoux et al., 1982; Fischer, 2005; the structure pictures are from http://www.webelements.com, 2007; see text for more references).

still measurable homogeneity ranges for the three stable oxides (see, e.g. for NbO_2 and Nb_2O_5, Schäfer et al., 1969; Naito et al., 1980). However, there are discrepancies between the results of the different studies (as reported for instance by Marucco, 1973, and Marucco et al., 1976). This issue will be presented in more detail in section 5.4.5 which discusses the influence of eventual deviations from the exact stoichiometric composition of the NbO, NbO_2, and Nb_2O_5 reference materials on the accuracy and precision of the EELS-quantification results obtained in the present work. The phase diagram proposed by Elliott (1960) for the Nb-O system is shown in Fig. 2.1.2.

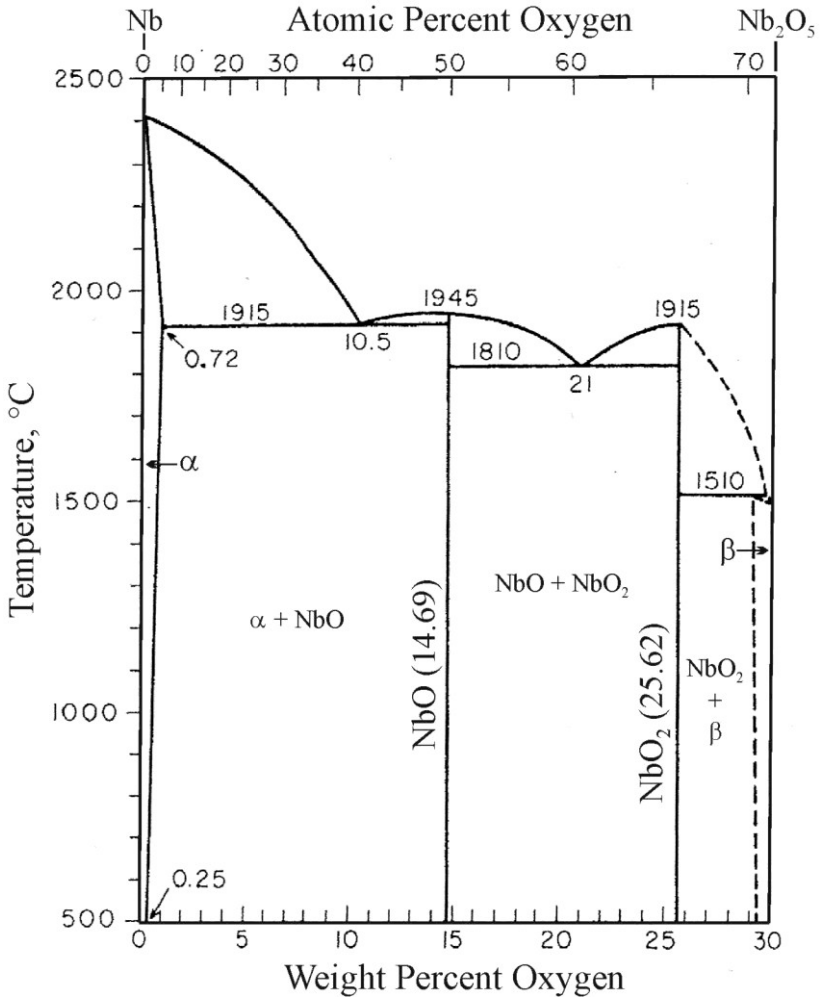

Fig. 2.1.2. Niobium-Oxygen phase diagram (Elliott, 1960).

2.1.1 Niobium (Nb)

Niobium was discovered in 1801 by Charles Hatchett who originally gave it the name of columbium (Cb) (Hatchett 1802*a*, 1802*b*; Griffith & Morris, 2003). After a complex and controversial history (Clarke, 1914), the name of niobium (Nb) has finally been adopted for this element in 1950 by the International Union of Pure and Applied Chemistry (IUPAC) which has the international authority to assign a name to a chemical element (Rayner-Canham & Zheng 2008).

Physical properties

Niobium has the atomic number 41 and is a soft, ductile transition metal belonging to the group 5 and period 5 of the periodic table. Its electronic configuration is $[Kr].4d^4.5s^1$. Thus, niobium, like the other transition metals, is characterized by an electronic structure where the outer shell (5s energy level in the case of Nb) contains electrons while one of the d inner shell (4d energy level) is not completely filled (DeArdo, 2001). It crystallizes in a body-centered cubic (bcc) lattice belonging to the $Im\bar{3}m$ space group (no. 229) (Pialoux et al., 1982). It is a refractory metal which conducts heat well and is characterized by a high melting point, at 2477°C, and a boiling point around 4744°C. The density of 8.57 g/cm^3 is moderate compared to the majority of high melting point refractory metals, being only 51 % of tantalum at 16.65 g/cm^3 (Graham & Sutherlin, 2001). Pure niobium conducts electricity with a resistivity of about 13.4 μΩ·cm at 0°C (corresponding to a conductivity around $7.5 \cdot 10^4$ S/cm, Gmelin, 1970). It is a superconductor below the transition temperature $T_c \sim 9.3$ K (Franchy et al., 1996). Niobium is a valve metal characterized by a high resistance to corrosion in many environments (Graham & Sutherlin, 2001; Persico et al., 2001).

Niobium is a highly reactive metal. Like its neighbours in the group 5 of the periodic table (vanadium and tantalum) and the elements of the group 4 (titanium, zirconium, hafnium) and 6 (chromium, molybdenum, tungsten), niobium forms together with small atomic elements such as carbon, nitrogen, boron and silicon, very stable carbides, nitrides, borides and silicides, which are classified as hard metal alloys and are characterized by high bond energy resulting in a high modulus of elasticity and a high melting point (Jeglitsch, 2001). Due to its electronic properties, niobium is also characterized by a high affinity and binding energy to oxygen (Halbritter, 1987). Oxygen is easily dissolved in the open body centred lattice of niobium where it occupies octahedral interstitial sites (Norman, 1962; Pialoux et al., 1982). The solid solubility of oxygen in niobium increases with temperature. According to Elliott (1960), the oxygen solubility determined by metallographic examinations amounts to 0.25 wt. % (1.43 at. %) at 500°C and reaches the maximal value of 0.72 wt. % (4.0 at. %) at 1915°C (see Fig. 2.1.2). At higher oxygen concentrations, niobium can form numerous oxides with varying properties (see the sections below). Oxygen in solution is a potent hardener and will decrease the ductility of the matrix (Graham & Sutherlin, 2001). The dissolution of oxygen also leads to an increase of the lattice parameter of the Nb crystal (Gmelin, 1970, Pialoux et al., 1982) and significantly affects the electrical properties. At 0°C, the electrical resistivity increases by approximately 4.1 μΩ·cm per at. % of oxygen dissolved in Nb (Gmelin, 1970). The superconducting transition temperature T_c decreases by 0.93 K per at. % of oxygen in the Nb matrix (Halbritter, 1987).

Native oxide layer on niobium

The existence of an unavoidable oxide layer at the surface of niobium handled in air or in the presence of oxygen was often mentioned and studied in the literature (see e.g. Halbritter, 1987; Franchy et al., 1996; Graham & Sutherlin, 2001; Grossman et al., 2002; Kovacs et al., 2003; Batchelor et al. 2007). Most of the studies devoted to this subject were conducted in relation to superconducting applications of niobium (see below; Lindau & Spicer, 1974; Halbritter, 1987; Grundner & Halbritter, 1980; Franchy et al., 1996; d'Acapito et al., 2000;

Arfaoui et al., 2002; Ciovati, 2006; Sebastian et al., 2006; Wu, 2006; Batchelor et al. 2007; Yoon et al, 2007; Delheusy et al., 2008). It is frequently suggested that this layer consists of near-stoichiometric Nb_2O_5 with a thickness of about 5-6 nm (Grundner & Halbritter, 1980; Halbritter, 1987; Wu, 2006). However, a niobium surface covered by an oxide layer is a very complex system and other niobium suboxides may be present at the interface between bulk niobium and the Nb_2O_5 layer (Lindau & Spicer, 1974; Grundner & Halbritter, 1980; Halbritter, 1987; Franchy et al., 1996; Delheusy et al., 2008). In addition, some authors mentioned oxide layers as thick as 25 nm (Kovacs et al., 2003) or with a composition deviating from Nb_2O_5 (Sebastian et al., 2006; Yoon et al, 2007). Hence, the composition and thickness of the native oxide layer is not completely clear up to now and depend on the niobium surface (processing techniques used to prepare it, crystallographic orientation) as well as on the ambient oxidation conditions (media to which the Nb surface is exposed, oxygen partial pressure, temperature, duration) (Lindau & Spicer, 1974; Grundner & Halbritter, 1980; Halbritter, 1987; Bai et al., 1996; d'Acapito et al., 2000; Graham & Sutherlin, 2001; Wu, 2006; Batchelor et al. 2007; Yoon et al, 2007). X-ray photoelectron spectroscopy (XPS) and Auger electron spectroscopy analyses seem to show that niobium exposed to air is covered by a NbO_x ($x \sim 1$) interface layer (≤ 1 nm) and a dielectric oxide layer of oxygen-deficient Nb_2O_5 ($\geq$ 2nm) (Grundner & Halbritter, 1980). According to XPS, Halbritter (1987) reported that for properly cleaned niobium, the thickness of the NbO_x ($x \leq 1$) interface layer is almost as large as that of the near-stoichiometric Nb_2O_5 layer after 0.5 h oxidation in air. In contrast, one week oxidation yields a strong increase of the Nb_2O_5 amount with respect to NbO_x (at 300 K, this growth of the Nb_2O_5 layer saturates at about 6 nm). Halbritter (1987) also showed that Ar-ion irradiation favors the formation of perturbed NbO_x ($x \leq 1$) at the expense of Nb_2O_5. More recently, two studies performed on electropolished niobium tips by means of 3-D local-electrode atom-probe tomography came to contradictory results (maybe due to slightly different preparation procedures of the Nb tips). Sebastian et al. (2006) observed a smooth transition from near-stoichiometric Nb_2O to near-stoichiometric Nb_2O_5 on the surface of the Nb tip, whereas Yoon et al. (2007) observed no continuous transition but a surface layer with an almost constant composition which can be interpreted by a mixture of NbO and NbO_2. Moreover, Delheusy et al. (2008) suggested a three-layer model for the native oxide formed after atmospheric pressure oxidation at room temperature, consisting of a sequence of NbO, NbO_2, and finally Nb_2O_5 from the Nb-metal/oxide interface.

Occurrence and applications

Niobium is sometimes regarded as a rare element but is actually more abundant than for instance tin, being widely dispersed in the earth crust with an occurrence of 20 ppm (Nowak & Ziolek, 1999; Griffith & Morris, 2003). In the nature, niobium does not occur as a free element and is generally found together with tantalum in the mineral $(Fe,Mn)M_2O_6$ (M = Nb, Ta) which is called columbite or tantalite, depending on the predominant metal M (Nowak & Ziolek, 1999, see also Eckert et al., 2001, for information on the processing of columbite-tantalite ores and the production of niobium). The principal source is Brazil, followed by Canada. A large majority of the produced niobium metal is used as a toughening and strengthening microalloying / alloying element in the steel industry for pipelines and

automotive and structural applications (Heisterkamp & Carneiro, 2001). Niobium is also an essential constituent for superalloys and more particularly nickel-based supperalloys which are widely used in the aircraft industry and constitute the second largest application of niobium. Niobium-based alloys and pure niobium are also materials of choice for corrosive, high-temperature, and superconducting applications. The oxidation of niobium may play an important role for some of these applications. In addition, niobium oxides and other Nb-based compounds are currently used or investigated for a wide range of sophisticated technology applications, such as solid electrolyte capacitors.

Applications in steels and superalloys

Niobium is added to a wide range of steels for improving processing, microstructure, properties and performance (DeArdo, 2001). The high affinity of niobium towards carbon results in the formation of a very stable carbide which is of great practical interest to optimize steels. Since niobium carbide is formed preferentially to chromium carbide, niobium can for instance be used to stabilize stainless steels against intergranular corrosion by lowering the content of carbon in the steel. Furthermore, the fact that niobium is a strong carbide-forming element is utilised at small niobium contents of 0.01 to maximum 0.20 wt. % for the prevention or the retardation of austenitic grain growth by fine and stable carbides (addition as microalloying element), or, at higher contents, for the formation of wear-resistant carbides (Jeglitsch, 2001). The retardation of the austenite recrystallisation leads to a grain refinement within the steel and consequently to higher strength and toughness (Heisterkamp & Carneiro, 2001). The precipitation of the particularly hard NbC carbide also strengthens the steel by impeding the movement of dislocations (Jeglitsch, 2001). Thus, under certain conditions, the addition of niobium in steel can directly be correlated to an observed yield-strength increase (Heisterkamp & Carneiro, 2001, DeArdo, 2001), even if the precise way through which niobium causes this effect sometimes remains elusive and may involve other mechanisms than grain refinement and precipitation hardening (DeArdo, 2001; Heisterkamp & Carneiro, 2001). Hence, high-strength microalloyed steels containing niobium are widely used for the transportation of oil and gas through pipelines (Heisterkamp & Carneiro, 2001), for building lightweight automobiles thereby reducing fuel consumption (Drewes & Walker, 2001; Heistercamp, 2001), for high rise buildings and for a variety of other special steel applications (Heisterkamp & Carneiro, 2001). Niobium is also well suited as an alloying element, for instance in the production of tool steels (Jeglitsch, 2001) or heat-resisting cast steel auto parts (Hayashi et al., 2001).

Nickel-based superalloys make use of the group 5 and 6 elements, e.g. niobium, which strengthen by solid solution formation, carbide precipitation, and coherent phase formation (Graham & Sutherlin, 2001; Heisterkamp & Carneiro, 2001). Thus, niobium is added to the most important nickel-based superalloys (5.1 wt. % of Nb in Inconel 718, 2.9 wt. % in Inconel 706, 3.6 wt. % in Inconel 625). These superalloys are widely used for aircraft engines, land-based turbines for power generation, chemical processing industries and a variety of applications requiring improved abrasion and corrosion resistance (Heisterkamp & Carneiro, 2001).

Applications as pure metal and as alloy basis

Niobium metal and niobium-based alloys (e.g. niobium-zirconium, niobium-tantalum) are used in industry for numerous applications based on their excellent resistance to a wide variety of corrosive environments (Graham & Sutherlin, 2001). These environments include mineral acids (e.g. nitric acid, phosphoric acid, sulphuric acid under certain conditions), most organic acids (e.g. acetic acid, citric acid, formic acid, lactic acid, tartaric acid), as well as most salts (e.g. chloride solution, seawater) and liquid metals (e.g. sodium, potassium). Due to this high corrosion resistance, niobium and its alloys are applied in more and more chemical processing applications (Graham & Sutherlin, 2001). Like other valve metals, niobium owes its corrosion resistance to the presence of a few nanometers thick, readily formed, adherent, passivating oxide film that may consist of NbO, NbO_2, Nb_2O_5 or a mixture of the three (El-Mahdy, 1997; Graham & Sutherlin, 2001; see above for more information on native oxide layers formed at the Nb surface).

Niobium and niobium-based alloys are also applied as high-temperature materials in a variety of areas such as in aircraft, nuclear and space industries (Hebda, 2001; Heisterkamp & Carneiro, 2001; Menon et al., 2001). The selection of niobium alloys was frequently favored over other refractory metals such as molybdenum, tantalum or tungsten owing to the relatively low density of niobium combined to its good characteristics of ductility at room temperature (Eckert et al., 2001; Heiterkamp, 2001). Indeed, commercial niobium alloys are relatively low in strength and extremely ductile and can be cold-worked over 70% before annealing becomes necessary, resulting in an ease of fabrication into complex parts (Eckert et al., 2001). The alloy C-103, which consists of 10 wt. % hafnium and 1 wt. % titanium added to niobium, is for instance used in rocket propulsion and satellite positioning systems (Hebda, 2001; Heisterkamp & Carneiro, 2001). Niobium alloys are envisaged as a potential new generation of refractory material system that could exceed the application temperatures of nickel-based superalloys (about 1150°C, Menon et al., 2001). However, the use of niobium-based alloys outside a controlled atmosphere is limited by the extremely poor oxidation resistance of niobium and its alloys at elevated temperatures (Hebda, 2001; Menon et al., 2001). The surface niobium-oxide layer formed during the oxidation process is not protective against further oxidation at high temperature (Heisterkamp & Carneiro, 2001). In air, niobium is fully oxidized into the stable high-temperature phase of Nb_2O_5 at temperatures above 1100°C (Gmelin, 1970). To overcome this problem, an oxidation-protection coating may be necessary. Thus, niobium alloys are often extensively coated in special processes, for instance with silicides (Eckert et al., 2001). Niobium can also be alloyed with an element that will oxidize preferentially to form the protective scale. Another approach involves multicomponent Nb-Ti-Si base systems to achieve high-temperature performance (Heisterkamp & Carneiro, 2001; Menon et al., 2001).

Superconducting applications

Superconductors based on niobium are the predominant materials used in practical applications of superconductivity (Krauth, 2001). Niobium exhibits the highest critical temperature of all elements and becomes superconducting at $T_c \sim 9.2\text{-}9.3$ K, which can be increased up to 10 K by strain (Halbritter, 1987; Franchy et al., 1996; Krauth, 2001). It is a

type II superconductor and is characterized at 0 K by a lower, upper, and thermodynamic critical magnetic field $B_{c1} \sim 185$ mT, $B_{c2} \sim 420$ mT, and $B_c \sim 200$ mT, respectively (Seeber, 1998). Also binary (e.g. Nb_3Sn: $T_c = 18{,}5$ K, Nb_3Al: $T_c = 19{,}1$ K, Nb_3Ga: $T_c = 20.0$ K) and ternary (e.g $Nb_{0.75}(GeAl)_{0.25}$: $T_c = 20.7$ K) compounds containing niobium show some of the highest T_c of the classical superconductors (Lindau & Spicer, 1974).

Niobium is the favorite metal for the fabrication of radio-frequency (rf) superconducting cavities for particle accelerators because of its excellent superconducting properties among the pure metals and easy formability (Proch et al., 2001; Ciovati, 2006; Batchelor et al, 2007). Niobium is also widely used as superconductor in the production of Josephson tunnel junctions for electronic applications such as SQUIDS (superconducting quantum interference devices) for very sensitive current and magnetic field sensors (Halbritter, 1987; Krauth, 2001). Nb-based superconducting tunnel junction devices can also be used to detect single photons for astronomical observations (Rando et al., 1996).
However, niobium presents a very high interstitial solubility and binding energy for oxygen, nitrogen, carbon and hydrogen (Grundner & Halbritter, 1980). These interstitial impurities, and particularly oxygen, can strongly deteriorate the superconducting behavior of niobium. For instance, for 1 at. % O homogeneously distributed in Nb, T_c is reduced by 10 % (Halbritter, 1987). Hence, the superconducting applications of bulk niobium, such as rf cavities, require niobium of high purity. In addition, the properties of the surface and near-surface region of niobium are of great interest (Lindau & Spicer, 1974; Schwartz & Halbritter, 1977; Franchy et al., 1996), amongst others because electromagnetic fields have a penetration range into the superconductor which is on the order of 60 nm, so that they can interact with the electronic system of this region (Batchelor et al., 2007; Yoon et al., 2007). The presence of surface oxides like the native oxides mentioned above can particularly affects the superconducting properties of rf cavities and tunnel junctions (Halbritter, 1987; Sebastian et al., 2006; Wu, 2006). Such oxides influence the concentration of oxygen atoms in the bulk and then the superconducting properties of the underlying metal (Arfaoui et al., 2002). In addition, the oxides may not be superconducting. Normal conducting defects in the surface produce heat and may ultimately drive the superconductor above the critical temperature resulting in breakdown of superconductivity (Proch et al., 2001). The evaporation of the interstitials and the achievement of Nb surfaces free of impurities are only possible by heating Nb in ultra high vacuum (UHV) above 2000 K (Halbritter, 1987). Nevertheless, the cooling rate of Nb in UHV is crucial, because a fresh Nb surface is the best (getter) pump in the UHV furnace, and appreciable amounts of impurities, especially O, are picked up by Nb (Halbritter, 1987). In addition, an exposure to air will immediately result in the oxidation of the Nb surface (see above).

The use of superconductors in magnet technology requires high upper critical magnetic fields B_{c2} (Proch et al., 2001). In order to be able to carry large bulk currents and to withstand high magnetic fields, niobium must be magnetically hardened by alloying and by introduction of pinning centers for the magnetic flux (Krauth, 2001). This is successfully achieved in the system NbTi. The commercial standard alloy Nb-47Ti (53 wt. % of Nb, 47 wt. % of Ti)

exhibits a T_c of about 9.6 K and an upper critical field, B_{c2}, of about 11 T at 4.2 K and 14 T at 2 K, respectively. The compound Nb_3Sn is applied at higher magnetic fields. It has a $T_c \approx 18$ K and a B_{c2} up to more than 25 T at 4.2 K depending on the exact chemistry and microstructure (Krauth, 2001). Thus, the Nb-based technical superconductors NbTi and Nb_3Sn have become the most important materials used to produce the high magnetic fields needed for different industrial and scientific applications (Krauth, 2001; Zeitlin, 2001). The most prominent applications are magnetic resonance imaging (MRI) in medicine and nuclear magnetic resonance (NMR) spectroscopy in biology, chemistry, and materials research. Nb-based superconductors are also widely used for high-energy physics apparatus. While pure niobium is applied in rf cavities to accelerate particle beams, superconducting magnets made up with NbTi are used to bend and focus the beams as well as in detectors to analyze particles collisions (Krauth, 2001). Hence, for instance, the large hadron collider (LHC) project at CERN required several hundreds of tonnes of NbTi alloy and several tens of tonnes of pure Nb for superconducting applications (Eckert et al., 2001; Krauth, 2001).

Further applications

Finally, a small fraction of the pure niobium and Nb-based compounds produced in the world is used in a large variety of technological areas such as electronics (e.g. electrolytic capacitors, battery alloys, piezoelectric devices), medical science (e.g. surgical implants), photonics (e.g. thin films), or catalysis (Eckert et al., 2001; Heisterkamp & Carneiro, 2001). Owing to its good biocompatibility and bone-bonding capability, Nb metal is for instance an attractive material for hard tissue replacements (Godley et al., 2004). Nb metal can also be used in metal insulator metal (MIM) tunnel diodes (Grossman et al., 2002), as electrode material for the construction of an impedimetric immunosensor (Helali et al., 2008), as well as to form anodes in solid electrolytic capacitors (Störmer et al., 2006; see also subchapter 2.2). Numerous Nb-compounds are for instance of great interest in heterogeneous catalysis where they are used as catalyst components or added to small amounts to catalysts (Nowak & Ziolek, 1999). In addition, binary oxides consisting of niobium and oxygen find numerous applications, e.g. in electronics, optics, or sensor technology. Some examples are given in more detail in the following sections. At last, it can be added that complex niobium-oxide phases made up of niobium and oxygen together with another element, e.g. an alkaline-earth or alkali metal, present a rich crystal chemistry (Turzhevsky et al., 1994). This results in a wide variety of materials with different, and sharply changeable with composition, peculiarities of electronic structure, state distributions, chemical bonding, and magnetic and electric characteristics, which may also be of great interest for application purposes (Turzhevsky et al., 1994).

2.1.2 The lower oxides of niobium: NbO_x with $0 < x \leq 2$

NbO_x with $0 < x < 1$

Oxygen is easily dissolved in the bcc lattice of niobium, yielding a so-called α-solid solution (Norman, 1962; Gmelin, 1970; Halbritter, 1987), but as already mentioned in section 2.1.1 this solubility is limited to a certain oxygen concentration which increases with temperature. However, niobium under certain conditions can take up more oxygen than that correspondent saturation value, and this supersaturation may allow the formation of suboxide phases (Norman, 1962). Thus, three different suboxides can be observed with stoichiometries between those of Nb and NbO. These oxides, referred to as NbO_x, NbO_y, and NbO_z, form only by oxidation of niobium, or by ageing of niobium that is supersaturated with oxygen in definite ranges of temperature and oxygen pressures (Niebuhr, 1966). In the supersaturated α-solid solution, NbO_x, NbO_y, and NbO_z represent consecutive precipitation steps occurring to relax strain (Niebuhr, 1966; Gmelin, 1970; Halbritter, 1987). They are metastable, appear to have metallic character, and present superlattice structures related to the original niobium-metal lattice (Brauer et al., 1962; Norman, 1962; Niebuhr, 1966; Gmelin, 1970). NbO_x forms at 270-500°C and contains an oxygen concentration between about 2.6 and 3.6 wt. %, corresponding to the ideal formula Nb_6O with a wide homogeneity range. NbO_y forms at 330-500°C and may correspond to the formula Nb_4O. NbO_z forms at 400-700°C and its exact composition is unknown (Niebuhr, 1966; Gmelin, 1970).

Niobium monoxide (NbO)

At the composition NbO, the original lattice of the Nb metal breaks down completely and a new crystal structure occurs (Gmelin, 1970). The stable niobium monoxide phase NbO exhibits a defective rock-salt structure with 25% ordered vacancies in the Nb- and O-sublattices which can be described by the space group $Pm\bar{3}m$ (no. 221) (Gmelin, 1970; Pialoux et al., 1982). Thus, among all transition-metal monoxides, the structure of NbO presents the highest number of point defects and is unique in that the Nb atoms are coordinated to only four O atoms in a square planar array (Gannon & Tilley, 1977; Kurmaev et al., 2002). NbO has a density of ~ 7.3 g/cm^3 and melts at about 1935-1945°C (Elliott, 1960; Niebuhr, 1966). In NbO, the Nb atoms occur in a formal oxidation state of +2 and their electronic configuration is assumed to be [Kr].4d^3. The electronic properties of Nb and its oxides are defined by the d-electrons of Nb. In oxidation, O covalently binds these conduction electrons depleting the conduction band (Halbritter, 1987). Hence, with respect to bulk Nb, the density of conduction electrons is already reduced in NbO and NbO_2, and Nb_2O_5 is finally insulating (Halbritter, 1987). However, NbO still exhibits a very high room-temperature conductivity characteristic of metallic behavior (Rao et al., 1970; Hulm et al., 1972). According to Hulm et al. (1972), its electrical resistivity amounts to about 21 μΩ·cm at 25°C (corresponding to a conductivity around $4.8 \cdot 10^4$ S/cm). Moreover, stoichiometric NbO becomes superconducting below the transition temperature T_c ~ 1.61 K (Okaz & Keesom, 1975). In addition, Hulm et al. (1972) observed that a composition deviation as little as 0.5 at. % on the low-oxygen (niobium-rich) side of stoichiometric NbO results in a sharp increase of T_c up to about 6 K (however, it should be noted that the results of Okaz & Keeson

(1975) are not in agreement with this observation). Indeed, contrary to other transition-metal monoxides like for instance TiO or VO, NbO does not present a large extension of the single-phase field (Brauer, 1941; Rao et al., 1970; Hulm et al., 1972; Okaz & Keesom, 1975). Hence, according to X-ray studies, Hulm et al. (1972) observed that a composition deviation by as little as 0.5 at. % on either side of stoichiometric NbO produces a mixed-phase sample (see section 5.4.5 for more information on the existence range of NbO).
Owing to its metallic conductivity, NbO is used in Nb-based electrolytic capacitors, where it can advantageously replace Nb-metal as anode material (Qiu et al., 2002; Li et al., 2006; Olszta & Dickey, 2008; see also subchapter 2.2).

Niobium dioxide (NbO_2)
At room temperature the stable niobium dioxide NbO_2 is a tetragonal crystal with a distorted rutile structure in which chains of edge-sharing NbO_6 octahedrons are cross-linked by corner-sharing (Cheetham & Rao, 1976). The corresponding space group is $I4_1/a$ (no. 88) and NbO_2 has a density of approximately 5.9 g/cm^3 (Gmelin, 1970). At ~ 800-810°C NbO_2 undergoes a reversible second-order phase transition resulting at high temperature in a regular rutile structure (Gmenlin, 1970; Pialoux et al., 1982; Jiang & Spence, 2004). According to Elliott (1960), NbO_2 melts at about 1915°C. The formal Nb-oxidation state of NbO_2 is +2 and the corresponding electronic structure is [Kr].4d^1. At room temperature NbO_2 is a n-type semiconductor characterized by a conductivity of the order of 10^{-4} S/cm and a small band gap of approximately 0.5 eV (Adler, 1968; Gmelin, 1970). The above-mentioned phase transition is accompanied by a change in the electric properties and NbO_2 becomes a metallic conductor above ~ 800-810°C (Adler, 1968; Cheetham & Rao, 1976; Naito et al., 1980). NbO_2 appears to deviate slightly but measurably from stoichiometry at high temperatures. For instance, according to Marucco et al. (1976), the composition range of NbO_2 in thermodynamic equilibrium goes from $NbO_{2.000}$ to $NbO_{2.006}$ at 1100°C (see section 5.4.5 for more information on the existence range of NbO_2). In addition, Schäfer et al. (1969) reported that very small composition deviations with respect to stoichiometric $NbO_{2.000}$ can significantly influence the electrical conductivity at room temperature.
NbO_2 finds applications in diverse technological areas, as shown for instance by two recent studies (Helali et al., 2008; Sasaki et al., 2008). NbO_2 can for instance be used together with Nb metal to form electrodes for impedimetric immunosensors (Helali et al., 2008). Owing to the excellent chemical stability of NbO_2 in acid solutions, NbO_2 nanoparticles can also be used in the synthesis of high-activity $Pt/NbO_2/C$ electrocatalysts for oxygen-reduction reaction (ORR) in proton exchange membrane fuel cell (PEMFC). Sasaki et al. (2008) demonstrated that these new NbO_2-based electrocatalysts exhibit enhanced ORR performances compared to commercial Pt/C electrocatalysts, which should allow to improve the efficiency of the energy conversion in PEMFCs. Simultaneously, the use of NbO_2 enables to lower the noble-metal (Pt) content in the electrocatalysts. In addition, it was also shown that the electrocatalysts synthesized with NbO_2 nanoparticles show better performances than those based on Nb_2O_5 nanoparticles, probably because of the different electronic structures and electric properties of the two oxides.

2.1.3 Niobium pentoxide (Nb_2O_5) and the oxides Nb_2O_{5-y} with $0 < y < 1$

Polymorphism and non-stoichiometric phases

From the energetic point of view, the pentoxide Nb_2O_5 is the most stable niobium oxide, even more stable than NbO and NbO_2 which nevertheless also have a large negative free energy of formation themselves (Gmelin, 1970; Lindau & Spicer, 1974; Venkataraj et al., 2002). Nb_2O_5 occurs in an amorphous and several crystalline modifications with complex structures (see, e.g., Schäfer et al., 1966; Gmelin, 1970; Kato & Tamura, 1975; Ann McConnell et al., 1976; Kato, 1976; Hibst & Gruehn, 1978; Heurung & Gruehn, 1982; Meyer & Gruehn, 1982c; Brayner & Bozon-Verduraz, 2003). To identify the different crystalline modifications, various nomenclatures using Roman or Greek letter prefixes were reported (Gatehouse & Wadsley, 1964; Gmelin, 1970; Rosenfeld et al., 1994). In the following, the most commonly used terminology is employed, which was introduced by Brauer (1941) and completed (amongst others) by Schäfer et al. (1966).

The "high-temperature" monoclinic phase H-Nb_2O_5 is the thermodynamically most stable Nb_2O_5 modification and more generally the most stable niobium-oxide form. Hence, the Nb-O system prefers to form this most favorable state under equilibrium conditions if enough oxygen is available (Venkataraj et al., 2002). It is the case in air where niobium and all its different oxides (inclusive the various Nb_2O_5 polymorphs) are fully oxidized and transformed into the H-Nb_2O_5 modification at high temperatures above ~1000-1100°C, at which the atoms become mobile enough to kinetically allow these structural rearrangements and changes in stoichiometry (Schäfer et al., 1966; Gmelin, 1970; Rosenfeld et al., 1994; Venkataraj et al., 2002). H-Nb_2O_5 belongs to the space group P2 (no. 3) and is characterized by a monoclinic unit cell containing 14 formula units, i.e. 28 Nb atoms and 70 O atoms (Gatehouse & Wadsley, 1964). The structure contains 3 × 4 and 3 × 5 ReO_3-type blocks of corner-shared NbO_6 octahedron. These blocks are joined by octahedral edge-sharing into a three-dimensional structure leaving tetrahedral sites partly, but systematically, occupied by one Nb atom out of the 28 in each unit cell (Gatehouse & Wadsley, 1964). In addition to the high-temperature phase, Nb_2O_5 also exists in a multitude of other crystalline polymorphic forms, whose occurrence strongly depends on the preparation method and on annealing conditions and which can present different properties (see, e.g., Schäfer et al., 1966; Gmelin, 1970; Rosenfeld et al., 1994; Nowak & Ziolek, 1999; Brayner & Bozon-Verduraz, 2003). Thus, Schäfer et al. distinguished in 1966 between TT-, T-, B-, M-, H-, N-, and P-Nb_2O_5, and the same year Gruehn (1966) observed another modification called R-Nb_2O_5. Numerous further phases were reported later on. For instance, Hibst & Gruehn (1978) and Meyer & Gruehn (1982c) observed 15 and five new metastable Nb_2O_5 modifications, respectively, by investigating the products of diverse oxidation procedures of NbO_x phases ($2,4 < x < 2,5$). Like H-Nb_2O_5, many polymorphs are related to the ReO_3 structure (N-Nb_2O_5, e.g., consists of 4 × 4 blocks of corner-shared NbO_6 octahedrons; Ann McConnell et al., 1976). Nevertheless, some other polymorphs present entirely different structures like for instance the orthorhombic "low-temperature" T-Nb_2O_5 phase, whose Nb atoms are mainly surrounded by seven or six O atoms forming pentagonal bipyramids or distorded octahedrons respectively, while the few remaining Nb atoms are coordinated to nine O atoms in interstitial sites (Kato & Tamura,

1975; Nowak & Ziolek, 1999). Furthermore, it should be noted that besides the numerous crystalline phases, Nb_2O_5 can be also prepared in an amorphous state. Slightly distorted NbO_6, NbO_7 and NbO_8 sites were reported as structural units in amorphous Nb_2O_5 (Nowak & Ziolek, 1999).

Based on the principle of crystallographic shear which allows accommodation of stoichiometric changes by structural adjustment that preserves the cation coordination (e.g. by changing the way to join octahedrons with one another: by sharing edges or by sharing corners), the above mentioned stoichiometric Nb_2O_5 polymorphs are accompanied by the possibility to build non-stoichiometric Nb_2O_{5-y} phases (Andersson & Wadsley, 1966; Ann McConnell et al., 1976; Halbritter et al., 1987). Hence, two homologous series of structurally related niobium-oxide phases were distinguished between NbO_2 and Nb_2O_5 with the general formulas $Nb_{3n+1}O_{8n-2}$ (whose member n = 9 is Nb_2O_5) and $Nb_{3n}O_{8n-3}$ (however it should be noted that only few members of each series effectively exist; Gatehouse & Wadsley, 1964; Gmelin, 1970; Kimura, 1973). More especially in the range of $Nb_2O_{4.8}$ to Nb_2O_5, metastable niobium-oxide phases of five different compositions are reported, which can be members of one of the homologue series or be composed of a combination of the structural units of "neighbor" oxides (see e.g., Schäfer et al., 1969; Gmelin, 1970; Kimura, 1973; Hussain et al., 1986). They correspond to the ideal composition formulas $Nb_{12}O_{29}$ (member n = 4 of the $Nb_{3n}O_{8n-3}$ series), $Nb_{22}O_{54}$ (member n = 7 of $Nb_{3n+1}O_{8n-2}$, sometimes termed $Nb_{11}O_{27}$ in the literature), $Nb_{47}O_{116}$ (whose structure is probably a combination of those of $Nb_{22}O_{54}$ and $Nb_{25}O_{62}$; Gruehn & Norin, 1969), $Nb_{25}O_{62}$ (member n = 8 of $Nb_{3n+1}O_{8n-2}$), and $Nb_{53}O_{132}$ (whose structure is probably a combination of those of $Nb_{25}O_{62}$ and H-Nb_2O_5; Gruehn & Norin, 1967). These crystalline oxides are mainly constructed with blocks of NbO_6 octrahedras and, as a minor part, with NbO_4 tetrahedrons (Gmelin, 1970; Kimura, 1973). They are likely to appear only under certain conditions, and some of them can crystallize in different phases or present extended composition ranges (see, e.g., Schäfer et al., 1969; Gmelin, 1970; Naito et al., 1980; Hussain et al., 1986). Hence, $Nb_{12}O_{29}$ can for instance exist in a monoclinic or an orthorhombic phase depending on its preparation temperature (Hibst & Gruehn, 1978; Hussain et al., 1986), and according to Kimura (1973), the existence range of $Nb_{22}O_{54}$ extends from $NbO_{2.448}$ to $NbO_{2.454}$ at 1300°C.

Physical properties

The physical properties of Nb_2O_5 can sometimes be confusing, since they may depend on the considered Nb_2O_5 phase as well as on its formation procedure (see, e.g., Gmelin 1970). According to Elliott (1960), Nb_2O_5 melts at about 1495°C. Whereas the density of H-Nb_2O_5 and some other crystalline pentoxide modifications is around 4.5 g/cm^3, values up to approximately 5.3 g/cm^3 were reported for B-Nb_2O_5 (Gruehn, 1966; Schäfer et al., 1966; Gmelin, 1970; Halbritter, 1987). In the case of amorphous Nb_2O_5, a value of 5.12 g/cm^3 is given by Schäfer et al. (1966), but lower values down to 4.36 g/cm^3 were also reported depending on the formation procedure (Gmelin, 1970; Venkataraj et al., 2002). Halbritter (1987) even mentioned a density as low as 3.4 g/cm^3 for a so-called "microcrystalline amorphous" Nb_2O_5 with a high concentration of defects. The formal Nb-oxidation state of Nb_2O_5 is +5 and the corresponding electronic structure of the Nb atoms is [Kr].4d^0, i.e. all of

the d-electrons have been transferred to the O 2p-band and the Nb 4d-band is empty (Kurmaev et al., 2002). As a result, Nb_2O_5 is insulating (Halbritter, 1987). The experimental band-gap width of Nb_2O_5 is generally measured in the order of 3.3 eV to 3.9 eV (Ghanashyam Krishna & Bhattacharya, 1999; Kurmaev et al., 2002; Venkataraj et al., 2002; Brayner & Bozon-Verduraz, 2003; Lira-Cantu et al., 2006). However, in the case of passive films, values as high as 5.2 eV are reported (Schultze & Lohrengel, 2000). Moreover, Brayner & Bozon-Verduraz (2003) experimentally observed an increase of the band gap from 3.4 eV to 4.2 eV as the size of the measured Nb_2O_5 particles decreases from about 40 nm to 4.5 nm, and they ascribed this modification to a quantum-size effect. The dielectric constant ε_r of Nb_2O_5 depends on the investigated modification and in case of crystalline Nb_2O_5 may be strongly anisotropic (see, e.g., Gmelin, 1970). Hence, Cho et al. (1994) reported for instance that the dielectric constant of a single Nb_2O_5 crystal with the T-type structure varies from 60 to 200 depending on the orientation, while H-Nb_2O_5 has a dielectric constant of approximately 100. For monocrystalline Nb_2O_5 lower values in the range of 35 to 50 can also be found in the literature (Kukli et al., 2001). The dielectric properties of amorphous Nb_2O_5 are not perfectly clear and can depend on the formation conditions of the oxide (Cavigliasso et al., 1998; Masse et al., 2006). Thus, in the case of anodic oxide films, Cavigliasso et al. (1998) determined dielectric constants in the range of 49 to 120 depending on the forming electrolyte. However, the most generally accepted value for the dielectric constant of amorphous Nb_2O_5 is in the order of 41, which is often taken as a reference while comparing Nb_2O_5 to other insulating oxides for dielectric applications (Schwartz et al., 1961; Zillgen et al., 2002; Fischer, 2005; Zednicek et al., 2005; Störmer et al., 2009; the values $\varepsilon_r \sim 42$ or 43 are given in the following references: Eckert et al., 2001; Kovacs et al., 2003; Kim et al., 2005). A very wide range of values is found in the literature for the conductivity of Nb_2O_5. For instance, Macek & Orel (1998) mentioned a conductivity of about 10^{-11}–10^{-12} S/cm (however it is not clear whether these values apply to amorphous Nb_2O_5, to TT-Nb_2O_5, or to both), whereas Schäfer et al. (1969) measured a quite high value (for an insulator) of $3 \cdot 10^{-6}$ S/cm for the crystalline H-Nb_2O_5 phase, and Cavigliasso et al. (1998) determined lower values in the range of $1 \cdot 10^{-13}$ to $9 \cdot 10^{-13}$ S/cm for amorphous Nb_2O_5 films formed by anodic oxidation. Another low value of $1 \cdot 10^{-16}$ S/cm is reported at room temperature for amorphous Nb_2O_5 by Fischer (2005) who summarized some literature data on the conductivity of stoichiometric and near-stoichiometric Nb_2O_5. Nevertheless, it is well accepted in the literature that the Nb_2O_5 conductivity is strongly affected by deviations in stoichiometry (Gmelin, 1970; Halbritter, 1987; Kukli et al., 2001). Small oxygen deficiencies can result in a strong increase of the conductivity accompanied by a n-type semiconducting behavior (see, e.g., Schäfer et al., 1969; Marucco, 1974; Naito et al., 1980). According to Schäfer et al. (1969) H-Nb_2O_5 is characterized at 1300°C by an extremely narrow single-phase field extending from $NbO_{2.489}$ to $NbO_{2.500}$ (see section 5.4.5 for more information on the existence range of Nb_2O_5). At room temperature the authors measured a very sharp increase of the conductivity σ as the composition O/Nb decreases from 2.500 (pure stoichiometric Nb_2O_5, $\sigma = 3 \cdot 10^{-6}$ S/cm), 2.495 ($\sigma = 4 \cdot 10^{1}$ S/cm), to 2.489 ($\sigma = 3 \cdot 10^{3}$ S/cm). In their thermodynamic studies of the system NbO_2-Nb_2O_5 at high temperatures, Marucco (1974) and Naito et al. (1980) also observed an increase of the conductivity with decreasing O/Nb ratio. These

observations could be correlated to oxygen-vacancies and niobium-interstitial defects and they do not only concern the phase field of Nb_2O_5 but also all intermediate regions between NbO_2 and Nb_2O_5 (Schäfer et al., 1969; Kimura, 1973; Marucco, 1974; Naito et al., 1980; Halbritter, 1987). Hence, the different sub-stoichiometric Nb_2O_{5-y} metastable phases ($0 < y < 1$) show n-type semiconductivity (Gmelin, 1970; Marucco, 1974; Naito et al., 1980). Schäfer et al. (1969) measured the following conductivities at room temperature: $3 \cdot 10^2$ S/cm for $Nb_{53}O_{132}$ (O/Nb ~ 2.491), $5 \cdot 10^2$ S/cm for $Nb_{25}O_{62}$ (O/Nb ~ 2.480), and $2 \cdot 10^3$ S/cm for $Nb_{12}O_{29}$ (O/Nb ~ 2.417). Thus, the stoichiometry plays a major role in the use of Nb_2O_5 for dielectric applications.

Applications

Nb_2O_5 (amorphous or crystalline) presents a wide spectrum of technical applications, ranging from catalysis to biomaterial, sensor, optical, and microelectronic applications. For instance, Nb_2O_5 (notably in the form of nanoparticles) can be used as catalyst for the hydrogen storage properties of magnesium (Friedrichs et al., 2006; Hanada et al., 2006; Hanada et al., 2007) and for oxygen-reduction reactions in proton exchange membrane fuel cells (Sasaki et al., 2008; see also in section 2.1.2 the paragraph concerning the applications of NbO_2). More especially, amorphous hydrated niobium pentoxide $Nb_2O_5 \cdot nH_2O$ (also called niobic acid) shows high catalytic activity, selectivity, and stability for acid-catalyzed reactions in which water molecules participate or are liberated (Nowak & Ziolek, 1999; Brayner & Bozon-Verduraz, 2003; Tanabe, 2003; for more information on the structure of hydrated niobium oxide, see also Ushikubo et al., 1996). Several examples of reactions catalyzed by niobic acid are developed by Tanabe (2003), including esterification, hydrolysis, hydration, dehydration, condensation and alkylation reactions.

Nb_2O_5 is a valuable candidate for biomaterial applications due to its high resistance to corrosion, thermodynamic stability and low cytotoxicity (Velten et al., 2004; Karlinsey, 2006). Thus, Nb_2O_5 coatings (thickness < 200 nm) produced by means of the sol-gel process were found to be well biocompatible, and depending on their purity and topographical properties at the nanometer scale, they induce a range of desirable cellular responses and may therefore have direct applications in bone tissue engineering (Velten et al., 2004; Eisenbarth et al., 2007).

Depending on their thickness, Nb_2O_5 films present sensing properties which may be applied in different types of humidity, oxygen and hydrogen sensors (Kurioka et al., 1993; Rosenfeld et al., 1993; Hyodo et al., 2006). Furthermore, Nb_2O_5 is studied for applications in electrochemical biosensors for detecting DNA hybridization events with high sensitivity (Rho et al., 2008).

Nb_2O_5 finds diverse optical applications owing to its high refractive index and low optical absorption in the visible and near-infrared light range combined with its good chemical and thermal stability as well as its good mechanical and corrosion resistance (Lai et al., 2005; Masse et al., 2006). Hence, in order to achieve a high refractive index and good chemical resistance against environmental influences, Nb_2O_5 can for instance be added up to 30 % in optical glasses for special lenses (Eckert et al., 2001). Nb_2O_5 also plays an important role as one of the components that are substituted for lead oxide PbO to produce “environmental

friendly" optical glasses (Morishita & Onozawa; 2001). Moreover, the addition of Nb_2O_5 in large amount in borophosphate glasses was shown to result in promising materials for optical amplification devices for long-distance communication systems (Petit et al., 2006). Owing to their nonlinear optical properties, Nb_2O_5-based glasses are also possible candidates for optical switching (Royon et al., 2007). Further optical applications making use of Nb_2O_5 in the form of thin films concern, e.g., optical waveguides, anti-reflective coatings and high quality optical interference filters (Lai et al., 2005; Leitel et al., 2006; Masse et al., 2006). Finally, the crystal-structure dependent electrochromic properties of Nb_2O_5 layers are studied for applications in so-called "smart windows" that change their optical properties (transmittance or reflection) in a reversible manner when a voltage is applied and a current flows through them (Macek & Orel, 1998; Orel & al., 1998; Heusing et al., 2006).
Due to its high dielectric constant, Nb_2O_5 is an attractive insulator to replace the conventional dielectric oxides in microelectronic devices (Masse et al., 2006). For instance, dielectric Nb_2O_5 nanolayers can find applications in complementary metal-oxide-semiconductor (CMOS) devices, in metal-insulator-metal (MIM) tunnel diodes, or in MIM capacitors with high capacitance density (Kukli et al., 2001; Grossman et al., 2002; Kim et al, 2005; Matsui et al., 2005). In addition, a high technological potential has also been attributed to Nb-based solid electrolyte capacitors with Nb_2O_5 dielectric layers formed by anodic oxidation on Nb or NbO (Zillgen et al., 2002; Zednicek et al., 2005; see also subchapter 2.2).
Some of the main examples of (possible) applications of Nb_2O_5 were given above, but the list is not exhaustive. Other applications include, e.g., the use of Nb_2O_5 as thin film in hybrid solar cells (Lira-Cantu et al., 2006) or as dopant in functional ceramic materials, for instance to control the phase-transitional behavior of lead zirconate titanate (PZT) ceramics (Sun et al., 2001).

2.1.4 Summary

In this subchapter it has been shown that the niobium-oxygen system is particularly rich. Niobium oxides already find a multitude of practical applications and are investigated to enable new ones. Since the properties of niobium oxides can change dramatically as a function of their stoichiometry, many of these applications depend on the precise composition of the employed oxides. In addition, the strong relationship between niobium and oxygen can also play an important role in the use of niobium and niobium-based alloys for corrosive, high-temperature and superconducting applications. Furthermore, the different applications of niobium and its oxides often involve components/defects of submicrometric size. Hence, a tool allowing the investigation of the stoichiometry of niobium oxides at a nanometer scale can be of great practical interest. The example of the application of niobium and niobium oxides in solid-electrolyte capacitors is developed in more details in the following subchapter.

2.2 Nb-based solid electrolyte capacitors

High-capacitance surface mounted device (SMD) solid electrolyte capacitors are widely used as, e.g., buffer, smoothing, or filter elements in small electronic devices. They find applications in personal computers and notebooks, cellular phones, digital cameras as well as in the automotive and telecommunication industries (Park & Lee, 2004; Zednicek et al., 2005). These passive components are commonly made of tantalum (Ta) as anode material and of tantalum pentoxide (Ta_2O_5) as the dielectric, where amorphous Ta_2O_5 layers are formed on porous Ta-metal power compacts by anodic oxidation. The capacitance in these capacitor structures is given in a rough approximation by $C = \varepsilon_r \cdot \varepsilon_0 \cdot A/d$ (parallel-plate model) with the permittivity of the dielectric ε_r (also termed dielectric constant), the vacuum permittivity ε_0, the overall area A and the thickness d of the dielectric layer (Störmer et al., 2009). Such Ta-based capacitors offer high reliability and volumetric efficiency (high capacitance per unit of volume, Persico et al., 2001; Qiu et al., 2001). However, owing to the steadily increasing demand and the relative scarcity of tantalum in the nature, alternative material systems were/are searched to supplement the Ta-Ta_2O_5 technology (Schwartz et al., 1961; Persico et al., 2001; Qiu et al., 2001).

2.2.1 Fabrication process

In principle, every conducting metal may be an appropriate substitute for Ta, provided that it presents a good electrical conductivity and that its surface can be completely covered by a homogeneous dielectric oxide layer. The valve metal niobium, which appears next to tantalum in the same group of the periodic table, has always been considered as a logical substitute since it has similar chemical properties and, more particularly, a similar behavior under anodization (see, e.g., Schwartz et al., 1961; Fischer et al., 2003; Zednicek et al., 2004; Störmer et al., 2006). Thus, niobium-based solid electrolyte capacitors present the advantage that they can be produced using a fabrication process similar to that employed in the well-established Ta-capacitor technology. The main steps of the fabrication are represented in Fig. 2.2.1 (see also, e.g., Fischer, 2005; Störmer et al., 2006). A high-purity niobium metal powder with high specific surface area is pressed and sintered into a porous niobium anode. During the pressing, a tantalum wire is embedded into the powder to ensure electrical contact (the mechanical properties of niobium wires are not sufficient for that use, Fischer et al., 2002). Then, amorphous nanoscale dielectric oxide layers (thickness of the order of 100 nm, expected to consist of Nb_2O_5) are formed on the sintered niobium compact by two anodic oxidation steps occurring in an aqueous electrolyte solution and separated by a thermal annealing process in air. In a next step, the anodized porous body is equipped with a solid electrolyte cathode. Manganese dioxide (MnO_2) is mainly chosen as cathode material (partly because of its interesting "self-healing" ability, see e.g. Djebara & Nguyen, 2004; Pala, 2005). It is applied by impregnation with an aqueous manganese nitrate ($Mn(NO_3)_2$) solution and subsequent pyrolysis at elevated temperatures. The MnO_2 cathode is contacted by means of

further coatings consisting of graphite and silver paints and the whole capacitor is finally encapsulated into epoxy resin.

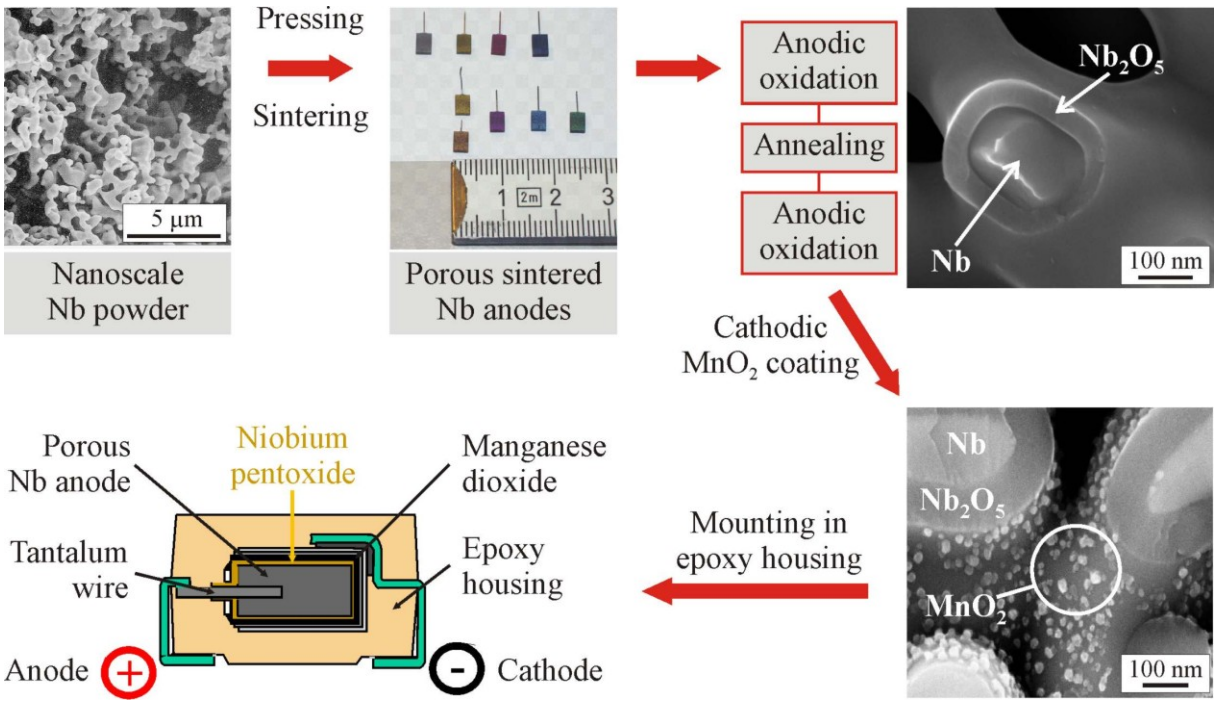

Fig. 2.2.1. Main steps of the fabrication process of Nb-based solid electrolyte capacitors. Anode material: sintered niobium powder. Dielectric material: anodically grown niobium pentoxide. Cathode material: manganese dioxide. Adapted from Fischer (2005).

2.2.2 Advantages of Nb over Ta

The Nb-Nb_2O_5 material system presents different advantages over Ta-Ta_2O_5. Nb has approximately half the density of Ta, which offers both economic and weight advantages (Schwartz et al., 1961). Furthermore, Nb_2O_5 is characterized by a higher dielectric constant of ($\varepsilon_{rNb2O5} \sim 41$, see section 2.1.3 for more information on the dielectric constant of amorphous Nb_2O_5) than Ta_2O_5 ($\varepsilon_{rTa2O5} \sim 27$, Schwartz et al., 1961; Zillgen et al., 2002). This is particularly interesting for capacitor applications, since the capacitance increases with the dielectric constant. However, besides the capacitance, the maximal voltage that can be applied to the capacitor is another important performance parameter. The rated voltage of the solid electrolyte capacitors depends on the formation voltage of their dielectric oxide layers. Thus, from a miniaturization point of view, the advantage of the high dielectric constant of Nb_2O_5 is partly cancelled by the higher oxide growth rate per volt of Nb_2O_5 compared to that of Ta_2O_5 (typical oxidation constants around 3 nm/V and 2 nm/V, respectively, but these values may depend on other anodization parameters like the temperature or the forming electrolyte, Schwartz et al., 1961; Cavigliasso et al., 1998; Eckert et al., 2001; Kovacs et al., 2003; Störmer et al., 2006) resulting in thicker oxide layers at a given formation voltage (the capacitance decreases with increasing dielectric-layer thickness d). Nevertheless, the fact that the Nb_2O_5 dielectric grows thicker than Ta_2O_5 also has one advantage: the dielectric operates

at lower field strength for a given voltage rating (lower electrical stress, Yi, 2003; Zednicek et al., 2003).
Thus, the main advantage of Nb is its much higher abundance in the nature compared to Ta (estimates range from 30 to 100 times more abundant, Persico et al., 2001) yielding significantly lower raw-material price.
Moreover, with respect to the lead-free and restriction of hazardous substances (RoHS) regulations, the Nb-based capacitor technology also presents some advantages over that relying on aluminium (see, e.g., Yi, 2003; Pala, 2005).

2.2.3 Problems and solutions

Nb was considered as a possible alternative to Ta in electrolyte capacitors already in the early sixties of the past century (Shtasel & Knight, 1961; Schwartz et al., 1961; Ling & Kolski, 1962). However, a broader industrial use of Nb for the fabrication of high-performance capacitors has long been prevented by the lack of sophisticated Nb powders (Eckert et al., 2001). Indeed, solid electrolyte capacitor applications require Nb powders of high chemical purity with a high specific surface area which allows the storage of high charges (capacitance proportional to the overall area A; Schnitter et al., 2003). These difficulties were overcome a few years ago by leading capacitor powder producing companies (Eckert et al.; Zillgen et al., 2002). By means of a new process based on magnesium vapor reduction it is now possible to manufacture Nb powders with physical properties comparable to commercially used capacitor-grade Ta powders (see, e.g., Eckert et al., 2001; Schnitter et al., 2003; Störmer et al., 2006). As a consequence, commercial Nb-based capacitors that have the potential to replace Ta capacitors in certain fields of application were launched on the market within the last few years (Zillgen et al., 2002; Zednicek et al., 2004).

However, the first Nb-based solid electrolyte capacitors proved to have instable and potentially large direct leakage currents (DCL) as well as large equivalent series resistances (ESR) compared to typical Ta-based capacitors (Persico et al., 2001; Li et al., 2006). These problems are attributed to the complexity of the Nb-O system (see subchapter 2.1). Indeed, one drawback of Nb over Ta is its stronger chemical affinity to oxygen and the existence of its numerous suboxides beside the desired Nb_2O_5, resulting in a more pronounced sensitivity of the Nb-based capacitor to thermal processing damage (Smyth & Tripp, 1966; Qiu et al., 2002; Kovacs et al., 2003). Oxygen presents a high thermally driven diffusion rate in Nb systems and tends to migrate into the Nb-metal anode, degrading the insulating properties of the dielectric (which are highly sensitive to O-deficiencies, see section 2.1.3) and thus the capacitor performance (Qiu et al., 2002; Yi, 2003; Prymak et al., 2004). The electrical characteristics and thermal stability of Ta-based capacitors could be greatly improved by a heat-treatment step after the anodic oxidation to saturate the tantalum anode adjacent to the oxide layer with oxygen. A second anodic oxidation step restores the desired Ta_2O_5 stoichiometry of the dielectric layers (Persico et al., 2001). However, Nb exhibits a much higher oxygen solubility than Ta, and an annealing step between the anodic oxidation steps is

not sufficient to produce a thermally stable anode / dielectric interface (Persico et al., 2001). In addition, after the last anodic oxidation step the anode / dielectric system is required to endure extreme process conditions with repeated high-temperature cycling, for instance during the application of the MnO_2-cathode or during (lead-free) solder reflow to ensure the connection between the SMD capacitor and a printed circuit board (Qiu et al., 2001; Fischer, 2005; Pala, 2005). Thus, the performance of the Nb-based capacitors may be affected by thermal instabilities from the very beginning of their life and it is particularly important to understand the influence of heat treatments on the stoichiometry of the anodic oxide layers.

If the Nb/Nb_2O_5 system is heat treated in air, a steady state may occur, owing to a process in three steps (see, e.g., Qiu et al., 2002): 1) oxygen is removed from the oxide by the Nb anode, leaving the adjacent oxide oxygen-deficient; 2) oxygen vacancies diffuse across the oxide to the outer surface; 3) at the surface the vacancies are filled by oxygen from the ambient air. Hence, this is expected to result in a gradient of oxygen vacancies across the oxide layer, with the highest value adjacent to the anode (Qiu et al., 2002). The dramatic effects that even a very small oxygen deficiency can have on the electrical properties of Nb_2O_5 were already mentioned in section 2.1.3 (see, e.g., Schäffer et al., 1969). In addition, further Nb suboxides like NbO and NbO_2 which have completely different properties compared to Nb_2O_5 could form at the Nb/Nb_2O_5 interface. In order to explain the results of capacitance measurements performed after heat treatment on Nb/Nb_2O_5 capacitor structures, several authors proposed a schematic model relying on a significant diminution of the width of the effective dielectric layer (Qiu et al., 2002; Fischer, 2005; Störmer et al., 2009; see also Fig. 5.4.3). The parts of the oxide layer whose conductivity exceeds a certain value σ_0 are considered to have no capacitive electrical response anymore but a purely resistive one and thus to act as an extension of the electrode (Smyth & Tripp, 1966). The parts with a conductivity lower than σ_0 act as dielectric. In terms of oxygen deficiency, this corresponds to an oxide region with high oxygen deficiency adjacent to the Nb-metal, which "electrically acts" as anode, and to an outer oxide region with lower deficiencies, which corresponds to the effective dielectric layer. However, up to now, the existence of such oxygen-deficiency gradients / oxygen-deficient regions across the Nb-oxide layer could not be detected in a direct and precise experimental way. More generally, a characterization technique allowing a precise and accurate chemical analysis at the nanoscale within the oxide layers and at the anode / dielectric interfaces would be of great interest if not essential to better understand the Nb-based capacitors and further improve them.

One possibility to overcome the thermally-driven degradation of the anodic Nb-oxide layers consists in doping the Nb-anode with nitrogen or oxygen in order to reduce the rate of oxygen diffusion from the oxide layer into the anode (Persico et al., 2001; Qiu et al., 2002; Yi, 2003). Particularly, the complete replacement of Nb by NbO as anode material clearly improved the capacitor characteristics (Qiu et al., 2001; Qiu et al., 2002; Yi, 2003; Zednicek et al., 2004; Li et al., 2006), yielding the commercialization of such NbO capacitors (Zednicek et al., 2004; Pala, 2005). Indeed, NbO is a ceramic material characterized by a high metallic conductivity just slightly lower than that of Nb metal (see Fig. 2.1.1) and well within the requirements of a

capacitor material (Qiu et al., 2002). Furthermore, NbO powder has a similar morphology to that of Ta and Nb and can be processed the same way to form porous anodes and high quality dielectric layers (Qiu et al., 2001; Yi, 2003). Thus, owing to the reduced oxygen gradient across the NbO-anode / Nb_2O_5-dielectric interface, the driving force for oxygen migration into the conducting anode is reduced compared to that occurring when pure Nb is used as anode material (Qiu et al., 2002; Li et al., 2006). In addition, NbO as anode material presents some other advantages over Nb and Ta comprising a better burning resistance and efficient self-healing properties (Yi, 2003; Zednicek et al., 2004; Zednicek et al., 2005; Pala, 2005). However, in terms of electrical properties like, e.g., the forming ratio (the ratio of forming voltage to rated voltage of final capacitor – it limits the capacitance per voltage (CV) efficiency of the capacitor) even this solution does not match the capability of Ta-based capacitors (Prymak et al., 2004). Moreover, when NbO is used as anode material the migration of oxygen through the dielectric interface cannot be completely excluded (Qiu et al., 2001; Zednicek et al., 2005) and a comprehensive understanding of the relations between processing parameters, microstructure stoichiometry and electrical properties is still not achieved (Störmer et al., 2009), calling for spatially resolved chemical analyses for further developments.

The stoichiometry variations which may occur within the nanoscale Nb_2O_5 dielectric layers after a heat treatment as well as the possible presence of further amorphous suboxides at the interface cannot be detected by means of selected area electron diffraction (SAED) or high resolution transmission electron microscopy (HRTEM) (Störmer et al., 2006). In contrast, electron energy loss spectroscopy (EELS) in conjunction with (scanning) transmission electron microscopy is well suited for chemical characterizations at high spatial resolution (see, e.g., Brydson, 2000; Keast et al., 2001; Sigle, 2005). In the present work, nanoscale oxide layers anodically grown on (undoped) Nb anodes are thus investigated by means of EELS (see chapter 5). In the discussion the results are compared with those obtained by some other authors (see section 5.4.6). More particularly, some aspects of the work of Störmer et al. (who investigated the microstructural and electrical properties of anodically formed oxide films on Nb, 2006; 2009) and of Olszta & Dickey (who also employed EELS to investigate Nb-based capacitor structures, 2008) are briefly presented there (see also section 2.3.2).

2.3 Investigated materials

2.3.1 Stoichiometric reference materials

Four crystalline reference materials are investigated in the present work, namely metallic Nb (formal oxidation state of 0) and its three stable oxides NbO (+2), NbO_2 (+4), and Nb_2O_5 (stable H-modification, +5).

Commercial high-purity bulk materials from *Alfa Aesar* and *H.C. Starck Inc.* were used as reference materials for Nb and NbO, respectively. The Nb material was obtained in the form of about 0.13 mm thick metal foils, whereas the NbO material consisted in a sintered powder. The NbO_2 reference material was obtained in the form of a high-purity powder from *Alfa Aesar*. For H-Nb_2O_5, stoichiometric needles supplied by PD Dr. C. Rüscher (*University of Hannover, Germany, department of mineralogy*) were used.
Prior to the EELS investigations, the crystal structure of the reference materials (described in subchapter 2.1) were checked either by SAED or by X-ray diffraction (XRD) (see subchapter 4.1) to exclude the presence of a second phase (the deviations from stoichiometric composition of the investigated oxide phases are negligible, see section 5.4.5).

2.3.2 Nb-based capacitor structures

In the present work Nb-based capacitor structures are investigated. Fig. 2.3.1 shows a high magnification scanning electron microscopy (SEM) image of a fracture surface of such a capacitor structure which consists of an approximately 130 nm thick amorphous niobium oxide layers anodically grown on porous sintered (undoped) niobium anodes. Thus, these structures are not complete capacitors but correspond to the stage after the first anodic oxidation step of the fabrication process described in section 2.2.1 (see also Fig. 2.2.1). In addition, to check the influence of a heat treatment on the stoichiometry of the oxide layers (OL) and on the interface between anode and oxide layer, some capacitor structures were also subjected to a further annealing step in air. Hence, on the whole, four types of capacitor structures (Cap) achieved after different annealing steps were investigated in the present work, as summarized in Table 2.3.1.

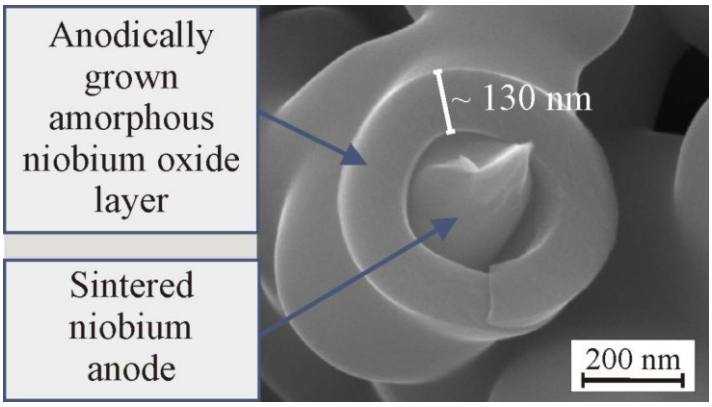

Fig. 2.3.1. Scanning electron microscopy (SEM) micrograph showing a typical capacitor structure investigated in the present work (fracture surface). It consists of approximately 130 nm thick amorphous niobium oxide layers anodically grown (1 wt.% H_3PO_4 solution, 65°C, U_{Ox} = 40 V for 180 min) on porous sintered niobium powder compacts (anode). After the anodic oxidation step, some of the capacitor structures were subjected to a further annealing step.

Table 2.3.1. Capacitor structures investigated in the present work: annealing steps they were previously subjected to (in air) and corresponding denomination. The oxide layers (OL) and the anodes (An) of the different capacitor structures will be denominated by means of the same subscripts (e.g. OL_{No_Anneal} and An_{No_Anneal}).

Annealing step	none	5 h at 300°C	1 h at 320°C	1h at 350°C
Denomination of the capacitor structures	Cap_{No_Anneal}	$Cap_{300°C\text{-}5h}$	$Cap_{320°C\text{-}1h}$	$Cap_{350°C\text{-}1h}$

These capacitor structures were supplied by the *Institut für Werkstoffe der Elektrotechnik (IWE)* of the *Universität Karlsruhe*. Their preparation was described in detail by Störmer et al. (2009; see also Fischer, 2005; Störmer et al., 2006). Following the commercial capacitor fabrication process (see section 2.3.1) the sample preparation first involved uniaxial die pressing (up to a pressing density of 2.9 g/cm^3) and vacuum sintering ($p = 10^{-4}$ Pa, 1260°C) of capacitor-grade metal powder. Pure niobium powders from *H.C. Starck Inc.* described in detail by Schnitter et al. (2003) were used for that purpose. Then, in order to form the amorphous nanoscale dielectric layer, the well established manufacturing process of commercial solid electrolyte tantalum capacitors was applied which is based on a two-stage anodic oxidation (galvanostatic and potentiostatic, note that these two stages do not correspond to the two anodic oxidation steps mentioned in section 2.2.1, but that it is the first oxidation step alone which occurs in two stages) in an electrolyte solution. The first anodization stage (galvanostatic) is characterized by a constant current flow until the potential reaches the desired formation voltage U_{Ox}. During the second stage (potentiostatic) this formation potential is fixed for the desired anodization time while the current flow decays. In the present case, the metal-powder compacts were anodized in 1 wt.% aqueous solution of phosphoric acid H_3PO_4 at 65°C by using a maximum current density of 150 mA/g, a formation voltage of 40 V and an anodization time during the potentiostatic stage of 180 min. These experimental conditions were shown to result in highly reproducible oxide layers with respect to layer thickness and homogeneity (Störmer et al., 2006). The oxidation was performed in a polycarbonate oxidation cell using a stainless steel counter electrode, whereas a Knürr-Heinzinger PTN 250-2 galvanostat / potentiostat was used as power supply.

After this anodization process, samples were arbitrarily selected to perform EELS investigations without additional annealing. Other samples were subjected to a further annealing process performed in a KENDRO UT 6060 oven in air.

The investigated annealing steps (temperature, duration) were chosen with respect to the results of the electrical and microstructural investigations of Fischer (2005) and Störmer et al. (2006; 2009) who investigated similar Nb-based capacitor structures prepared under the same conditions as those described above. Annealing steps resulting in strongly different properties were selected in order to maximize the chance of observing stoichiometric variations which can be related to these electrical and microstructural differences. Fischer (2005) and Störmer et al. (2009) measured capacitances C_{meas} that they transformed into specific charge values Q according to $Q = C_{meas} \cdot U_{Ox}$, where U_{Ox} represents the formation voltage (40 V). By normalizing the specific charge with respect to the mass of the capacitor anode m_{Anode}, the

mass-specific charge Q/m_{Anode} was obtained (also denoted as specific capacitance within the capacitor-fabricating industry) which provided a basis for comparison of different samples. With increasing annealing temperature the authors first observed an increase of Q/m_{Anode} up to a maximum value achieved for 300°C (see Fig. 5.4.2). Then, further increasing the annealing temperature from 300°C to 350°C resulted in a decrease of Q/m_{Anode}. Hence, in addition to capacitor structures prepared without annealing, capacitor structures annealed at 300°C and 350°C were chosen for EELS investigations.

Fisher (2005) observed a decrease of Q/m_{Anode} when the annealing time at 300°C increases from 1 h to 5 h. However, even after 5 h annealing at 300°C, Q/m_{Anode} is still clearly higher than without annealing or after only 1 h annealing at 350°C. In addition, whereas without annealing or after annealing below 300°C SAED investigations of the anode only revealed reflections corresponding to a purely bcc Nb metal structure, some additional diffraction intensities begin to appear at an annealing temperature of 300°C. These additional reflections are assigned to the formation of a Nb_6O superstructure in oxygen-oversaturated Nb metal (Fischer, 2005; Störmer et al., 2006). After 1 h annealing at 300°C, only a few isolated Nb grains exhibited this superstructure, whereas after 5 h a majority of grains were concerned (Fischer, 2005). Thus, from this microstructural point of view 5 h annealing at 300°C resulted in a more pronounced difference when compared to as-anodized samples (without annealing) than only 1 h annealing. At annealing temperatures above 300°C (like, e.g., at 320°C, see Störmer et al., 2006; 2009) all the Nb grains presented a Nb-O superstructure, even after an annealing step of only 1 h. Hence, samples after an annealing step of 5 h at 300°C were investigated in the present work, since - as just discussed above - they exhibited strong electrical and microstructural differences compared to those prepared without annealing or with an annealing step at 350°C.

Like in the case of an annealing temperature of 300°C, Q/m_{Anode} decreases when the annealing time at 350°C increases from 1 h to 5 h (Fischer, 2005). However, 5 h annealing at the high temperature of 350°C dramatically damaged the oxide layers (partial crystallization), making them unsuitable for capacitor applications (personal communication of Dr. H. Störmer, 2006). Hence, it was preferred to investigate a less extreme case and capacitor structures annealed at 350°C for only 1 h were selected.

In addition, in another series of EELS experiments (performed at the ZEISS Libra FE microscope, whereas $Cap_{300°C\text{-}5h}$ and $Cap_{350°C\text{-}1h}$ were analyzed at the LEO 922 Omega and VG HB501UX microscopes, see chapter 5) capacitor structures annealed for 1 h at 320°C were also investigated.

Chapter 3

Electron energy-loss spectroscopy in a transmission electron microscope

In a transmission electron microscope, a beam of fast electrons (primary energy of typically some 100 keV) is projected on a thin sample (thickness of typically some 10 nm). The interaction of the incident electrons with matter is schematically represented in Fig. 3.1.1. If the sample is thin enough, most of the electrons pass through the material without scattering (Verbeeck 2002). The incident electrons can also undergo elastic scattering (interaction with atomic nuclei), changing their direction. The analysis of the elastically scattered electrons enables the characterization of the crystalline / amorphous structure of the sample (via, e.g., selected area electron diffraction / SAED). The incident electrons have also a certain probability of being scattered inelastically (mostly through interaction with the electrons of the sample), losing some of their energy by transferring it to the sample and also (slightly) changing direction. In that case, the sample is excited to a higher energy state and, while relaxing it can emit Auger electrons or X-ray photons whose analysis, e.g. by means of energy-dispersive X-ray spectroscopy (EDXS), reveals information about the chemical composition of the sample.

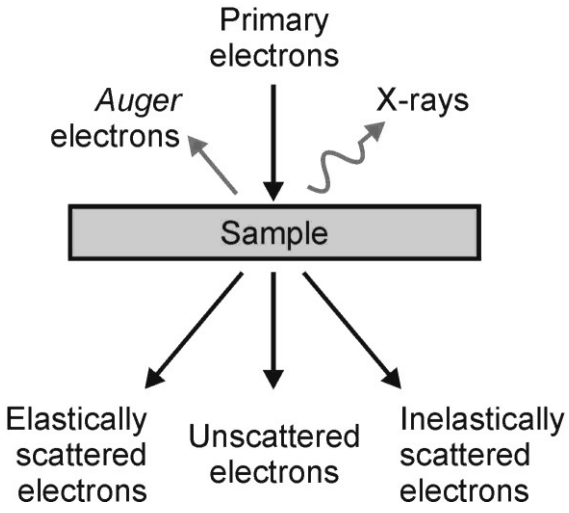

Fig. 3.1.1. The interaction of a primary electron beam with a thin sample.

EELS is used to study inelastically scattered electrons. It is a particularly rich and powerful analytical method giving chemical and structural information at the high spatial resolution associated to transmission electron microscopy (TEM). Particularly interesting are the energy loss near-edge structure (ELNES) which can be interpreted as a signature of the electronic structure of the investigated material (cf. section 3.2.6), and quantitative EELS whose goal is the determination of elemental compositions (cf. section 3.2.7). Further EELS techniques provide information on, e.g., band gap, optical properties (refraction index, absorption coefficient, reflectivity), bond lengths, or the band structure of crystals. A complete description of all the TEM and EELS techniques is beyond the scope of this chapter which focuses only on some basics which should help to understand the original results of the present work. For more details on the theory and practice of TEM-EELS, the further reading of appropriate textbooks, reviews, and doctoral theses is recommended (this chapter is principally inspired by Egerton, 1986; Williams & Carter, 1996; Brydson, 2000; Brydson, 2001; Keast et al., 2001; Verbeeck, 2002; Schneider, 2003; Ahn, 2004; Sigle 2005; Egerton, 2009). In addition, the results presented in chapters 4 and 5 as well as the associated discussions will give practical examples of ELNES and quantitative EELS analyses and some methodological aspects will be further described and developed there.
Finally, in the last section of this chapter some literature data concerning the use of EELS with respect to the investigation of niobium oxides and Nb-based capacitors are mentioned. The experimental setups applied for such investigations in the present work are also presented there.

3.1 Basics of TEM

The subject of TEM is very briefly addressed here (for more information, see, e.g., Williams & Carter, 1996). In analogy to a light transmission microscope, a transmission electron microscope is based on a multi-stage lens system. But instead of optical glass lenses, TEM makes use of electron lenses to generate an image of the sample region traversed by electrons. In such lenses, the passage of an electric current through coils creates a rotation symmetrical magnetic field affecting the path of electron rays (*Lorentz* force). These lenses suffer from severe aberrations which are the main resolution-limiting factor in TEM (without instrumental limitations, the optimum resolving power of an imaging method directly depends on the wavelength of the probing particle, which amounts to about 2.5 pm for a 200 keV electron). However, the recent development of aberration correctors allows an imaging resolution below 0.1 nm in modern transmission electron microscopes (see, e.g., Dahmen et al., 2008; Kaiser et al., 2008).

3.1.1 The image and diffraction modes in TEM

In a transmission electron microscope the electrons emitted by a source (there exist several types of electron sources, see section 3.2.2) are accelerated towards an anode up to a final beam energy typically between 100 and 400 keV. The sample is then illuminated by means of an appropriate condenser-lens system. The microscope can operate in two different modes differing in the type of figure which is displayed on the viewing screen: the image mode and the diffraction mode. Fig. 3.1.2 schematically shows the corresponding electron ray paths between the sample (object) illuminated with a parallel electron beam and the viewing screen (Schneider, 2003). The electrons transmitted by the sample form a diffraction pattern in the back focal plane of the objective lens. There, all electrons emerging in the same direction from any point within the sample are focused into one and the same point. Particularly, in the case of a crystalline material constructive interference of elastically scattered electrons is confined to discrete angles resulting in discrete diffracted beams (reflections) in the objective back focal plane. In contrast, the transmitted electrons form an image (one-stage magnified) in the image plane of the objective lens. There, all electrons emerging from one and the same point of the sample are collected in one and the same image point. Depending on its excitation (lens current), the intermediate lens can focus either on the image plane (Fig. 3.1.2a) or on the back focal plane (Fig. 3.1.2b) of the objective lens.

The image mode

In the image mode (Fig. 3.1.2a) the image plane of the objective lens is imaged and magnified by means of the intermediate lens into the object plane of the projector lens (two-stage magnified image). Thus a further magnified image of the sample is generated in the final image plane (three-stage magnified image), i.e. on the viewing screen of the microscope (please note that in practice more than one projector lens is used to generate the final *n*-stage magnified image which can correspond to a total magnification of up to one million times). In a wave-mechanical description of the imaging process both the amplitude and the phase of the incident electron wave can be modified by the interaction with the sample. Hence, the obtained TEM image consists of a combination of amplitude contrast (subdivided into scattering-absorption contrast, also called mass-thickness contrast, and diffraction contrast) and at higher magnification phase contrast (caused by the interference between unscattered and scattered electrons and allowing high-resolution - atomically-resolved - TEM). By inserting an objective aperture in the back-focal plane of the objective lens, one can select the scattered / unscattered beams which should contribute to the formation of the image. If solely the (elastically) unscattered beam (direct beam) can pass through the aperture, a so-called bright-field (BF) image is generated which shows the local intensity of the direct beam. If a specific diffracted beam is selected a dark-field (DF) image is achieved. In that case, only those regions of the sample having scattered the electrons in the selected direction appear bright in the resulting image. This diffraction contrast enables e.g. the visualization of structure disturbances such as dislocations, stacking faults or grain boundaries in a crystalline material with higher resolution compared to BF imaging.

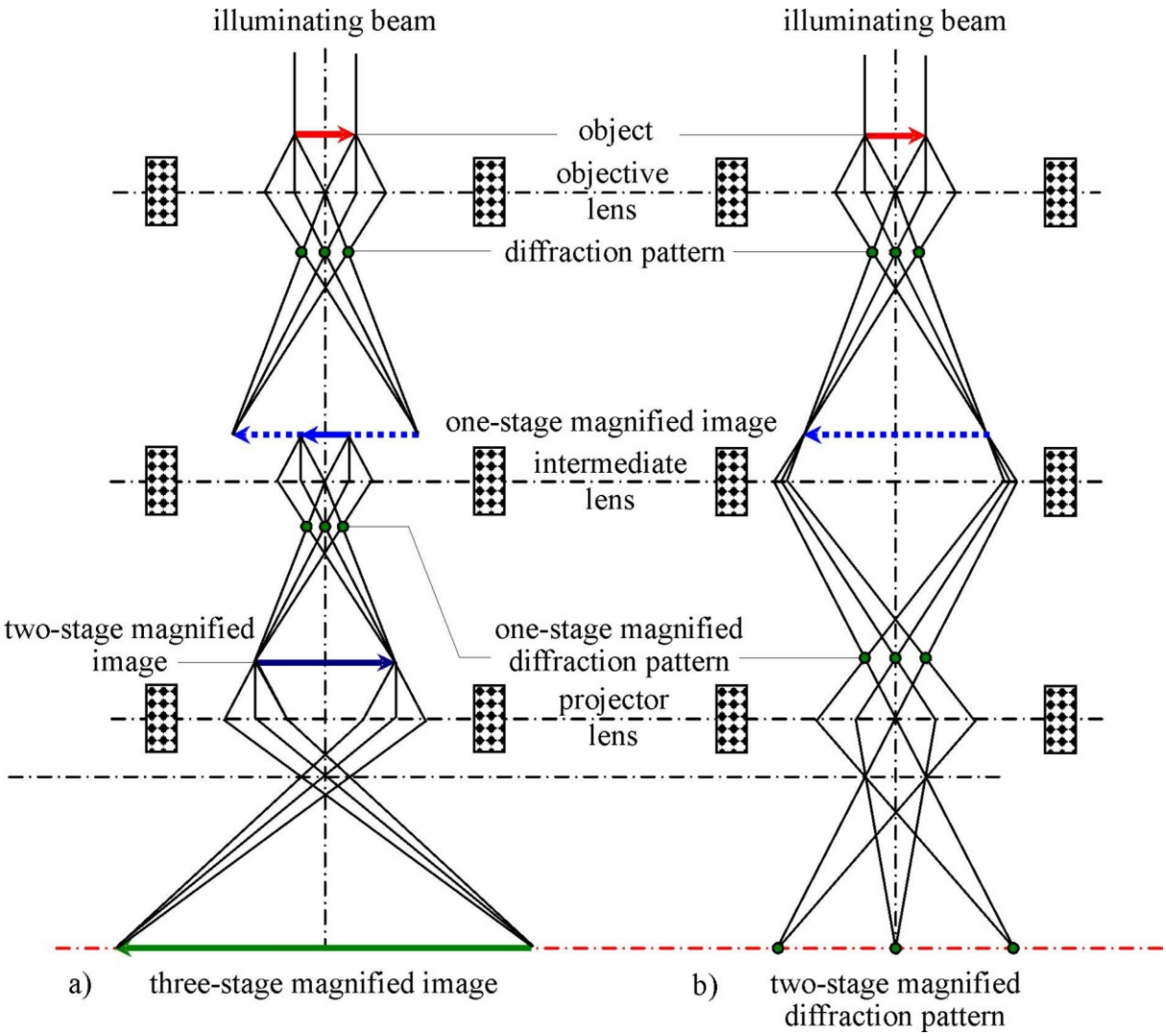

Fig. 3.1.2. Ray paths in a three-stage transmission electron microscope: **a)** image mode; **b)** diffraction mode (from Schneider, 2003).

The diffraction mode

In the diffraction mode (Fig. 3.1.2b), the back focal plane of the objective lens is imaged and magnified by means of the intermediate lens into the object plane of the projector lens (one-stage magnified diffraction pattern). Thus, a (two-stage) magnified diffraction pattern is generated on the viewing screen of the microscope. Each point in the pattern is related to a specific scattering angle.

The selected area electron diffraction (SAED) method allows to correlate the imaged sample region and the diffraction pattern. By means of an aperture (the so-called SAED aperture) positioned in the image plane of the objective lens one can select the sample region which should contribute to the diffraction pattern. The lateral resolution of SAED is typically limited to about 100 nm in dependence on the physical size of the smallest SAED aperture and microscope parameters (magnification in the image plane of the objective lens, aberrations).

In the case of a single-crystalline material, the incident electrons interact with regularly spaced atomic planes (the so-called lattice planes, where the atoms themselves are arranged in a regular pattern) resulting in constructive interference of elastically scattered electrons in

well-defined directions given by Bragg's law. Depending on the orientation of the crystal with respect to the incident electron beam, different diffraction patterns consisting of intense discrete reflections are obtained, whose analysis allows the characterization of the crystal structure. Examples of diffraction patterns are shown in Figs. 4.1.1 and 5.4.4. In particular, when a so-called zone-axis of the single-crystal is aligned in parallel orientation to the incident electron beam, it is possible to establish a correlation between the position of the reflections in the resulting pattern and the lattice parameters of the crystal.

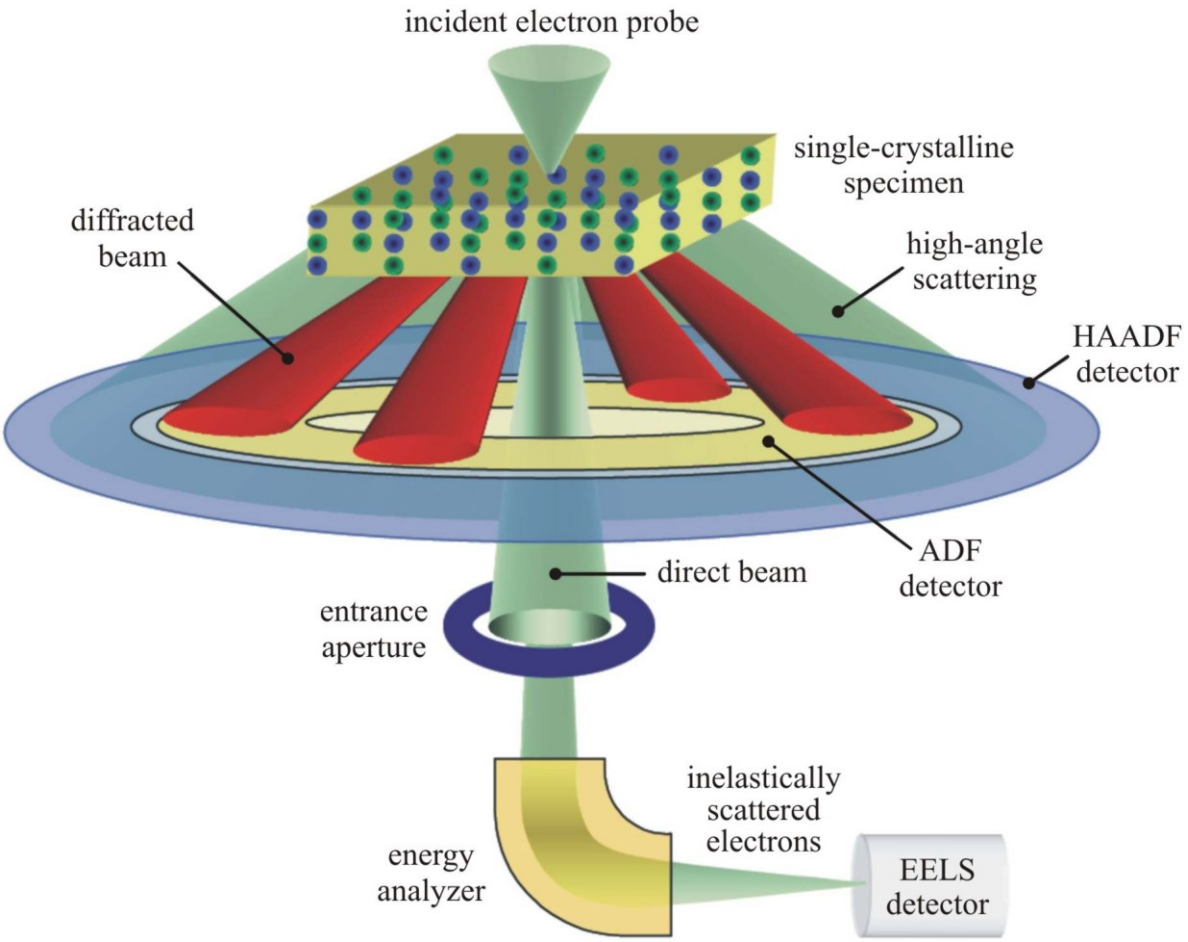

Fig. 3.1.3. The STEM imaging mode: electron optics and detector arrangement (from Schneider, 2003).

3.1.2 Scanning Transmission Electron Microscopy (STEM)

STEM is a variant of the TEM imaging system. In the scanning TEM mode a small electron probe (typically nanometer-sized, probes below 0.1 nm are possible by means of aberration correctors, see e.g., Hartel et al., 2007) is focused on the sample and scanned in a two-dimensional raster across the area of interest in the sample plane. The principle of STEM imaging is schematically shown in Fig. 3.1.3. Modern transmission electron microscopes are often equipped with scanning coils allowing the microscope to be used in the STEM mode. There also exist microscopes working exclusively in the STEM mode. Here, lenses are used

to focus the electron probe but in contrast to all possible TEM modes no additional lens is necessarily required behind the sample for image formation. Indeed, STEM images are recorded electronically by gathering of differently scattered electrons via appropriate detectors. At each point of the scanned sample area the transmitted signal of interest is measured and contributes to the intensity of a corresponding point in the image. Three signals can usually be recorded. A BF detector inserted on the optical axis (not shown in Fig. 3.1.3) can collect electrons which have not been scattered or have undergone relatively small angles of scattering (generally inelastically scattered electrons). An annular dark-field (ADF) detector with collection angles typically ranging from 10 to 50 mrad can collect electrons from *Bragg*-diffracted beams. Finally, a high-angle annular dark-field (HAADF) detector collects electrons scattered through high angles typically larger than 50-70 mrad. In the last case, the contrast in the achieved HAADF image generally results from the dependence of electron scattering on the atomic number Z of the atoms within the sample. The high-angle elastic scattering cross section is proportional to the square of Z (Rutherford scattering) and, consequently, the contrast (termed Z-contrast) is dominated by the chemical composition.
Finally, as represented in Fig. 3.1.3, it is also possible to equip the microscope with an electron spectrometer allowing EELS. Thus, without an inserted BF detector the analysis of the inelastically scattered electrons can result in one EEL spectrum for each investigated point of the sample.

3.2 Basics of EELS

Many processes can cause energy to be lost by the primary electron traversing the sample. The most important for the present work is the excitation of a single inner shell atomic electron to a higher unoccupied energy state, as schematically shown in Fig. 3.2.1. In the following, it is briefly presented how the study of this process by means of EELS can yield information on the chemical and structural environment of the ionized atom as well as on the chemical composition of the sample.

3.2.1 The EEL spectrum

The energy distribution of the inelastically scattered electrons can be represented in a so-called electron energy-loss spectrum (see Fig. 3.2.2), where the intensity (i.e. the number of transmitted fast electrons) is shown as a function of the energy loss (i.e. the decrease in kinetic energy of the fast electrons). Such a spectrum can be divided in two different regions, namely the low-loss region and the core-loss region.

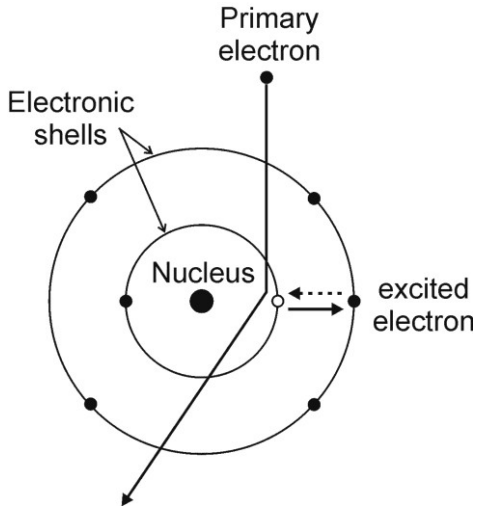

Fig. 3.2.1. Inelastic scattering occurring as a result of *Coulomb* repulsion between a fast incident electron and an inner-shell atomic electron, which is excited to a higher energy state (the deexcitation is shown by a broken arrow). Such scattering events give rise to core-loss ionization edges in the EEL spectrum.

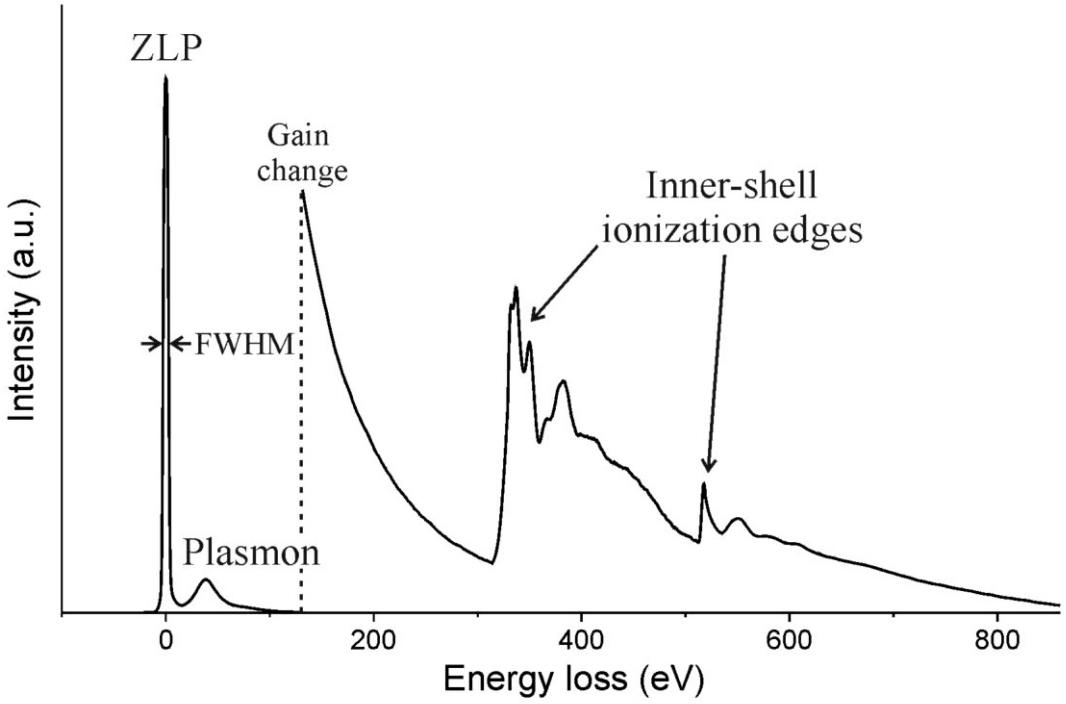

Fig. 3.2.2. Schematic EEL spectrum.

The low-loss region

The low-loss region extends from 0 to about 50 eV. The first and most intense feature (if the sample is thin enough) in the spectrum is the zero-loss peak (ZLP). It includes the electrons transmitted without scattering and the elastically scattered electrons, but also those electrons that have suffered minor energy losses which are not resolved by the spectroscopy system (mostly electrons losing some 10 – 100 meV by exciting phonons). The full width at half

maximum (FWHM) of the ZLP is generally used as a measure of the energy resolution dE of the system (typically 1 – 2 eV, see also section 3.2.2).
Beyond the ZLP, the low-loss region is dominated by the excitation of strong collective oscillations of the valence electrons known as plasmons. For materials having free electrons (like, e.g., metals) the plasmon peaks are sharp and particularly pronounced and their energy position is related to the square root of the free-electron density (Williams & Carter, 1996). However, in insulators and semiconductors the valence electrons are no longer free and broader plasmon-like peaks occur due to the damping of the plasmon oscillations by scattering with the ion-core lattice (Brydson, 2001).
Interband transitions corresponding to single electron excitations from the valence to the conduction band may also cause further peaks in the low-loss region. For semiconductors and insulators the region directly to the right of the ZLP contains information on the band gap (see, e.g., Rafferty & Brown, 1998). However, the band-gap analysis requires a particularly good energy resolution and the full knowledge of the shape of the ZLP which forms a background to the involved valence excitations (Rafferty et al., 2000; Verbeeck, 2002; Erni & Browning, 2005).
In addition, information on the sample thickness is also available in the low-loss spectrum, which will be described in more detail in section 3.2.4.

The core-loss region
The core-loss region extends from about 50 eV to 2000 – 3000 eV. The upper limit is determined by the detectability of the EEL signal whose intensity decreases with increasing energy loss (the intensity at 2000 eV is typically eight orders of magnitude less than that at the ZLP, Brydson, 2001). Superimposed on a background caused by the excitation events at lower energy loss, this region exhibits ionization edges (also termed core-loss edges) stemming from the excitation of single inner-shell atomic electrons to unoccupied states above the Fermi level. The onset energy corresponds to the lowest unoccupied state. The ionization features have the appearance of edges rather than peaks mostly because not only this onset energy is transferred to the inner-shell electrons but also some additional kinetic energy.
The various edges are classified according to the initial state of the excited electron using the standard spectroscopic notation summarized in Table 3.2.1. They are indicated by means of a letter generally followed by one or more numbers in subscript. The letter (K, L, M etc.) indicates the atomic shell which has been excited and corresponds to the principal quantum number n (1, 2, 3 etc.). The subscript refers to the total angular-momentum quantum number j of the excited electron which equals the angular-momentum quantum number l (0, 1, 2, 3 corresponding to the s, p, d, f subshells, respectively) plus or minus the spin quantum number s (1/2). For instance, $M_{2,3}$ indicates the excitation of the 3p subshell which is spin-split into $3p_{1/2}$ (j = 1/2, M_2) and $3p_{3/2}$ (j = 3/2, M_3) states. The degeneracy of the initial state is given by $2j$+1 and determines the number of electrons which can be in that state. In addition, if the transmitted electrons are collected over small scattering angles, then the dipole-selection rules limit the allowed transitions to those in which l changes by + or – 1. Hence, different edges from the same element are probing different symmetries of the final state.

Table 3.2.1. Standard spectroscopic nomenclature: overview of the most important edges (Adapted from Brydson, 2001; Verbeeck, 2002).

Edge	Initial state	Degeneracy	Dipole-allowed final-state symmetry
K	$1s_{1/2}$	2	p
L_1	$2s_{1/2}$	2	p
L_2	$2p_{1/2}$	2	s or d
L_3	$2p_{3/2}$	4	s or d
M_1	$3s_{1/2}$	2	p
M_2	$3p_{1/2}$	2	s or d
M_3	$3p_{3/2}$	4	s or d
M_4	$3d_{3/2}$	4	p or f
M_5	$3d_{5/2}$	6	p or f
N_1	$4s_{1/2}$	2	p
N_2	$4p_{1/2}$	2	s or d
N_3	$4p_{3/2}$	4	s or d
N_4	$4d_{3/2}$	4	p or f
N_5	$4d_{5/2}$	6	p or f
N_6	$4f_{5/2}$	6	d or g
N_7	$4f_{7/2}$	8	d or g

Since the onset energy of a given edge is determined by the binding energy of a particular electron subshell, which is a characteristic quantity of the atom type, the edges occurring in the spectrum directly indicate which elements are present in the sample. However, the ionization edges contain even much more information about the investigated material. Particularly, a given edge is characterized by a fine structure (ELNES) determined by the chemical and structural environment of the atom undergoing excitation (see section 3.2.6), whereas the intensity under the edge can be used for elemental quantification (see section 3.2.7).

3.2.2 Experimental aspects

Electron spectrometer and imaging energy filter

EEL spectra are measured by means of an electron spectrometer. In its most basic form, the spectrometer relies on a single magnetic prism which generates a uniform magnetic field perpendicular to the electron beam. Within this field, the electrons follow trajectories that are arcs of circles and are deflected through an angle of typically about 90°. However, according to the *Lorentz* force, the radius of the circular path and thus the exact deflection angle depends

on the velocity of the considered electron, i.e. on its kinetic energy. Hence, the electrons emerge from the spectrometer spatially dispersed as a function of their energy (and therefore energy loss), and owing to the focusing properties of the prism (see, e.g., Egerton 2009) this results in the formation of a spectrum in the energy-dispersive plane of the spectrometer. Mostly, in a TEM-EELS system, a charge-coupled device (CCD) camera is used as detector, which allows the simultaneous recording of wide regions of the EEL spectrum (parallel recording).

Moreover, electrons that have suffered specific energy losses can be selected by the introduction of a mechanical slit in the energy-dispersive plane. This enables energy-filtered TEM (EFTEM). Behind the slit, the selected electrons can be used to form a two-dimensional image or diffraction pattern by means of further electron-optic elements. In that case, the energy-loss system is termed imaging energy filter.

There are basically two types of energy-filter systems: the in-column and post-column systems. The Gatan imaging filter (GIF) is for instance one popular post-column system. It is a single magnetic-prism energy filter that can be attached below any existing TEM/STEM microscope without altering the optical elements of the microscope column. In contrast, the Omega filter is an example of in-column filter that has to be placed in the optical path of the microscope. It is incorporated into the projector system and consists of four magnetic prisms arranged symmetrically in the form of a Greek letter Ω. This design allows to preserve a vertical TEM column since the electron beam – after having been bent into the shape of an Ω – emerges along the original optic axis. Compared to the GIF, one drawback of the Omega filter is that it cannot be added to an existing TEM column. However, the inherent symmetry of the Omega filter causes various aberrations to vanish, whereas the 90° design (based on a single magnetic prism) of the GIF induces numerous aberrations that have to be corrected by additional multipole lenses behind the filter.

Important experimental parameters

Three experimental parameters are particularly important while performing quantitative EELS and should be carefully controlled: the incident beam energy E_0, the convergence semi-angle α, and the collection semi-angle β. Indeed, the combination of these three parameters determines in which proportion the total emitted EEL signal is recorded with respect to the inelastic-scattering angle (see also sections 4.4.1 and 4.4.8). Thus, in the first instance, only spectra that have been taken by means of one and the same set of parameters can be accurately compared with each other in a quantitative manner. The incident beam energy is directly given by the microscope high voltage used to accelerate the primary electrons. The probability that a primary electron traversing the sample is scattered due to a particular inelastic process depends on E_0. The convergence and collection semi-angles are schematically represented in Fig. 3.2.3. The convergence semi-angle is the half-angle of the incident-electron cone illuminating the sample. In the case of a perfectly parallel illumination, α would be zero. The collection angle is the maximum scattering angle that is accepted by the spectrometer for an incident electron travelling along the optic axis of the microscope. As a general trend, the scattering angle for inelastic excitations increases with energy loss (see next

section). Hence, a variation of α and β does not have an equivalent influence on all the EEL spectral features.

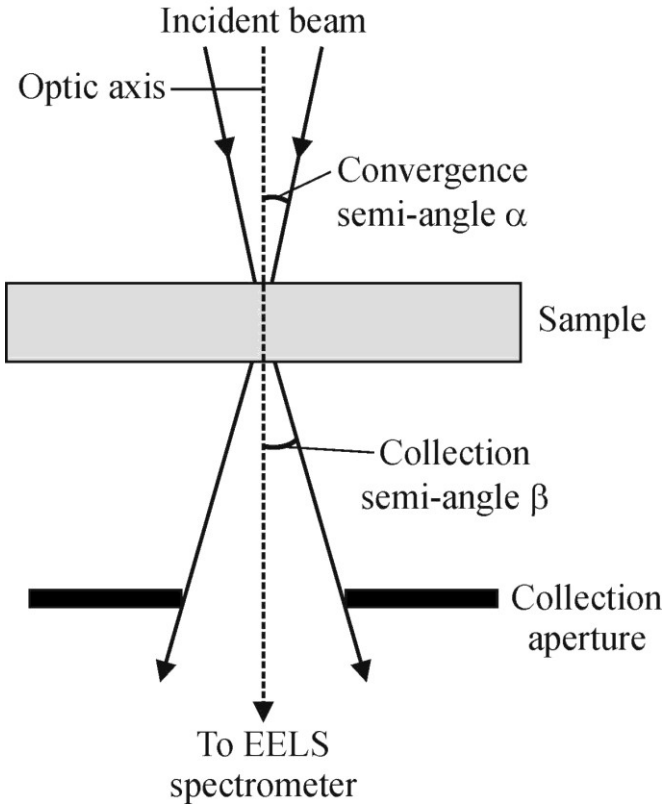

Fig. 3.2.3. Schematic diagram of the electron beam path showing the convergence and collection semi-angles in an EELS experiment.

In addition to the three above-mentioned parameters, a fourth experimental parameter plays a crucial role while analyzing ELNES, namely the energy resolution dE. The importance of this parameter on the relative height and splitting of the ELNES details is outlined in section 4.4.8. The energy resolution is mainly limited by the non-monochromaticy of the primary electrons, which depends on the electron source. The electrons are produced either by thermionic emission (electrons are emitted by heating a source typically made of W or LaB_6) or by field emission (electrons are emitted by applying an intense electric field to a source typically made of a single-crystalline W tip) or by a combination of both (*Schottky* emitter, typically made of a ZrO_2-coated W tip). The energy spread of the emitted electron beam is in the order of 1.5 eV for a thermionic lanthanum hexaboride (LaB_6) source, 0.8 eV for a Schottky field emitter, and 0.4 eV for a pure cold-field emitter. Moreover, the energy spread of the incident electrons can be reduced by means of newly developed monochromators. Thus, energy resolutions below 0.1 eV were recently achieved (see, e.g., Essers et al., 2008). A monochromator consists of an energy filter directly implemented in the electron gun of the microscope and tuned to select a narrow energy range at the center of the emitted energy distribution (Egerton, 2009). In addition to the energy spread of the electron source, further instrumental aspects may affect the energy resolution, like, e.g., instabilities in the electronics (high tension, spectrometer currents), or high electromagnetic stray fields in the laboratory

environment. For instance, fluctuations of the accelerating high voltage yield corresponding fluctuations of the position of spectrum on the detector.

3.2.3 Physical fundamentals

When high-energy electrons pass through the sample, the probability of inelastic scattering is described by a so-called inelastic-scattering cross section σ as a function of the solid scattering angle Ω and the energy loss E. The double-differential cross section $\mathrm{d}^2\sigma/(\mathrm{d}\Omega\mathrm{d}E)$ represents the fraction of incident electrons which are scattered into a solid angle $\mathrm{d}\Omega$ with an energy loss between E and $E+\mathrm{d}E$. According to the *Bethe* theory (see, e.g., Egerton, 1986; Brydson, 2001) it can be expressed by

$$\frac{d^2\sigma}{d\Omega dE} = \frac{4\gamma^2 R}{Ek_0^2}\left(\frac{1}{\theta^2+\theta_E^2}\right)\frac{df}{dE} \qquad (3.2.1)$$

where γ is the relativistic factor (depending on the primary energy of the incident electron E_0), R = 13.61 eV is the *Rydberg* energy, k_0 is the magnitude of the incident wave vector (= $2\pi/\lambda_0$, where λ_0 is the wavelength), θ is the scattering angle, θ_E is a characteristic angle of scattering, and the term $\mathrm{d}f/\mathrm{d}E$ is known as the generalized oscillator strength (GOS) per unit energy loss. The relativistic factor for a particle of velocity v is given by $\gamma = (1 - v^2/c^2)^{-1/2}$ where c is the velocity of light. The characteristic scattering angle θ_E for the energy loss E is defined as $\theta_\mathrm{E} \sim E/(\gamma m_0 v^2)$, where m_0 is the electron rest mass.

Apart from the GOS term, the angular dependence in Eqn. 3.2.1 comes from the term $\left(\theta^2+\theta_E^2\right)^{-1}$, which is a Lorentzian distribution of half width equal to θ_E, and the energy-loss dependence results from the $1/E$ and angular terms, which together lead to a monotonic decay (E^{-1} for large θ, E^{-3} for very small θ, Egerton, 2009). However, $\mathrm{d}f/\mathrm{d}E$ also contains a strong E-dependence. In addition, it also depends on the momentum transfer vector **q**, which represents the change in the wave vector of the incident electrons owing to inelastic scattering ($\mathbf{q} = \mathbf{k_0} - \mathbf{k_f}$, where $\mathbf{k_0}$ and $\mathbf{k_f}$ are the incident and inelastically scattered wave vectors, respectively) and whose magnitude is given approximately as a function of θ by the expression

$$q^2 = k_0^2\left(\theta^2+\theta_E^2\right) \qquad (3.2.2).$$

The GOS term $\mathrm{d}f/\mathrm{d}E$ is a property of the atom (or material) undergoing excitation. In the case of inner-shell ionization, it is related to the matrix element of the transition between the initial and final state of the excited atomic electron (see, e.g., Brydson, 2001). It can be calculated analytically for a single hydrogen atom and the resulting analytical formula can be adapted to other atoms by suitable scaling (see, e.g., Egerton, 1986; Verbeeck, 2002; Egerton 2009). For example, a plot of the hydrogenic GOS for K-shell ionization of oxygen as a function of scattering angle and energy loss is shown in Fig. 3.2.4 (Schneider, 2003). Here, the angular dependence is given by the dimensionless term $\ln(qa_0)^2$ with the *Bohr* atomic radius a_0. The plot displays the so-called *Bethe* surface and shows that in TEM forward scattering (high

d*f*/d*E* at small momentum transfer) is predominant for energy losses close to an ionization edge (E_K). For higher losses d*f*/d*E* presents a maximum at high values of momentum transfer (corresponding to high values of θ) yielding the so-called *Bethe* ridge, but the forward scattering is maintained owing to the convolution with $\left(\theta^2 + \theta_E^2\right)^{-1}$ (Schneider, 2003).

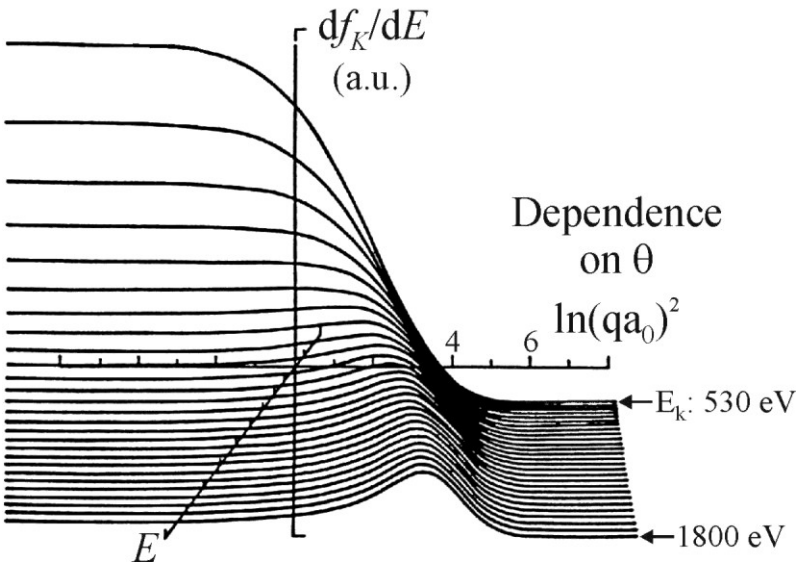

Fig. 3.2.4. Generalized oscillator strength df_K/dE calculated as a function of q and E for the scattering of 80 keV electrons by exciting the oxygen K shell. The calculations were performed by means of a hydrogenic model. From Schneider (2003).

Thus, in spite of the complicated θ-dependence of d*f*/d*E*, the double-differential cross section $d^2\sigma/(d\Omega dE)$ is well described by a Lorentzian function of θ with FWHM = θ_E because for small values of θ the GOS is approximately independent of θ (cf. $qa_0 < 1$ in Fig. 3.2.4), and because in practice the *Bethe* ridge occurs at relatively high scattering angles for which the Lorentzian function is already close to zero (Verbeeck, 2002). However, d*f*/d*E* clearly contributes to the *E*-dependence of $d^2\sigma/(d\Omega dE)$ (cf. the strong *E*-dependence of d*f*/d*E* at small momentum transfer in Fig. 3.2.4).
Moreover, in the case of 100 keV incident electrons θ_E is of the order of 0.3 mrad for an energy loss of 100 eV, which is much smaller than typical *Bragg* angles. Since the majority of inelastic scattering events occurs at losses below 100 eV, this example indicates that the Lorentzian distribution of inelastic scattering is generally much more forward-directed than elastic scattering (but it should also be noted that θ_E becomes quite appreciable for high energy losses, Sigle, 2005).

3.2.4 Determination of the sample thickness

The low-loss spectrum contains information on the thickness of the excited sample. With increasing sample thickness, the probability of inelastic scattering increases and the incident electron can undergo several independent losses. The occurrence of these multiple scattering

events obeys *Poisson* statistics in dependence on the so-called relative thickness t/Λ, where t is the sample thickness and Λ is the mean free path for inelastic scattering (see, e.g., Egerton, 1986). As a result of this behavior, the relative thickness can be determined by

$$\frac{t}{\Lambda} = \ln\left(\frac{I_{tot}}{I_0}\right) \qquad (3.2.3)$$

where I_{tot} is the total intensity in the EEL spectrum (corresponding to all the electrons reaching the spectrometer) and I_0 the intensity contained in the zero-loss peak (corresponding to the electrons that have lost no energy), as schematically shown in Fig. 3.2.5 (so-called log-ratio method, Malis et al., 1988). In practice, the intensity in the EEL spectrum falls so rapidly with increasing energy loss that the integration of the spectrum intensity up to $E \sim 100$ - 200 eV is generally sufficient to obtain a good approximation of I_{tot}.

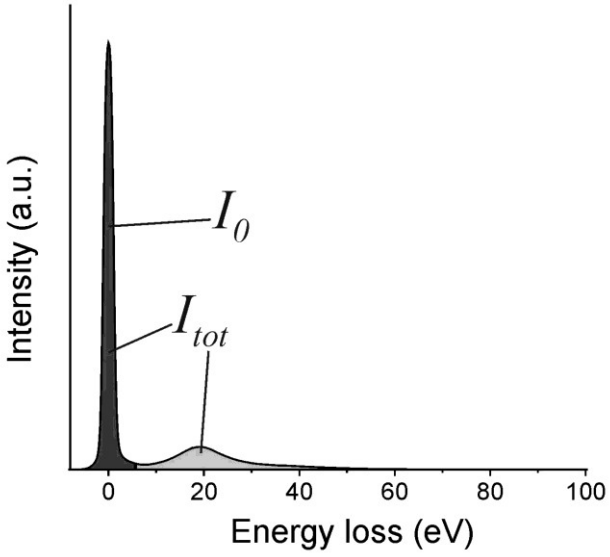

Fig. 3.2.5. Schematic low-loss spectrum showing the intensities I_0 and I_{tot} used for thickness determination by means of the log-ratio method.

The knowledge of the relative thickness allows to take the sample thickness into consideration while comparing two spectra in terms of ELNES or within the framework of an elemental quantification analysis. The accuracy of the comparison will be limited if the spectra result from two specimen regions exhibiting strongly different values of t/Λ because the contribution of multiple scattering to the intensity modulations in the spectra will differ. Nevertheless, as indicated in section 3.2.5, a given core-loss spectrum can be corrected for the effects of multiple scattering by means of a deconvolution procedure making use of a corresponding low-loss spectrum. Here, t/Λ can serve as a criterion to judge if such corrections are necessary.

The mean free path Λ represents the average distance that a fast electron will travel through the sample before being inelastically scattered (or between two inelastic scattering events) and depends on the investigated material. If it is known, the absolute sample thickness t can be

determined by means of Eqn. 3.2.3. A parametrization based on many experimental measurements was proposed by Malis et al. (1988), which describes Λ as a function of the "effective" atomic number Z_{eff} of the analyzed compound, the incident beam energy E_0, and the collection semi-angle β (if β is larger than the convergence semi-angle α):

$$\Lambda = \frac{106FE_0}{E_m \ln\left(\frac{2\beta E_0}{E_m}\right)} \tag{3.2.4}$$

$$F = \frac{1 + E_0/1022}{(1 + E_0/511)^2} \tag{3.2.5}$$

$$E_m = 7.6Z_{eff}^{0.36} \tag{3.2.6}$$

where Λ is in nm, E_0 in keV, and β in mrad. The expression for Z_{eff} is

$$Z_{eff} = \frac{\sum_i f_i Z_i^{1.3}}{\sum_i f_i Z_i^{0.3}} \tag{3.2.7}$$

where for each element i in the analyzed compound f_i is the atomic fraction of the element in the compound and Z_i its atomic number. Thus, in the case where the analyzed material is composed of only one element Z_{eff} is equal to the atomic number Z of that element. The accuracy of the determination of the absolute thickness t on the basis of Eqn. 3.2.3 in combination with the parameterization of Malis et al. is estimated to be better than ± 20 % (Malis et al., 1988). However, note that in the first instance Eqn. 3.2.4 is valid when $\beta > \alpha$. In the cases where $\beta \approx \alpha$ or $\beta < \alpha$ the accuracy may be affected and a correction required.

3.2.5 Spectra post-acquisition processing

Before performing ELNES or quantitative EELS investigations, the raw acquired spectra need to be corrected for background and if necessary for multiple scattering.

Background subtraction

The background under a given ionization edge needs to be removed. This background is composed of the tails of the low-loss excitations plus those of the ionization edges occurring at lower energy loss. Thus, owing to the complex contributions of different interaction phenomena it is not possible to calculate the real background *ab initio*. However, in energy regions away from the low loss and sufficiently beyond any preceding ionization edge the background intensity I_B of a limited energy interval can generally be modelled by a power-law function

$$I_B = A \cdot E^{-r} \tag{3.2.8}$$

where E is the energy loss and A and r are constants depending on both the investigated material and experimental conditions (Egerton, 1986; Brydson 2001; Schneider, 2003). The

commonly employed background-subtraction procedure is represented in Fig. 3.2.6. The parameters A and r are estimated by fitting the model to the experimental background within an energy window positioned immediately before the edge. Then, the modelled background is extrapolated beyond the edge onset and subtracted on the assumption that the fitting parameters A and r remain constant. Because of this assumption and noise in the fitted experimental data, this procedure contains some incertitude, especially at energy losses well above the edge onset. In addition, owing to the presence of neighbouring edges or strong plasmon contributions, the background might diverge from the classical power-law model and exponential or polynomial fitting functions are sometimes found to give better results.

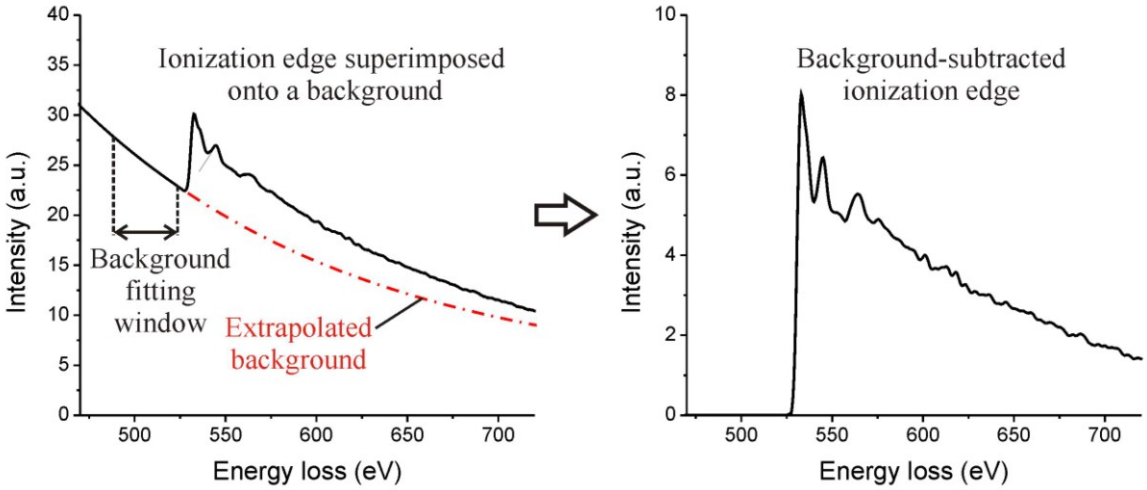

Fig. 3.2.6. Schematic representation of the background-subtraction procedure under an ionization edge: the background is fitted by means of an adapted function (generally a power law) within an energy window positioned immediately before the edge, extrapolated beyond the edge onset, and subtracted.

Multiple-scattering removal

Multiple scattering affects the E-dependent intensity modulations in the EEL spectrum of a given material, which may limit the comparison with spectra taken from the same material or from other ones. The effects of multiple scattering can be removed from the spectra by means of deconvolution techniques. Two *Fourier*-transform methods are routinely employed, the so-called *Fourier*-Log and the *Fourier*-Ratio methods, which are described in more detail elsewhere (see, e.g. Egerton, 1986; Williams & Carter, 1996; Verbeeck, 2002).

The *Fourier*-Log method requires the whole spectrum including ZLP as input data and makes use of the consideration that the probability of multiple scattering follows *Poisson* statistics. It is employed for the correction of low-loss spectra. But it is of limited use for core-loss edges occurring at $E > 100$ eV owing to the large dynamic range required for the parallel recording of such core-loss signals together with the much more intense ZLP. An example of *Fourier*-Log deconvolution is shown in Fig. 3.2.7 for a low-loss spectrum taken from a thick Nb specimen.

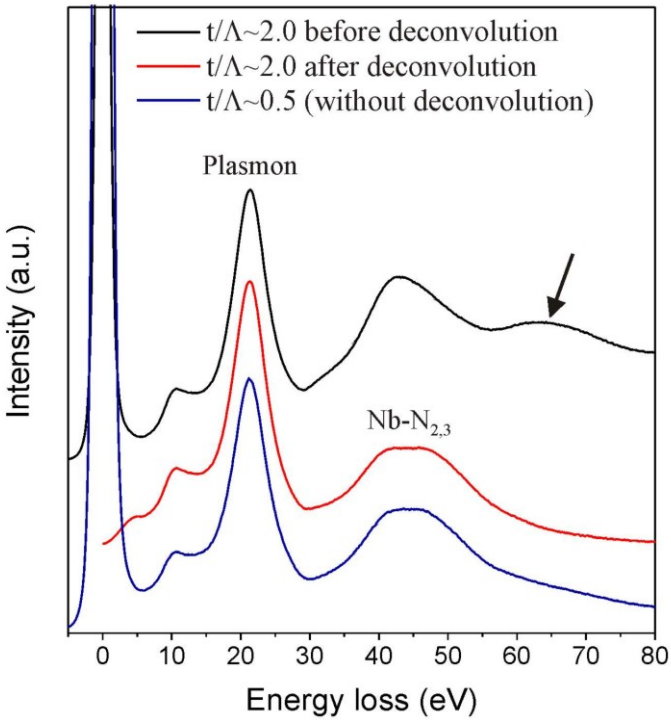

Fig. 3.2.7. Low-loss spectrum from a particularly thick (t/Λ ~ 2.0) Nb-specimen before and after *Fourier*-Log deconvolution. The intense plasmon peak occurs around 21 eV and in the ideal case of single scattering the bump starting at about 29 eV is attributed to Nb-$N_{2,3}$ excitations. It can for instance be observed that the bump indicated by an arrow is removed by the deconvolution (note that the ZLP is also removed during the deconvolution procedure). For comparison, a low-loss spectrum taken from a thinner (t/Λ ~ 0.5) Nb-specimen is also shown (without deconvolution).

Owing to the high probability of low-loss excitations (yielding the high intensity in the low-loss spectrum) the multiple scattering affecting a given core-loss edge mainly involves low-loss excitations in addition to the inner-shell ionization event of interest. Hence, in first approximation, the experimentally observed multiple-scattering spectrum can be considered as the ideal single-scattering spectrum convoluted with the low-loss spectrum (Fig. 3.2.8). The single-scattering spectrum can then be obtained via the *Fourier*-Ratio method by deconvoluting the experimentally measured spectrum by means of a corresponding low-loss spectrum measured from the same specimen region. The example given in Fig. 3.2.8 for an O-K edge shows that multiple scattering can strongly influence the intensity distribution under the edge.

Nevertheless, in order to check for possible artefacts and errors related to the *Fourier*-transform routines (e.g., due to the fact that the deconvolution procedures only consider the energy dimension but ignore the angular dimension) it is recommended to compare deconvoluted spectra obtained over a range of specimen thickness with each other or with non-deconvoluted spectra obtained from thinner specimen regions where multiple scattering is less of a problem (Williams & Carter, 1996; Verbeeck, 2002). For instance, in the case of the deconvoluted low-loss spectrum (t/Λ ~ 2.0) shown in Fig. 3.2.7 the good resemblance to the non-deconvoluted spectrum achieved for t/Λ ~ 0.5 (in contrast to the dissimilar raw

$t/\Lambda \sim 2.0$ spectrum before deconvolution) indicates that the *Fourier*-Log procedure worked reasonably well.

For reliable ELNES and quantitative EELS analyses it is generally recommended to correct the spectra for multiple-scattering effects by means of deconvolution procedures, especially when they are recorded from specimen regions where t/Λ exceeds 0.3-0.5 (Brydson, 2001). However, it will be discussed in section 4.4.6 that other approaches than deconvolution are possible to take the specimen-thickness related errors into consideration while performing quantitative EELS.

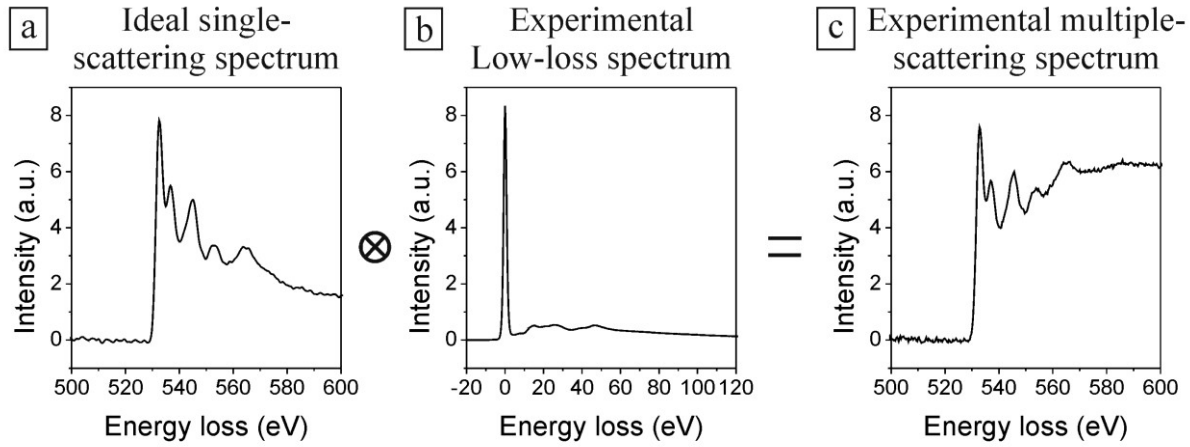

Fig. 3.2.8. Representation of the multiple-scattering contribution to a core-loss edge: convolution of an ideal single-scattering spectrum **(a)** with a low-loss spectrum **(b)** resulting in the experimentally observed multiple-scattering spectrum **(c)**. The experimental spectra (b) and (c) shown as an example were taken from a particularly thick ($t/\Lambda \sim 1.4$) Nb_2O_5 specimen. The spectrum (c) corresponds to a background-subtracted O-K edge. The "ideal" single-scattering spectrum (a) was obtained via *Fourier*-ratio deconvolution of the multiple-scattering spectrum (c) by means of the corresponding low-loss spectrum (b).

3.2.6 Energy loss near-edge structure (ELNES)

In the case of the excitation of an inner-shell atomic electron, the GOS is closely related to the matrix element of the transition between the initial and final state of the excited electron (see, e.g., Brydson, 2001). In addition, the ionization process depends on the available final states, i.e. in a solid material, on the overall electron distribution due to the atom undergoing excitation and its neighbours. As a result, the energy-differential cross section (i.e. the probability of the transition, and hence the intensity in the ionization edge) can be approximated by

$$\frac{d\sigma}{dE} \propto |M(E)|^2 N(E) \qquad (3.2.9)$$

where - at an energy loss E - $M(E)$ is an atomic transition matrix (a set of matrix elements corresponding to transitions to different individual final states) governing the overlap between

the initial and all the possible final states and *N(E)* is the density of final states (see, e.g., Brydson, 2000; Brydson, 2001; Keast et al., 2001).

The transition-matrix term is responsible for the basic edge shape. Some examples of basic shapes are schematically represented in Fig. 3.2.9. For instance, dipole-allowed transitions from an initial state of *s* symmetry to final *p* states (observed, e.g., at K-edges, see section 3.2.1 and Table 3.2.1) give rise to a characteristic sawtooth shape as shown in Fig. 3.2.9a. However, in the case of an ionization edge from a solid material, a large amount of fine structure is generally superimposed on this basic edge shape, as for instance observable for the sawtooth O-K edge shown in Fig. 3.2.8a. These intensity fluctuations are a solid-state effect resulting from the density of state (DOS) term in Eqn. 3.2.9 and is in general particularly pronounced within the first 30-50 eV above the edge onset, where it is termed energy loss near-edge structure (ELNES).

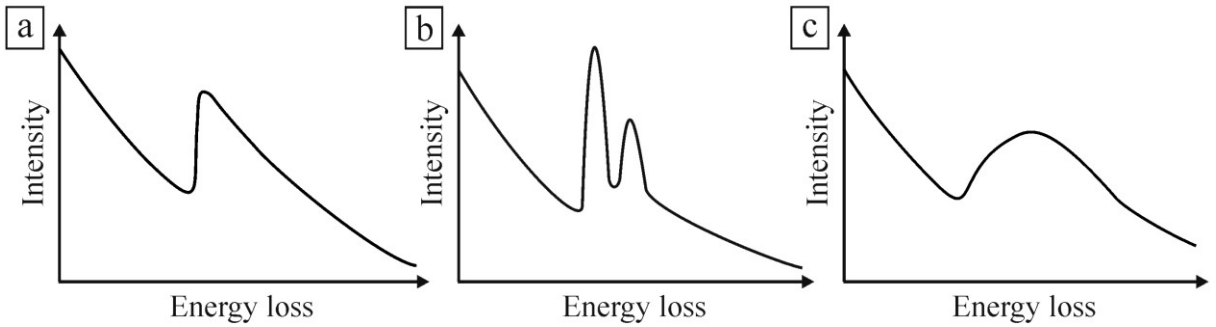

Fig. 3.2.9. Schematic representation of different basic shapes of ionization edges (adapted from Brydson, 2001). **(a)** Sawtooth shape, observed, e.g., at K-edges. **(b)** White lines, observed, e.g., at the $L_{2,3}$ edges of 3d and 4d transition metals. **(c)** Delayed maximum, observed, e.g., at the $M_{4,5}$ edges of 4d transition metals.

For the transition-matrix element to be non-zero, the final state must fulfil some conditions which define the subset of the total DOS that is effectively probed by ELNES (Brydson 2001; Keast et al., 2001; Verbeeck, 2002). The final state needs to be unoccupied (above the *Fermi* level) and must have an appreciable degree of overlap with the well-localized initial atomic core state (with other words, the final state must have a component localized on the same particular atomic site on which the initial core state is localized). Moreover, in the dipole approximation (assumption of a small momentum transfer **q**) the final state must have an appropriate symmetry (only transitions in which the angular-momentum quantum number *l* changes by ± 1 are allowed; the dipole approximation is valid under most experimental conditions but "dipole-forbidden" transitions may become significant if large collection angles – typically β > 30-40 mrad – are employed; Brydson, 2001; Keast et al., 2001). As a result, *N(E)* should be regarded as a local (site-projected) symmetry-projected unoccupied DOS. Under the common assumption that the transition-matrix elements vary slowly with energy, the ELNES measured on a particular ionization edge directly reflects this specific DOS.

The probed DOS strongly depends on the local coordination of the atom undergoing excitation, i.e. on its chemical and structural environment. Hence, the corresponding ELNES can directly be regarded as a coordination fingerprint of the investigated material (see for instance the ELNES data of 3d transition-metal oxides given by Paterson & Krivanek, 1990*a*; Paterson & Krivanek, 1990*b*, Kurata et al., 1993; Mitterbauer et al., 2003). This dependence on the coordination can be used for phase identification if the ELNES from an unknown phase is compared with those measured from reference materials of known compositions and structures (fingerprint method).

The ELNES is also sensitive to the valence (oxidation state) of the atom undergoing excitation. Changes in the oxidation state can shift the edge onset (so-called "chemical shift", see section 4.4.3 for more information). It can also affect the intensity distribution in the ELNES (see, e.g., Brydson, 2001). For instance, the $L_{2,3}$ edges of 3d transition metals exhibit so-called white lines (cf. Fig. 3.2.9b) and it is generally observed that the relative intensity of the L_3 white line with respect to L_2 white line depends on the valence of the metal. This dependence can be used for oxidation-state identification (see, e.g., Schmid & Mader, 2006, as an example of variations in the L_3/L_2 intensity ratios of manganese and iron, respectively, as a function of the metal-oxidation state in different manganese oxides and iron oxides). However, the relationship of the L_3/L_2 intensity ratio with the transition-metal d-band occupancy is still not well understood and different values of the ratio can be found for one particular atom type at constant formal oxidation state, indicating that other parameters can significantly affect the intensity ratio (see, e.g., Brydson et al., 1993). Pearson et al. (1988; 1993) developed an analysis method allowing a more direct correlation between the appropriately normalized total white-line intensity (L_2+L_3) and the d-band occupancy for both 3d and 4d transition metals (see sections 4.2.7 and 4.4.4 and e.g. Graetz et al., 2004, for more information on the normalized white-line intensity method). Nevertheless, the intensity investigation of white-lines is generally more complex and uncertain for 4d transition metals (also exhibiting $L_{2,3}$ white lines) than for 3d metals (Pearson et al., 1993).

Finally, it should be noted that a comprehensive interpretation of ELNES features as a signature of the electronic structure of a material is generally not straightforward and a theoretical calculation of the DOS is useful for that purpose. Different methods allow to model the ELNES of solids which are described elsewhere (for more information and references see, e.g., Keast et al., 2001; Hébert, 2007).

Beyond the pronounced ELNES features, further fine structures in the form of broader and weaker intensity oscillations are generally superimposed on the tail of the ionization edge and may reach several hundred eV above the edge onset. These weak oscillations are termed extended energy-loss fine structure (EXELFS) and contain structural information on the nearest and second-nearest neighbour bond lengths (see, e.g., Egerton, 1986; Williams & Carter 1996; Brydson, 2001).

3.2.7 Quantitative EELS analysis

The background-subtracted intensity I_A under a given inner-shell ionization edge A caused by the excitation of atoms of a specific element a is related to the total number of atoms a in the specimen volume interacting with the incident electron beam, to the intensity of the incident beam, and to the probability of interaction given by the cross-section σ_A for the specific inner-shell ionization event (see, e.g., Egerton, 1986; Verbeeck, 2002). In principle, the absolute atomic concentration C_a of element a in the specimen can be determined. In practice however, this requires the knowledge of the exact incident-beam current and the specimen thickness. These factors are not always accessible with accuracy and it is generally more useful to determine relative atomic concentration ratios of two different elements (relative concentrations are sufficient to characterize the stoichiometry of a material), in which case the problematic factors cancel out.

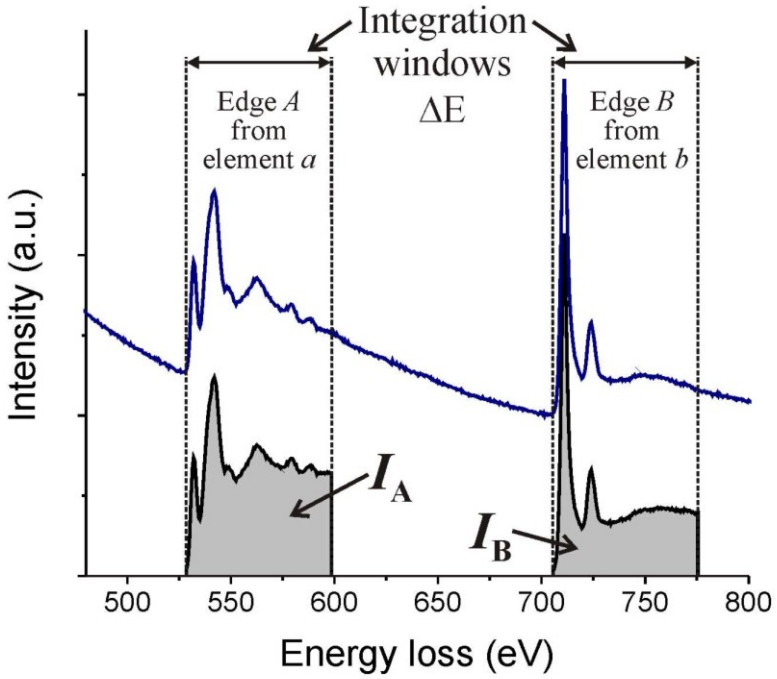

Fig. 3.2.10. Background-subtracted intensity I_A (I_B) under the inner-shell ionization edge A (edge B) caused by the excitation of atoms of the element a (element b). The measured intensities are used to quantify the atomic concentration ratio C_a/C_b in the specimen under investigation (Eqn. 3.2.10). The raw reference spectrum shown as an example was taken on Fe_2O_3 (edge A: O-K; edge B: Fe-$L_{2,3}$) and comes from the EELS Atlas implemented in the Digital Micrograph software (Ahn & Krivanek, 1983).

The atomic concentration ratio C_a/C_b of two elements a and b is determined by measuring the background-subtracted intensities under two different edges, one resulting form the ionization of a atoms (edge A) and the other from b atoms (edge B), as shown in Fig. 3.2.10. In practice, the inelastic interactions effectively considered by the EELS experimental setup (and therefore the corresponding partial cross sections σ_A and σ_B as well as the measured intensities

I_A and I_B) depend on the parameters E_0, β, and α, (cf. section 3.2.2). In addition, the intensity under an edge must be integrated over a finite energy window ΔE (generally starting at the edge onset and having a width of typically some 50-100 eV) which further limits the corresponding partial cross section (see, e.g., Brydson, 2001). Thus, the atomic concentration ratio is given by (see, e.g., Egerton, 1986; Williams & Carter, 1996; Brydson, 2001):

$$\frac{C_a}{C_b} = \frac{\sigma_B(E_0,\beta,\alpha,\Delta E)}{\sigma_A(E_0,\beta,\alpha,\Delta E)} \cdot \frac{I_A(E_0,\beta,\alpha,\Delta E)}{I_B(E_0,\beta,\alpha,\Delta E)} \qquad (3.2.10).$$

Whereas the intensity ratio in Eqn. 3.2.10 can directly be derived from an appropriate EEL spectrum of the material under investigation, the partial cross-section ratio must be either calculated or derived from measurements on a reference material. In the last case the cross-section ratio is commonly termed experimental *k*-factor (Malis & Titchmarsh, 1986):

$$k_{A-B}(E_0,\beta,\alpha,\Delta E) = \frac{\sigma_A(E_0,\beta,\alpha,\Delta E)}{\sigma_B(E_0,\beta,\alpha,\Delta E)} = \frac{C_b}{C_a} \cdot \frac{I_A(E_0,\beta,\alpha,\Delta E)}{I_B(E_0,\beta,\alpha,\Delta E)} \qquad (3.2.11).$$

Thus, by measuring I_A and I_B from a spectrum of a reference material with known composition C_b/C_a one can determine $k_{A\text{-}B}$ (Eqn. 3.2.11). By introducing the obtained $k_{A\text{-}B}$ in Eqn. 3.2.10, the concentration ratio C_a/C_b of a material of unknown composition can then be determined by measuring I_A/I_B from a spectrum of that material.
The calculation of theoretical cross sections is generally based on either the hydrogenic model (Egerton, 1979; Egerton, 1986) or the *Hartree-Slater* model (Leapman et al., 1980; Rez, 1982; Ahn & Rez, 1985). However, these models cannot predict solid-state effects such as fine structures. The accuracy of quantification using calculated theoretical cross-section ratios is typically of the order of 5-30 % (see, e.g. Hofer & Golob, 1988; Auerhammer et al., 1989) but can be worse, particularly when quantification is performed by means of M-edges (see also section 4.4.7). For a better EELS-quantification accuracy, the use of experimental *k*-factors is generally recommended over that of calculated cross-section ratios (Hofer & Kothleitner, 1993; 1996; Williams & Carter, 1996; Schneider, 2003).

3.3 EELS investigation of niobium and niobium oxides

3.3.1 Literature data

When the present work began (in 2003), only few EELS reference data were available in the literature for niobium and its three stable oxides (NbO, NbO_2, and Nb_2O_5). Some reference spectra taken from Nb_2O_5 were published in the "EELS Atlas" (Ahn & Krivanec, 1983). Niobium was also investigated by Pearson et al. (1993) within the framework of their study of the $L_{2,3}$ edges of 3d and 4d transition metals. However, the present work is the first systematic study of niobium and all its three stable oxides which includes plasmon fingerprinting and

ELNES of all the relevant ionization edges. Concerning quantitative EELS, cross-section ratios were already measured on oxidic standards by the use the Nb-$M_{4,5}$ and the O-K edges (measurements on Nb_2O_5, Hofer et al., 1988) or the Nb-$L_{2,3}$ and O-K edges (Hofer et al., 1996; composition of the measured standard not mentioned by the authors). Nevertheless, they were not employed to quantify Nb compounds with known or unknown composition, and no work was performed systematically on all the three stable oxides. In addition, data on quantification by means of the Nb-$M_{2,3}$ edges were missing.
Parallel to the present work (and its related publications: Bach et al., 2004; 2005; 2006; 2007*a*; 2007*b*; 2009*a*; 2009*b*) further niobium-oxides EELS data were published. Jiang & Spence (2004) investigated the O-K edge of NbO_2 (including electronic-structure calculations). Olszta et al. (2006) proposed some ELNES data for the Nb-$M_{4,5}$, Nb-$M_{2,3}$, and O-K edges of niobium and its stable oxides and also performed quantitative EELS by means of the Nb-$M_{4,5}$ and O-K edges of the three oxides. In addition, Olszta et al. (2007; 2008) also investigated Nb-based capacitor structures by means of EELS. It will be further referred to these different studies while presenting and discussing the results of the present work in chapters 4 and 5.

3.3.2 Experimental setup of the present work

In the present work niobium, its three stable oxides (NbO, NbO_2, and Nb_2O_5), and niobium-oxide layers in Nb-based capacitor structures are investigated in terms of low-loss fingerprinting and ELNES of the Nb-$N_{2,3}$, Nb-$M_{4,5}$, Nb-$M_{2,3}$, Nb-M_1, Nb-$L_{2,3}$ and O-K edges (see subchapter 2.3 for more information on the investigated materials). Chemical shifts and normalized Nb-$L_{2,3}$ white-line intensities are considered. Systematic quantitative EELS analyses are performed on the oxides (NbO, NbO_2, Nb_2O_5, and oxide layers) by means of the combination of either the Nb-$M_{4,5}$ and O-K edges or the Nb-$M_{2,3}$ and O-K edges. In addition, the Nb-anodes in capacitor structures as well as the interfaces between anodes and oxide layers are also characterized by means of EELS.

TEM-sample preparation
TEM requires thin samples that can be traversed by fast electrons. In the case of niobium oxides and 200 keV incident electrons the thickness should be inferior to about 50 nm for optimal EELS-investigation conditions.
For Nb, NbO, and the Nb-based capacitor structures TEM samples were prepared using standard techniques which involves diamond-wire cutting, ultrasonic drilling, mechanical grinding, dimpling and Ar^+-ion thinning until perforation (see, e.g., Williams & Carter, 1996). In the case of the capacitor structures Xe^+ ions were sometimes used instead of Ar^+ in the ion-thinning process (see section 5.4.4).
The NbO_2 TEM samples were prepared by dispersing a small amount of powder (cf. section 2.3.1) in acetone, ultrasonic mixing of this dispersion and nebulizing it on a copper mesh (3 mm in diameter) covered with a holey carbon film as support.

For Nb_2O_5, the TEM-sample preparation involved the successive embedding of the needles (cf. section 2.3.1) in epoxy glue and an aluminum oxide tube, diamond cutting, mechanical grinding, dimpling and Ar^+-ion thinning. To avoid electric charging during the electron microscopy investigations, the TEM samples were coated with carbon with the electron-transparent regions of interest protected by masks.

Transmission electron microscopes and experimental parameters

Four different transmission electron microscopes were used for the acquisition of EELS spectra. The majority of experiments were conducted at the *Laboratorium für Elektronenmikroskopie* of the *Universität Karlsruhe* using a 200 keV LEO 922 Omega with a LaB_6 cathode and an in-column Omega energy filter. Two further microscopes were used at the *Max-Planck-Institut für Metallforschung* in Stuttgart: a 200 keV field-emission ZEISS Libra FE equipped with a monochromator and a corrected Omega filter, and a 100 keV VG HB501UX cold field-emission scanning transmission electron microscope with a post-column Gatan Enfina spectrometer. Moreover, some measurements were also performed at the *Electron Microscopy for Materials Research (EMAT)* of the *University of Antwerp* by means of a 300 keV JEOL JEM-3000F field-emission transmission electron microscope fitted with a post-column Gatan Imaging Filter (GIF).

The spectra taken with the LEO 922 Omega, JEOL JEM-300F and VG HB501UX were recorded in the diffraction mode of the microscope (image coupling) whereas the ZEISS Libra FE was operated in the image mode (diffraction coupling). Using the LEO 922 Omega the core-loss spectra were typically recorded with an electron probe of about 25 nm in diameter. At the ZEISS Libra FE and JEOL JEM-300F the selected specimen regions contributing to the spectra also had diameters of a few ten nm. In contrast, spectra were acquired with a better spatial resolution (electron-probe size of only 0.5 nm) by means of the VG HB501UX microscope. Typical experimental conditions for the collection semi-angle β, convergence semi-angle α and energy resolution dE are listed in Table 3.3.1.

Table 3.3.1. Electron energy, convergence and collection semi-angles, approximate energy resolution (determined from the FWHM of the ZLP) for the microscopes used in the present study. Note that other values of β and α were occasionally applied at the LEO microscope. These values are given in the sections presenting the corresponding results.

	Electron energy E_0 [keV]	Convergence semi angle α [mrad]	Collection semi angle β [mrad]	Energy resolution dE [eV]
LEO 922 Omega	200	11.2	12.3	2.1 – 2.4
JEOL JEM-3000F	300	1.6	4.8	1.2
VG HB501UX	100	10.0	6.5	0.6 - 1.5
ZEISS Libra FE	200	0.4	2.3	0.3

For the used conditions of electron-probe size, probe-current density, and acquisition time no significant electron-beam damage was detected during the EELS analyses performed in the present work, except for some occasional carbon contamination resulting in the growth of a C-K edge when several spectra are successively acquired from one and the same sample area. Finally, note that SAED patterns were recorded on some of the reference materials (see subchapter 4.1 and Fig. 4.1.1). In addition to the LEO 922 Omega, a 200 keV Philips CM200 FEG/ST field-emission transmission electron microscope was also used for that purpose (*Laboratorium für Elektronenmikroskopie* of the *Universität Karlsruhe*).

Analysis software packages

The spectra post-treatment (background extrapolation and subtraction, correction for multiple scattering via *Fourier*-transform deconvolution techniques, see section 3.2.5) and the determination of the relative specimen thickness t/Λ (via the analysis of low-loss spectra, see section 3.2.4) were performed using routines implemented in the Gatan Digital Micrograph or SIS EsiVision software.

Further details concerning the used experimental conditions/procedures are given directly in the appropriate sections presenting and discussing the results.

Chapter 4

EELS investigations of reference niobium oxides

4.1 Structural characterization of the reference materials

The crystal structure of the Nb, NbO, and Nb_2O_5 reference materials was checked by selected-area electron diffraction (SAED) using a Philips CM200 FEG/ST (field emission gun) and a LEO 922 Omega transmission electron microscope. Both instruments were operated at 200 kV. SAED patterns were recorded from each reference material in several orientations. Moreover, the resulting diffraction patterns were compared with simulations in order to achieve confirmation whether the investigated reference materials really correspond to the stoichiometric niobium metal, niobium monoxide and niobium pentoxide high-temperature phase (the homogeneity ranges of the different Nb-oxide phases are negligible, so that a confirmation of the phase corresponds to a confirmation of the stoichiometry, see section 5.4.5 for more information on the homogeneity ranges). The simulations of the diffraction patterns were performed using the JEMS (Java version of Electron Microscopy Software) software (Stadelmann, 1987) with crystallographic data corresponding to the stoichiometric structures described in subchapter 2.1 (Gatehouse & Wadsley, 1964; Gmelin, 1970; Pialoux et al., 1982). JEMS is a computer package allowing one to simulate diffraction patterns, but also high-resolution TEM images (available online at http://cimewww.epfl.ch/people/stadelmann/jemsWebSite/jems.html).
Fig. 4.1.1 shows the experimentally determined diffraction patterns from [111]-oriented Nb (Fig. 4.1.1a), [001]-oriented NbO (Fig. 4.1.1c), and [101]-oriented Nb_2O_5 (Fig. 4.1.1e) as well as the corresponding simulations (Fig. 4.1.1b, d, and f, respectively). The mean Nb lattice parameter as determined from the experimental diffraction patterns was found to be $a = 0.326$ nm which is consistent with the crystallographic data ($a = 0.3300$ nm, 1.2% relative error) supplied in literature (Pialoux et al., 1982). Also for NbO, the achieved lattice parameter $a = 0.424$ nm is in good agreement with the literature value of $a = 0.4212$ nm (Pialoux et al., 1982), the relative error being in that case around 0.7%. With regard to Nb_2O_5 the following parameters were found: lattice constant a = 2.141 nm (literature value is 2.116 nm - Gatehouse & Wadsley, 1964 - relative error of 1.2 %), b = 0.384 nm (literature: 0.3822 nm, 0.5 % error), c = 1.89 nm (literature: 1.935 nm, 2.4 % error), and angle $\beta = 118.2°$

(literature: 119.8°, 1.3 % error). The resulting good agreement of the experimental diffraction patterns with reference values confirms the presence of stoichiometric Nb_2O_5.

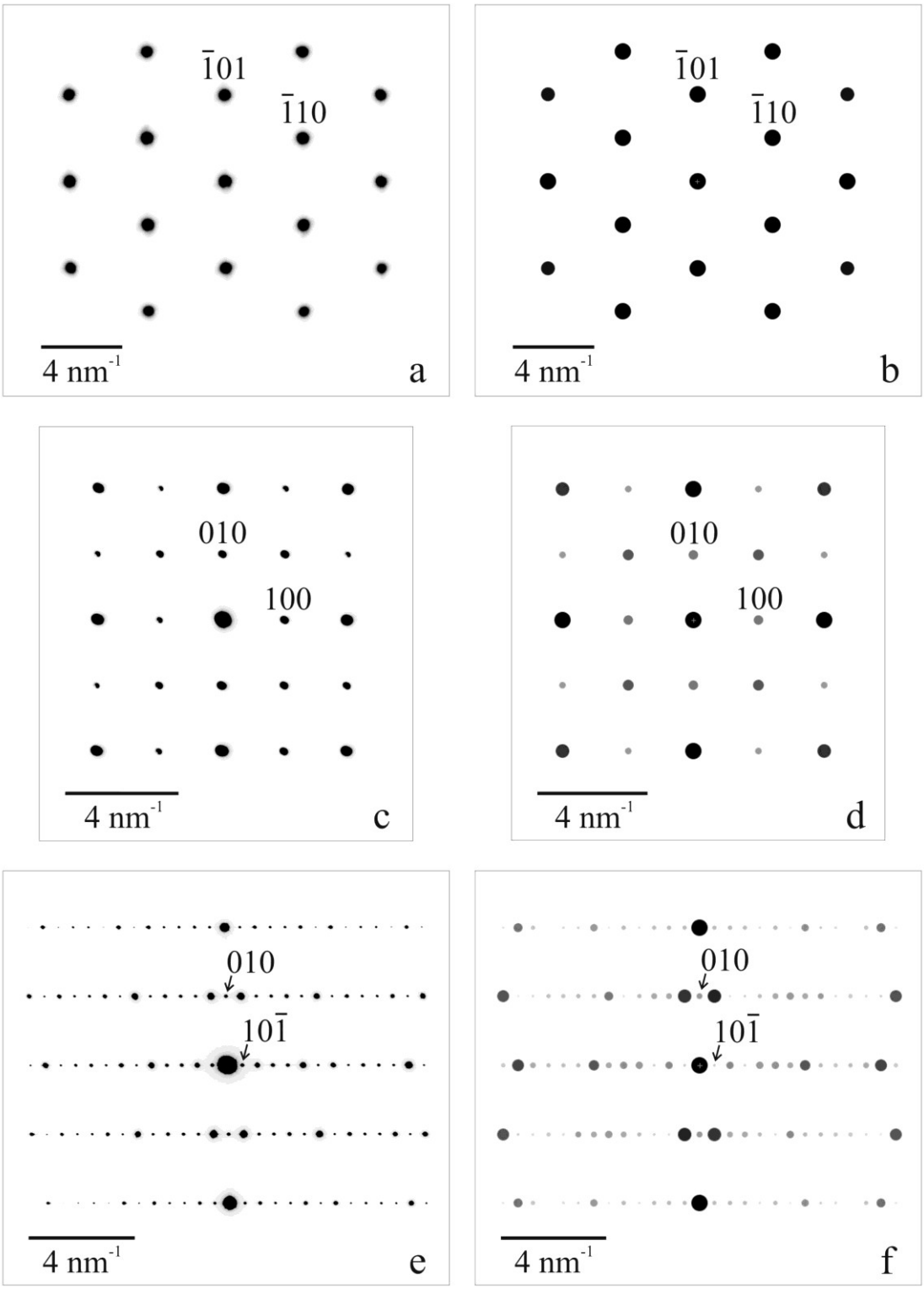

Fig. 4.1.1. Electron diffraction pattern from Nb in [111] orientation (a), NbO in [001] orientation (c) and from Nb_2O_5 in [101] orientation (e) and the corresponding JEMS-simulations (b, d, and f, respectively). The following lattice parameters were determined experimentally: a = 0.326 nm for Nb, a = 0.424 nm for NbO, the values for Nb_2O_5 are a = 2.141 nm, b = 0.384 nm, c = 1.89 nm, and β = 118.2°

The NbO_2 reference material was available in the form of powder, whereas Nb, NbO, and Nb_2O_5 were investigated as bulk materials. Its crystal structure was checked via x-ray diffraction (XRD) by means of a Siemens D5000 powder diffractometer utilizing $Cu_{K\alpha}$ radiation and equipped with a position-sensitive detector (PSD). The diffracted signal was measured in the *Bragg-Brentano* configuration for diffraction angles 2θ in the range of 20.000° to 89.929° (acquisition step of 0.071°). The resulting XRD pattern was compared to reference patterns published in the Powder Diffraction File™ database PDF-2 (best match with the file PDF no. 43-1043). PDF-2 contains experimental powder data collected by the *International Centre for Diffraction Data* (ICDD) and data collected, edited and standardized from the data bases provided by the *Fachinformationszentrum Karlsruhe* (FIZ) and the *National Institute of Standards and Technology* (NIST).

The XRD pattern recorded from NbO_2 in the present work is shown in Fig. 4.1.2 together with a simulated reference diffraction pattern coming from the PDF-2 database (no. 00-043-1043). The reference pattern was calculated using the crystallographic data corresponding to the structure described in section 2.1.2 for stoichiometric NbO_2 (lattice constant $a = b = 1.3696$ nm and $c = 0.5981$ nm - Cheetham & Rao, 1976). The good agreement observed between the calculated and experimentally determined positions of the peaks confirms the crystal structure of the NbO_2 reference material and no impurities were apparent in the XRD data.

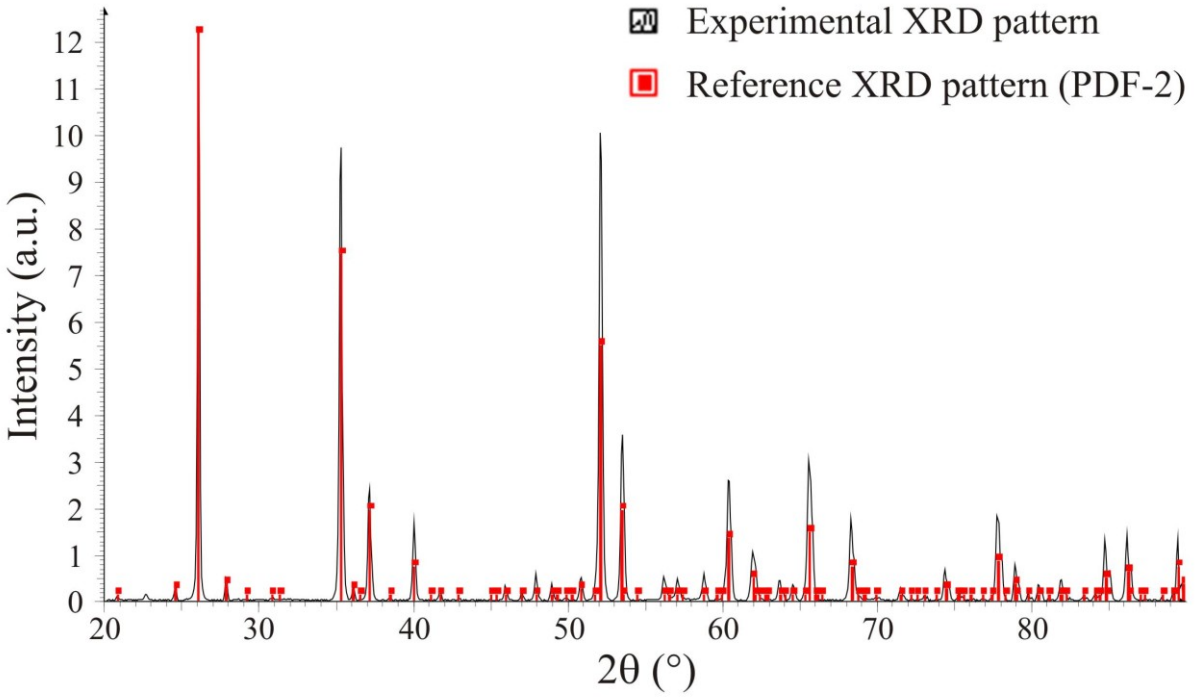

Fig. 4.1.2. X-ray diffraction pattern recorded from NbO_2 and the corresponding reference pattern calculated with the crystallographic data of stoichiometric NbO_2 (Cheetham & Rao, 1976) and provided by the PDF-2 data base.

4.2 Low-loss fingerprinting and ELNES results

The ELNES of an ionization edge is highly sensitive to the specific local environment of the atom undergoing excitation, and thus provides a fingerprint of the investigated phase (see section 3.2.6). Therefore, the recording of reference spectra is essential for the study of unidentified phases. In this subchapter, the results of the ELNES investigations performed on the four stoichiometric reference materials (Nb, NbO, NbO_2, and Nb_2O_5) are presented. These results will be used in chapter 5 to analyse the Nb-based capacitor structures.

Fig. 4.2.1 represents a montage of three EEL spectra recorded on NbO_2 using the LEO 922 microscope. They are shown as measured, i.e. without any correction. For more clarity, there are gain changes at 161 eV and 2235 eV, and in order to improve the visibility of diverse spectral components, the spectra were taken at different specimen regions with different thicknesses. Fig. 4.2.1 thus shows the main EELS features appearing for the niobium–oxygen system. With increasing energy loss there are the plasmon around 21 eV, the Nb-$N_{2,3}$, -$M_{4,5}$ and –$M_{2,3}$ edges at about 34 eV, 205 eV, 363 eV, respectively, the O-K edge at about 532 eV, and finally the Nb-L_3 and –L_2 edges around 2371 eV and 2465 eV, respectively. In addition to major edges, a less intense minor edge should also be mentioned: the Nb-M_1 edge is hardly recognizable as a slope variation around 468 eV on Fig. 4.2.1, but its presence has to be kept in mind, as it can disturb the background subtraction under the O-K edge.

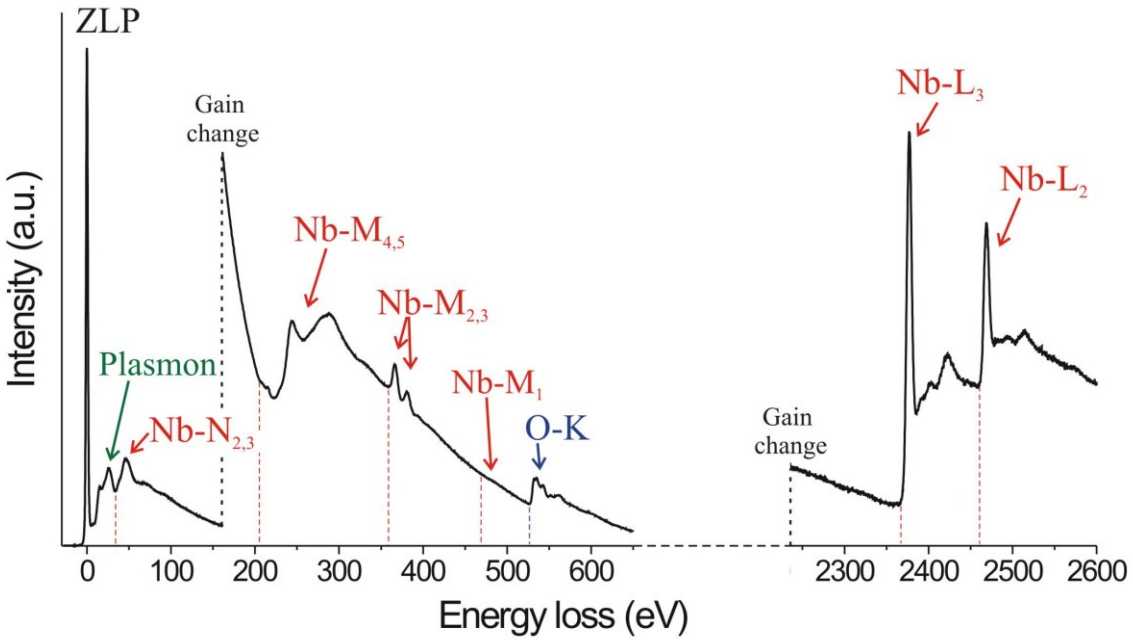

Fig. 4.2.1. EEL spectra showing the plasmon and major edges occurring for niobium oxides.

All the above-mentioned EELS features were investigated for the four reference materials using the LEO 922 microscope with an energy resolution of approximately 2.1 – 2.4 eV, and the resulting spectra constitute the core of this subchapter on ELNES. It may appear

surprising to perform ELNES with an energy resolution poorer than 2 eV, but it will be shown that in the present case it is good enough to recognize distinct fine structures characteristic for the different materials. Some edges were also occasionally recorded for a part of the reference materials using the JEOL, the ZEISS Libra or the VG microscopes, providing an insight with better energy resolution into the corresponding fine-structures details.
The spectra which are shown in the figures of the following sections were generally corrected for background and multiple scattering. If it is not the case, it will expressly be mentioned.

4.2.1 Low-loss fingerprinting

The features occurring in the low-loss range of the spectrum result from collective plasma oscillations and single electron inter- and intra-band transitions. These different electron excitation modes are sensitive to the chemical configuration and electronic properties of the specimen. Like the ELNES of a core-loss edge, the features of the low-loss region can thus provide a phase fingerprint of the material (see e.g., Brydson, 2001). Nevertheless, these characteristic features lie on the tail of the intense zero-loss peak (ZLP), which is simultaneously recorded. To minimize this background contribution and to achieve an optimal signal/noise ratio of the data, the intensity of the signal of interest should be as high as possible relative to that of the ZLP. Hence, in that case it is preferable to investigate specimens with a relative thickness t/Λ greater than 0.5. However, a multiple scattering removal procedure is then required to properly access the fingerprint, and the specimen should anyway be kept thin enough to avoid artefacts due to the deconvolution algorithm.

Fig. 4.2.2a shows representative low-loss spectra acquired from the four reference materials using the LEO 922 microscope. Besides the plasmon, the low-loss spectra also exhibit the Nb-$N_{2,3}$ edges, which are described in more detail in the next section. The relative thickness of the investigated specimen regions was ranging from 1.2 to 2. The spectra were corrected for multiple scattering using the *Fourier*-log deconvolution technique, and the ZLP and its tail were also removed during this procedure (SIS EsiVision software). Since the poor energy resolution produces broad ZLP tails, and the tail subtraction is quite inaccurate, the first details in the low-loss region observed below ~5-7 eV are probably not free of artefact and cannot directly be interpreted. However, the plasmon exhibits enough characteristic fine structures to clearly distinguish the four reference materials when the niobium oxidation state increases from 0 to +5.
Whereas the low-loss spectrum of Nb is characterized by a small peak at ~ 10.6 eV followed by a sharp intense peak at 21.3 eV (marked by the letter a' and b' in Fig. 4.2.2a, respectively), the plasmon of the reference niobium oxides exhibit a triple "peak" structure (letters a, b and c in Fig. 4.2.2a). The position of the "peaks" is reported in Table 4.2.1, but some of these features only appear in the form of shoulders (a and b for NbO, b for NbO_2 and Nb_2O_5), leading to an approximate position measurement. Hence, the given values should just be considered as a rough indication. No continuous trend can be observed in the positions of the peaks while the niobium oxidation state increases from +2 by NbO to +4 by NbO_2 and then to

+5 by Nb_2O_5. A clear shift of all peaks to higher energy losses occurs between NbO and NbO_2 (+1.3 eV on average), whereas a less obvious shift to lower energies seems to take place between NbO_2 and Nb_2O_5 (-0.3 eV on average). Generally, by considering only the two oxides with extreme oxidation states (NbO (+2) and Nb_2O_5 (+5)), a shift to higher energy losses with increasing niobium oxidation state can still be recognized (+1.0 eV on average).

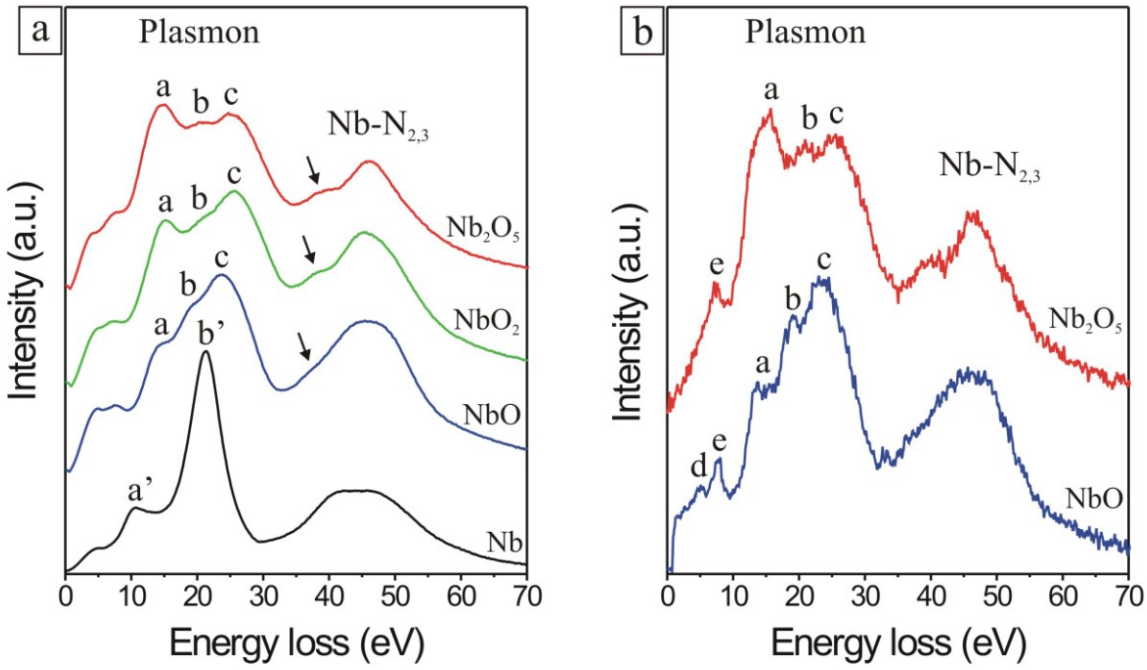

Fig. 4.2.2. EEL reference low-loss spectra recorded from: **a)** Nb, NbO, NbO_2, and Nb_2O_5 using the LEO 922 microscope (dE ~ 2.1 eV, E_0 = 200 keV, β = 12.3 mrad, α = 11.2 mrad), **b)** NbO and Nb_2O_5 using the ZEISS Libra FE microscope (dE ~ 0.3 eV, E_0 = 200 keV, β = 2.3 mrad, α ~ 0.4 mrad). The ZLP was subtracted and the multiple scattering removed from the spectra.

Table 4.2.1. Position (energy loss in eV) of the characteristic features occurring in the low-loss spectra acquired from the four reference materials using the LEO 922 microscope (cf. Fig. 4.2.2).

↓ material	peak →	a (a')	b (b')	c
Nb_2O_5 (+5)		14.9 eV	~ 20.6 eV	25.2 eV
NbO_2 (+4)		15.2 eV	~20.8 eV	25.6 eV
NbO (+2)		~ 14.6 eV	~ 19.4 eV	23.6 eV
Nb (0)		10.6 eV	21.3 eV	∅

The information content of the peaks' position being limited, the most pronounced criterion influencing the shape of the plasmon and thus allowing to characterize the three reference oxides is the strongly different relative height of the three peaks. As the niobium oxidation state increases from +2 by NbO to +4 by NbO_2 and then to +5 in the case of Nb_2O_5, the

shoulder (a) observed for NbO becomes gradually a distinct peak and its intensity increases continuously compared to that of the peak (c). Thus, at the same time the peaks appear to shift to higher energies the intensity of the first peak (a) increases compared to the two next peaks (b) and (c), which corresponds to a relative displacement of intensity to lower energy.
The width of the plasmon provides another characteristic feature allowing to distinguish the four reference materials. Generally, the plasmon lines are broader in insulators and semiconductors than in conductors (Brydson, 2001, see also section 3.2.1). In the present case the plasmon becomes gradually broader as the niobium oxidation state increases from 0 by Nb to +5 by Nb_2O_5. The intensity depression between the plasmon and the Nb-$N_{2,3}$ edges is not deep enough by NbO_2 to afford a measure of the full width at half maximum of the plasmon intensity. The full width at 60% of the maximum of the plasmon intensity was thus chosen to quantify the above mentioned trend. The following values were measured: 5.3 eV, 16.0 eV, 19.5 eV and 20.3 eV for Nb, NbO, NbO_2 and Nb_2O_5, respectively.

The low-loss region of the two reference oxides with extremely different niobium oxidation states was also examined with a much better energy resolution (about 0.3 – 0.4 eV) using the Libra FE microscope equipped with a monochromator. It should be noticed that the experimental parameters α and β were also different from those during the use of the LEO 922 microscope (cf. Table 3.3.1). The relative thickness of the investigated specimen regions was about 1.4 for Nb_2O_5 (+5) and 2.4 for NbO (+2). In Fig. 4.2.2b the resulting spectra are shown after ZLP subtraction and *Fourier*-log deconvolution (Gatan Digital Micrograph software). In spite of the different recording parameters, the "fingerprints" of the plasmons remain identical to those recorded with the LEO microscope (Fig. 4.2.2a). The few weak differences seem only to result from the better energy resolution of the spectral details. Thus, in the case of NbO, the triple peak structure appears much more pronounced at a high energy resolution: the shoulder (a), observed with a resolution of ~ 2.1 eV in Fig. 4.2.2a, takes the form of a wide step at a resolution of ~ 0.3 eV in Fig. 4.2.2b, whereas the shoulder (b) now appears as a distinct peak. Also for Nb_2O_5, the peak (b) is better recognized with the higher energy resolution of the Libra. For both NbO and Nb_2O_5, the relative heights of the different peaks stay similar to those obtained with the LEO microscope, still allowing to differentiate between the two oxides.
Moreover, the better energy resolution of the Libra leads to a less expanded tail of the ZLP compared to that observed for the LEO microscope, enabling to certainly identify new distinctive features in the range of the first 10 eV of the low-loss spectra. Whereas NbO is characterized by two peaks at ~ 5.0 eV and 7.7 eV (marked by the letters d and e in Fig. 4.2.2b, respectively), only one peak at ~ 7.4 eV appears for Nb_2O_5 (letter e in Fig. 4.2.2b).

4.2.2 Nb-$N_{2,3}$ ELNES

The Nb-$N_{2,3}$ edges are mainly attributed to transitions of Nb 4p electrons to the unoccupied 4d and 5s states. Fig. 4.2.3 represents the four Nb-$N_{2,3}$ edges resulting from the reference low-loss spectra shown in Fig. 4.2.2a after background subtraction. Due to the presence of the

plasmon immediately in front of the Nb-$N_{2,3}$ edges, the background should be fitted within very narrow energy windows (~ 3 to 5 eV in width) positioned directly on the intense tail of the plasmon. Hence, the reliability of the background extrapolation under the edges was limited, making the subtraction procedure particularly uncertain. Nevertheless, the fine structure of the edges allows a fingerprinting of the four reference materials.

The Nb-$N_{2,3}$ edges of Nb are characterized by a large bump presenting an intensity plateau (arrow in Fig. 4.2.3). With increasing niobium oxidation state, the top of the bump becomes sharper and sharper and more rounded, whereas a shoulder gradually emerges in front of it (arrows on the NbO, NbO_2 and Nb_2O_5 spectra in Fig. 4.2.3). The shoulders are even more pronounced without background removal (arrows in Fig. 4.2.2a).

A chemical shift by about 4-5 eV to higher energy seems to take place as the niobium oxidation state increases from 0 by Nb to +5 by Nb_2O_5. However, as the plasmon width also differs as a function of the oxidation state, and due to the strong overlapping of the plasmon tail with the Nb-$N_{2,3}$ signal (Fig. 4.2.2a), the background subtraction does not allow an accurate restitution of the edge onset position, and the apparent energy shift should carefully be considered.

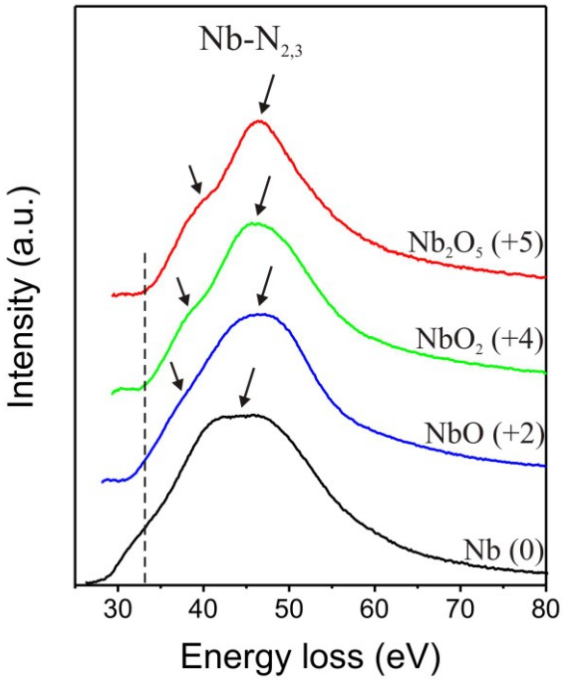

Fig. 4.2.3. EEL reference spectra showing the Nb-$N_{2,3}$ edges recorded on Nb, NbO, NbO_2, and Nb_2O_5 using the LEO 922 microscope (dE ~ 2.1 eV, E_0 = 200 keV, β = 12.3 mrad, α = 11.2 mrad). The spectra were corrected for multiple scattering (*Fourier*-log deconvolution of the low-loss spectra) and for background.

4.2.3 Nb-$M_{4,5}$ ELNES

The Nb-$M_{4,5}$ edges are principally associated with the transition of Nb 3d electrons to unoccupied 4f and 5p states. Representative reference spectra recorded from Nb, NbO, NbO_2,

and Nb_2O_5 at the LEO 922 microscope are shown in Fig. 4.2.4a after background removal and multiple-scattering correction (*Fourier*-ratio deconvolution). The four stoichiometric materials exhibit different fine structures of the Nb-$M_{4,5}$ edges. Nb is characterized by three successive shoulders followed by a large bump (marked by the letters a, b c and d in Fig. 4.2.4a, respectively). As the niobium oxidation state increases from 0 by Nb to +5 by Nb_2O_5, the shoulders (a) and (c) gradually become distinct peaks, whereas the shoulder (b) disappears. The bump (d) occurs sharper for NbO, and its intensity maximum clearly shifts to higher energy losses with increasing oxidation state from +2 up to +5 by Nb_2O_5.

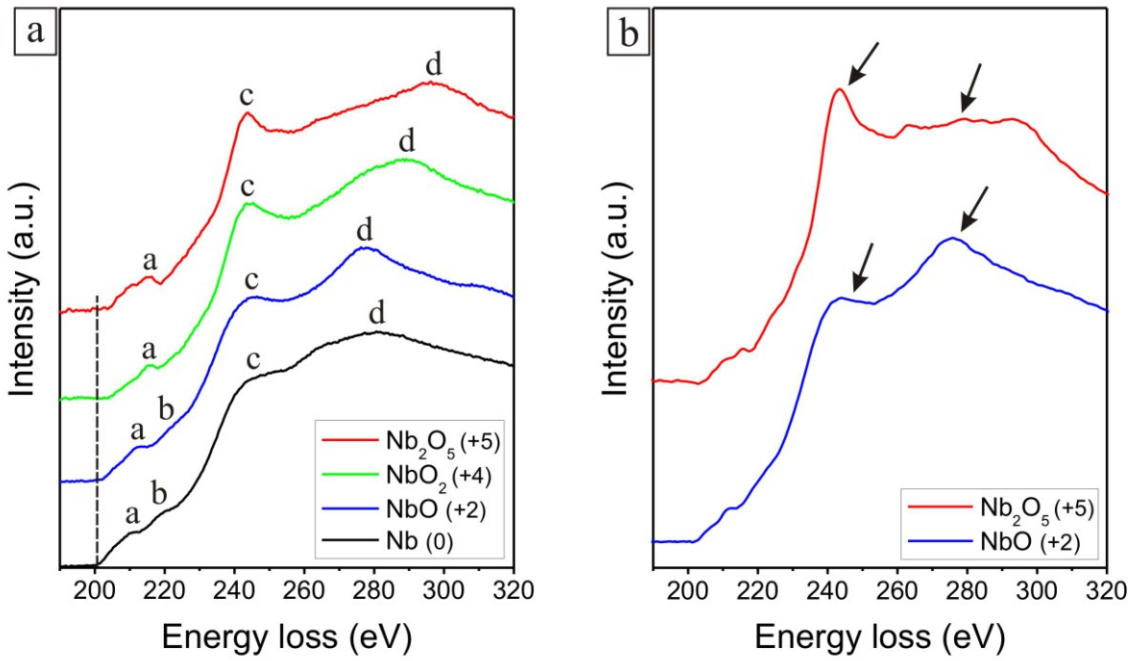

Fig. 4.2.4. EEL reference spectra showing the Nb-$M_{4,5}$ edges recorded from: **a)** Nb, NbO, NbO_2, and Nb_2O_5 using the LEO 922 microscope (dE ~ 2.1 eV, E_0 = 200 keV, β = 12.3 mrad, α = 11.2 mrad), **b)** NbO and Nb_2O_5 using the JEOL JEM-3000F microscope (dE ~ 1.2 eV, E_0 = 300 keV, β = 4.76 mrad, $\alpha \sim \beta/3$). The spectra were corrected for background and multiple scattering.

Owing to the delayed maximum shape of the Nb-$M_{4,5}$ edges, a precise localization of the edge onset is limited by the noise and the quality of the background subtraction in the range of few eV preceding the edge. However, two low-loss spectra including ZLP were recorded immediately before and after the acquisition of each core-loss spectrum, in order to check for a possible energy drift of the spectrum during its exposure on the CCD camera. Moreover, for each reference material, the Nb-$M_{4,5}$ edges were measured roughly on the same region of the CCD camera. Such a procedure minimizes the influence of eventual artefacts in the energy axis calibration of the camera while measuring the relative energy shift of the edge onset of the different materials. Hence, the investigation of the chemical shift of the Nb-$M_{4,5}$ edges should be reasonably accurate. For each reference material, the data processing was performed on four different spectra. The resulting chemical shifts relative to the onset of the Nb-$M_{4,5}$ edges of Nb can be seen in Fig. 4.2.5 as a function of the niobium oxidation state.

Thus, a chemical shift of about 4 eV to higher energy is here clearly observable as the niobium oxidation state increases from 0 by Nb to +5 by Nb_2O_5.

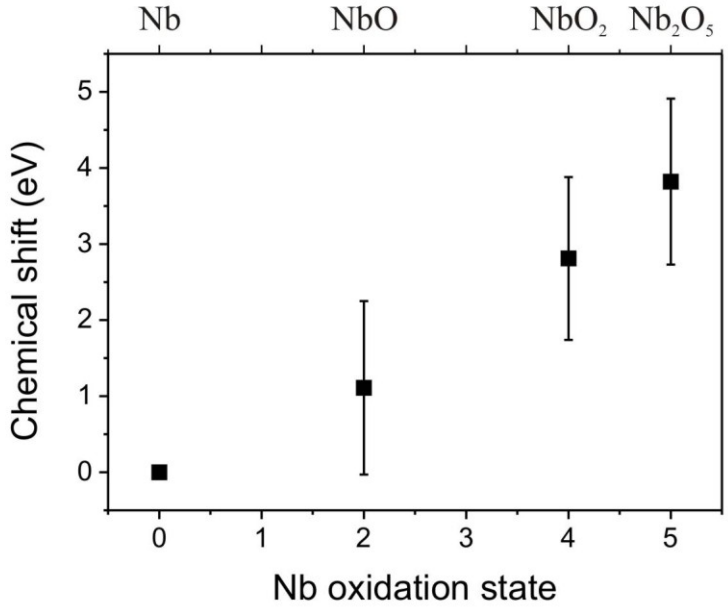

Fig. 4.2.5. Chemical shift of the Nb-$M_{4,5}$ edges as a function of the niobium oxidation state of the reference materials. The onset of the Nb-$M_{4,5}$ edges of Nb was chosen as a reference and subtracted from that of the other materials. For each material, four spectra recorded with the LEO microscope were analyzed.

The Nb-$M_{4,5}$ edges of NbO (+2) and Nb_2O_5 (+5) were also investigated with a better energy resolution (about 1.2 eV) using the JEOL JEM-3000F microscope. The experimental parameters E_0, α and β were different from those at the LEO 922 microscope (cf. Table 3.3.1). The corresponding spectra shown in Fig. 4.2.4b allow a clear distinction between the two reference oxides with (+2) and (+5) oxidation state, respectively. The Nb-$M_{4,5}$ edges of NbO can be characterized by a shoulder at about 245 eV followed by a large bump (arrows in Fig. 4.2.4b), whereas the Nb-$M_{4,5}$ edges of Nb_2O_5 show a characteristic peak followed by a kind of plateau (arrows in Fig. 4.2.4b).
Some dissimilarities observable between the JEOL and the LEO reference spectra can be attributed to the different experimental parameters employed (E_0, α and β). For instance, no intensity plateau after 260 eV energy loss was observed on the Nb_2O_5 spectra recorded with the LEO 922 microscope, but an intensity increase (bump (d) in Fig. 4.2.4a).

4.2.4 Nb-$M_{2,3}$ ELNES

The Nb-$M_{2,3}$ edges are mainly attributed to the transition of Nb 3p electrons to unoccupied 4d and 5s states and present a typical white-line shape. Representative reference spectra recorded on Nb, NbO, NbO_2, and Nb_2O_5 by means of the LEO 922 microscope are given in Fig. 4.2.6 without any correction (Fig. 4.2.6a) and after background and multiple scattering correction

(Fig. 4.2.6b). The background subtraction under the Nb-$M_{2,3}$ edges is complicated by the intense tail of the preceding Nb-$M_{4,5}$ edges. Exponential or log-polynomial functions were found to be more adequate than the classical power-law model to fit the background, but without the assurance that the energy dependency of the background does not vary under the edge. Moreover, the profile of the Nb-$M_{4,5}$ edges tail differs for the different reference materials (arrows in Fig. 4.2.6a) and thicknesses, making an ELNES comparison between the reference spectra even more arbitrary, especially when the relative height of different features has to be analyzed.

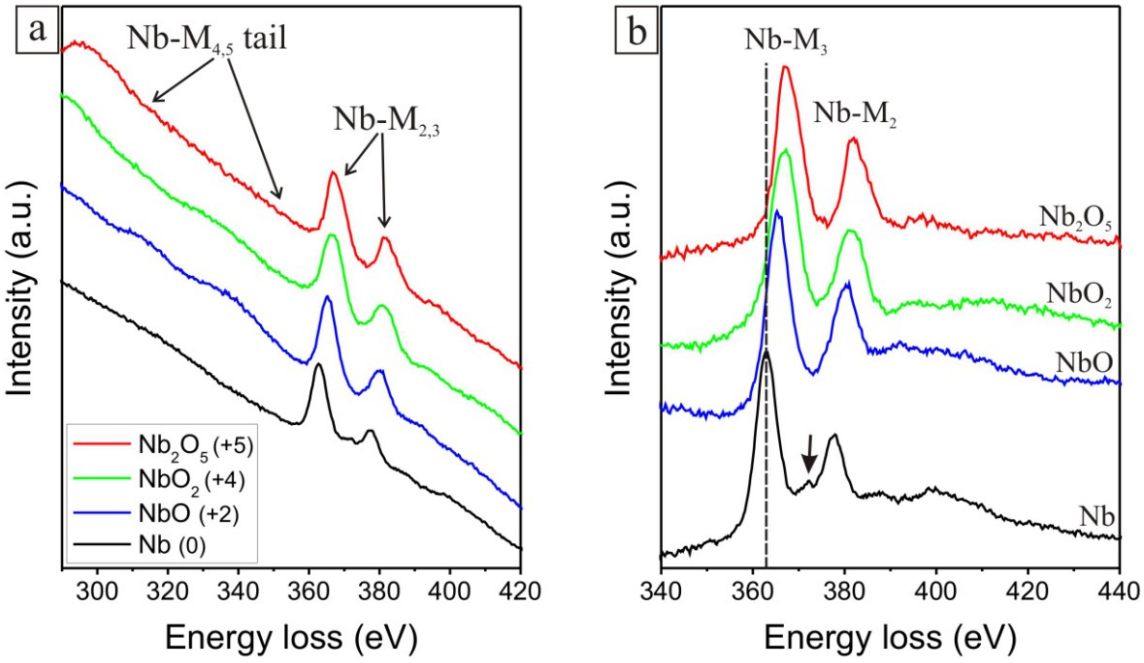

Fig. 4.2.6. EEL reference spectra recorded from Nb, NbO, NbO_2, and Nb_2O_5 using the LEO 922 microscope (dE ~ 2.1 eV, E_0 = 200 keV, β = 12.3 mrad, α = 11.2 mrad) and showing: **a)** the tail of the Nb-$M_{4,5}$ edges and the Nb-$M_{2,3}$ edges without correction, **b)** the Nb-$M_{2,3}$ edges after background and multiple scattering correction.

Few characteristic features are observed for the Nb-$M_{2,3}$ ELNES at dE ~ 2.1 eV. In the spectrum recorded from Nb a little peak occurs between the two white lines (arrow in Fig. 4.2.6b), but the general shape of the Nb-$M_{2,3}$ edges is quite the same for the three reference oxides. Due to the complicated background subtraction, the investigation of the variations of the M_3 to M_2 white-line intensity ratio as a function of the niobium oxidation state is not accurate, and no clear trend could be revealed. Nevertheless, with increasing niobium oxidation state from 0 by Nb to +5 by Nb_2O_5, it could be noticed that the continuum intensity beyond the white lines decreases relatively to the intensity maximum in the spectrum and a chemical shift to higher energy of about 4 eV can again be measured.

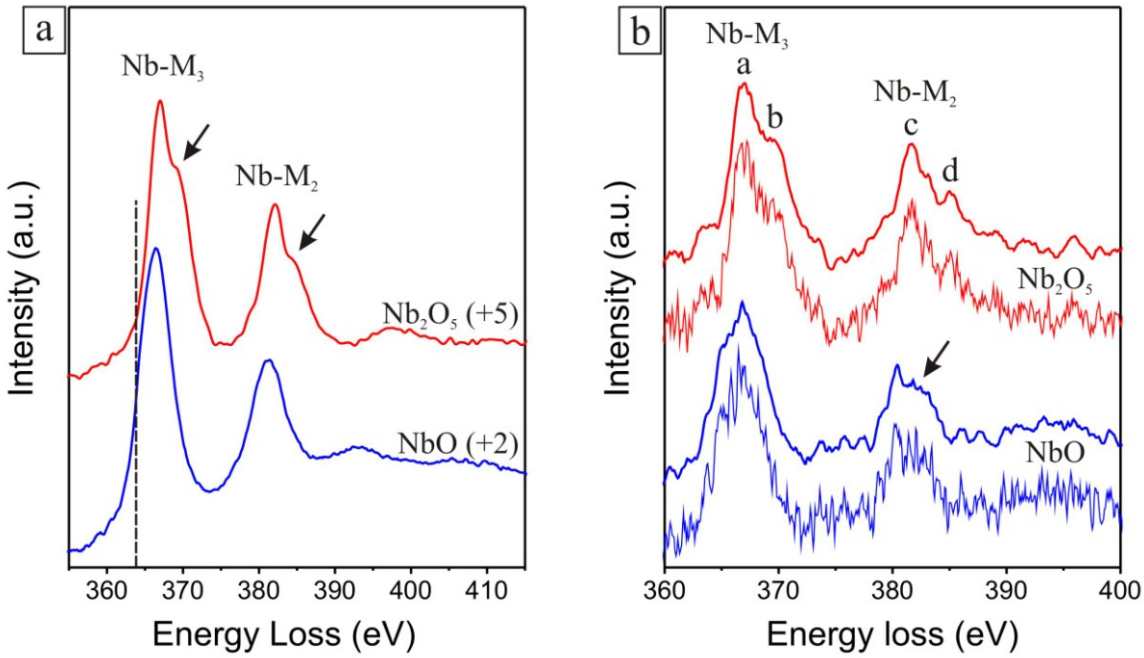

Fig. 4.2.7. EEL reference spectra showing the Nb-$M_{2,3}$ edges recorded on NbO and Nb_2O_5 using: **a)** the JEOL JEM-3000F microscope (dE ~ 1.2 eV, E_0 = 300 keV, $\beta = 4.76$ mrad, $\alpha \sim \beta/3$), **b)** the ZEISS Libra FE microscope (dE ~ 0.3 eV, E_0 = 200 keV, $\beta = 2.3$ mrad, $\alpha \sim 0.4$ mrad). The spectra were corrected for background and multiple scattering. For both reference materials in b), the upper spectrum is a smoothed version of the raw-data below.

The JEOL JEM-3000F microscope and the ZEISS Libra FE microscope were used to inspect the Nb-$M_{2,3}$ ELNES of NbO and Nb_2O_5 with better energy resolution. Spectra recorded with the JEOL microscope at an energy resolution of about 1.2 eV are shown in Fig. 4.2.7a. Characteristic fine structures are clearly visible. While the Nb-M_3 and -M_2 white lines of Nb_2O_5 are characterized by shoulders (arrows in Fig. 4.2.7a), indicating the presence of double-peak structures, such a fine structure could not be detected for NbO. In order to investigate chemical shifts, the same procedure was performed to record the spectra as that described in section 4.2.3 for the examination of the Nb-$M_{4,5}$ edges using the LEO microscope. In addition, the Nb-M_3 edge in the core-loss spectra and the ZLP in the low-loss spectra were acquired roughly at the same region of the CCD camera, minimizing the influence of eventual calibration artefacts of the camera not only on chemical shift measurements but also on the determination of the absolute energy position of the edge onset. The position of the Nb-$M_{2,3}$ edges was measured at the front half maximum of the M_3 white line, i.e. at the low-energy side of the half height of the edge, for two NbO and two Nb_2O_5 core-loss spectra. This value was found at 363.8 ± 0.2 eV for NbO and at 365.2 ± 0.3 eV for Nb_2O_5 (energy resolution of 1.2 eV) indicating a chemical shift to higher energy of about 1.4 ± 0.5 eV as the niobium oxidation state increases from +2 to +5. The error partly results from the spectrum drift occurring between the acquisitions of the two low-loss spectra corresponding to each core-loss spectrum. Moreover, it should again be noticed that the

accuracy of these measurements may be disturbed by the imprecise background subtraction procedure.

To try to resolve eventual double-peak structures in the Nb-M_2 and –M_3 white lines of NbO, measurements were carried out using the Libra microscope equipped with a monochromator. The monochromator yields an energy resolution of 0.3 eV, but leading to less intense and thus noisier spectra. Fig. 4.2.7b presents NbO and Nb_2O_5 reference spectra before and after a slight smoothing procedure with respect to the noise. The double-peak structures appear more pronounced for Nb_2O_5, especially on the smoothed Nb-M_2 white line (peaks c and d in Fig. 4.2.7b), whereas still no double-peak structure can clearly be distinguished for NbO. At the most, a shoulder can be suspected on the smoothed Nb-M_2 white line (arrow in Fig. 4.2.7b), but without the assurance that it is no artefact resulting from the original noise.

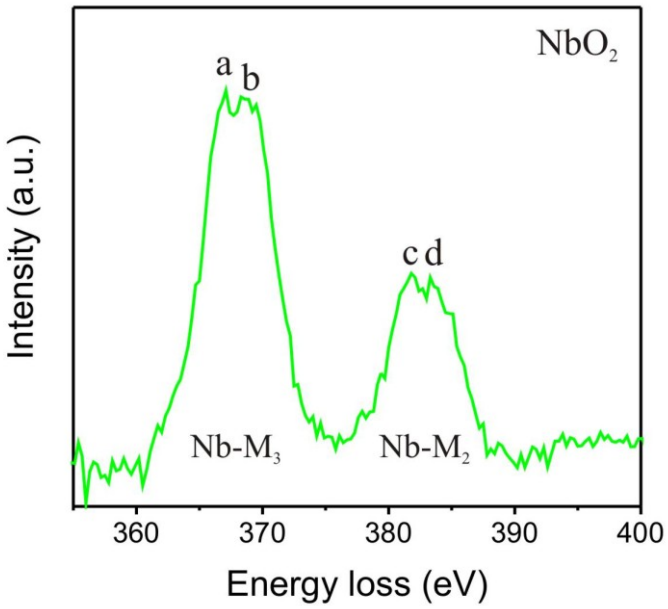

Fig. 4.2.8. EEL reference spectrum showing the Nb-$M_{2,3}$ edges recorded on NbO_2 using the VG HB501UX microscope (dE ~ 0.6 eV, E_0 = 100 keV, β ~ 6.5 mrad, α ~ 10 mrad). The spectrum was corrected for background and multiple scattering.

Finally, double-peak structures were also observed on the Nb-M_3 and M_2 white lines of NbO_2 using the VG HB501UX microscope at an energy resolution of about 0.6 eV (letters a and b for Nb-M_3, c and d for Nb-M_2 in Fig. 4.2.8). No spectra were acquired at the same conditions (dE, E_0, α, β) on NbO or Nb_2O_5, but a rough comparison can be drawn with the Nb-$M_{2,3}$ edges recorded via the JEOL and Libra microscopes (Fig. 4.2.7). For both white lines, the double-peak structures of NbO_2 and Nb_2O_5 differ in the relative height of the two peaks. Whereas the two peaks have approximately the same height for NbO_2 (Fig. 4.2.8), the second peak is always less intense than the first one in the case of Nb_2O_5 (Fig. 4.2.7). Indeed, in spite of the different experimental parameters (E_0, α, β) employed at the JEOL and the Libra microscopes to examine Nb_2O_5, the resulting Nb-$M_{2,3}$ spectra exhibit similar double-peak structures (Fig. 4.2.7). Hence, although another set of parameters was used to investigate

NbO_2, it can be assumed that the relative height of the peaks is a significant feature enabling to distinguish NbO_2 and Nb_2O_5.

4.2.5 Nb-M_1 ELNES

The Nb-M_1 edge is principally associated with the transition of Nb 3s electrons to unoccupied 5p states. Background-subtracted reference spectra recorded from Nb, NbO, NbO_2, and Nb_2O_5 by using the LEO 922 microscope are shown in Fig. 4.2.9. The Nb-M_1 edge is a weak feature which has the form of a large noisy bump (Fig. 4.2.9a). In the case of the reference oxides it precedes the much more intense O-K edge (Fig. 4.2.9b). Except for NbO, exponential functions were preferred to the commonly assumed power-law model for the background fit. Indeed, the background subtraction is perturbed by the tails of the preceding Nb-$M_{4,5}$ and -$M_{2,3}$ edges as well as by the very low signal-to-background ratio (see for instance Fig. 4.2.1 for NbO_2), which makes a separation between the edge and background features such as EXELFS oscillations very uncertain. Thus, after the background subtraction procedure, the EELS data probably already contain substantial errors. Moreover, the raw Nb-M_1 data were already very noisy. Under these circumstances, a correction for multiple scattering to reveal fine-structure details made no sense. It was all the more unnecessary for the spectra shown in Fig. 4.2.9, since they were acquired from specimen regions with quite similar relative thicknesses ranging from 0.42 to 0.51.

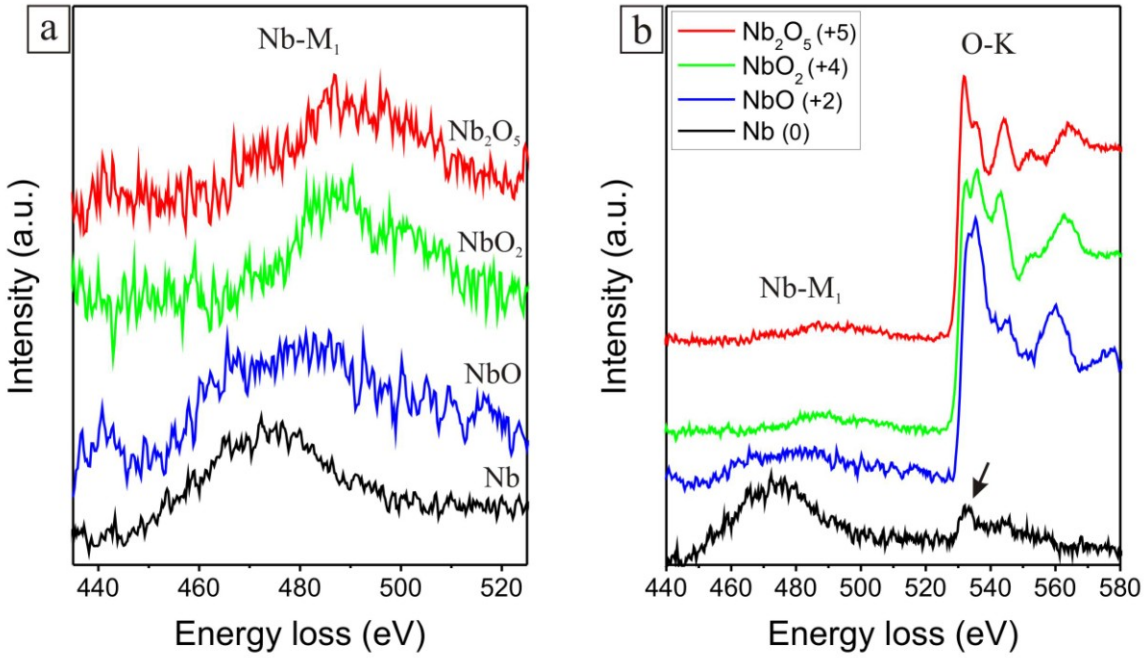

Fig. 4.2.9. EEL reference spectra recorded on Nb, NbO, NbO_2, and Nb_2O_5 using the LEO 922 microscope (dE ~ 2.1 eV, E_0 = 200 keV, β = 12.3 mrad, α = 11.2 mrad) and showing: **a)** the Nb-M_1 edge (equalized intensity maxima), **b)** the Nb-M_1 edge followed by the O-K edge (O-K edge intensity maximum equalized for the reference oxides). The spectra were corrected for background but not for multiple scattering.

Due to the imprecision of the background subtraction and the poor signal to noise ratio, an ELNES analysis of the Nb-M_1 edge for the different materials is hardly reliable and of low interest compared to the investigation of the clear characteristic features provided by the other edges. The fact that the Nb-M_1 edge seems to arise at much lower energy loss for Nb and NbO than for NbO_2 and Nb_2O_5 may for instance be a real particularity of the edge or may also just result from the superposition of the edge and broad background oscillations. Thus, there is thus not much to report on the Nb-M_1 edge, except that this bump is in spite of everything clearly visible for each reference material and that with increasing niobium oxidation state its intensity decreases relative to that of the O-K edge (Fig. 4.2.9b). Hence, it is important to notice that due to its position, this minor edge may influence the reliability of the background subtraction under the O-K edge when a high accuracy is required.
Moreover, it can already be observed that a trace of oxygen is found in the Nb assumed to be pure (arrow in Fig. 4.2.9b indicating an O-K edge). This is principally related to a native oxide layer grown at the metal surface during exposure to air, and will be described more in detail in the following section.

4.2.6 O-K ELNES

The origin of the O-K edge is mainly attributed to a transition of O 1s electrons to unoccupied 2p states. For the reference niobium oxides, this core-loss edge exhibits the most distinct characteristic fine structures. Representative reference spectra recorded on NbO, NbO_2, and Nb_2O_5 with the LEO 922 microscope are shown in Fig. 4.2.10a after background removal and multiple scattering correction. The weak preceding Nb-M_1 edge is not problematic for the qualitative fingerprinting of the O-K edge, and the classical power law model was satisfyingly employed for subtracting the background. The O-K edge is characterized by a double-peak structure just above the ionization edge (marked by the letters a and b in Fig. 4.2.10a), followed by different peaks and bumps, characteristic for NbO, NbO_2 and Nb_2O_5. The double-peak structure differs for the three reference oxides in the relative height of the two peaks as well as in their energy splitting. For NbO it is hardly observable at the energy resolution of the LEO 922 microscope (~2.1 eV), but when it is distinctly enough measurable, the splitting $E_b - E_a$ is found to be around 2.2 eV. This splitting increases to 3.0 eV for NbO_2 and 3.8 eV for Nb_2O_5, also demonstrating that it is a significant feature for identifying the oxidation state of the niobium-oxide phase.

To better resolve the O-K edge, reference spectra were also acquired on NbO and Nb_2O_5 using the JEOL JEM-3000F microscope (Fig. 4.2.10b). At an energy resolution of 1.2 eV, the double-peak structure of NbO is here unambiguously distinguished (peak a and b in Fig. 4.2.10b), and the splitting $E_b - E_a$ is around 2.8 eV for NbO and 4.1 eV for Nb_2O_5. Due to a better counting statistic, the peaks and bumps following the double-peak structure (letters c, d and e in Fig. 4.2.10b) are also better defined than with the LEO microscope (particularly for NbO), and their characteristic energy positions are reported in Table 4.2.2. However, although

the JEOL and the LEO microscopes differs in their experimental parameters (E_0, α, β), the general shape of the obtained spectra stay roughly unchanged, especially in the case of Nb_2O_5.

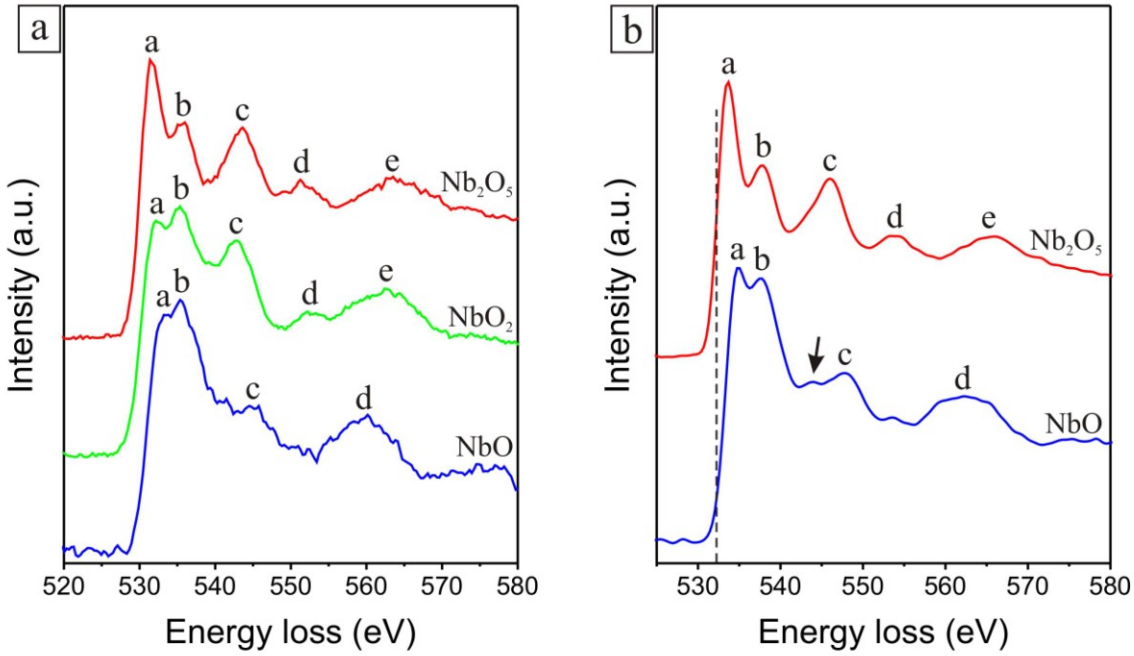

Fig. 4.2.10. EEL reference spectra showing the O-K edges recorded from: **a)** NbO, NbO_2, and Nb_2O_5 using the LEO 922 microscope (dE ~ 2.1 eV, E_0 = 200 keV, β = 12.3 mrad, α = 11.2 mrad), **b)** NbO and Nb_2O_5 using the JEOL JEM-3000F microscope (dE ~ 1.2 eV, E_0 = 300 keV, β = 4.76 mrad, $\alpha \sim \beta/3$). The spectra were corrected for background and multiple scattering.

Table 4.2.2. Position (energy in eV) of the characteristic features observed at the O-K edge of Nb_2O_5 and NbO. The energy loss of the peak (a) was chosen as a reference and subtracted from that of the other features. Measurements were performed for spectra acquired with the JEOL JEM-3000F microscope at an energy resolution of about 1.2 eV (cf. Fig. 4.2.10b).

↓ material	relative peak position →	$E_b - E_a$	$E_c - E_a$	$E_d - E_a$	$E_e - E_a$
Nb_2O_5 (+5)		4.1 eV	12.4 eV	20.3 eV	~ 31.8 eV
NbO (+2)		2.8 eV	~ 12.5 eV	27.3 eV	∅

The absolute energy position of the O-K edge was determined by means of the same method as that employed for the Nb-$M_{2,3}$ edges (see section 4.2.4). The O-K edge position was measured at the front half maximum intensity of the edge on three NbO and two Nb_2O_5 core-loss spectra, where at an energy resolution of 1.2 eV 533.2 ± 0.2 eV was found for NbO and 532.2 ± 0.2 eV for Nb_2O_5. This indicates a chemical shift to lower energy of about 1 ± 0.4 eV as the niobium oxidation state increases from +2 to +5.

In the case of NbO_2, the O-K ELNES was analyzed using the VG HB501UX microscope at an energy resolution of about 1 eV. A representative reference spectrum is shown in Fig. 4.2.11a. The general shape of the O-K edge remains highly similar to that recorded from NbO_2 with the LEO microscope (Fig. 4.2.10a). It can just be noted that the two peaks (a) and (b) are more distinctly separated, where the splitting of the double-peak structure $E_b - E_a$ is around 3.5 eV.

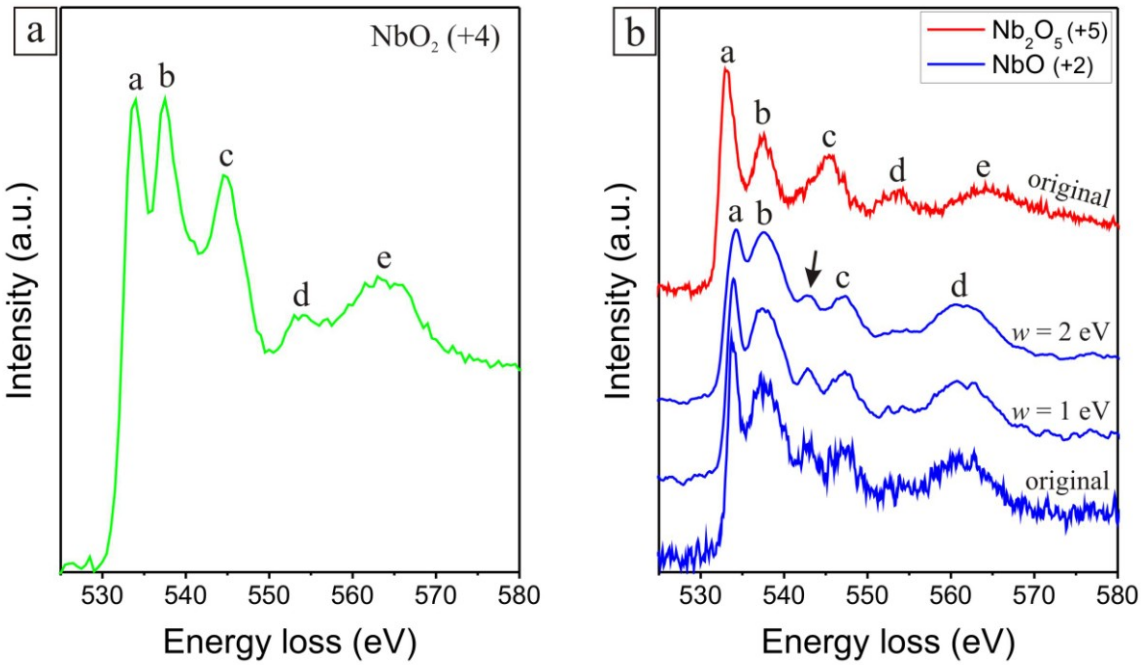

Fig. 4.2.11. EEL reference spectra showing the O-K edges recorded from: **a)** NbO_2 using the VG HB501UX microscope (dE ~ 1.0 eV, E_0 = 100 keV, β ~ 6.5 mrad, α ~ 10 mrad), **b)** NbO and Nb_2O_5 by means of the ZEISS Libra FE microscope (dE ~ 0.3 eV, E_0 = 200 keV, β = 2.3 mrad, α ~ 0.4 mrad). The spectra were corrected for background and multiple scattering. Three variants of the same NbO spectrum are presented in (b), the original noisy spectrum and two smoothed versions obtained using 1 eV and 2 eV wide intervals.

The ZEISS Libra FE microscope was employed in order to check whether more fine details of the O-K edge can be observed at an energy resolution of 0.3 eV. Typical reference spectra (after background removal and multiple scattering correction) obtained from NbO and Nb_2O_5 are shown in Fig. 4.2.11b. A filter implemented in the Digital Micrograph software was used to smooth the very noisy NbO spectrum. It acts by replacing the value in each spectrum channel by the average number of counts per channel in an energy interval of width w (in eV) centered on the particular channel in question. Fig. 4.2.11b shows the O-K edge of NbO in its original form, and after two smoothing procedures using an 1 eV and a 2 eV, respectively, wide interval.

At an energy resolution of 0.3 eV, the splitting $E_b - E_a$ is found around 3.5 eV for NbO and 4.3 eV for Nb_2O_5. Whereas the double-peak structure of NbO is characterized by two peaks of approximately identical height when recorded with the LEO or the JEOL microscopes (letters a and b in Fig. 4.2.10a and Fig. 4.2.10b), for acquisition by means of the Libra microscope in

the original NbO spectrum the first peak (a) is distinctly higher than the second one (b) (Fig. 4.2.11b). Nevertheless, the smoothing procedure also acts as an artificial deterioration of the energy resolution, and with increasing width of the smoothing interval the second peak becomes more intense relatively to the first one. With a 2 eV wide interval the two peaks again present similar heights (Fig. 4.2.11b). Moreover, after smoothing with a 2 eV wide interval, the apparent splitting $E_b - E_a$ is reduced by 0.5 eV compared to that measured on the unsmoothed spectrum.

Due to the strong noise, the Libra microscope did not enable to clearly identify new O-K ELNES features which were not before detected by the JEOL and the LEO microscopes at poorer energy resolution. It can just be noticed that some details are more or less pronounced. For instance, the little bump marked by an arrow in Fig. 4.2.10b and recorded on NbO with the JEOL microscope appears much better separated from the peak (c) while acquired with the Libra microscope (arrow in Fig. 4.2.11b).

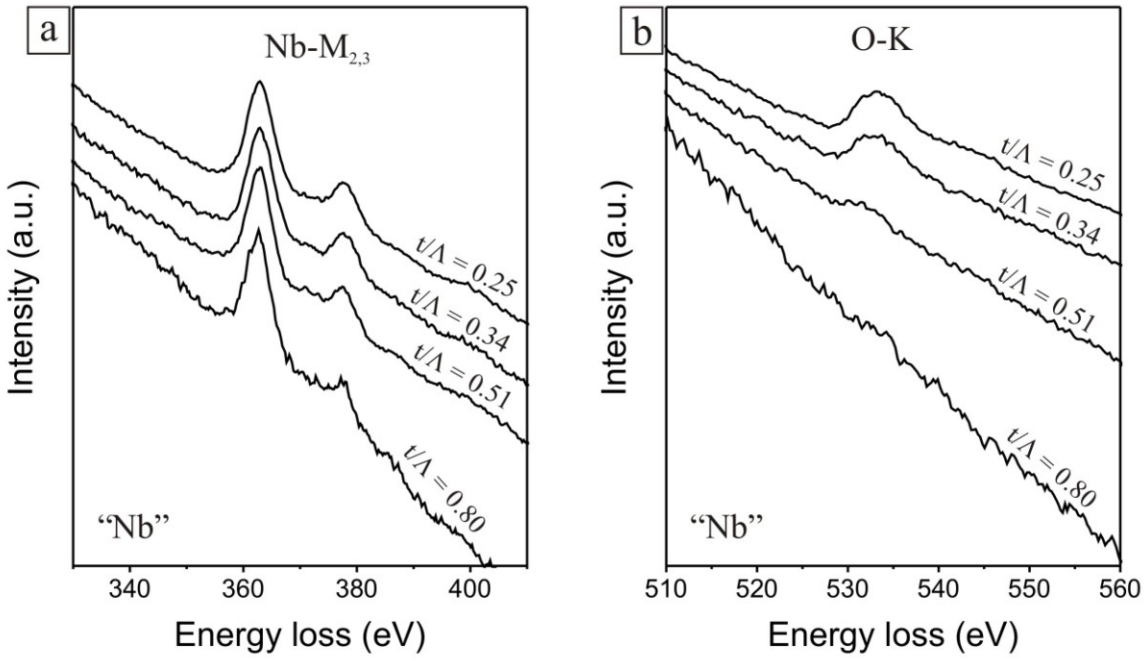

Fig. 4.2.12. Spectra recorded on originally metallic Nb at different specimen regions with varying relative thicknesses t/Λ and using the LEO 922 microscope (dE ~ 2.4 eV, E_0 = 200 keV, β = 12.3 mrad, α = 0 - 11.2 mrad). The spectra show: **a)** the Nb-$M_{2,3}$ edges (equalized Nb-M_3 white-line intensity), **b)** the following O-K edge (intensity of the spectra proportional to that of the corresponding Nb-$M_{2,3}$ spectra). The convergence semi-angle α was not identical for all the acquisitions, but always smaller than the collection semi-angle β.

Finally, although it is assumed as a first approximation that the Nb reference material has an oxidation state of 0, the Nb reference spectra also exhibit an O-K edge. Fig. 4.2.12 represents four spectra recorded on "Nb" at different specimen regions with varying relative thicknesses. No background or multiple scattering corrections were performed. Fig. 4.2.12a shows the four Nb-$M_{2,3}$ edges after equalization of the intensity of their Nb-M_3 white lines and Fig. 4.2.12b shows the associated O-K edges after proportional signal amplification.

It is recognized that even if the oxygen concentration was homogeneous in the specimen, the signal to background ratio and the signal-to-noise ratio of the O-K edge would decrease as the sample thickness increases. However, with increasing thickness the O-K edge signal also falls dramatically relative to the intensity of the Nb-$M_{2,3}$ edges. This behavior indicates that the main part of the oxygen atoms are probably not homogeneously distributed in Nb, but is more likely located in a surface layer whose thickness is quite independent from the total sample thickness. Thus, the oxygen found can be interpreted as the presence of a native niobium-oxide layer at the surface of the pure Nb metal.

The existence of an unavoidable oxide layer at the surface of niobium handled in air or in the presence of oxygen was often mentioned and studied in the literature (see e.g. Halbritter, 1987; Franchy et al., 1996; Kovacs et al., 2003; Delheusy et al., 2007). However, the composition and thickness of this native oxide layer is not completely clear up to now (see section 2.1.1 for more information). It is frequently assumed that this layer principally consists of near-stoichiometric Nb_2O_5 after oxidation in air at 300 K, but Halbritter (1987) showed that Ar-ion irradiation favors the formation of perturbed NbO_x ($x \leq 1$) at the expense of Nb_2O_5. In the present study the Nb TEM samples were less than 10 min in the air between the final stage of their preparation which consists in Ar^+-ion etching and their transfer into the high vacuum of the LEO 922 Omega (~ 10^{-5} Pa).

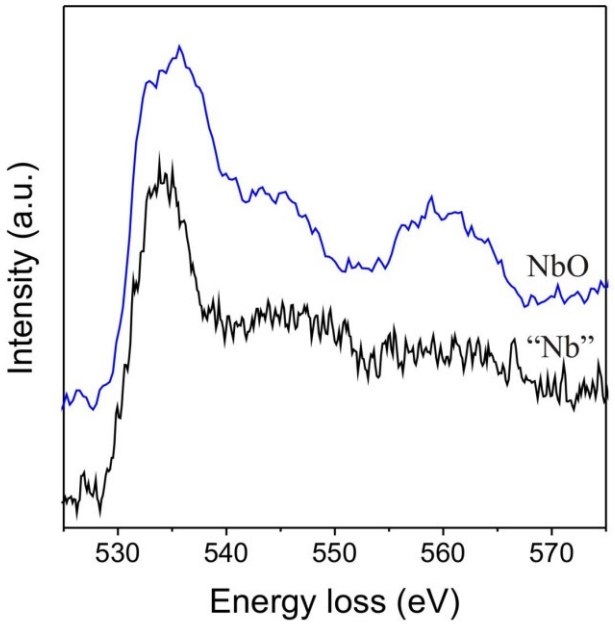

Fig. 4.2.13. EEL spectra showing the O-K edges recorded from "Nb" and NbO using the LEO 922 microscope (dE ~ 2.1 eV, E_0 = 200 keV, β = 12.3 mrad, α = 11.2 mrad). The spectra were corrected for background and multiple scattering.

Compared to the O-K ELNES of the crystalline reference oxides, the general shape of the O-K edge recorded on Nb is the most similar to that of NbO. Fig. 4.2.13 shows O-K edges acquired on Nb and NbO using the LEO microscope. The spectra were corrected for background and multiple scattering. No double-peak structure can be observed on the O-K

edge recorded on Nb, but only one intense peak just above the ionization edge. Nevertheless, depending on the effective energy resolution, which can for instance be influenced by the signal-to-noise ratio or the spectrum drift during the core-loss acquisition, in the majority of cases the double-peak structure was also not clearly identified on the NbO spectra recorded with the LEO microscope, and for example cannot be recognized on the NbO spectrum shown in Fig. 4.2.13. The further O-K structure beyond the intense peak appears much less pronounced for "Nb" than for NbO. However, if the O-K signal of Nb is induced by a surface-oxide layer, this one could present a more disordered structure than the crystalline reference oxide. The observed structure would thus still remain compatible with a stoichiometry near NbO. Indeed, the deformation of the local atomic configuration and the loss of far order in the disordered oxide could lead to a blurred fine structure compared to that observed for the crystalline one. Moreover, the poor signal-to-noise ratio of the "Nb" data also contributes to a damping of the structure.

4.2.7 Nb-$L_{2,3}$ ELNES

Finally, at high energy losses, there are the Nb-$L_{2,3}$ edges which present a white-lines shape and are mainly attributed to the transition of Nb 2p electrons to unoccupied 4d and 5s states. Representative spectra recorded via the LEO microscope on the four reference materials are visible in Fig. 4.2.14, here the background is subtracted and the spectra are corrected for multiple scattering. In order to record most of the EELS signal at high energy loss, the collection semi-angle β and convergence semi-angle α were chosen larger than those employed for the acquisition of the other core-loss edges with the LEO microscope. The different spectra are characterized by differing structures just beyond the white lines. Whereas for Nb a smooth intensity decrease is observed at the bottom of the L_3 white line, Nb_2O_5 shows a more abrupt drop followed by a little bump (arrows in Fig. 4.2.14). More or less well-defined bumps between the two white lines also enable to distinguish the four reference materials.

No clear trend could be noticed in the variations of the L_3 to L_2 white-line intensity ratio as a function of the niobium oxidation state, but once again a chemical shift of about 4 eV to higher energy losses is observed as the niobium oxidation state increases from 0 by Nb to +5 by Nb_2O_5. Because of the signal weakness at high energy loss, the exposure time used to record the Nb-$L_{2,3}$ edges was about ten times longer than that employed for the other core-loss edges, resulting in a higher risk of spectrum drift during the acquisition. Moreover, in order to avoid ghost peaks which may overlap the weak EELS signal at long exposure time, no low-loss spectrum (with intense ZLP) was taken before the recording of the Nb-$L_{2,3}$ edges. Only one low-loss spectrum was taken after each core-loss spectrum to roughly check for the energy-axis calibration. The procedure applied to determine the chemical shift of the Nb-$L_{2,3}$ edges is thus less accurate than that described for the Nb-$M_{4,5}$ edges in section 4.2.3. However, compared to the delayed maximum Nb-$M_{4,5}$ edges, the Nb-$L_{2,3}$ edges are advantageous because of their sharp edge onset, and compared to the Nb-$M_{2,3}$ edges the background subtraction is much less complicated. The position of the Nb-$L_{2,3}$ edges was

measured at the front half maximum of the L_3 white line. In Fig. 4.2.15 the chemical shifts measured relative to the Nb-$L_{2,3}$ edges position of Nb are shown as a function of the niobium oxidation state.

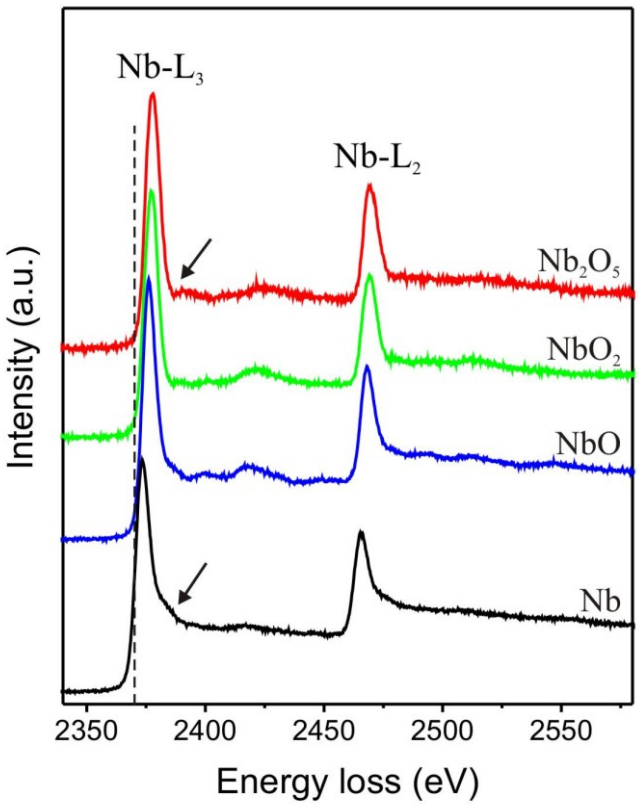

Fig. 4.2.14. EEL reference spectra showing the Nb-$L_{2,3}$ edges of Nb, NbO, NbO_2, and Nb_2O_5 using the LEO 922 microscope (dE ~ 2.4 eV, E_0 = 200 keV, β = 18 mrad, α = 12.6 mrad). The spectra were corrected for background and multiple scattering.

Finally, with increasing niobium oxidation state from 0 by Nb to +5 by Nb_2O_5, it can be noticed that the continuum intensity beyond the white lines decreases compared to the white-lines intensities. Indeed, the sharp and intense L_3 and L_2 white lines are correlated to the excitations of $2p_{3/2}$ and $2p_{1/2}$ core electrons to empty bound 4d states. Hence, the intensity of the white lines directly reflects the local density of unoccupied niobium 4d states, whereas the intensity of the continuum only depends on the number of niobium atoms interacting with the primary electrons. By dividing the sum of the L_3 and L_2 white-line intensities by the continuum intensity, a linear correlation may be expected between the thus normalized $L_{2,3}$ intensity and the niobium 4d occupancy in the measured material.

Pearson et al. investigated that way the $L_{2,3}$ edges for elemental metals of the 3d and 4d transition series (Pearson et al., 1988; Pearson et al., 1993). They reported a nearly linear decrease of the normalized white-line intensities with increasing d-state occupancy across each series. In addition, the normalized white-line intensity of a transition metal is not only a function of the d-state occupancy, but also depends on the radial matrix elements for the excitations of the 2p core electrons. After correcting the normalized white-line intensities for the effects of the matrix elements, Pearson et al. obtained better linear correlations between

these intensities and the density of d-states, enabling to estimate d-occupancy changes that might occur, for example, during alloying (Pearson et al., 1993). However, such corrections appear less helpful for the investigation of the different oxides of one single transition metal, namely niobium in the present work.

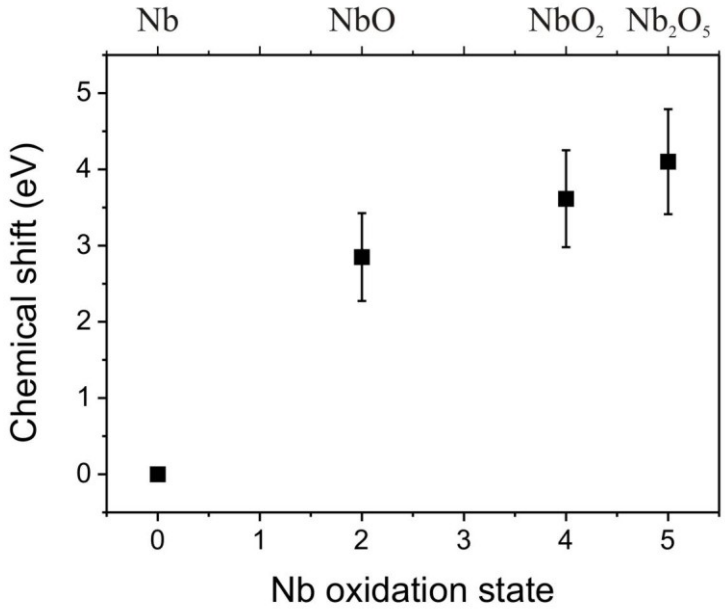

Fig. 4.2.15. Chemical shift of the Nb-$L_{2,3}$ edges as a function of the niobium oxidation state of the reference materials. The position of the Nb-$L_{2,3}$ edges of Nb was chosen as a reference and subtracted from that of the other materials. The analyzed spectra were recorded with the LEO microscope.

In order to check for the possibility of a quantitative characterization of the niobium oxidation state using solely the Nb-$L_{2,3}$ edges, the four representative spectra recorded on the reference materials (cf. Fig. 4.2.14) were analyzed. After background removal and multiple scattering correction, the intensity under the Nb-$L_{2,3}$ edges results from excitations of the niobium 2p electrons to bound 4d states as well as from transitions to continuum states. The critical step of the characterization procedure is to isolate the bound-state contribution from the continuum one. By analogy with the shape of the Cu and Ag $L_{2,3}$ edges, which have no white lines, Pearson et al. empirically modelled the continuum intensity of the other 3d and 4d transition metals by step functions underneath the L_3 and L_2 peaks (Pearson et al., 1988; Pearson et al., 1993). However, the optimal energy-axis position of the step functions was uncertain. In a second method, Pearson et al. used a straight line from the base of the L_3 peak onset to the first minimum above the peak to separate the L_3 white line intensity from the continuum in the case of 3d transition metals (Pearson et al., 1988). A similar approach was chosen because of its simplicity for a first attempt to analyse the spectra of niobium oxides.

For instance Fig. 4.2.16a illustrates the method employed to determine the normalized Nb-$L_{2,3}$ white-line intensity for NbO_2. A straight line was drawn from the base of each white-line onset to the intersection of the falling edge of the white line with the following continuum background. In the case of Nb and NbO, the lines were drawn only up to the first pronounced

slope variation beyond each peak. Obviously, since the white lines observed for transition metals result from transitions to energetically narrow d-bands, they are expected to be sharp. It was thus assumed that the smoothly decreasing intensity above the white lines - marked , e.g., by an arrow in Fig. 4.2.14 in the case of the L_3 edge recorded on niobium – is not any more correlated to excitations to bound 4d states. The total white-line intensity was calculated by adding the L_3 and L_2 peak intensities integrated above the drawn lines. The obtained value was then divided by the intensity integrated in a 55 eV wide normalization window starting 30 eV above the front half maximum of the L_3 white line. The resulting normalized white-line intensity is shown in Fig. 4.2.16b as a function of the formal 4d state occupancy for the four reference materials. To determine the 4d state occupancy, elemental Nb was assumed to be in a $4d^4 5s^1$ valence electron configuration and in the case of the oxides, two niobium valence electrons were assumed to be transferred to each oxygen atom (starting by the electrons in 5s states). A clear decrease of the normalized intensity can be observed with increasing 4d occupancy. Moreover, the experimental data can be reasonably well fitted using a linear function. The following linear fit is obtained with a correlation coefficient of - 0.977:

$$I_{L3+L2} = 0.75 - 0.069 n_{4d} ,$$

where I_{L3+L2} is the normalized white-line intensity, and n_{4d} the 4d state occupancy.

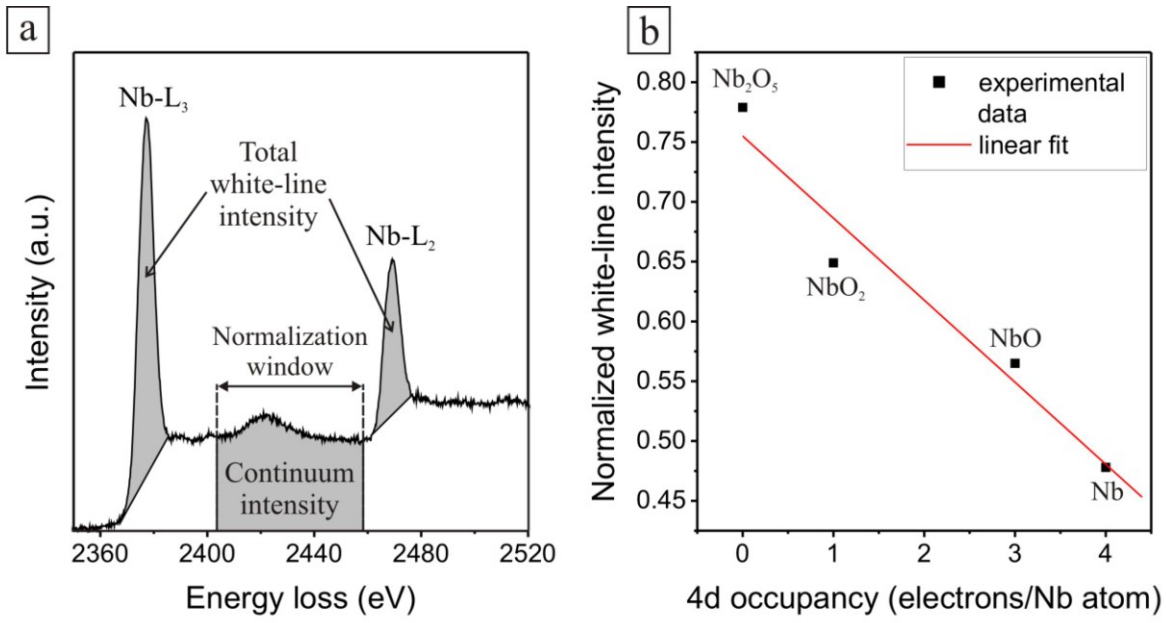

Fig. 4.2.16. a) Background-subtracted and multiple-scattering corrected Nb-$L_{2,3}$ edges of NbO_2 showing the isolated total white-line intensity and the 55 eV wide normalization energy window starting 30 eV above the front half maximum of the L_3 peak. The normalized Nb-$L_{2,3}$ white-line intensity is calculated by dividing the total white-line intensity by the continuum intensity. **b)** Normalized white-line intensity as a function of the Nb 4d state occupancy of Nb, NbO, NbO_2, and Nb_2O_5. The measurements were performed on the four reference spectra recorded with the LEO 922 microscope and shown in Fig. 4.2.14. The linear fit to experimental data gives $I_{L3+L2} = 0.75(1 - 0.092 n_{4d})$ with a correlation coefficient of – 0.977.

4.3 Quantitative EELS results

In the previous subchapter, it has been shown that Nb, NbO, NbO_2 and Nb_2O_5 can be qualitatively distinguished by investigating the ELNES fingerprints of their different edges. Moreover, several features like for instance the energy splitting $E_b - E_a$ of the O-Kedge double-peak structure (see Fig. 4.4.1) or the chemical shifts of the niobium edges (see e.g. Fig. 4.2.5 and Fig. 4.2.15) already allow some kind of quantitative characterization of the niobium oxidation state. The detailed investigation of the normalized Nb-$L_{2,3}$ white-line intensity can also provide a powerful tool enabling a quantitative distinction of the different niobium oxides as a function of the occupancy of the niobium 4d orbitals (see Fig. 4.2.16). Nevertheless, these different characterization methods do not correspond to what is generally understood by quantitative EELS. The principal and most direct way to get quantitative information on the stoichiometry of a material using EELS is due to the fact that the number of counts under an inner-shell ionization edge can be considered to be proportional to the number of atoms present (Egerton, 1986). The elemental quantification method based on this property is illustrated and developed here by presenting the results obtained from the reference niobium oxides (in the present subchapter) and by discussing these results (in subchapter 4.4). Hence, it will be shown that the reference oxides can be distinguished in a quantitative manner by measuring the intensities under one given niobium edge and the O-K edge and calculating the intensity ratio of the corresponding ionization edges. So-called *k*-factors can then be derived from the resulting ratios (Malis & Titchmarsh, 1986; see section 3.2.7) and will be used in the next chapter (5) to analyze the element composition of niobium-based capacitor structures.

Most of the results presented in the next sections were obtained with the LEO 922 microscope (dE ~ 2.1 eV, E_0 = 200 keV, β = 12.3 mrad, α = 11.2 mrad). *k*-factors gathered by the JEOL JEM-3000F microscope (dE ~ 1.2 eV, E_0 = 300 keV, β = 4.76 mrad, $\alpha \sim \beta/3$) and the VG HB501UX microscope (dE ~ 1.5 eV, E_0 = 100 keV, β = 6.5 mrad, α = 10 mrad) are also given in section 4.3.6.

4.3.1 Choice of the ionization edges for quantification

EELS quantification consists in comparing the intensity measured under one edge resulting from the ionization of one given element *a* with the edge intensity of another element *b* in order to get an information on the relative occurrence of these two elements in the investigated material (see section 3.2.7). Several factors can be considered to choose the edges for quantification:

a) the two edges should be preferentially close enough to be recorded simultaneously on the same spectrum;

b) they should emerge far enough from preceding edges at lower energy losses in order to allow an as reliable as possible background subtraction and also far enough from

following edges (due to the excitation of another element) at higher energy losses to avoid signal overlapping;

c) they should be as intense as possible or at least have a good signal-to-background ratio, and present sharp onsets or at least a good signal-to-noise ratio.

Finally, in order to decide between different possible edges for one of the elements, e.g. for *a*, intensity ratios can be calculated. The intensity measured under each *a* edge is divided by the intensity integrated under the chosen *b* edge. The more convenient *a* edge which provides the best compromise between the different above-mentioned decisive factors is pragmatically that leading to the lower standard deviation when averaging intensity ratios resulting from numerous different spectra.

In the case of niobium oxides, oxygen is only represented by the O-K edge, but several niobium edges can be chosen to perform quantification (see Fig. 4.2.1). The reliability of the background subtraction under the Nb-$N_{2,3}$ edges is affected by the presence of the plasmon immediately before the edge onset (see Fig. 4.2.2a). In addition, the dynamic of the CCD camera mounted on the LEO microscope does not allow to record simultaneously the intense Nb-$N_{2,3}$ edges in the low-loss region and a sufficiently high O-K signal for quantification. Thus, the use of the Nb-$N_{2,3}$ edges would require to match low-loss spectra with O-K spectra with respect to intensity and energy axis. The background subtraction under the Nb-$M_{2,3}$ edges is complicated by the tail of the preceding Nb-$M_{4,5}$ edges (see Fig. 4.2.6a and section 4.2.4). The Nb-M_1 edge is particularly weak and lays on the tail of the Nb-$M_{4,5}$ and –$M_{2,3}$ edges, leading to very poor signal-to-background and signal-to-noise ratios and to an inaccurate background fit (see Fig. 4.2.9 and section 4.2.5). Moreover, using the Nb-$L_{2,3}$ edges can yield an accurate quantification (Hofer et al., 1996), but it is limited by the stability of the employed experimental setup (LEO microscope and its CCD camera) which requires long acquisition times at high energy losses and does not allow to record the O-K edge and the Nb-$L_{2,3}$ edges in one and the same run. Indeed, specimen drift and contamination during the acquisition as well as a drift of the condenser aperture – whose relative position with respect to the objective aperture influences the angular distribution of the effective signal collected at the LEO microscope – would make a match between an O-K spectrum and a Nb-$L_{2,3}$ one imprecise.

Therefore, the best quantitative results are expected from the use of the Nb-$M_{4,5}$ edges. However, the potential quantitative applicability of the Nb-$M_{2,3}$ and –M_1 edges was also checked by calculating intensity ratios. The corresponding results are presented in the next section.

4.3.2 Determination of intensity ratios and *k*-factors

In order to distinguish the three reference oxides in a quantitative manner, the intensities under the background-subtracted Nb-M_1 (I_{NbM1}), Nb-$M_{2,3}$ ($I_{NbM2,3}$) or Nb-$M_{4,5}$ ($I_{NbM4,5}$) edges, respectively, and the background-subtracted O-K (I_{OK}) edge were measured and the ratios of the corresponding ionization edges I_{NbM1}/I_{OK}, $I_{NbM2,3}/I_{OK}$, and $I_{NbM4,5}/I_{OK}$ were calculated.

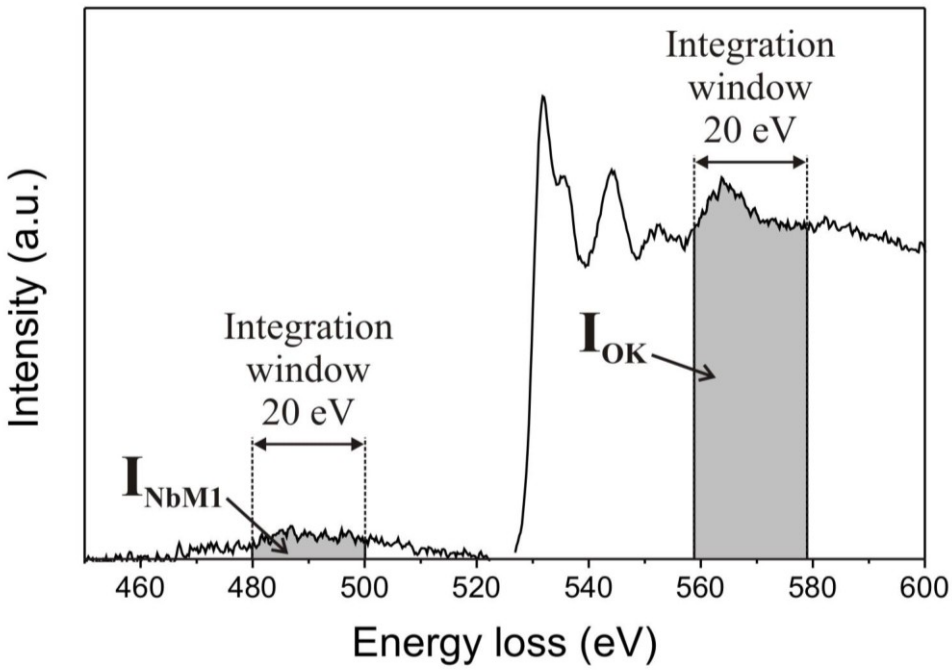

Fig. 4.3.1. Intensities of the Nb-M_1 (I_{NbM1}) and the O-K (I_{OK}) edges measured after background subtraction over 20 eV integration windows (LEO 922 microscope).

It may seem strange to search for quantitative information in an edge apparently as inappropriate as the Nb-M_1 edge. It was already mentioned that the Nb-M_1 edge is particularly noisy and that its intensity is very weak and can hardly be separated from the underlying tails of the Nb-$M_{4,5}$ and Nb-$M_{2,3}$ edges (see section 4.2.5). Nonetheless, the analysis of this edge yields an interesting introduction to quantitative EELS. Owing to the noise and the uncertain background subtraction (see section 4.2.5 for more information on calculating the background under the Nb-M_1 edge), the Nb-M_1 edge onset cannot clearly be identified. Thus, the intensity under the Nb-M_1 edge was integrated over a narrow 20 eV wide energy window arbitrarily positioned between approximately 480 eV and 500 eV, as shown in Fig. 4.3.1. The intensity under the O-K edge was measured within a 20 eV wide window starting 30 eV above the edge onset in order to avoid the energy range exhibiting strong near-edge fine structures (cf., e.g., section 4.4.7 for more details on the choice of integration windows). For each reference oxide, the measurements were performed on two spectra recorded at the LEO microscope from specimen regions with a relative thickness in the range of 0.4 to 0.5, resulting in I_{NbM1}/I_{OK} intensity ratios of 0.17 and 0.15 for NbO, 0.070 and 0.063 for NbO_2, and 0.065 and 0.058 for Nb_2O_5. As expected, the intensity ratio globally decreases with increasing oxygen concentration in the material. NbO_2 and Nb_2O_5 cannot definitely be distinguished from one another, but clearly differ from NbO. Thus, it seems that in spite of everything, the marginal Nb-M_1 signal already allows some kind of quantitative EELS, which is a promising result for the further quantitative investigations using more adequate Nb edges.

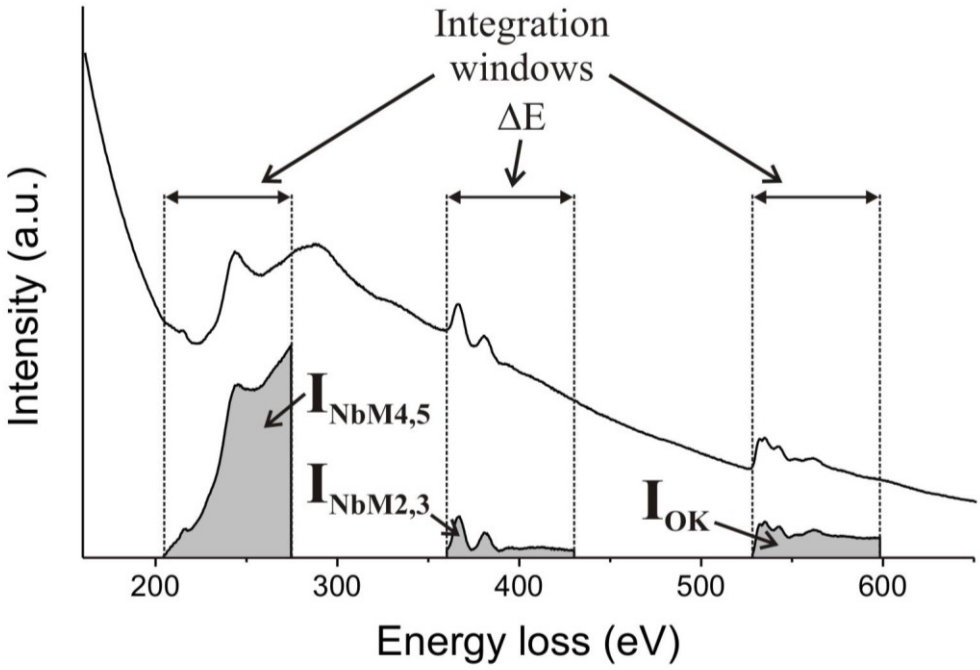

Fig. 4.3.2. Intensities under the Nb-$M_{4,5}$ ($I_{NbM4,5}$), the Nb-$M_{2,3}$ ($I_{NbM2,3}$) and the O-K (I_{OK}) edges measured after background subtraction over an integration window ΔE starting at the very edge onset (LEO 922 microscope). The spectrum shown as an example was taken on NbO_2.

For quantification by means of the Nb-$M_{2,3}$ or Nb-$M_{4,5}$ edges, the intensities $I_{NbM2,3}$ or $I_{NbM4,5}$, respectively, and I_{OK} were integrated over a certain energy window ΔE beyond the ionization thresholds as shown in Fig. 4.3.2. The proper choice of the width of the energy window is discussed in detail in section 4.2.3. A width of 70 eV was used to do the first quantification tests presented here. For each reference niobium oxide, 12 spectra were taken with the LEO microscope from specimen regions with a relative thickness in the range of 0.2 to 0.6, and were analyzed to determine the $I_{NbM2,3}/I_{OK}$ and $I_{NbM4,5}/I_{OK}$ intensity ratios. The results were averaged, leading to $I_{NbM2,3}/I_{OK}$ intensity ratios of 1.28 ± 0.07 (i.e. ±5.5% relative standard deviation) for NbO, 0.641 ± 0.028 (±4.4%) for NbO_2 and 0.482 ± 0.016 (±3.3%) for Nb_2O_5, and to $I_{NbM4,5}/I_{OK}$ intensity ratios of 9.46 ± 0.25 (±2.6%) for NbO, 4.74 ± 0.09 (±1.9%) for NbO_2 and 3.76 ± 0.06 (±1.6%) for Nb_2O_5. In each case, i.e. using either the Nb-$M_{2,3}$ edges or the Nb-$M_{4,5}$ edges, the measured intensity ratios enable a clear quantitative distinction between all three oxides. The fact that for all three oxides the relative standard deviations (in %) obtained for the $I_{NbM2,3}/I_{OK}$ intensity ratios are systematically higher than those measured for the $I_{NbM4,5}/I_{OK}$ intensity ratios indicates that the Nb-$M_{4,5}$ edges allow a more precise quantification than the Nb-$M_{2,3}$ edges.

Of course, the precision with which intensity ratios can be determined depends on the quality of the procedures applied to remove the background from the analyzed edges. The background under the Nb-$M_{4,5}$ edges is not perturbed by preceding edges at lower energy

losses and a classical power-law model works well for its subtraction. A 20 to 25 eV wide fitting region ending about 5 eV before the edge onset was typically chosen.

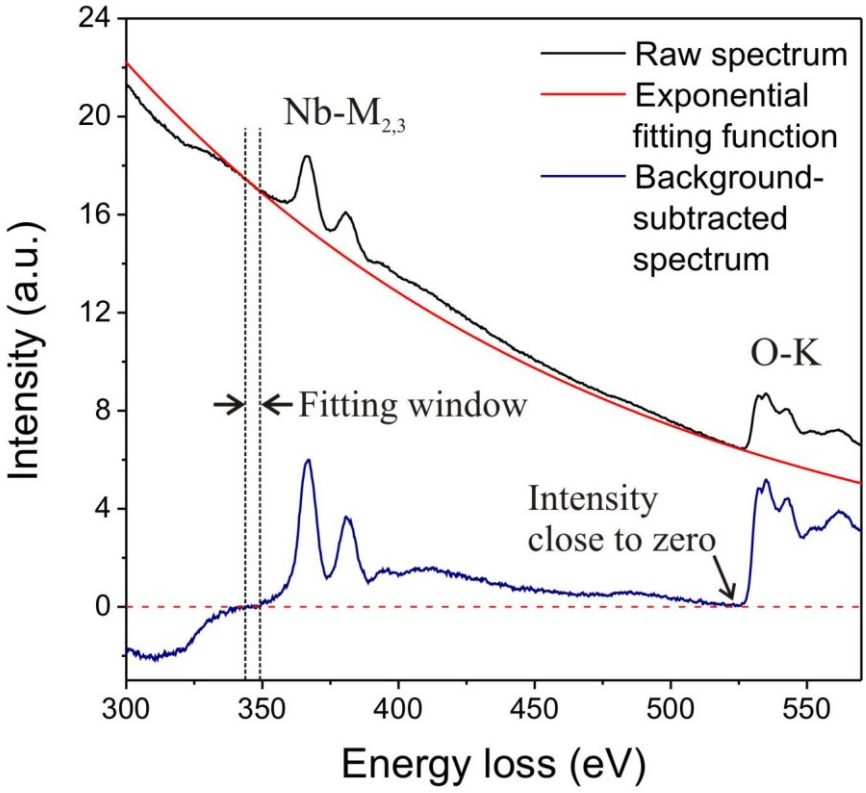

Fig. 4.3.3. Background subtraction under the Nb-$M_{2,3}$ edges using an exponential fitting function ($I = a \cdot e^{-b.E}$, with a and b two fitting parameters, I the intensity and E the energy loss). For better visibility the background-subtracted signal is amplified by a factor of two in comparison to the raw spectrum. The fitting window was so chosen that the intensity of the background-subtracted signal is close to zero in front of the O-K edge onset. For the NbO_2 spectrum presented here as an example, an only 5.4 eV wide fitting window ending approximately 11 eV before the Nb-$M_{2,3}$ edge onset was used. In this particular case, it can be noticed that the background fit is especially poor in the 60 eV wide region which precedes the edge onset.

The case of the Nb-$M_{2,3}$ edges is much more critical. It was already shown in section 4.2.4 that the shape of the energy region preceding the edge onset is strongly influenced by the tail of the Nb-$M_{4,5}$ edges and differs for the different reference oxides (see Fig. 4.2.6a). Exponential functions were found to be more adequate than a power-law model to fit the background under the Nb-$M_{2,3}$ edges, but their application remains highly uncertain. Indeed, a minimal variation in the width or position of the background fitting region can lead to dramatically different results. Thus, constant fitting-window width and position could not be employed. In order to get coherent results, the fitting window was chosen so that after background subtraction, the intensity in front of the O-K edge (i.e. about 160 eV past the Nb-$M_{2,3}$ onset) is close to zero, as shown in Fig. 4.3.3. To fulfil this condition, narrow fitting windows of only few eV in width should sometimes be used, leading, when a larger energy region is observed, to a poor fit of the background preceding the Nb-$M_{2,3}$ edge. Hence, the

employed procedure certainly introduces some systematic error in the resulting background-subtracted edge, but with the assumption that this "artificial" error remains in the same order of magnitude for the different niobium oxides.

Table 4.3.1. $I_{NbM4,5}/I_{OK}$ intensity ratios measured from one NbO spectrum by means of different widths of the fitting window for background extrapolation under the O-K edge. The upper limit of the fitting window was kept constant at 526.1 eV, i.e. at about 5 eV before the O-K edge onset. All the other parameters used to analyse the NbO spectrum were also kept constant.

Width of the window for background extrapolation under the O-K edge	$I_{NbM4,5}/I_{OK}$
56 eV (from 470.1 to 526.1 eV)	9.59
47.1 eV (from 479.0 to 526.1 eV)	9.41
40.1 eV (from 486.0 to 526.1 eV)	9.26
30 eV (from 496.1 to 526.1 eV)	9.52
22 eV (from 504.1 to 526.1 eV)	9.28

Table 4.3.2. $I_{NbM4,5}/I_{OK}$ intensity ratios measured from one NbO spectrum for different positions of the fitting window for background extrapolation under the O-K edge. The width of the fitting window was kept constant at 40.1 eV. All the other parameters used to analyse the NbO spectrum were also kept constant.

Position of the window for background extrapolation under the O-K edge (40.1 eV wide)	$I_{NbM4,5}/I_{OK}$
from 487.6 to 527.7 eV	9.27
from 486.0 to 526.1 eV	9.26
from 484.5 to 524.6 eV	9.38
from 481.7 to 521.8 eV	9.38
from 479.9 to 520 eV	9.58
from 474.7 to 514.8 eV	9.53

The width of the energy region where a fitting window can be positioned for background extrapolation under the O-K edge is limited to about 50 eV by the presence of the Nb-M_1 edge at about 468 eV. An approximately 30 eV wide window ending some 5 eV before the edge onset was generally used to fit the background by means of a power-law function. In order to check for the influence of the Nb-M_1 edge on the precision of the quantification, $I_{NbM4,5}/I_{OK}$ intensity ratios were measured by varying the size and the position of the fitting window chosen for background extrapolation under the O-K edge. This test was performed on one spectrum recorded from NbO, where the intensity of the oxygen edge is quite low, which

can increase the errors while comparing the obtained intensity ratios. One representative NbO spectrum was chosen, for which an $I_{NbM4,5}/I_{OK}$ intensity ratio of 9.40 was initially measured. For both edges (Nb-$M_{4,5}$ and O-K), power-law functions were used for the fitting of the background. The size and position of the windows used for background extrapolation and integration under the Nb-$M_{4,5}$ edges were kept constant, as well as the size and position of the window for integration under the O-K edge. In each case, 70 eV wide integration windows were used. However, different fitting window sizes were applied to extrapolate the background under the O-K edge. The resulting $I_{NbM4,5}/I_{OK}$ intensity ratios are given in Table 4.3.1. No clear trend could be observed in the variations of the intensity ratio as a function of the window size. These results were obtained while keeping the upper limit of the window constant at about 5 eV before the O-K edge onset. Obviously, different positions can also lead to slightly different results. The values obtained from different positions of the extrapolation window while keeping its width constant at 40.1 eV are presented in Table 4.3.2. Here again, the shifting of the window to lower energies seems to have a limited small effect on the measured intensity ratios. On the whole, ten values for the intensity ratio were obtained from the investigated spectrum and were averaged leading to $I_{NbM4,5}/I_{OK} = 9.42 \pm 0.13$, i.e. to a standard deviation of ± 1.4 %. The analysis of twelve different NbO spectra led to a standard deviation of ± 2.6 % for the intensity ratio ($I_{NbM4,5}/I_{OK} = 9.46 \pm 0.25$). Thus, it is clear that the uncertainties resulting from the size and the position of the extrapolation window contribute to the total error of the quantification method. Nevertheless, they remain reasonably low, so that in spite of the Nb-M_1 edge, the width and the position of the fitting window for background subtraction under the O-K edge does not appear to have a critical influence on the obtained value for the $I_{NbM4,5}/I_{OK}$ intensity ratio.

Moreover, errors resulting from the choice of the position of the integration windows add to the background subtraction ones. It is particularly problematic when edges with a delayed maximum shape are used, like for example the Nb-$M_{4,5}$ ones, due to the difficulty to localize the edge onset with high precision. In order to evaluate these errors, the NbO spectrum which was used to check the influence of the fitting window was further analyzed. The same parameters as those originally set to obtain an $I_{NbM4,5}/I_{OK}$ intensity ratio of 9.40 were reapplied, except for the position of the integration window under the Nb-$M_{4,5}$ edges, which was shifted by about 0.6 eV (i.e. by two channels at a dispersion of approximately 0.3 eV per channel) to lower energies and of 0.6 eV to higher energies, respectively, leading to an $I_{NbM4,5}/I_{OK}$ intensity ratio of 9.24 and 9.57, respectively. On the whole, a shift of the integration window by 1.2 eV to higher energies caused in that case a relative increase of the $I_{NbM4,5}/I_{OK}$ intensity ratio of 3.5% (between 9.24 and 9.57).

In order to use the results obtained from known niobium oxide reference materials for investigating the stoichiometry within nanoscale oxide layers in niobium-based capacitors, a next step in the quantification procedure is to derive a sensitivity factor, the *k*-factor (Malis & Titchmarsh, 1986), from the measured intensity ratios. It represents the ratio of the partial ionization cross-sections for the investigated inner-shell scattering events under a particular set of defined experimental parameters, including the incident beam energy E_0, the collection

semi-angle β, the convergence semi-angle α, and the chosen energy window ΔE (see section 3.2.7). Under the assumption that the "real" background is removed from the investigated edges, i.e. that the intensities measured under the edges correspond accurately to the occurrence of the particular inelastic scattering events that they are supposed to represent, the *k*-factor allows a correlation between relative atomic concentration ratios and intensity ratios. Rewriting Eqn. 3.2.11 for the specific case of niobium oxides, the *k*-factor is given by

$$k_{NbM-OK}(E_0,\beta,\alpha,\Delta E)=\frac{\sigma_{NbM}(E_0,\beta,\alpha,\Delta E)}{\sigma_{OK}(E_0,\beta,\alpha,\Delta E)}=\frac{C_O}{C_{Nb}}\cdot\frac{I_{NbM}(E_0,\beta,\alpha,\Delta E)}{I_{OK}(E_0,\beta,\alpha,\Delta E)} \quad (4.3.1)$$

with σ_{NbM} and σ_{OK} the partial cross-sections for the Nb-M edges (Nb-$M_{4,5}$ or Nb-$M_{2,3}$) and O-K edges and C_{Nb} and C_O the niobium and oxygen atomic concentrations in the specimen. In the case of the reference niobium oxides, the C_{Nb}/C_O atomic concentration ratios are known, and the *k*-factors determined in this manner can later be used to characterize niobium oxide phases with unknown stoichiometry.

However, the accuracy of the quantitative distinction between different oxides by means of intensity ratios or *k*-factors may depend on the choice of the integration window ΔE, which was not discussed yet.

4.3.3 Choice of the integration window

Constant energy windows ΔE starting at the base of the edge onset were used to integrate the intensities under the background subtracted Nb-$M_{2,3}$ ($I_{NbM2,3}$), Nb-$M_{4,5}$ ($I_{NbM4,5}$) and O-K (I_{OK}) edges (see Fig. 4.3.2). A large integration window should be chosen in order to minimize the influence of the near-edge fine structure, which reflects the structural and chemical environment of the ionized atom but not directly the element content in the specimen. Such solid-state effects are particularly strong for edges with white lines (see section 4.2.7), as for example in our case observable at the Nb-$M_{2,3}$ edges. However, errors in background extrapolation generally rise with energy loss well above edge onset, which requires a compromise for the width of ΔE.

The two reference oxides with extremely different stoichiometries, NbO with a nominal atomic concentration ratio $C_{Nb}/C_O = 1$, and Nb_2O_5 with a nominal value $C_{Nb}/C_O = 0.4$, were investigated to find an optimum ΔE. For both oxides, the 12 spectra previously analyzed to determine the intensity ratios given in section 4.3.2 were further examined. Fig. 4.3.4 shows the *k*-factors derived by using Eqn. (4.3.1) from measurements on NbO and Nb_2O_5 as a function of the width of the integration window. The *k*-factors were obtained using either the Nb-$M_{2,3}$ edges (Fig. 4.3.4a) or the Nb-$M_{4,5}$ edges (Fig. 4.3.4b). Since some spectra exhibit a weak C-K edge around 284 eV due to slight carbon contamination during the acquisition, and in order to avoid the superposition of this C-K signal with the measured Nb-$M_{4,5}$ intensities, only nine NbO spectra and seven Nb_2O_5 spectra were taken into consideration when 90 eV, 110 eV and 130 eV wide integration windows were used for the determination of *k*-factors by means of the Nb-$M_{4,5}$ edges (Fig. 4.3.4b).

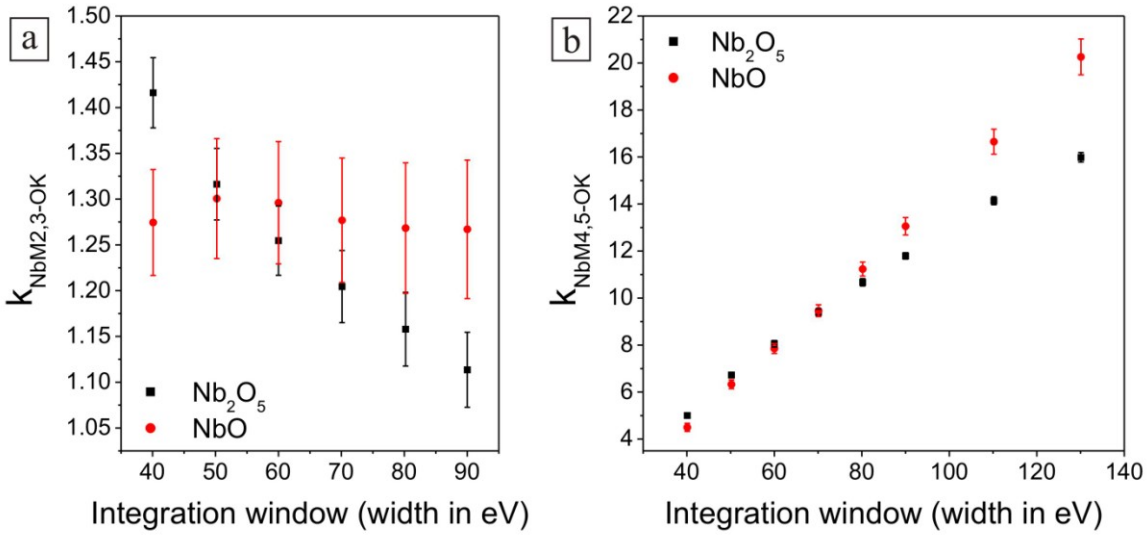

Fig. 4.3.4. *k*-factors determined for NbO and Nb_2O_5 by means of the Nb-$M_{2,3}$ (**a**) and Nb-$M_{4,5}$ (**b**) edges as a function of the width of the integration window ΔE. The averaged *k*-factors result from measurements on 12 NbO and 12 Nb_2O_5 spectra, respectively, recorded with the LEO 922 microscope (E_0 = 200 keV, β = 12.2 mrad, α = 11.1 mrad). Due to slight carbon contamination during the acquisition of some spectra, only nine NbO spectra and seven Nb_2O_5 spectra were used to derive the *k*-factors shown in (b) for integration windows wider or equal to 90 eV.

For reliable quantification, similar *k*-factors should be achieved with both reference niobium oxides. Using the Nb-$M_{2,3}$ edges the *k*-factors obtained from both materials with a 50 eV wide integration window were found to be in agreement, $k_{NbM2,3-OK}$ = 1.30 ± 0.07 (i.e., ±5.4% standard deviation) from the 12 NbO spectra and $k_{NbM2,3-OK}$ = 1.32 ± 0.04 (±3.0%) from the 12 Nb_2O_5 spectra. The relative deviation between the resulting mean values (1.30 and 1.32) is of only 1.5%, and is thus smaller than the corresponding standard deviations (5.4% and 3.0%) and also smaller than their difference (5.4% - 3.0% = 2.4%). Hence, for the present experimental parameters (LEO 922 microscope: E_0 = 200 keV, β = 12.3 mrad, α = 11.2 mrad, ΔE = 50 eV) a *k*-factor $k_{NbM2,3-OK}$ = 1.31 ± 0.05 (±3.8%) results from averaging of the 24 spectra measured from NbO and Nb_2O_5.

Using the Nb-$M_{4,5}$ edges, a 70 eV wide window is found to be a good compromise, yielding a *k*-factor $k_{NbM4,5-OK}$ of 9.46 ± 0.25 (±2.6 %) for NbO and 9.40 ± 0.15 (±1.6 %) for Nb_2O_5. Here, the *k*-factors determined for NbO and Nb_2O_5 are in even better agreement than those for Nb-$M_{2,3}$ edges, with a relative deviation between the mean values (9.46 and 9.40) of only 0.6%. The mean value of all 24 spectra (LEO 922 microscope: E_0 = 200 keV, β = 12.3 mrad, α = 11.2 mrad, ΔE = 70 eV) is $k_{NbM4,5-OK}$ = 9.43 ± 0.20 (±2.1%).

4.3.4 Quantification tests: NbO_2

In order to check for the reliability of the *k*-factors obtained in the previous section by means of NbO and Nb_2O_5, a quantification test was conducted on NbO_2. Using the Nb-$M_{4,5}$ edges and a 70 eV wide integration window for quantification, an $I_{NbM4,5}/I_{OK}$ intensity ratio of 4.74 ± 0.09 ($\pm 1.9\%$) was found from 12 NbO_2 spectra (see section 4.3.2). A representative spectrum yielding an intensity ratio of 4.73 was chosen to perform a first test. It was quantified by means of Eqn. (4.3.1) using the *k*-factor resulting from 12 NbO and 12 Nb_2O_5 spectra ($k_{NbM4,5\text{-}OK} = 9.43 \pm 0.20$) leading to an atomic concentration ratio C_{Nb}/C_O of 0.502 ± 0.011 ($\pm$ 2.2%), which has to be compared with the nominal value $C_{Nb}/C_O = 0.500$ for NbO_2. With a relative deviation of only 0.4% the measured value and the nominal one are found to be in very good agreement. Using the Nb-$M_{2,3}$ edges for quantification, the analysis of the same NbO_2 spectrum with an integration window width of 50 eV yields an $I_{NbM2,3}/I_{OK}$ intensity ratio of 0.709. Quantification by means of the *k*-factor obtained from 24 NbO and Nb_2O_5 spectra ($k_{NbM2,3\text{-}OK} = 1.31 \pm 0.05$) results in an atomic concentration ratio C_{Nb}/C_O of 0.541 ± 0.021 ($\pm$ 3.9%). With a relative deviation of 7.9%, the agreement between measured and nominal values is much poorer than that achieved by quantification using the Nb-$M_{4,5}$ edges.

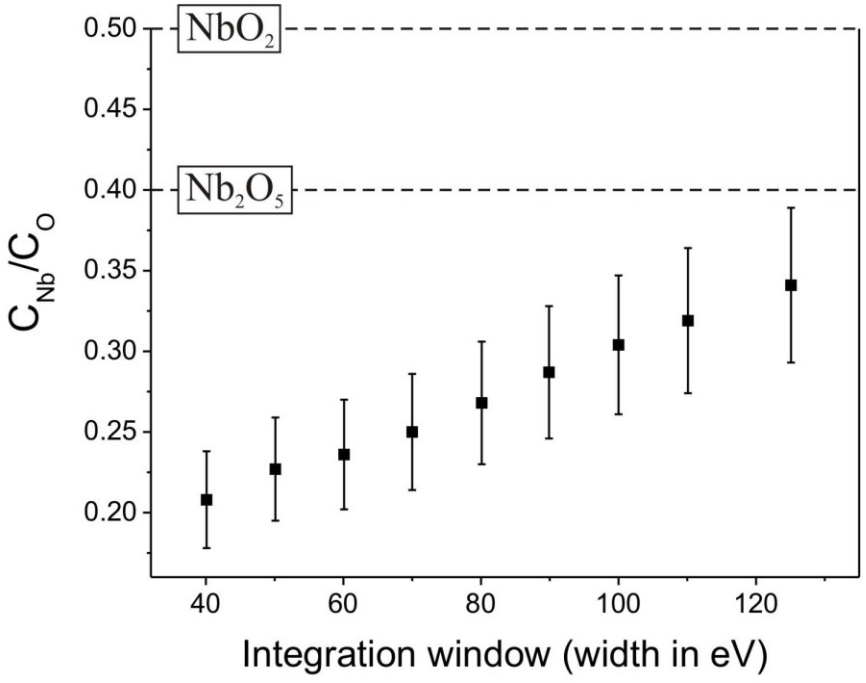

Fig. 4.3.5. C_{Nb}/C_O atomic concentration ratios determined by means of the Nb-$M_{4,5}$ and O-K edges of one NbO_2 spectrum as a function of the width of the integration window ΔE. Theoretical cross sections calculated for the Nb-$M_{4,5}$ and O-K edges by the *Hartree-Slater* model were used for quantification (EELS routine in the Gatan Digital Micrograph software). The analyses were conducted on one representative NbO_2 spectrum yielding an $I_{NbM4,5}/I_{OK}$ intensity ratio of 4.73 when a 70 eV wide integration window is used.

Using the EELS quantification routine implemented in the Gatan Digital Micrograph software the same NbO_2 spectrum was also quantified by means of theoretical cross sections computed for the Nb-$M_{4,5}$ and O-K edges. The empirical *k*-factor in Eqn. (4.3.1) is replaced by the $\sigma_{NbM4,5}/\sigma_{OK}$ partial cross-section ratio calculated by the *Hartree-Slater* model (Leapman et al., 1980; Rez, 1982; Ahn & Rez, 1985). Since the measured $I_{NbM4,5}/I_{OK}$ intensity ratio is still required for the determination of the atomic concentration ratio, the representative NbO_2 spectrum with an intensity ratio of 4.73 for ΔE = 70 eV should also deliver representative results when quantification is conducted by means of theoretical cross sections. The use of *Hartree-Slater* cross sections yielded an atomic concentration ratio C_{Nb}/C_O of 0.250 ± 0.036 (±14.4%), which strongly differs from the nominal value for NbO_2 (C_{Nb}/C_O = 0.500), where the same energy windows for background extrapolation and for integration (ΔE = 70 eV) under the Nb-$M_{4,5}$ and O-K edges were applied as previously for the quantification via the empirical *k*-factor $k_{NbM4,5\text{-}OK}$. In order to check for the existence of an optimal integration window ΔE, its width was varied while keeping its lower limit constant at the corresponding edge onset. The resulting atomic concentration ratios are given in Fig. 4.3.5. With increasing ΔE, the values obtained for C_{Nb}/C_O get closer to the nominal one, but even with an integration window as wide as 125 eV (since the spectrum ends at around 657 eV, the maximum width for integration under the O-K edge is limited to 125 eV), the relative deviation between the mean value of the reached atomic concentration ratio C_{Nb}/C_O = 0.341 ± 0.048 (± 14.1%) and the nominal value remains very high at 37.8%. Thus, the experimental *k*-factors, even that derived from the Nb-$M_{2,3}$ edges, allow much more reliable quantitative results than the theoretical cross sections calculated for the Nb-$M_{4,5}$ and O-K edges.

As a last test, all the 12 NbO_2 spectra treated in section 4.3.2 were quantified using the empirical *k*-factors achieved from the 24 NbO and Nb_2O_5 spectra. Quantification by means of the Nb-$M_{4,5}$ edges (ΔE = 70 eV, $k_{NbM4,5\text{-}OK}$ = 9.43 ± 0.20) gives a C_{Nb}/C_O atomic concentration ratio of 0.503 ± 0.014 (± 2.8%). The good agreement with the nominal value (0.6% relative deviation) and the reasonably low standard deviation demonstrate the efficiency of the applied quantification procedure, and a *k*-factor $k_{NbM4,5\text{-}OK}$ = 9.44 ± 0.20 (±2.1%) results from averaging of all the 36 spectra measured on NbO, NbO_2 and Nb_2O_5.
Using the Nb-$M_{2,3}$ edges for quantification, the 12 NbO_2 spectra yields an $I_{NbM4,5}/I_{OK}$ intensity ratio of 0.677 ± 0.028 (±4.1%) by means of ΔE = 50 eV. Thus, the intensity ratio of 0.709 obtained from the NbO_2 spectrum chosen for the first quantification test was not representative for the other 11 spectra. Quantification of all 12 spectra with $k_{NbM2,3\text{-}OK}$ = 1.31 ± 0.05 results in an atomic concentration ratio C_{Nb}/C_O = 0.517 ± 0.029 (± 5.6%), which is, with a relative deviation of 3.3%, in a better agreement with the nominal value than the result obtained above from the quantification of one single spectrum (7.9% relative deviation). Moreover, considering the standard deviation, the achieved C_{Nb}/C_O is in that case consistent with NbO_2, and the *k*-factor resulting from all the 36 NbO, NbO_2 and Nb_2O_5 spectra is $k_{NbM2,3\text{-}OK}$ = 1.32 ± 0.06 (±4.5%). Nevertheless, the use of the Nb-$M_{2,3}$ edges still leads to much less reliable quantification than the use of the Nb-$M_{4,5}$ ones.

From the different analyses conducted up to here it appears that the Nb-$M_{4,5}$ edges enable more precise (lower standard deviation of the I_{NbM}/I_{OK} intensity ratio) and more accurate (lower relative deviation between measured and nominal C_{Nb}/C_O atomic concentration ratios) quantitative results than the Nb-$M_{2,3}$ edges. Hence, the further quantitative investigations, whose results are presented in the next sections, principally base on the use of the Nb-$M_{2,3}$ edges.

4.3.5 Influence of the specimen thickness on quantitative EELS

The specimen thickness is an important parameter for quantification, which was not yet considered. On the whole, 14 NbO spectra, 25 NbO_2 spectra and 14 Nb_2O_5 spectra were acquired from specimen regions with a relative thickness t/Λ in the range of 0.2 to 0.6. The relative thickness was systematically determined from one low-loss spectrum recorded immediately before or after each core-loss spectrum. The 53 reference spectra were quantified by means of the Nb-$M_{4,5}$ edges, leading for the used experimental parameters (LEO 922 microscope: E_0 = 200 keV, β = 12.3 mrad, α = 11.2 mrad, ΔE = 70 eV) to $k_{NbM4,5\text{-}OK}$ = 9.45 ± 0.20 (±2.1%). A mean value of 0.41 was found for the relative thickness by averaging the measurements conducted on the 53 low-loss spectra corresponding to the quantified core-loss spectra. Fig. 4.3.6 shows the individual *k*-factors derived from each spectrum as a function of the relative thickness of the measured specimen region. For each reference oxide, the experimental data were fitted using a linear function (cf. Fig. 4.3.6). The impact of the specimen thickness on the $k_{NbM4,5\text{-}OK}$-factor is not obvious. However, considering the linear fits, it seems that the *k*-factors resulting from Nb_2O_5 and NbO_2 tend to increase with decreasing relative thickness from 0.5 to 0.2, whereas those of NbO increase for a rise of t/Λ from 0.4 to 0.6.

Two approaches can be used to better apprehend and to limit the eventual negative effects of the specimen thickness on quantification. The first one consists in limiting the relative-thickness range used for quantification. The second is to correct the spectra for multiple scattering.
By considering only the spectra with a relative thickness in the range of 0.3 to 0.5 for quantification (see Fig. 4.3.6), an averaged *k*-factor $k_{NbM4,5\text{-}OK}$ = 9.39 ± 0.17 (±1.8%) is obtained from 8 NbO, 20 NbO_2 and 9 Nb_2O_5 spectra (LEO 922 microscope: E_0 = 200 keV, β = 12.3 mrad, α = 11.2 mrad, ΔE = 70 eV). The averaged relative thickness corresponding to the 37 quantified spectra is t/Λ = 0.42. The better standard deviation of the *k*-factor (±1.8%) compared to that resulting from all the 53 spectra (±2.1%) indicates the possibility to gain more precise quantitative results when the specimen thickness is taken into account. The 20 NbO_2 spectra were quantified by the *k*-factor resulting from the 17 NbO and Nb_2O_5 spectra yielding an atomic concentration ratio C_{Nb}/C_O of 0.502 ± 0.013 (± 2.6%). The agreement with the nominal value C_{Nb}/C_O = 0.500 for NbO_2 remains very good (0.4% relative deviation), demonstrating the accuracy of the quantification procedure.

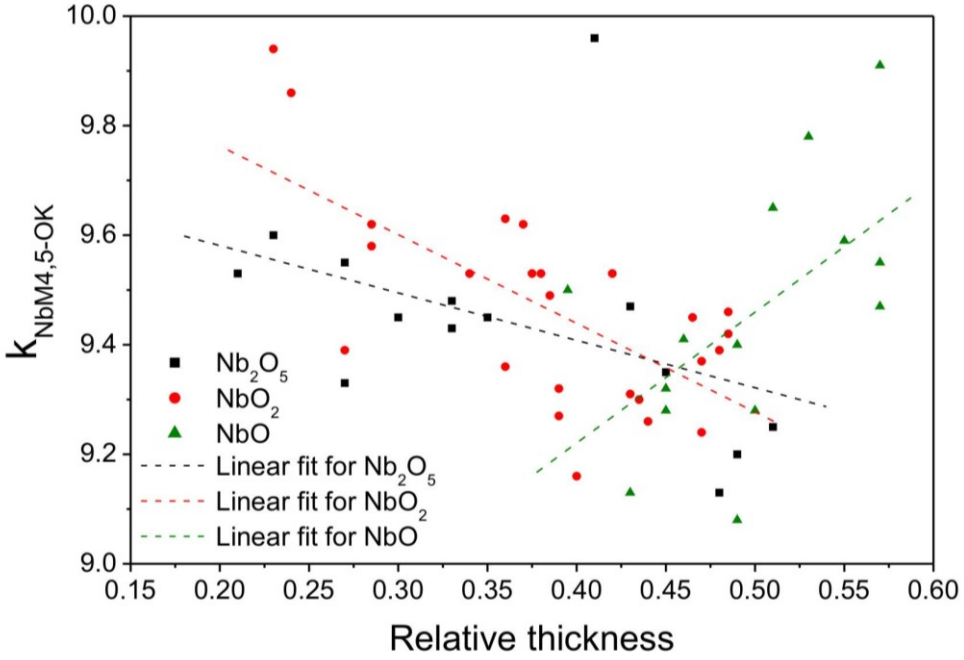

Fig. 4.3.6. *k*-factors determined by means of the Nb-$M_{4,5}$ edges from 53 reference spectra as a function of the relative thickness of the measured specimen region (LEO 922 microscope: E_0 = 200 keV, β = 12.3 mrad, α = 11.2 mrad, ΔE = 70 eV). Linear functions were fitted to the data resulting from each reference niobium oxide.

The multiple-scattering correction of the core-loss spectra is conducted via *Fourier*-ratio deconvolution by means of the low-loss spectra recorded immediately before or after the acquisition of each core-loss spectrum. Without deconvolution the 25 NbO_2 spectra taken from specimen regions with t/Λ in the range of 0.23 to 0.49 gives an $I_{NbM4,5}/I_{OK}$ intensity ratio of 4.73 ± 0.09 (±1.9%), whereas after deconvolution a value of 5.20 ± 0.08 (±1.5%) is found (ΔE = 70 eV). For each spectrum, for background extrapolation and integration under the O-K edge as well as for background extrapolation under the Nb-$M_{4,5}$ edges the same windows (identical width and position) were used to calculate the intensity ratio with deconvolution compared to the quantification without deconvolution. Depending on how exactly the onset of the Nb-$M_{4,5}$ edges can be localized before and after deconvolution, only the position of the integration window under the Nb-$M_{4,5}$ edges was sometimes slightly different. Hence, the standard deviation of the averaged intensity ratio is reduced from 1.9% to 1.5% by the *Fourier*-ratio deconvolution, indicating that the disturbing effects of the specimen thickness can be limited by multiple-scattering correction to get a more precise quantification.
Unfortunately, most of the low-loss spectra corresponding to the NbO and Nb_2O_5 core-loss spectra present an artefact in the form of a little peak appearing a few eV in front of the ZLP. This artefact, whose origin was unknown when the spectra were taken at the LEO microscope, could later be correlated with an error occurring during the readout of the CCD camera when short acquisition times around 50 ms were used. It introduces a slight error in the *k*-factor measured from *Fourier*-ratio deconvoluted spectra, which can affect both the precision and the accuracy of the quantification (see section 4.4.6 for a definition of precision

and accuracy). Only two NbO and two Nb_2O_5 core-loss spectra could be acquired in combination with artefact-free low-loss spectra after the readout problem of the CCD camera was fixed. This is not enough to quantify the NbO_2 spectra in order to check for the accuracy of the procedure or to examine whether a 70 eV wide integration window is still a good compromise between background and fine-structures errors when the spectra are corrected for multiple scattering. However, the integration-window width for quantification without deconvolution was determined by investigating spectra resulting from a wide relative-thickness range of 0.2 to 0.6. Within this range the strength of the effects of multiple scattering is expected to differ strongly. In spite of these different multiple-scattering effects an optimal integration window could be identified. Thus, there is no reason why in a first approximation it should not be assumed that the same integration window still leads to a good compromise between background and fine-structure errors occurring for the three reference oxides in the ideal case where the multiple-scattering contributions are removed from the spectra (after deconvolution). Hence, a 70 eV wide integration window is also used for the determination of *k*-factors from *Fourier*-ratio deconvoluted spectra.

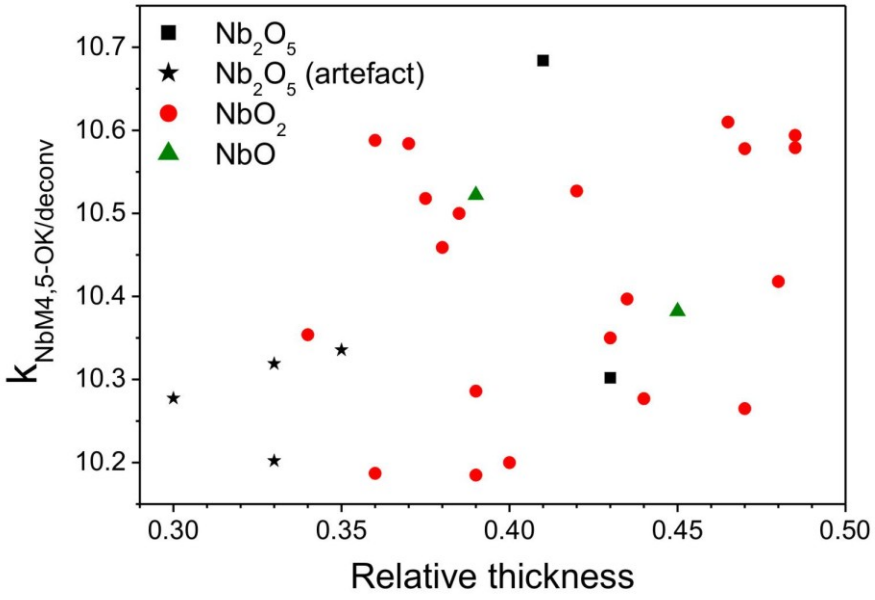

Fig. 4.3.7. *k*-factors determined by means of the Nb-$M_{4,5}$ edges from 28 *Fourier*-ratio deconvoluted reference spectra as a function of the relative thickness of the measured specimen region (LEO 922 microscope: E_0 = 200 keV, β = 12.3 mrad, α = 11.2 mrad, ΔE = 70 eV). For four Nb_2O_5 spectra the low-loss spectra used for deconvolution were not free of artefacts (see text).

The two approaches, limitation of the relative-thickness range and deconvolution, were combined to calculate a *k*-factor from the 20 NbO_2, two NbO and two Nb_2O_5 spectra which were acquired from specimen regions with t/Λ between 0.3 and 0.5 and whose associated low-loss spectra are free of artefacts. In order to limit a little bit the proportion of NbO_2 spectra used for the determination of the *k*-factor and to add spectra resulting from thin specimen regions to the statistic, four Nb_2O_5 spectra with corresponding non artefact-free low-loss

spectra were also included in the calculation. These four spectra were taken in a relative-thickness range of 0.30 to 0.35, where multiple scattering is still relatively low, so that the deconvolution errors associated with the artefacts of the low-loss spectra were also limited. Fig. 4.3.7 shows the individual *k*-factors determined from each deconvoluted spectrum as a function of the relative thickness. The 28 spectra corrected for multiple scattering yield an averaged *k*-factor $k_{\mathrm{NbM4,5\text{-}OK/deconv}} = 10.41 \pm 0.15$ (±1.4%) and the corresponding relative thickness amounts 0.40. In determining *k*-factors, the observed decrease of the standard deviation from 2.1% for the 53 spectra analyzed without deconvolution to 1.4% for the 28 deconvoluted spectra with t/Λ between 0.3 and 0.5 illustrates the gain in precision, which can be achieved by taking the sample thickness into consideration.
A further example of the specimen-thickness effects on the measured *k*-factors is given in the next section (cf. Fig. 4.3.8).

4.3.6 Compilation of *k*-factors for different experimental parameters

Some of the experimental *k*-factors given above for the LEO 922 microscope are reported in Table 4.3.3 together with those derived from spectra taken with different parameters at the JEOL JEM-3000F and VG HB501UX microscopes.

Using the JEOL JEM-3000F microscope for quantification, the measurements were conducted on four NbO spectra and four Nb_2O_5 spectra by means of the Nb-$M_{2,3}$ edges. The spectra were recorded from specimen regions with large relative thicknesses ranging from 0.46 up to 1.40. The averaged relative thickness corresponding to all the eight reference spectra amounts to 0.96 and *Fourier*-ratio deconvolution was thus used to determine intensity ratios and *k*-factors. Using 70 eV wide integration windows starting at the very edge onsets, different $I_{\mathrm{NbM2,3}}/I_{\mathrm{OK}}$ intensity ratios were obtained, namely 1.46 ± 0.13 for NbO and 0.552 ± 0.015 for Nb_2O_5, which allows a clear quantitative distinction between the two reference oxides. The *k*-factors derived from these intensity ratios by means of Eqn. (4.3.1) were found to be in agreement with one another: $k_{\mathrm{NbM2,3\text{-}OK}} = 1.46 \pm 0.13$ (±8.9%) from the NbO intensity ratio and $k_{\mathrm{NbM2,3\text{-}OK}} = 1.38 \pm 0.04$ (± 2.9 %) from Nb_2O_5. Hence, for the present experimental parameters (JEM 3000F/GIF: E_0 = 300 keV, β = 4.76 mrad, $\alpha \approx \beta/3$, ΔE = 70 eV) a *k*-factor $k_{\mathrm{NbM2,3\text{-}OK}} = 1.42 \pm 0.10$ (± 7.0 %) results from averaging of the eight spectra measured from NbO and Nb_2O_5.

Seven core-loss spectra were recorded on Nb_2O_5 at the VG microscope and were quantified using the Nb-$M_{4,5}$ edges by means of 70 eV wide integration windows starting at the edge onsets. The spectra were acquired from specimen regions with different relative thicknesses in the range of 0.14 to 0.66 leading to different $I_{\mathrm{NbM4,5}}/I_{\mathrm{OK}}$ intensity ratios and consequently to different *k*-factors, as shown in Fig. 4.3.8a (data without deconvolution). On the whole, an increase of the *k*-factor can be observed with decreasing relative thickness. Only one spectrum recorded at a relative thickness of 0.21 gives a value that diverges from this general trend. By

averaging the results obtained for the seven spectra, a *k*-factor $k_{NbM4,5\text{-}OK} = 13.77 \pm 0.88$ ($\pm$ 6.4 %) is found (VG HB501UX microscope: E_0 = 100 keV, β = 6.5 mrad, $\alpha \approx$ 10 mrad, ΔE = 70 eV) and the corresponding mean relative thickness amounts to 0.35. The individual *k*-factors achieved after a *Fourier*-ratio deconvolution of each spectrum are also visible in Fig. 4.3.8a as a function of the relative thickness, and the mean value of all seven spectra is $k_{NbM4,5\text{-}OK/deconv} = 14.68 \pm 0.57$ ($\pm$ 3.9 %). The reduction of the standard deviation from 6.4% to 3.9% by means of *Fourier*-ratio deconvolution indicates that an important part of the errors occurring when the *k*-factor is determined without deconvolution is due to multiple scattering. For each spectrum the relative deviation between the *k*-factors determined with and without *Fourier*-ratio deconvolution is presented in Fig. 4.3.8b in dependence on the relative thickness. The clear increase of the relative deviation with increasing specimen thickness illustrates the rising influence of multiple-scattering on the measured spectra.

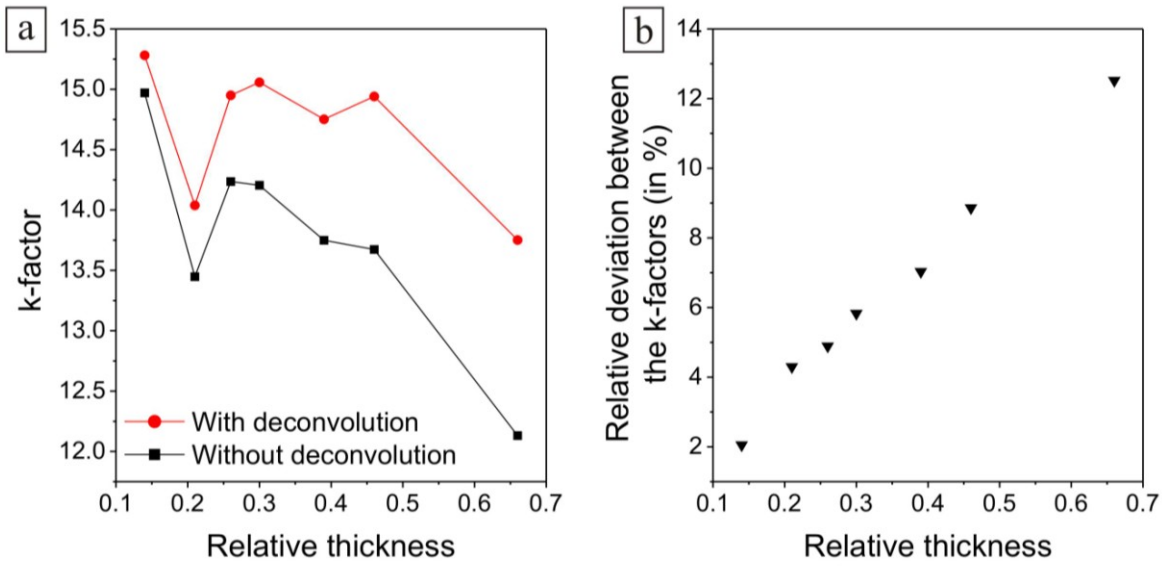

Fig. 4.3.8. *k*-factors determined with and without *Fourier*-ratio deconvolution (**a**) and corresponding relative deviation between the obtained values (**b**) as a function of the relative thickness. The *k*-factors were derived by means of the Nb-$M_{4,5}$ edges (ΔE = 70 eV) from seven Nb_2O_5 spectra taken on specimen regions differing in thickness via the VG HB501UX microscope (E_0 = 100 keV, β = 6.5 mrad, α = 10 mrad).

The experimental *k*-factors calculated here will be applied in the next chapter to characterize nanoscale oxide layers in Nb-based capacitor structures. In order to quantify spectra of unknown oxides recorded from specimen regions differing in thickness, different combinations of the Nb_2O_5 reference spectra were computed without *Fourier*-ratio deconvolution to determine averaged *k*-factors corresponding to different mean values of the relative thickness. Four *k*-factors obtained for different relative thicknesses are given in Table 4.3.3.

Table 4.3.3. Compilation of experimental *k*-factors determined for different experimental parameters from reference spectra taken on NbO, NbO_2 and Nb_2O_5 using the LEO 922, the JEOL JEM-3000F, and the VG HB501UX microscopes.

Microscope: experimental parameters	Used edges	ΔE	Analyzed reference spectra	t/Λ – range $\Rightarrow$ mean t/Λ	*Fourier*-ratio deconvo-lution	*k*-factor $k_{NbM-OK} = \frac{C_O}{C_{Nb}} \cdot \frac{I_{NbM}}{I_{OK}}$
LEO 922 Omega: E_0 = 200 keV β = 12.3 mrad α = 11.2 mrad	Nb-$M_{2,3}$ O-K	50 eV	12 NbO 12 NbO_2 12 Nb_2O_5	0.21 - 0.57 $\Rightarrow$ 0.42	no	1.32 ± 0.06 (±4.5%)
	Nb-$M_{4,5}$ O-K	70 eV	14 NbO 25 NbO_2 14 Nb_2O_5	0.21 - 0.57 $\Rightarrow$ 0.41		9.45 ± 0.20 (±2.1%)
			8 NbO 20 NbO_2 9 Nb_2O_5	0.30 - 0.50 $\Rightarrow$ 0.42		9.39 ± 0.17 (±1.8%)
			2 NbO 20 NbO_2 6 Nb_2O_5	0.30 - 0.49 $\Rightarrow$ 0.40	yes	10.41 ± 0.15 (±1.4%)
JEOL JEM-3000F: E_0 = 300 keV β = 4.76 mrad $\alpha \approx \beta/3$	Nb-$M_{2,3}$ O-K	70 eV	4 NbO 4 Nb_2O_5	0.46 - 1.40 $\Rightarrow$ 0.96	yes	1.42 ± 0.10 (± 7.0 %)
VG HB501UX: E_0 = 100 keV β = 6.5 mrad $\alpha \approx$ 10 mrad	Nb-$M_{4,5}$ O-K	70 eV	6 Nb_2O_5	0.14 - 0.46 $\Rightarrow$ 0.29	no	14.05 ± 0.55 (±3.9%)
			5 Nb_2O_5	0.21 - 0.46 $\Rightarrow$ 0.32		13.86 ± 0.35 (±2.5%)
			4 Nb_2O_5	0.26 - 0.46 $\Rightarrow$ 0.35		13.97 ± 0.30 (±2.1%)
			6 Nb_2O_5	0.21 - 0.66 $\Rightarrow$ 0.38		13.57 ± 0.77 (±5.7%)

In order to complete this collection of experimental *k*-factors, literature data are compiled in Table 4.3.4. In addition to the *k*-factors, the number of evaluated spectra, the type of reference Nb oxide, ΔE, and information on the relative thickness t/Λ of the data set are given (if available).

Table 4.3.4. Compilation of experimental *k*-factors available in the literature for the Nb-O system.

Microscope: experimental parameters	Used edges	ΔE	Analyzed reference spectra	t/Λ	*Fourier*-ratio deconvolution	*k*-factor $k_{Nb-O} = \frac{C_O}{C_{Nb}} \cdot \frac{I_{Nb}}{I_O}$
Philips EM420 E_0 = 120 keV β =5.9 mrad α = 2.4 mrad Hofer et al. (1988)	Nb-$M_{4,5}$ O-K	50 eV	10 Nb_2O_5	≤ 0.40	no	8.35 ± 0.31 (± 3.7 %)
		100 eV				17.9± 0.2 (± 1.1 %)
JEOL 2010F E_0 = 200 keV β =6.9 mrad α = 2.5 mrad Olszta et al. (2006)	Nb-$M_{4,5}$ O-K	75 eV	10 NbO 10 NbO_2 10 Nb_2O_5	≤ 0.4	yes	14.3 ± 0.8 (± 5.6 %)
		100 eV				18.5 ± 0.7 (± 3.8 %)
		125 eV				21.3 ± 0.9 (± 4.2 %)
		150 eV				23.8 ± 1.1 (± 4.6 %)
JEOL 2010F E_0 = 200 keV β = 7.25 mrad α = 10.55 mrad Olszta et al. (2008)	Nb-$M_{4,5}$ O-K	60 eV	Niobium oxide standards	not mentioned	not mentioned	20.6
Philips CM20 E_0 = 200 keV β =7.6 mrad α < 1.5 mrad Hofer et al. (1996)	Nb-$L_{2,3}$ O-K	50 eV	≥ 5	0.1 – 0.3	no	0.0264 ± 3.0 %
		100 eV				0.0296 ± 4.2 %

4.3.7 First application: investigation of the native oxide layer grown on Nb

The determination of the thickness of the native oxide layer on Nb provides an example for the application of the derived *k*-factors. In section 4.2.6 it was shown that an O-K edge can be observed in the EEL spectra acquired on reference Nb when thin specimen regions are investigated (see Fig. 4.2.12). This O-K signal was interpreted as the presence of a native niobium oxide layer at the surface of the pure Nb metal. Moreover, the general shape of the measured O-K edges was quite similar to that observed for NbO (see Fig. 4.2.13). In the following, it is supposed that the "Nb" specimen consists of the original Nb reference material sandwiched between two equally sized oxide layers grown at its upper and lower surfaces as shown in Fig. 4.3.9. In addition, it is assumed that within the investigated regions the three layers are homogeneous in thickness and that their surfaces and interfaces are plane-parallel and lie perpendicular to the direction of the incident electron beam in the microscope.

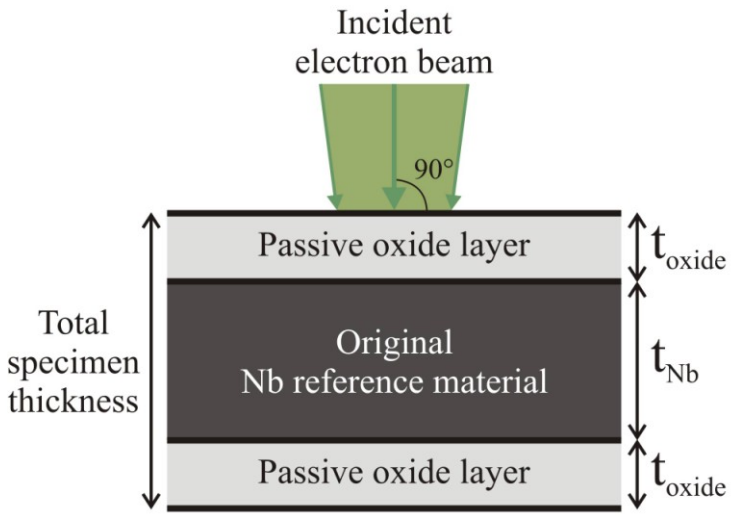

Fig. 4.3.9. Schema of the "Nb" reference material showing the composition and geometry expected for the investigated specimen region and its assumed orientation with respect to the incident electron beam in the microscope.

In order to gain more information on the thickness of the oxide layers, quantitative EELS was conducted on a core-loss spectrum recorded on Nb via the LEO 922 microscope (E_0 = 200 keV, β = 12.3 mrad, α = 11.2 mrad). A relative thickness t/Λ of approximately 0.27 was found by analyzing a low-loss spectrum taken from the same specimen region. The core-loss spectrum was quantified by means of the O-K and Nb-$M_{4,5}$ edges with 70 eV wide integration windows starting at the onsets of the edges as shown in Fig. 4.3.10, resulting in an $I_{NbM4,5}/I_{OK}$ intensity ratio of 39.0. Using $k_{NbM4,5\text{-}OK}$ = 9.45 ± 0.20 determined from 53 reference spectra corresponding to a range of relative thickness of about 0.2 to 0.6 this intensity ratio gives an atomic concentration ratio C_{Nb}/C_O = 4.13 ± 0.09.

Thus, when the oxide layers and the Nb-metal are considered together, there is roughly one oxygen atom for 4.13 Nb atoms in the complete specimen. Assuming that there is no oxygen in the pure Nb reference material and that the surface oxide layers consist of NbO, 24.2% of the niobium atoms should be in the oxide layers. With other words, there is 24.2 mol of NbO against 75.8 mol of pure Nb in the specimen. Considering the body-centred structure of Nb with a lattice parameter a = 0.3300 nm (Pialoux et al., 1982), a molar volume V_{Nb} of 10.8 cm^3 can be calculated for pure Nb. In the case of crystalline NbO, the defective rock-salt structure with 25% atom missing and a lattice parameter a = 0.4212 nm (Pialoux et al., 1982) yields a molar volume V_{NbO} of 15.0 cm^3. Under the assumption that in the oxide layer the molar volume of amorphous NbO is quite similar to that of crystalline NbO, the ratio of the thickness of the pure Nb layer (t_{Nb}) to the total thickness of oxide in the specimen ($2t_{NbO}$) is about $(75.8V_{Nb})/(24.2V_{NbO})$ = 2.26, i.e. the two oxide layers represent approximately 30.7% of the total specimen thickness.

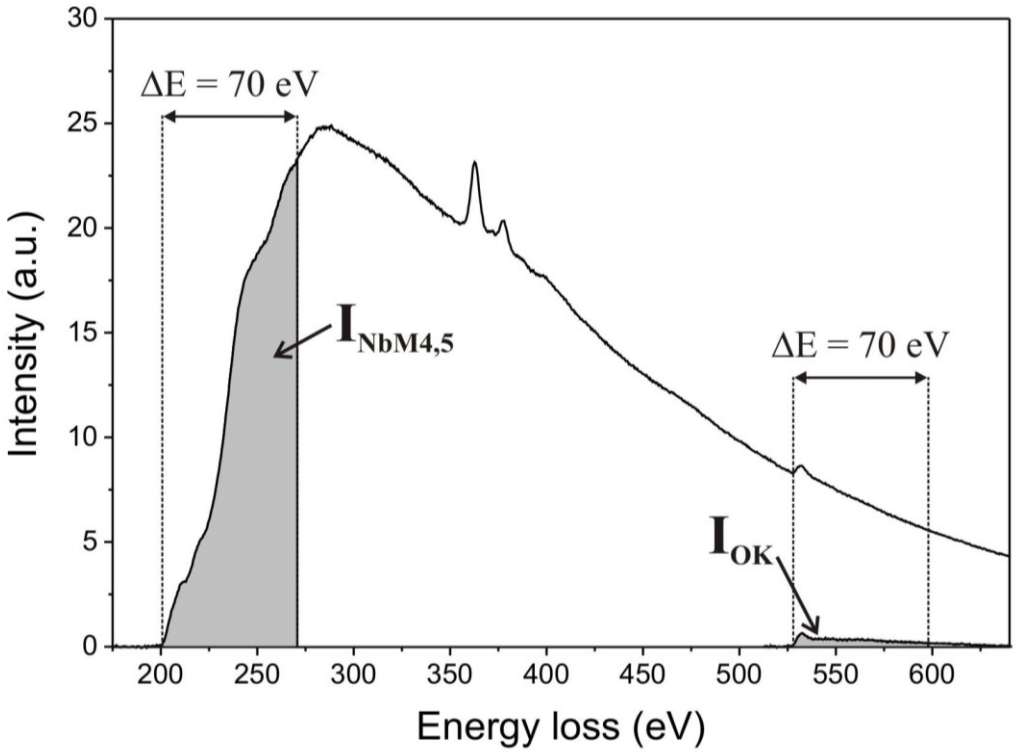

Fig. 4.3.10. Quantitative investigation of an EEL spectrum acquired from the "Nb" reference material at a specimen region with a relative thickness of 0.27: measurement of the intensities under the background-subtracted Nb-$M_{4,5}$ ($I_{NbM4,5}$) and O-K (I_{OK}) edges over a 70 eV wide integration window ΔE starting at the very edge onsets (LEO 922 microscope).

In order to derive the absolute thickness from the relative one, an estimate of the inelastic mean free path Λ is required for the specimen. It is assumed that the effective inelastic mean free path Λ_{eff} of one electron going through the specimen is given by a linear combination of the mean free paths within Nb (Λ_{Nb}) and NbO (Λ_{NbO}), where the contribution of each material is only fixed by the ratio of its thickness to the total thickness of the specimen – i.e. $\Lambda_{eff} \sim 0.693\Lambda_{Nb} + 0.307\Lambda_{NbO}$ in the present case. The value of Λ for each material (Λ_{Nb} and Λ_{NbO}) can be obtained from the experimental parameterization proposed by Malis et al. (1988) (see section 3.2.4). The accuracy of the thickness determined on the basis of the analysis of a low-loss spectrum in combination with the parameterization of Malis et al. is estimated to be better than ± 20 % (Malis et al., 1988). However, in the present case β is only slightly larger than α, which may affect the accuracy of the value obtained for Λ (Malis et al., 1988). Nonetheless, due to the logarithmic dependence on β of the parameterization (cf. Eqn. 3.2.4) and the quite high semi-angles used (β = 12.3 mrad, α = 11.2 mrad), this error should be limited. For pure Nb Z_{eff} amounts to 41 (in that case $Z_{eff} = Z$) and following the prescription of Malis et al. (1988) about 28.5 is found in the case of NbO (cf. Eqn. 3.2.7), so that one obtains Λ_{Nb} = 88 nm and Λ_{NbO} = 98 nm for the used experimental parameters (E_0 = 200 keV, β = 12.3 mrad). Hence, the effective mean free path Λ_{eff} amounts to about 91 nm, and considering the relative thickness of 0.27 the absolute thickness of the investigated specimen region is found to be approximately 25 nm, leading to a total oxide thickness of

approximately 7.6 nm. Under the assumption that the two oxide layers upside and underneath the pure Nb material have the same thickness, the thickness of one single native oxide layer is then $t_{NbO} \sim 3.8$ nm.

It should be noticed that the used *k*-factor was determined from the investigation of NbO, NbO_2 and Nb_2O_5 spectra. The resulting quantification is very likely less accurate when the C_{Nb}/C_O atomic concentration ratio of the investigated material is greater than 1 (NbO_x with $x < 1$), compared to a ratio between 1 and 0.4 (stoichiometry between NbO and Nb_2O_5). Indeed, as the O-K signal becomes weaker (compare e.g. Fig. 4.3.10 for "Nb" with Fig. 4.3.2 for NbO_2) and that of Nb-M_1 stronger, the accuracy of the background extrapolation and the precision of the intensity integration under the O-K edge deteriorate. Hence, for the here investigated spectrum (Fig. 4.3.10) a fitting window of only 11 eV in width should be used for the background modeling under the O-K edge in order to avoid negative intensities a few 10 eV above the onset of the background-subtracted edge. On the other hand, 30 eV wide fitting windows were typically applied to extrapolate the background under the O-K edge of NbO, NbO_2 and Nb_2O_5.
Thus, the quantification procedure used to determine the $I_{NbM4,5}/I_{OK}$ intensity ratio for the "Nb" specimen is not any more perfectly identical to that applied to derive the *k*-factor. Possibly, the O-K intensity obtained for "Nb" is slightly underestimated compared to that measured from NbO, NbO_2 and Nb_2O_5, which would mean that the thickness of the oxide layer is also underestimated. However, a power-law function could still be applied to model the background and the above-mentioned error is probably not such important compared to the other errors, which may occur while determining the thickness.
Indeed, owing to the empirical parameterization used to derive the inelastic mean free path, and, more generally, because of the numerous assumptions made, the value of 3.8 nm obtained for the oxide-layer thickness should only be considered as a rough estimate. Nevertheless, the order of magnitude is expected to be correct.

According to the O-K ELNES, the native oxide layer analyzed in the present work mainly presents a stoichiometry near NbO (Section 4.2.6) but different compositions are mentioned in the literature (see, e.g., Grundner & Halbritter, 1980; Franchy et al., 1996; Sebastian et al., 2006; see also section 2.1.1 for more details). Particularly, native oxide layers consisting mainly of near-stoichiometric Nb_2O_5 are reported (Grundner & Halbritter, 1980; Halbritter, 1987; Wu, 2006). According to Halbritter (1987) this Nb_2O_5 layer presents a "microcrystalline amorphous" structure. The possibility that the native oxide consists of a combination of oxide phases of different compositions is also suggested (Lindau & Spicer, 1974; Grundner & Halbritter, 1980; Yoon et al, 2007; Delheusy et al., 2008). In addition, the EELS spectra taken from the "Nb" reference are characterized by poor signal-to-noise ratios and are only compared to reference spectra of crystalline oxides. However, amorphous Nb_2O_5 may have another signature than the investigated crystalline phase because a blurred and less pronounced O-K ELNES can be expected. Thus, it cannot be excluded that the O-K ELNES observed for "Nb" results from a combination of near-stoichiometric NbO (main part) with some other niobium oxide phases (to a lesser proportion).

Hence, as a test, the thickness of the specimen was determined for comparison under the extreme assumption that the oxide layers consist of Nb_2O_5. In that case, 9.69% of the Nb atoms of the specimen are expected to be in the oxide layers, meaning that on the whole there is about 4.85 mol of Nb_2O_5 in relation to 90.3 mol of pure Nb in the specimen. The density of amorphous Nb_2O_5 is assumed to be around 5.12 $g.cm^{-3}$ as given by Schäfer et al. (1966). Other sources give lower values for the density (see, e.g., Gmelin, 1970), but a large one was chosen here to maximize the difference between the resulting oxide-layer thickness (t_{Nb2O5}) and that found above for NbO (t_{NbO}). Considering the atomic masses of Nb (~ 92.9 u) and oxygen (~ 16.0 u) a molar volume V_{Nb2O5} of about 51.9 cm^3 can then be derived for amorphous Nb_2O_5. Thus, the ratio $t_{Nb}/(2t_{Nb2O5})$ of the thickness of the pure Nb layer to the total thickness of the oxide layers is about $(90.3V_{Nb})/(4.85V_{Nb2O5}) = 3.87$, meaning that the oxide layers represent approximately 20.5% of the total specimen thickness. Furthermore, with $Z_{eff} = 21.0$ for Nb_2O_5 the inelastic mean free path $\Lambda_{Nb2O5} \sim 107$ nm can be determined using the parameterization of Malis et al. (1988), leading to $\Lambda_{eff} \sim 0.795\Lambda_{Nb} + 0.205\Lambda_{NbO} \sim 92$ nm for the specimen. On the basis of $t/\Lambda \sim 0.27$ the total thickness of the specimen amounts again to about 25 nm, yielding a thickness $t_{Nb2O5} \sim 2.6$ nm for one single native oxide layer. Whereas the relative deviation between the C_{Nb}/C_O atomic concentration ratios of NbO and Nb_2O_5 amounts to 85.7%, the relative deviation between the corresponding thicknesses t_{NbO} and t_{Nb2O5} is only of about 37.5%. Thus, the assumed stoichiometry of the oxide layer does not dramatically influence the order of magnitude of the resulting thickness found.

The order of magnitude ($t_{oxide} \sim 3$ nm) is consistent with the observations of Grundner and Halbritter (1980) and comparable with the results obtained by other authors. In the present study the Nb TEM samples were less than 10 min in the air between the final stage of their preparation (Ar^+-ion etching) and transfer into the high vacuum of the LEO 922 Omega ($\sim 10^{-5}$ Pa). According to X-ray photoelectron spectroscopy and Auger electron spectroscopy analyses, Grundner and Halbritter (1980) reported that a NbO_x ($x \sim 1$) interface layer (≤ 1 nm) and a dielectric oxide layer of oxygen-deficient Nb_2O_5 ($\geq$ 2nm) could not be avoided at the surface of Nb handled in air less than 0.5 h. They observed that the Nb_2O_5 layer grows further in air up to 6 nm in some weeks. However, d'Acapito et al. (2000) derived from extended X-ray absorption fine structure (EXAFS) spectra an oxide thickness of only 2.3 nm after having exposed a pure metallic Nb film to air for several weeks. By fitting the results of electric measurements performed on Nb/NbO*x*/Ag metal-insulator-metal junctions to a theoretical model, Grossman et al. (2002) also determined that the native oxide formed by exposing a Nb surface to air (controlled temperature and humidity) for approximately 3 days has a thickness of ~ 2.8 nm. Finally, a thickness t_{oxide} around 3 nm is also comparable with the results obtained by Delheusy et al. (2008) using X-ray reflectivity and core-level spectroscopy. They found that the natural oxide formed on a Nb(110) surface after 10 h in air at room temperature has a total thickness of 2.03 nm.

4.4 Discussion

In the present work, the ELNES of the different core-loss edges occurring for the niobium-oxygen system was measured on Nb, NbO, NbO_2 and Nb_2O_5. A low-loss fingerprint was also recorded for each reference material. The results, especially those obtained for the Nb-$M_{4,5}$, Nb-$M_{2,3}$ and O-K edges as well as for the plasmon losses, allow a clear qualitative distinction between the four reference materials. Hence, the phase sensitivity of the details of the EELS features should enable to characterize niobium oxides of unknown stoichiometry by means of reference spectra. Quantitative EELS analyses were also performed on oxidic standards to check their potential applicability to the Nb-O system. The good agreement between the results obtained for the three reference oxides by means of the Nb-$M_{4,5}$ edges (see the quantification tests conducted on NbO_2 in sections 4.3.4 and 4.3.5) demonstrate that experimental *k*-factors are a powerful tool for the quantitative determination of the stoichiometry of niobium oxides. In the following, several aspects of the ELNES and quantitative EELS investigation methods and of the results obtained on niobium oxides are discussed in more detail.

4.4.1 Influence of the experimental parameters on the ELNES results

Influence of the incident beam energy, convergence semi-angle, and collection semi-angle

The inelastic scattering of fast electrons by a solid is predominantly a forward-directed phenomenon. Different experimental setups allowing different incident beam energies E_0, collection semi-angles β, and convergence semi-angles α were used to perform ELNES. The combination of the three above-mentioned parameters determines in which proportion the total emitted EEL signal is recorded with respect to the scattering angle. Thus, the fact that the general shape of the investigated EELS features was generally independent of the microscope used for acquisition can be related to the choice of these parameters. The so-called characteristic scattering semi-angle for an energy loss E is given by $\theta_E \sim E/(\gamma m_0 v^2)$, where m_0 is the electron rest mass, v the electron velocity (depending on E_0), and $\gamma = (1 - v^2/c^2)^{-1/2}$ is the relativistic factor with c being the velocity of light (see, e.g., Egerton, 1986, see also section 3.2.3). It is generally accepted that most of the inelastic scattering related to the excitation of a core-loss edge occurs at angles less than 10 θ_E (Verbeeck, 2002).

In the case of plasmons, however, a collection semi-angle slightly higher than 10 θ_E may be required to record more than the half of the scattering, when the incident electrons have an energy higher than 100 keV (Egerton, 1986). Nevertheless, for an incident beam energy $E_0 = 200$ keV and considering a typical energy loss of about 21 eV for the plasmons of the reference materials, θ_E is found to be particularly small around 0.061 mrad, so that it can be assumed that the collection angle of 2.3 mrad used at the Libra microscope is already sufficient to capture most of the inelastic scattering. Hence, it is also expected that the

increase of the collection and convergence semi-angles from $\beta = 2.3$ mrad and $\alpha \sim 0.4$ mrad at the Libra microscope to $\beta = 12.3$ mrad and $\alpha = 11.2$ mrad at the LEO microscope does not have a dramatic influence on the collected signal, and it could indeed be observed that the plasmon fingerprints measured at the two 200 kV microscopes are nearly identical for NbO as well as in the case of Nb_2O_5 (see Fig. 4.2.2).

In order to take the influence of α into consideration while discussing in which proportion the inelastic signal is collected, one can define an effective collection semi-angle by $\beta_{eff} = (\alpha^2 + \beta^2)^{1/2}$ (Verbeeck, 2004). It is clear that the electrons which are scattered at an angle β_{eff} are not all collected, but a great part of them can contribute to the acquired signal. For NbO the shape of the Nb-$M_{4,5}$ edges recorded by means of the JEOL JEM-3000F microscope (E_0 = 300 keV, $\beta = 4.76$ mrad, $\alpha \sim \beta/3$) with $\beta_{eff} \sim 5.0$ mrad is similar to that obtained with β_{eff} = 16.6 mrad using the LEO microscope (E_0 = 200 keV, $\beta = 12.3$ mrad, $\alpha = 11.2$ mrad), indicating that once again the three experimental parameters do not affect significantly the energy distribution of the gathered signal, when their values are changed from those used at the JEOL microscope to those of the LEO. Contrary, by means of the LEO microscope a bump marked by the letter (d) in Fig. 4.2.4a is obtained around 295 eV for Nb_2O_5, whereas such a structure cannot be observed using the JEOL microscope. At $E = 295$ eV the characteristic scattering semi-angle is found around 0.60 mrad for the JEOL microscope (E_0 = 300 keV) and amounts to about 0.86 mrad in the case of the LEO microscope (E_0 = 200 keV). Thus, the ratio β_{eff}/θ_E of the effective collection semi-angle to the characteristic scattering semi-angle is less than 10 in the case of the JEOL microscope (~8.3), whereas a higher value of approximately 19.3 is achieved by the LEO microscope, showing that the latter allows the collection of a more widely spread signal. The additional intensity observed with the LEO microscope can then be attributed to electrons which are scattered at "high" angles and are not collected using the JEOL microscope.

In the case of the O-K edge, the general shape of the reference spectra recorded by different experimental setups is also very similar for each reference oxide (see Figs. 4.2.10 and 4.2.11), at least after a smoothing of the noise by means of a 2 eV wide interval in the case of the NbO spectrum taken at the Libra microscope (Fig. 4.2.11b). Considering a typical energy loss $E = 545$ eV for the O-K fine structure the β_{eff}/θ_E ratio ranges for the used experimental parameters from approximately 1.5 at the Libra microscope to about 10.5 at the LEO. Because of this ratio, being much lower than 10 in the case of the Libra microscope, it can be expected that a significant amount of the O-K signal is not collected. Nonetheless, the fact that the distinct fine structures obtained for NbO and Nb_2O_5 by means of the LEO and JEOL ($\beta_{eff}/\theta_E \sim 4.5$) microscopes are already observable at the Libra one indicates that an important part of the electrons responsible for these characteristic features are strongly enough forward scattered to be captured by means of a collection angle lower than 1.5 θ_E.

For E = 2400 eV a convergence semi-angle $\alpha = 11.2$ mrad and a collection semi-angle $\beta = 12.3$ mrad would lead to a β_{eff}/θ_E ratio of only 2.4 by means of the LEO microscope operated at E_0 = 200 keV. Thus, in order to collect a little bit more signal during the acquisition of the Nb-$L_{2,3}$ edges the convergence and collection semi-angles were chosen

larger than those applied to record the other core-loss edges, viz. $\alpha = 12.6$ mrad and $\beta = 18.0$ mrad yielding $\beta_{eff}/\theta_E \sim 3.1$ (Fig. 4.2.14).

Influence of the energy resolution

In the range where the values of E_0, α and β were chosen, the combination of the three parameters showed little influence on the shape of the recorded spectra. In contrast, the energy resolution dE obviously affects the details of the observed fine structures. Indeed, the energy resolution controls in which proportion the inelastic-scattering signal resulting from a given excitation of the specimen overlaps with the signal resulting from another excitation associated to a slightly different energy loss of the incident electrons. Thus, as the energy resolution was improved from dE ~ 2.1 eV at the LEO microscope to dE ~ 0.3 eV at the Libra, the triple-peak structure of the plasmon of NbO appeared much more pronounced (letters a, b and c in Fig. 4.2.2) and new features became visible in the low-loss region (letters d and e in Fig. 4.2.2b). Double-peak structures could clearly be observed for the Nb-M_3 and Nb-M_2 white lines of Nb_2O_5 at dE ~ 0.3 eV (letters a, b, c and d in Fig. 4.2.7b) as well as for those of NbO_2 at dE ~ 0.6 eV (letters a, b, c and d in Fig. 4.2.8), whereas such fine structures could not be detected at dE ~ 2.1 eV (Fig. 4.2.6). Hence, these two examples show that a variation of the energy resolution leads to more or less well-defined fine-structure details.

In addition, the relative height of the different ELNES features as well as their energy splitting can also be influenced by the energy resolution. The O-K edge provides an interesting example to illustrate these effects. The impact of a deterioration of the energy resolution can be "simulated" by applying the smoothing filter described in section 4.2.6 to the raw data. It can be assumed that an increase of the width w of the energy interval employed by the filter corresponds to an increase of the value of dE. The filter was applied to an original spectrum recorded at the Libra microscope with dE ~ 0.3 eV and showing the O-K edge of NbO. The result can be seen in Fig. 4.2.11b. With increasing w the peak (b) becomes more intense relatively to the peak (a), and their energy splitting $E_b - E_a$ decreases. Thus, in the case of the O-K edge, the energy resolution can strongly influence the double-peak structure observable just above the edge onset (letters a and b in Fig. 4.2.10 and Fig. 4.2.11). Moreover, it was already mentioned that for each reference oxide the general shape of the O-K edge remains roughly independent from the different experimental parameters E_0, α, and β employed for its acquisition using the LEO, the JEOL, the Libra, and the VG microscopes. Hence, it can be assumed that for each reference oxide the splitting $E_b - E_a$ measured for the double-peak structure mainly depends on the energy resolution of the used experimental setup. The validity of this assumption is confirmed by the comparison of the splitting measured for NbO_2 at the VG microscope (present work: E_0 = 100 keV, $\beta \sim 6.5$ mrad, $\alpha \sim 10$ mrad) with that obtained by Jiang and Spence (2004) using a Philips EM400 microscope ($E_0 = 100$ keV, $\beta \sim 5$ mrad, α not mentioned: probably ~ 0 mrad). In spite of partly different experimental parameters E_0, β, and α the same value $E_b - E_a$ ~ 3.5 eV was found in both cases by means of the same energy resolution dE ~ 1 eV. Leaving the other experimental parameters aside, the splitting $E_b - E_a$ measured on the three oxides is thus given in Fig. 4.4.1 as a function of solely the energy resolution. A clear increase of the apparent

splitting can be observed for all three standard oxides as the energy resolution becomes better. Moreover, at each energy resolution the splitting increases with increasing niobium oxidation state, enabling to distinguish between the three oxides.

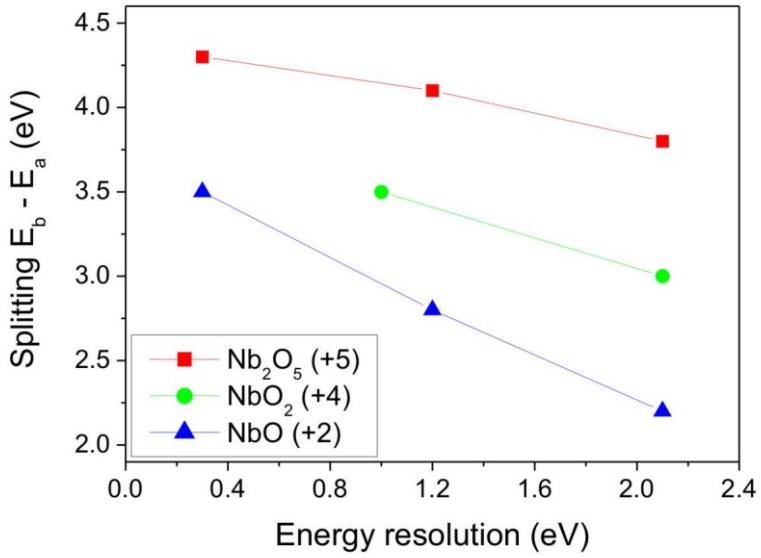

Fig. 4.4.1. Splitting $E_b - E_a$ of the double-peak structure of the O-K edge as a function of the energy resolution of the recording experimental setup. Measurements were performed on NbO, NbO_2, and Nb_2O_5 using the LEO 922, the JEOL JEM-3000F, the ZEISS Libra FE, and the VG HB501UX microscopes (see section 4.2.6).

The effective energy resolution and consequently the resulting ELNES can also be influenced by other parameters like for instance the signal-to-noise ratio. Hence, it could not be clearly determined whether the shoulder observed on the smoothed Nb-M_2 white line of NbO (arrow in Fig. 4.2.7b) by means of the Libra microscope is real – and thus indicates a possible double-peak structure – or results from the strong noise of the raw data. The energy dispersion used to record the spectrum on a CCD camera can also be a limiting parameter. Using a JEOL 2010F microscope (E_0 = 200 keV, β = 6.9 mrad, α = 2.5 mrad) at an energy resolution of 1.5 eV, Olszta et al. (2006) observed no double-peak structure for the O-K edge of NbO, but only one major peak just above the edge onset. However, considering the results of the present work, the double-peak structure would be expected to be visible at dE = 1.5 eV. One possible explanation for this discrepancy is that the large energy dispersion of 0.5 eV per channel used by Olszta et al. did not allow to resolve this double-peak structure of NbO. For comparison, a dispersion of 0.3 eV per channel was used at the JEOL microscope (E_0 = 300 keV, β = 4.76 mrad, $\alpha \sim \beta/3$) to observe the O-K double-peak structure with a slightly better resolution of about 1.2 eV (Fig. 4.2.10b), and a dispersion around 0.25 eV.channel^{-1} was typically employed at the LEO microscope (E_0 = 200 keV, β = 12.3 mrad, α = 11.2 mrad) with dE ~ 2.1 eV (Fig. 4.2.10a).

Influence of the specimen thickness

In addition to the above-discussed recording parameters, other experimental parameters related to the specimen or to the procedures applied to analyse the raw data can also influence the achieved ELNES. With increasing sample thickness, the probability of multiple scattering increases, resulting in a redistribution of the ELNES intensity of a given edge. For instance, if an incident electron transfers 535 eV of its primary energy to an oxygen 1s electron in the specimen, it is expected to contribute to the signal observed at an energy loss of around 535 eV on the EEL spectrum (the precision of the exact position depends on the energy resolution). However, if the same incident electron is involved in a second inelastic scattering process and loses 20 eV while exciting a plasmon, it ends up with a total energy loss of 555 eV and thus contributes to the spectral signal appearing at around 555 eV. Thus, depending on the sample thickness, multiple scattering can influence the relative height and the energy splitting of the different ELNES features, and can also add new details to the ELNES. Hence, a correction for multiple scattering is required for a reliable comparison between data recorded on specimen regions with different thicknesses. However, such a correction is generally not of prime importance for the analysis of the ELNES within the range of few eV following immediately the edge onset (compare, e.g., Fig. 3.2.8c to Fig. 3.2.8a). Indeed, the ELNES only becomes highly sensitive to multiple scattering above a given energy past the edge onset corresponding to the energy loss from which on the plasmon intensity rises. Moreover, the deconvolution techniques applied for multiple-scattering correction add noise to the original spectrum, and like all the procedures which transform the raw data they are not free of artefacts and should be used with caution.

Influence of the background-subtraction procedure

The choice of the window for fitting the background under the edge as well as the particularly used fitting model can also affect the relative height of the different ELNES features. For instance, it has been shown in sections 4.2.4 and 4.3.2 that the background subtraction under the Nb-$M_{2,3}$ edges is particularly uncertain (see Fig. 4.2.6a and Fig. 4.3.3), and consequently, a reliable investigation of the M_3 to M_2 white-line intensity ratio or of the normalized Nb-$M_{2,3}$ white-line intensity (see section 4.2.7 for more information on normalized white-line intensity) could not be performed. In the case of the Nb-$N_{2,3}$ edges, the background subtraction is complicated by the intense tail of the plasmon (see section 4.2.2). The shoulders observed for the three reference oxides at the low-energy side of the Nb-$N_{2,3}$ edges appear much less pronounced after background removal (arrows on the NbO, NbO_2 and Nb_2O_5 spectra in Fig. 4.2.3) than before (arrows in Fig. 4.2.2a). This demonstrates the importance of the background-subtraction procedure for an accurate analysis of the ELNES of a given edge. Nevertheless, for phase fingerprinting the Nb-$N_{2,3}$ edges could be considered with background: the shoulder remains a pertinent characteristic feature, even if it is not any longer a pure ELNES detail but a combination of the Nb-$N_{2,3}$ edges signal with the plasmon tail signal.

4.4.2 O-K ELNES of the reference niobium oxides

The differences in the double-peak structure of the O-K ELNES (see Figs. 4.2.10 and 4.2.11) can be qualitatively explained by the ligand-field theory, if one considers in a rough approximation that the niobium atoms in NbO, NbO_2 and Nb_2O_5 are octahedrally coordinated to six oxygen atoms. This leads to a splitting of the formerly degenerate Nb 4d orbitals into the upper e_g orbital set (d_{x2-y2} and d_{z2}) and the slightly lower in energy t_{2g} set (d_{xy}, d_{xz} and d_{yz}) (Orgel, 1960). The energy difference between the two orbital sets is determined by the ligand-field splitting. The O 2p orbitals being hybridized with the Nb 4d orbitals, the first peak (a) in Figs. 4.2.10 and 4.2.11 could be identified in a first approximation as the t_{2g} component of the Nb 4d-O 2p orbital overlapping, and the second peak (b) as the e_g component of this overlapping. For a given ligand, the magnitude of the ligand-field splitting generally increases with the oxidation state of the metal ion (Orgel, 1960), which could explain why at each energy resolution (see Fig. 4.4.1), the higher energy splitting of the double-peak structure is observed for Nb_2O_5 (Nb^{5+}) and the lower one for NbO (Nb^{2+}), while an in-between value is obtained for NbO_2 (Nb^{4+}). On the whole, it can be noted that the degree of peak splitting is a direct measure of the oxidation state.

Using the JEOL microscope it was found that the peaks (a) and (b) of the double-peak structure of NbO have approximately the same height, whereas in the case of Nb_2O_5 the peak (a) is clearly higher than (b) (see Fig. 4.2.10b). Comparing the raw NbO and Nb_2O_5 spectra obtained with the Libra microscope at an energy resolution of 0.3 eV (see Fig. 4.2.11b), it can be observed that the difference in the relative height of the peaks (a) and (b) is less pronounced than that observed at the JEOL microscope with dE ~ 1.2 eV. However, the width of the peak (b) relatively to that of the peak (a) appears in that case much larger for NbO than for Nb_2O_5. By means of the LEO microscope at dE ~ 2.1 eV a lower relative height of the peak (a) versus the peak (b) is also found for NbO_2 when compared to Nb_2O_5 (see Fig. 4.2.10a). Nevertheless, at this energy resolution the relative height of the two peaks is quite similar for NbO and NbO_2 (Fig. 4.2.10a). In the previous section (4.4.1), it was shown that the energy resolution is of particular importance for the occurrence of fine-structure features. Thus, in spite of the different experimental parameters E_0, α, and β used at the VG and Libra microscopes, the O-K ELNES recorded from NbO_2 using the VG at dE ~ 1 eV (Fig. 4.2.11a) can be compared in a first approximation to that obtained from NbO at the Libra (dE ~ 0.3 eV) after a smoothing of the original spectrum by means of an energy interval w = 1eV (Fig. 4.2.11b). The relative height of the peak (a) versus the peak (b) is slightly higher for NbO than for NbO_2, but concurrently, compared to the width of the peak (a), the peak (b) of NbO is much larger than that of NbO_2. On the whole, all these different observations on the O-K double-peak structures of the three reference oxides indicate the same trend: the relative intensity of the first peak (a) versus the second peak (b) decreases with decreasing niobium oxidation state from +5 by Nb_2O_5 to +4 by NbO_2 and finally down to +2 by NbO. In order to understand the variation of the peak intensity ratios, the simplest effect that has to be considered is the electron counting (de Groot et al., 1989). The t_{2g} orbital set (d_{xy}, d_{xz} and d_{yz}) can accept six electrons at maximum and the e_g orbital set (d_{x2-y2} and d_{z2})

four. The niobium atoms in Nb_2O_5 (Nb^{5+}) are in a d^0 configuration and thus the ratio of empty orbitals t_{2g}/e_g is 6/4. The lower energy t_{2g} states being filled before the e_g states, the t_{2g}/e_g ratio falls to 5/4 for NbO_2 with niobium atoms in a d^1 configuration and then to 3/4 for NbO at a d^3 configuration. Thus, the relative intensity of the t_{2g} and e_g peaks depends on the Nb 4d state occupancy and this effect could qualitatively explain that the first peak (a) decreases in intensity compared to the second peak (b) from d^0 (Nb_2O_5), d^1 (NbO_2), to d^3 (NbO).

Nevertheless, this over-simplified interpretation of the double-peak structure neglects several important factors. Exchange effects can split the two orbital sets t_{2g} and e_g into four, according to the spin directions. This effect should principally concern NbO and to a lesser extent NbO_2, since the exchange splitting is proportional to the number of unpaired spins (Orgel, 1960), which is zero, one and three in d^0, d^1 and d^3 compounds, respectively. However, for niobium as a 4d transition metal, a low-spin behavior can be expected for NbO and NbO_2, meaning that all the t_{2g} orbitals are still lower in energy than any e_g orbital. Moreover, even with an energy resolution as good as 0.3 eV (Libra microscope) no further splitting of the peak (a) or of the peak (b) could clearly be observed for NbO (see Fig. 4.2.11b). Thus, if one of the peaks is split, either this splitting is to weak to be observed at $dE \sim 0.3$ eV, or it is masked by the strong noise of the Libra microscope. The e_g orbitals in octahedral compounds being directed towards the oxygen atoms, hybridize more strongly with the O 2p orbitals than the t_{2g} orbitals do, which can influence the peak intensity ratios (de Groot et al., 1989). Moreover, this interpretation of the double-peak structure was based on the assumption that the niobium atoms are octahedrally surrounded by oxygen. This should be right for NbO_2 in a distorted rutile structure, even if in that case the symmetry of the octahedron is not perfect and different Nb-O and Nb-Nb distances exist, which affects the amount of hybridization and can thus influence the t_{2g}/e_g intensity ratio and the ligand-field splitting (de Groot et al., 1989). Jiang & Spence (2004) also investigated the ELNES of the O-K edge of NbO_2 using a Philips EM400 microscope (E_0 = 100 keV, $\beta \sim 5$ mrad, α not mentioned: probably ~ 0 mrad) and by means of electronic structure calculations based on the linear augmented plane wave method in the local density approximation and performed using the WIEN2K program (Blaha et al., 2001). They found a good fit between these density functional theory calculations and the experimental spectrum, and also assigned the first two peaks of the O-K ELNES (a and b) as t_{2g} and e_g peaks, respectively. The assumption (Nb atoms octahedrally coordinated to six O atoms) is quite true for Nb_2O_5, which also contains NbO_4 tetrahedrons, but in a much smaller fraction than NbO_6 octahedrons (in the investigated H-Nb_2O_5 phase, only one Nb atoms out of 28 is in tetrahedral coordination whereas all the other Nb atoms are in octahedral coordination; Gatehouse & Wadsley, 1964). For NbO however, due to the 25 % atoms missing in the rock salt structure, the niobium atoms may be better described as being in a square planar oxygen environment (Gannon & Tilley, 1977; Wimmer et al., 1982; Kurmaev et al., 2002), the interpretation of the double-peak structure is becoming much less obvious.

4.4.3 Chemical-shift measurements

In EELS, the energy of a given ionization-edge threshold characterizes the difference in energy between the initial core level and the lowest-energy final state taking part to the transitions responsible for the edge (Egerton, 1986). Thus, the chemical shift of the edge onset may be attributed to changes of the effective charge of the atom undergoing excitation, which can affect both the initial and the final electronic energy levels involved in the ionization processes giving rise to the measured edge (Brydson, 2001). However, a reliable theoretical model for the prediction of the absolute energy of an edge onset is currently not available. In addition, the generally accepted idea that the effective physical charge belonging to a transition-metal atom depends on its oxidation state has recently been questioned (Raebiger et al., 2008; Resta, 2008). By performing first-principles quantum-mechanical calculations of the charge of transition-metal atoms embedded in an ionic or semiconducting crystal Raebiger et al. (2008) concluded that only negligible changes in the local transition-metal charge occur as the oxidation state is altered. Hence, chemical shifts observed as a function of the oxidation state should be reconsidered in terms of the degree of hybridization (Resta, 2008). Nonetheless, the formal oxidation state of a transition metal in a compound can still be regarded as being a parameter characterizing the compound. Thus, the empirical analysis of the chemical shift of a given edge can be used to determine the formal oxidation state of the corresponding element in an unknown compound i.e. to gain information on the composition of the compound.

Chemical shift of the Nb edges

A chemical shift of approximately 4 eV to higher energy was detected in this study for the Nb-$N_{2,3}$, -$M_{4,5}$, -$M_{2,3}$ and -$L_{2,3}$ edges as the formal Nb-oxidation state increases from 0 by Nb to +5 by Nb_2O_5. This agrees with results of Olszta et al. (2006) who reported a chemical shift by about 4 eV to higher energies for the Nb-$M_{2,3}$ edges between Nb and Nb_2O_5. In addition, according to X-ray absorption near-edge structure, the Nb-K edge (at about 18980 eV) also shifts toward higher energies by ca. 8 eV with increasing Nb-oxidation state from 0 to +5 (Sasaki et al., 2008). Chemical shifts of metal edges were already observed by EELS in many transition metal oxides and can be either positive or negative with increasing oxidation state (Leapman, 1982; Egerton, 1986; Brydson, 1992; Brydson, 2001). For instance, Wieske et al. (2002) measured a shift of the position of the V-L3 edge from 516.5 eV for VO (V^{2+}) to 519 eV for V_2O_5 (V^{5+}). Likewise, Su et al. (2001) analyzed reference spectra of VO, V_2O_3, VO_2, V_6O_{13}, and V_2O_5, to correlate the position of the V-L_3 edge with the oxidation state of vanadium. Using this correlation, the authors showed that the Ar^+-milling of V_2O_5 induces the reduction of V-ions by the loss of oxygen and to determine the average oxidation state of V-ions as a function of the milling time.

Determination of chemical shifts: experimental considerations

During a preliminary study using a ZEISS EM 912 Omega microscope equipped with an in-column Omega energy filter and with a 1 MByte CCD camera remote-controlled by the SIS EsiVision software, it was observed that the energy position measured for one given edge of

one given reference oxide could vary as a function of the position where the reference spectrum was recorded on the CCD camera. Before and after each core-loss measurement, the position of the ZLP was systematically checked with respect to its original position during the energy calibration of the detector system, which excludes the possibility that the observed discrepancies resulted from a shift of the spectrum on the spectrometer dispersion plane due to instabilities in the electronics (for instance fluctuations in the microscope high voltage or in the current of the magnetic prisms of the Omega filter). Hence, this artefact seems to indicate that the energy dispersion averaged from a given region on the CCD camera during the calibration of the energy axis is not perfectly representative for the local effective dispersion of all the regions of the CCD camera. This could for instance result from some spatial non-linearity or bending of the detector array. In any case, this problem shows that the energy loss, which can directly be read on the energy axis of the raw recorded spectrum, may be untrustworthy and depends on the accuracy of the calibration of the spectrometer dispersion settings.

Thus, in order to check for the chemical shift of one given EELS feature it is important to position systematically this feature for each investigated material on the same region of the CCD camera by adjusting the high voltage of the microscope. Such a procedure minimizes the number of CCD channels effectively involved in the measurement of the chemical shift and consequently the effects of eventual artefacts in the energy-axis calibration. If one wants to measure the absolute energy position of the feature, a reference EELS detail with known energy loss, typically the ZLP, should also be acquired at the same CCD position (thus limiting the number of channels taking part to the determination of the energy difference between both features). In that case, the difference between the high voltages used to record the ZLP and the feature of interest at the same position of the camera gives the searched absolute energy position. Hence, the accuracy of the measure depends on the reliability with which the accelerating voltage of the microscope can be varied to shift one particular spectral feature to a precise position on the detector system. The precision of determining the position of a feature (either the relative position for chemical-shift analysis or the absolute position) is also limited by the possible occurrence of an energy drift of the spectrum during its exposure on the CCD camera. Such drifts can for instance be caused by instabilities in the electronics of the high-tension or spectrometer power supplies or by changes in the magnetic environment close to the magnetic prisms of the spectrometer. Thus, in the present work, two low-loss spectra including ZLP were generally recorded immediately before and after the acquisition of each core-loss spectrum, in order to check for a possible energy drift of the spectrum during its acquisition. In doing so, the known energy loss of the ZLP allows to verify the actual position of the spectrum on the detector system.

Furthermore, the reliability of the determination of the position of an edge is also affected by a combination of other factors including the accuracy of background subtraction, the shape of the investigated edge, and the signal-to-noise ratio. For instance, the presence of the intense plasmon tail disturbs the background subtraction under the Nb-$N_{2,3}$ edges (see Fig. 4.2.2a), thus preventing an accurate measurement of the edge position and of the chemical shift. The delayed-maximum shape of the Nb-$M_{4,5}$ edges can also make the precise localization of the edge onset difficult, especially if in addition the spectrum suffers from poor signal-to-

background and signal-to-noise ratios (two parameters that can be influenced by the specimen thickness). In contrast, the Nb-$M_{2,3}$, O-K, and Nb-$L_{2,3}$ edges are characterized by sharp peaks just above the ionization threshold. However, the apparent edge onset still depends on the accuracy of the background subtraction and noise can partly mask the onset and perturb the top of the peaks. For these reasons, in the present work the positions of these edges were measured neither at their onsets nor at their intensity maxima but at the half maximum of the abrupt signal increase immediately following the edge onset. The greatest precision is expected for the measurements based on this definition, termed "front half maximum" in sections 4.2.4, 4.2.6, and 4.2.7. Finally, it should be noted that the energy resolution can also affect the values obtained for the position of an edge and for its chemical shift, this effect being more or less pronounced as a function of the particular point at which the position is measured on the spectrum (for instance at the edge onset, the intensity maximum or the front half maximum).

A more sensitive and simple approach: measurement of relative chemical shifts

For various reasons, the chemical shifts measured for the different niobium edges were not particularly precise (due to uncertain background subtractions for Nb-$N_{2,3}$ and Nb-$M_{2,3}$, due to the delayed-maximum shape for Nb-$M_{4,5}$, due to long exposure times for Nb-$L_{2,3}$). One general reason is the energy drift during the acquisition. Nevertheless, one particularity of the chemical shift of the O-K edge allows a more simple and precise chemical-shift characterization method for the niobium oxides than that described and applied in sections 4.2.3 and 4.2.4. This chemical-shift measurement is performed by means of one niobium edge, which can be recorded simultaneously with the O-K edge, for instance the Nb-$M_{2,3}$ edges.

The absolute energy positions of the Nb- $M_{2,3}$ and O-K edges were measured for NbO and Nb_2O_5 at the JEOL JEM-3000F microscope with an energy resolution of 1.2 eV (see sections 4.2.4 and 4.2.6). The Nb- $M_{2,3}$ edges were found at 363.8 ± 0.2 eV for NbO and at 365.2 ± 0.3 eV for Nb_2O_5, i.e. a chemical shift to higher energy of about 1.4 ± 0.5 eV occurs with increasing niobium oxidation state from +2 to +5. The O-K edge is around 533.2 ± 0.2 eV for NbO and 532.2 ± 0.2 eV for Nb_2O_5, indicating a chemical shift to lower energies of about 1 ± 0.4 eV as the niobium oxidation state rises from +2 to +5. Thus, the chemical shift of the O-K edge presents the particularity of occurring in the opposite energy direction in comparison to that observed for the Nb-$M_{2,3}$ edges (and, more generally, in comparison to those obtained for every measured niobium edge). Hence, a sensitive means enabling to characterize the oxidation state of the niobium-oxide phases is the energy difference between the position of the Nb-$M_{2,3}$ edges and that of the O-K edge $E_{OK} - E_{NbM2,3}$, which is 169.4 ± 0.4 eV for NbO and 167 ± 0.5 eV for Nb_2O_5. Another way to consider this criterion is to measure the chemical shift of the Nb-$M_{2,3}$ edges relatively to the position of the O-K edge. If the O-K edge position is taken as a reference, the Nb-$M_{2,3}$ edges are located at $E_{NbM2,3} - E_{OK} = -169.4 \pm 0.4$ eV for NbO and -167 ± 0.5 eV for Nb_2O_5, indicating a chemical shift to higher energies by 2.4 ± 0.9 eV as the niobium oxidation state increases from +2 to +5. Considering the errors, this result overlaps roughly the value derived from the measurements performed by Olszta et al. (2006), namely a relative chemical shift of the

Nb-M_3 edge in relation to the O-K edge of about 3.1 ± 0.6 eV to higher energies. However, the agreement is not complete. The discrepancy observed between the two mean values (2.4 eV in the present work, 3.1 eV from Olszta et al.) can partly result from the fact that Olszta et al. measured the positions of the Nb-M_3 and O-K edges at their inflection points, which slightly differs from the procedure applied in the present work.

The mean value measured for the relative chemical shift of the Nb- $M_{2,3}$ edges (2.4 eV) in the present work is higher than those obtained for the absolute chemical shifts of Nb-$M_{2,3}$ edges (1.4 eV) and O-K edge (1 eV) - it is their sum. However, the error is also higher (±0.9 eV). Nevertheless, this drawback only occurs in that particular case because the relative chemical shift was calculated from the absolute energy positions measured on different spectra for the Nb-$M_{2,3}$ edges and the O-K edge. The resulting data thus contain a great amount of error emerging from the spectrum drift, which may take place during the separate EELS acquisitions. The simultaneous recording of the Nb-$M_{2,3}$ and O-K edges in one single run would dramatically reduce the error resulting from spectrum drift. As both edges would suffer exactly the same drift during their acquisition and since only their relative energy position is of interest, this error could even tend to zero if the considered drift were reasonably low. Moreover, since the O-K edge would directly be available as a "reference" in the core-loss spectrum, the recording of two low-loss spectra for each core-loss spectrum would no longer be necessary (except eventually to exclude spectra from the statistic which experienced too extreme acquisition drifts). Thus, the chemical shift of the Nb-$M_{2,3}$ edges relative to the O-K edge position should be a more sensitive and easily measurable criterion than the absolute chemical shift.

Using the LEO 922 microscope, the above-discussed method was applied to analyse 12 NbO and 12 Nb_2O_5 spectra which include both the Nb-$M_{2,3}$ and O-K edges, resulting in an energy difference $E_{NbM2,3} - E_{OK}$ of approximately -167.9 ± 0.1 eV for NbO and -165.2 ± 0.1 eV for Nb_2O_5. The relative chemical shift of the Nb-$M_{2,3}$ edges with respect to the O-K edge can then be derived with a high precision and amounts to about +2.7 ± 0.2 eV as the niobium oxidation state increases from +2 to +5. As expected, the simultaneous recording of the Nb-$M_{2,3}$ and O-K edges in one and the same spectrum enables a much better precision than that obtained at the JEOL microscope by means of separate spectra (at best ± 0.4 eV for $E_{NbM2,3} - E_{OK}$ and ± 0.9 eV for the relative chemical shift). However, the mean values found for $E_{NbM2,3} - E_{OK}$ differs from those measured at the JEOL microscope (–169.4 eV for NbO and and –167 eV for Nb_2O_5). As the positions of the Nb-$M_{2,3}$ and O-K edges were measured at their respective front half maxima, a variation of the energy resolution is expected to have a quite similar influence on both $E_{NbM2,3}$ and E_{OK}, so that the different energy resolutions of the JEOL ($dE \sim 1.2$ eV) and LEO ($dE \sim 2.1$ eV) microscopes can not alone explain the observed discrepancies in the $E_{NbM2,3} - E_{OK}$ energy differences. Hence, these differences are attributed to artifacts in the energy-axis calibration. As a matter of fact, many CCD channels are used to measure $E_{NbM2,3} - E_{OK}$, therefore the accuracy of the resulting values may dramatically depend on the reliability of the calibration of the dispersion of the detector system. Nonetheless, as long as all the spectra are recorded at the same position on the CCD camera, the comparison between the obtained values should be accurate. Indeed, as the Nb-$M_{2,3}$ and O-K edges were systematically recorded on the same two regions of the detector system, only

few channels were involved in the measurement of $E_{NbM2,3} - E_{OK}$ for one reference oxide without being involved in the corresponding measurement for the other oxide. Hence, only few channels are effectively used to determine the relative chemical shift and the errors resulting from an inaccuracy of the dispersion calibration should in that case be negligible. Thus, the mean value of 2.7 eV measured for the relative chemical shift between NbO and Nb_2O_5 is expected to be reliable, and considering the poor precision of the measurement performed at the JEOL microscope (± 0.9 eV), it is found to be in good agreement with the mean value of 2.4 eV obtained there.

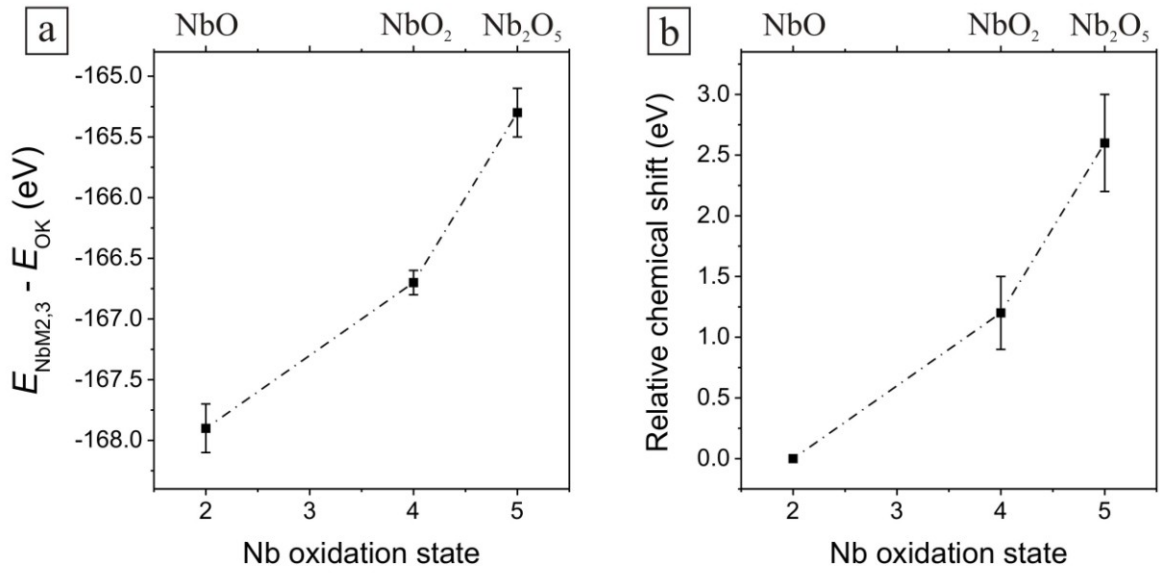

Fig. 4.4.2. Relative position of the Nb-$M_{2,3}$ edges with respect to that of the O-K edge $E_{NbM2,3} - E_{OK}$ **(a)** and corresponding relative chemical shift of the Nb- $M_{2,3}$ edges in relation to the O-K edge **(b)** as a function of the niobium oxidation state. The Measurements were performed on four NbO, six NbO_2 and four Nb_2O_5 spectra taken at the LEO 922 microscope. The relative position of the Nb-$M_{2,3}$ edges of NbO was chosen as a reference to calculate the relative chemical shifts. The accuracy of the values found for $E_{NbM2,3} - E_{OK}$ may depend on the reliability of the dispersion calibration of the detector system. Nonetheless, the values obtained for the relative chemical shift are excepted to be reliable and reproducible at other experimental setups.

To complete this analysis with NbO_2 data, the same data processing was also performed on four NbO, six NbO_2 and four Nb_2O_5 spectra, which were acquired with the LEO microscope at another position on the detector system than that used for the 24 NbO and Nb_2O_5 spectra analyzed above. The resulting $E_{NbM2,3} - E_{OK}$ energy differences and the corresponding relative chemical shifts are given in Fig. 4.4.2 as a function of the niobium oxidation state. Relatively to the O-K edge, the Nb-$M_{2,3}$ edges are found around $E_{NbM2,3} - E_{OK}$ = -167.9 ± 0.2 eV for NbO, -166.7 ± 0.1 eV for NbO_2, and -165.3 ± 0.2 eV for Nb_2O_5. Thus, the measurement of $E_{NbM2,3} - E_{OK}$ allows a clear distinction between the three reference oxides and should enable to characterize niobium oxides with unknown oxidation state. Moreover, the values found for NbO and Nb_2O_5 are approximately similar to that obtained above from the 12 NbO and

12 Nb_2O_5 spectra (-167.9 ± 0.1 eV and -165.2 ± 0.1 eV, respectively), indicating that in that particular case no strong discrepancy can be noticed in the dispersion calibration of the two different areas of the camera employed. The relative chemical shift measured between NbO and Nb_2O_5 amounts to about 2.6 ± 0.4 eV and is still in very good agreement with the values found above (2.4 ± 0.9 eV using the JEOL microscope and 2.7 ± 0.2 eV at the LEO), whereas a relative chemical shift of about 1.2 ± 0.3 eV to higher energies is obtained with increasing niobium oxidation state from +2 by NbO to +4 by NbO_2.

4.4.4 Normalized white-line intensities

Due to the inaccuracy of the background subtraction under the Nb-$M_{2,3}$ edges (see sections 4.2.4 and 4.3.2), the normalized Nb-$M_{2,3}$ white-line intensities were not investigated in the present work. The investigation method proposed by Pearson et al. (1988) was adapted by Olszta et al. (2006) in order to analyse the Nb-$M_{2,3}$ white-line intensities without background subtraction. In that case, the continuum signal chosen by the authors to normalize the white-line intensities has contributions from both the Nb-$M_{2,3}$ and Nb-$M_{4,5}$ edges. They found that the trend followed by the resulting normalized Nb-$M_{2,3}$ intensities with increasing 4d occupancy was in agreement with the atomic calculations for 4d transition metals without matrix-element corrections performed by Pearson et al. (1993). However, the obtained results did not allow a clear and direct differentiation between NbO_2 and Nb_2O_5. Due to the inaccurate background subtraction under the Nb-$M_{2,3}$ edges, the normalized Nb-$M_{2,3}$ white-line intensities were not investigated in the present work. In contrast, the procedure applied for analyzing the normalized Nb-$L_{2,3}$ white-line intensities (see section 4.2.7) enables to clearly distinguish between these two oxides (see Fig. 4.2.16): the relative deviation between the normalized intensities found for NbO_2 and Nb_2O_5 amounts to about 18%. This high sensitivity of the normalized intensities to the Nb 4d occupancy in the range of 0 (for Nb_2O_5) to 1 (for NbO_2) is of particular interest for the characterization of the niobium oxide layers in Nb-based capacitors, whose stoichiometry is expected to be close to Nb_2O_5.

In the present work, normalized Nb-$L_{2,3}$ white-line intensities I_{L3+L2} were experimentally determined for the Nb, NbO, NbO_2, and Nb_2O_5 reference materials (cf. section 4.2.7). If the normalized white-line intensity was a linear function of solely the 4d occupancy n_{4d} and was exactly zero in the hypothetical case where $n_{4d} = 10$ (no empty bound 4d states, i.e. no transition), the expected linear function would be:

$$I_{L3+L2} = K(1 - 0.10n_{4d}) ,$$

where K is a constant (Pearson et al., 1988; Pearson et al., 1993). The linear fit to the experimental data gave (Fig. 4.2.16):

$$I_{L3+L2} = 0.75 - 0.069n_{4d} = 0.75(1 - 0.092n_{4d}) ,$$

Taking into consideration that the measurements were only performed for 4d occupancies varying from 0 up to 4, the experimental and theoretical slopes (0.092 and 0.10, respectively)

are found to be in very good agreement. This indicates that the rough empirical method employed to separate the bound-state intensity from the continuum intensity works quite properly, even for Nb and NbO for which the positioning of the delimiting straight lines was not well-defined.
Only one spectrum was analyzed for each reference material, so that no statistic was performed. Nevertheless, the consistency of the obtained results indicates that the characterization method described in section 4.2.7 can easily be applied to the quantification of the 4d state occupancy of unknown niobium oxide phases, and thus to the determination of the niobium oxidation state. The method should efficiently be applicable to the investigation of nanoscale niobium oxide layers in Nb-based capacitor structures. Under the assumption that there is no dramatic change in the hybridization of the Nb 4d orbitals due to the different structure of the oxide layers (amorphous) and reference materials (crystalline) and that the oxide layers contain no other element except oxygen, whose presence could result in a charge transfer involving the Nb 4d states, the stoichiometry of the oxide layers can also be derived from the Nb 4d occupancy determined by the investigation of normalized Nb-$L_{2,3}$ white-line intensities.

4.4.5 Influence of the specimen thickness on quantitative EELS

The *k*-factors derived by means of the Nb-$M_{4,5}$ edges from 14 spectra taken on NbO at the LEO microscope are shown in Fig. 4.3.6 as a function of the relative thickness t/Λ of the measured specimen regions. The relative thickness ranges from about 0.4 to 0.6. In that range, it seems that the NbO *k*-factors increase with increasing t/Λ. In that particular case this trend can be interpreted by the weakness of the O-K signal measured for NbO. With increasing thickness the signal-to-noise and signal-to-background ratios of the weak O-K edge decrease and the background subtraction becomes more uncertain, so that the intensity measured after background subtraction under the O-K edge (I_{OK}) decreases relatively to that integrated under the more intense Nb-$M_{4,5}$ edges ($I_{NbM4,5}$). This leads to an increase of the *k*-factors, which is directly given by the $I_{NbM4,5}/I_{OK}$ intensity ratio for NbO.
In contrast, the *k*-factors determined at the LEO microscope from 25 NbO_2 and 14 Nb_2O_5 spectra seem to decrease with increasing relative thickness from 0.2 to 0.5 (Fig. 4.3.6). In that case, the O-K signal is more intense than that measured for NbO and, moreover, the spectra were recorded within a lower relative-thickness range compared to those taken on NbO, so that the signal-to-noise and signal-to-background ratios are better and the background-subtraction errors have less influence on the measured intensity ratios. The decrease of the *k*-factor with increasing relative thickness is even more clearly visible in Fig. 4.3.8a, showing the results obtained from 7 Nb_2O_5 spectra acquired at the VG microscope for t/Λ in the range of 0.14 to 0.66. This trend is attributed to the effects of multiple scattering, whose occurrence rises with increasing specimen thickness. As already mentioned in section 4.4.1, multiple scattering results in a redistribution of the intensity under a given edge, i.e. a certain proportion of the signal is “shifted” to higher energy losses by an amount of energy which depends generally on the plasmon energy. Thus, a large integration window ΔE generally

allows to minimize to some extent the effects of multiple scattering on the intensity measured under the edge, as the amount of signal shifted out of the integration window is reduced compared to the total intensity measured within the window. Furthermore, while determining the intensity ratio of two edges, the use of integration windows starting immediately at the edge onset and having the same width for both edges enables the multiple-scattering effects on the intensities of the two edges to compensate partly for each other (Egerton, 1986). However, this compensation is more efficient if the two edges have a similar shape. In the present case, the *k*-factors given in Figs. 4.3.6 and 4.3.8a were all derived by means of 70 eV wide integration windows starting at the very edge onset (see Fig. 4.3.2), but the O-K and Nb-$M_{4,5}$ edges present strongly different basic shapes. The O-K edge shows a sawtooth shape, whereas the Nb-$M_{4,5}$ edges are characterized by a delayed maximum. Hence, the strength of the multiple-scattering effects is not similar for both edges as a function of the energy loss above the edge onset. The maximum intensity of the O-K edge is typically located some 5 eV beyond the edge onset (see for instance Fig. 4.2.10 for the three reference oxides), so that the maximum amount of signal "shifted" due to multiple scattering is redistributed some 15 to 35 eV above the onset (for the three reference oxides, the broad plasmon shows an intense signal in an energy-loss range of about 10 eV to 30 eV as visible in Fig. 4.2.2). Thus the maximum influence of the multiple scattering is taken into consideration by the 70 eV wide integration window. Contrary, due to the delayed maximum of the Nb-$M_{4,5}$ edges, the maximum influence of the multiple scattering is in that case located at higher energy loss beyond the edge threshold and is not included in the integration window (the maximum intensity of the Nb-$M_{4,5}$ edges is more than 70 eV above the edge onset – see Fig. 4.2.4). Hence, the proportion of edge signal, which is redistributed out of the integration window as the sample thickness increases, is more important for the Nb-$M_{4,5}$ edges than in the case of the O-K edge, leading to a relative increase of I_{OK} with respect to $I_{NbM4,5}$. As the determined *k*-factors are proportional to the measured $I_{NbM4,5}/I_{OK}$ intensity ratios, this results in the trend observed for NbO_2 and Nb_2O_5, namely a decrease of the *k*-factors with increasing relative thickness. The *Fourier*-ratio deconvolution of the edges also enables to evaluate the effects of the specimen thickness. This procedure removes that signal from the edges which results from incident electrons involved in more than one inelastic scattering event. Since for the O-K signal the maximum influence of the multiple scattering is taken into account by the integration window, it strongly affects the intensity measured under the O-K edge. This can for instance be observed by analyzing one NbO_2 spectrum recorded from a specimen region with $t/\Lambda \sim 0.47$. Using 70 eV wide integration windows, deconvolution leads to a reduction of I_{OK} by about 22.5% whereas the decrease of $I_{NbM4,5}$ is of only 12.0%, yielding a 13.5% increase of the $I_{NbM4,5}/I_{OK}$ intensity ratio and thus of the *k*-factor. The single-scattering data obtained after deconvolution can be regarded as a resulting from an ideally thin specimen. Thus, the increase of the *k*-factor due to deconvolution is consistent with the observed increase of the *k*-factors with decreasing specimen thickness. Moreover, it can be noted that even at a relative thickness lower than 0.5 the effects of multiple scattering on quantitative EELS can be very strong. The seven Nb_2O_5 spectra recorded at the VG microscope were also deconvoluted by means of the *Fourier*-ratio method and the resulting *k*-factors are shown in Fig. 4.3.8a. The strength of the multiple-scattering effects can then be observed as a function

of the relative thickness by calculating the relative deviation between the *k*-factors determined for each spectrum with and without *Fourier*-ratio deconvolution (see Fig. 4.3.8b). The relative deviation is found around 2.1% at $t/\Lambda \sim 0.14$ and rises up to about 12.5% at $t/\Lambda \sim 0.66$, illustrating the intensification of the multiple-scattering effects on EELS quantification as the specimen thickness increases. On the whole, by averaging the *k*-factors determined from the seven spectra, a value $k_{NbM4,5\text{-}OK} = 13.77 \pm 0.88$ (±6.4%) was found without deconvolution, showing a relative deviation of 6.4% with respect to the mean value $k_{NbM4,5\text{-}OK/deconv} = 14.68 \pm 0.57$ (±3.9%) achieved after deconvolution (see section 4.3.6). Obviously, the strong influence of the specimen thickness can affect the precision of EELS quantification. This is pointed out by the fact that after a *Fourier*-ratio deconvolution of the data the standard deviation of the *k*-factors derived from the seven spectra amounts to only ± 3.9 %, whereas a larger value around ± 6.4 % was found by analyzing the spectra without correction for multiple scattering. Moreover, this clear influence of the deconvolution procedure on the precision of the resulting *k*-factor is one more argument proving that the measured decrease of the *k*-factor with increasing thickness is a real effect of the specimen thickness and not some kind of statistic error.

4.4.6 Precision of quantitative EELS

The following discussion is focused on the errors of the derived *k*-factors. We distinguish between the *precision* and *accuracy* of EELS quantification. Performing a set of repeated experimental measurements, the precision is given by the standard deviation of the results. Thus, it corresponds to the reproducibility of the measurement. It is often confused with the accuracy, which corresponds to the deviation between the mean value of the repeated measurements and the true value of the measured quantity, i.e. to the veracity of the measuring. The precision is mostly related to random (statistical) errors during the analysis, whereas the accuracy generally depends on systematic errors. Hence, high precision and high accuracy are not necessarily correlated and do not imply one another. But of course, both are required to get relevant results (see also, Bertoni & Verbeeck, 2008). The precision of EELS quantification is discussed in this section, whereas the next section will focus on the accuracy.

Three approaches to reduce the thickness-related errors

As mentioned in the previous section (4.4.5), the specimen thickness can strongly influence the measured *k*-factors and thus the precision of EELS quantification. Using the Nb-$M_{4,5}$ edges for quantification, two approaches were successfully used to improve the precision by limiting the influence of the thickness. The first one consists in limiting the relative-thickness range used for quantification. The standard deviation of the *k*-factor $k_{NbM4,5\text{-}OK}$ determined from 53 reference spectra acquired at the LEO microscope on specimen regions with a relative thickness t/Λ in the range of 0.21 to 0.57 amounts to about ±2.1% (see section 4.3.5 and Table 4.3.3). It is reduced to approximately ±1.8% by calculating the *k*-factor on the basis of only the 37 spectra recorded at t/Λ in the range of 0.3 to 0.5. The improvement in precision is even higher when the relative-thickness range initially considered is wider. Thus, the seven

Nb_2O_5 spectra taken at the VG microscope with t/Λ within 0.14 and 0.66 gave an error of ±6.4% for $k_{NbM4,5\text{-}OK}$, whereas the error is of only ±2.1% when only the four spectra with t/Λ in the range of 0.26 to 0.46 are analyzed.

The second approach enabling to reduce the thickness-related errors comprises the correction of the spectra for multiple-scattering effects via *Fourier*-ratio deconvolution. This method was applied to 25 NbO_2 spectra recorded at t/Λ in the range of 0.23 to 0.49 (LEO microscope) and allowed a decrease of the standard deviation of the $I_{NbM4,5}/I_{OK}$ intensity ratio from ±1.9% to ±1.5% (see section 4.3.5). As already pointed out in the previous section, the *Fourier*-ratio deconvolution of the seven Nb_2O_5 spectra taken at the VG microscope from specimen regions with strongly different relative thicknesses ($0.14 \leq t/\Lambda \leq 0.66$) even allowed a more impressive improvement of the precision of the resulting *k*-factor: ±3.9% after deconvolution compared to ±6.4% without deconvolution.

The two approaches, i.e. limitation of the relative-thickness range and deconvolution, were combined to analyse 28 reference spectra acquired at the LEO microscope from specimen regions with t/Λ between 0.3 and 0.49 (see section 4.3.5 and Table 4.3.3). The standard deviation while averaging the resulting *k*-factors is found as good as ±1.4%.

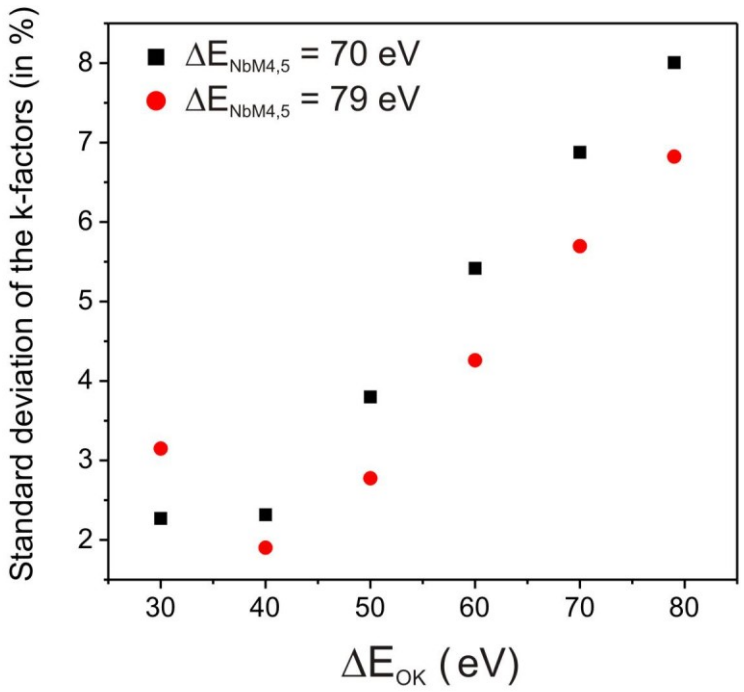

Fig. 4.4.3. Standard deviation of the *k*-factors determined from six Nb_2O_5 spectra as a function of the width of the integration window used to measure the intensity under the O-K edge (ΔE_{OK}). The *k*-factors were determined for $\Delta E_{NbM4,5}$ = 70 eV and 79 eV. The six Nb_2O_5 spectra were taken at the VG microscope from specimen regions with a relative thickness in the range of 0.14 to 0.66 (cf. Fig. 4.3.8a, the spectrum recorded at t/Λ = 0.21 was not included in the present analysis).

In addition, following the discussion conducted in the previous section (4.4.5), a third approach can be envisaged to limit the negative influence of the specimen thickness on the precision, when two edges presenting different basic shapes are used for quantification. In that

case, it was shown that the strength of the multiple-scattering effects is not similar for both edges as a function of the energy loss above the edge onset. Thus, the use of integration windows with different widths for the two edges could cancel the multiple-scattering effects when intensity ratios are determined. The smaller window should be used to integrate the intensity under the edge which shows the greater sensitivity to multiple scattering in the range of a few tens of eV above its onset. Hence, in the present case, the integration window under the O-K edge (ΔE_{OK}) should be smaller than that used to measure the Nb-$M_{4,5}$ intensity ($\Delta E_{NbM4,5}$). This method was tested on the Nb_2O_5 spectra recorded at the VG microscope. The *k*-factor derived - without *Fourier*-ratio deconvolution - from one spectrum recorded at $t/\Lambda = 0.21$ was found to diverge from the general trend observed as a function of the specimen thickness, namely a decrease of the *k*-factors with increasing relative thickness (see Fig. 4.3.8). For more clarity while investigating the influence of the use of different integration-window widths on the errors related to multiple-scattering, this spectrum was not included in the present test. The six remaining spectra originated from specimen regions with t/Λ in the range of 0.14 to 0.66 and led to $k_{NbM4,5\text{-}OK} = 13.83 \pm 0.95$ (±6.9%) by means of 70 eV wide integration windows for both the O-K and Nb-$M_{4,5}$ edges. To examine the effects of integration windows differing in width $\Delta E_{NbM4,5}$ was kept constant at 70 eV, whereas ΔE_{OK} was varied between 30 eV and 79 eV. As usual, the lower limit of each integration window was positioned at the very edge onset. The percental standard deviation of the *k*-factors resulting from the six spectra is shown in Fig. 4.4.3 as a function of ΔE_{OK}. A clear decrease of the standard deviation can be observed when ΔE_{OK} is smaller than $\Delta E_{NbM4,5}$, indicating an important improvement of the precision of the quantification procedure. For $\Delta E_{OK} = 40$ eV and 30 eV the standard deviation reaches a similar value of about ±2.3%, indicating that an optimum is probably present in-between. The same analysis was performed for $\Delta E_{NbM4,5} = 79$ eV (due to carbon contamination a higher value could not be used) and the results are also visible in Fig. 4.4.3. In that case, the presence of an optimum for ΔE_{OK} between 30 eV and 50 eV is well-defined. For $\Delta E_{OK} = 40$ eV the standard deviation amounts to about ±1.9%, which is even better than the best value found with $\Delta E_{NbM4,5} = 70$ eV (±2.3%). For comparison, the *Fourier*-ratio deconvolution of the six spectra leads to a standard deviation of ±3.6% for the resulting *k*-factors determined by means of 70 eV wide integration windows. Hence, in the present case the method described above seems to give better results than deconvolution, maybe because the optimum ΔE_{OK} also takes into consideration other errors than just those related to multiple scattering, like for instance errors in the background subtraction under edges acquired at different relative thicknesses. This new approach can thus be applied as an alternative to deconvolution (or when for some reason or another deconvolution is not possible) to investigate spectra resulting from specimen regions with strongly different thicknesses. However, the use of integration windows as small as 30 or 40 eV amplifies the influence of ELNES on EELS quantification. In the present case it was shown that the ELNES of the O-K edge differs strongly between NbO, NbO_2 and Nb_2O_5 (see Figs. 4.2.10 and 4.2.11). Moreover, the strength of the background-subtraction errors is likely to differ strongly between the different stoichiometries, when a wide specimen-thickness range is considered. Thus, in the case of Nb_2O_5 the optimum values found for ΔE_{OK} and

$\Delta E_{NbM4,5}$ and the resulting *k*-factor are probably not ideal to analyze NbO and NbO_2 with high precision and accuracy. With other words, in a system of two elements *a* and *b* giving rise to two edges with different shapes, the existence of integration windows leading to a good compromise between the errors related to ELNES, background subtraction, and multiple scattering is not assured for strongly different stoichiometries and specimen thicknesses. Nevertheless, by means of a *k*-factor derived from one single reference material, the method described above should in any case allow to analyze spectra recorded at different specimen thicknesses from a material whose stoichiometry is expected to be close to that of the reference. This method should then enable an optimum sensitivity for the investigation of the stoichiometric discrepancies between the examined material and the reference.

Comparison between the precisions achieved at the different microscopes: correlation with accuracy, energy dispersion, noise, and specimen thickness

While determining intensity ratios and *k*-factors, the precision achieved at the LEO microscope was generally better than that obtained at the VG and JEOL microscopes (see for instance Table 4.3.3). To explain this, it should first be noted that more spectra were acquired at the LEO microscope than at the two other instruments, enabling a better statistic. Using the Nb-$M_{2,3}$ edges for quantification, a *k*-factor $k_{NbM2,3\text{-}OK}$ was determined with a standard deviation of ±3.8% by analyzing 12 NbO and 12 Nb_2O_5 spectra (LEO microscope - see section 4.3.3). In contrast, a standard deviation of ± 7.0 % was obtained by averaging the data of only four NbO and four Nb_2O_5 spectra (JEOL microscope – see section 4.3.6 and Table 4.3.3). Using the Nb-$M_{4,5}$ edges to determine *k*-factors, 12 Nb_2O_5 spectra led to a standard deviation of ±1.6% (LEO microscope – see section 4.3.3) and seven Nb_2O_5 spectra to ± 6.4 % (VG microscope – see section 4.3.6).

The accuracy of EELS quantification can also influence the precision obtained while averaging *k*-factors determined from different reference materials, which can partly explain the poor standard deviation obtained with the JEOL microscope (± 7.0 % for $k_{NbM2,3\text{-}OK}$) compared to that with the LEO (±3.8%). Indeed, by means of the JEOL microscope, the relative deviation between the mean *k*-factor determined from the four NbO spectra ($k_{NbM2,3\text{-}OK}$ ~1.46) and that obtained with the four Nb_2O_5 spectra ($k_{NbM2,3\text{-}OK}$ ~1.38) amounts to approximately 5.6% (see section 4.3.6). For comparison, using the LEO microscope the mean *k*-factors resulting from 12 NbO spectra ($k_{NbM2,3\text{-}OK} = 1.30$) and 12 Nb_2O_5 spectra ($k_{NbM2,3\text{-}OK} = 1.32$) yield a relative deviation of only 1.5%. However, the influence of the accuracy is also observable on the results obtained at the LEO microscope, when NbO_2 data are included in the statistic. The 24 NbO and Nb_2O_5 spectra give a *k*-factor $k_{NbM2,3\text{-}OK} = 1.31 \pm 3.8\%$, whereas $k_{NbM2,3\text{-}OK} = 1.35 \pm 4.1\%$ is determined from 12 NbO_2 spectra (derived from the intensity ratio $I_{NbM4,5}/I_{OK} = 0.677 \pm 0.028$ (±4.1%) given in section 4.3.4). In that case, the relative deviation between the two *k*-factors amounts to about 3%, so that a deterioration of the standard deviation is observed by averaging the *k*-factors derived from all the 36 spectra: $k_{NbM2,3\text{-}OK} = 1.32 \pm 4.5\%$ (see section 4.3.4). Thus, errors originally related to the accuracy are projected on the precision.

In the case of the VG microscope, it should also be noted that the energy dispersion used to acquire the seven Nb_2O_5 spectra was about 0.5 eV per channel, whereas a dispersion of approximately 0.25 eV per channel was typically employed at the LEO microscope. A larger dispersion can amplify the statistical errors related to the positioning of the integration windows and can thus affect the precision. Moreover, quantitative EELS data are also influenced by such experimental parameters as primary electron energy, convergence and collection semi-angles, and measuring time (whose setting can be limited by contamination), which in relation to the detector system and the specimen thickness determine the intensity of the collected signal as well as its signal-to-noise and signal-to-background ratios. Especially at the VG microscope, the combination of these different parameters generally led to more noisy spectra compared to those taken with the LEO microscope.
However, the most important factor explaining the differences in the precision obtained at the different microscopes is again the specimen thickness. As discussed previously, the use of data resulting from large relative-thickness ranges deteriorates the precision of the quantification. In the present case, the 12 Nb_2O_5 spectra taken at the LEO microscope originated from specimen regions with a relative thickness in the range of 0.21 to 0.51, whereas a larger relative-thickness range of 0.14 to 0.66 is covered by the seven spectra recorded on the VG microscope. In addition, it was already pointed out that the analysis of only the four VG spectra with t/Λ in the range of 0.26 to 0.46 enables an important improvement of the standard deviation of the *k*-factor until ±2.1%. However, although in that case the range is smaller than that investigated at the LEO microscope, the standard deviation remains larger than the value found for the 12 reference spectra acquired at the LEO (± 1.6 %), showing that besides the specimen-thickness effects, the influence of the other above-mentioned factors on the precision is not insignificant. More generally, with increasing specimen thickness above 0.5 the signal-to-background and signal-to-noise ratios decline, making the background subtraction procedure and the localization of the edge onset more uncertain. Hence, independently from the multiple-scattering effects on the intensity of the analyzed edges, a deterioration of the quantification precision is expected at large thicknesses, which can explicate why in spite of the use of *Fourier*-ratio deconvolution a poor standard deviation is obtained at the JEOL microscope (±7.0%). Indeed, by means of the JEOL, the eight NbO and Nb_2O_5 spectra were taken at very large relative thicknesses between 0.46 and 1.40 (mean t/Λ around 0.96), whereas the 24 NbO and Nb_2O_5 spectra acquired at the LEO microscope resulted from specimen regions with t/Λ in the range of 0.21 to 0.57 (mean t/Λ around 0.43).

Comparison between the precisions achieved by means of the Nb-$M_{2,3}$ and Nb-$M_{4,5}$ edges: correlation with background subtraction and integration-window positioning

By means of the LEO microscope, the same 12 NbO, 12 NbO_2 and 12 Nb_2O_5 spectra which were analyzed by using the Nb-$M_{2,3}$ edges were also investigated via the Nb-$M_{4,5}$ edges (see sections 4.3.2, 4.3.3 and 4.3.4). For each reference oxide the Nb-$M_{4,5}$ edges yielded a more precise quantification than the Nb-$M_{2,3}$ edges. By averaging the *k*-factors determined from all the 36 spectra, the standard deviation amounts to approximately ± 2.1 % in the case of Nb-$M_{4,5}$ edges, whereas it is about ± 4.5 % for Nb-$M_{2,3}$ ones. To explain this difference it

should first be recalled that by means of the Nb-$M_{2,3}$ edges the agreement between the *k*-factor determined from the 12 NbO_2 spectra and that obtained with the 24 NbO and Nb_2O_5 spectra was not optimal (see above the remark concerning the accuracy and section 4.3.4). In addition, the difference can also be caused by the effect of fine structures, which is much stronger in the case of the Nb-$M_{2,3}$ white lines. However, the background fitting and subtraction procedures in relation to the specific Nb edge seem to be the most important factor, explaining the difference observed in the accuracy.

The influence of the background subtraction on the measured I_{NbM}/I_{OK} intensity ratios and the calculated *k*-factors will now be discussed in more detail. This decisive step is based on the assumption that the background has the same energy dependence after the edge onset as before. However, the width and the position of the background-fitting window preceding the ionization edge as well as the choice of the fitting function may lead to different results for the intensity measured under the edge, without any reliable way to check the physical pertinence of the obtained extrapolation under the edge (see for instance the different $I_{NbM4,5}/I_{OK}$ intensity ratios found by means of different fitting windows for the background extrapolation under the O-K edge of one NbO spectrum in Tables 4.3.1 and 4.3.2). This operation becomes even more uncertain when the quantified edge is close to another ionization edge occurring at lower energy, in which case the background may change its form in the fitting or integration regions. This is unfortunately the case for the Nb-$M_{2,3}$ edges, lying on the tail of the preceding Nb-$M_{4,5}$ edge that can explain the above-mentioned difference in the standard deviation (see sections 4.2.4 and 4.3.2). Indeed, as visible in Fig. 4.2.6a, the energy dependency of the background preceding the onset of the Nb-$M_{2,3}$ edges is erratic, so that a minimal variation in the width or position of the background fitting region can lead to dramatically different results for the intensity of the background-subtracted signal. To limit the imprecision and the inaccuracy of the subtraction procedure a condition was imposed on the background extrapolation: the intensity in front of the O-K edge should be close to zero after background subtraction. Since the Nb-$M_{2,3}$ edges (and the Nb-M_1 edge around 368 eV) are not particularly intense (except for the white lines) and since the distance between the onsets of the Nb-$M_{2,3}$ and O-K edges is quite important (more than 160 eV), this condition makes sense. To fulfil it, exponential functions were found to be more adequate than the commonly assumed power-law model that tends to lead to an unphysical background-subtracted Nb-$M_{2,3}$ signal with strongly negative intensities in front of the O-K onset. However, in spite of this condition, the background extrapolation clearly remains the weak point in terms of precision when EELS quantification is performed by means of the Nb-$M_{2,3}$ edges.

The positioning of the integration window can also contribute to the total random error of the quantification method. In the present case, it should more particularly affect the precision of the quantification using Nb-$M_{4,5}$ edges. Indeed, owing to the delayed-maximum shape of the Nb-$M_{4,5}$ edges, it is difficult to localize their onset with precision and a weak variation in the position of the integration window can lead to a significant difference in the measured $I_{NbM4,5}$ intensities. Nevertheless, this error is minimized by the choice of a large integration window. Hence, using a 70 eV integration window under the Nb-$M_{4,5}$ edges to analyse a NbO spectrum, a shift of the window of only 1.2 eV to higher energies was found to result in a relative increase of the $I_{NbM4,5}/I_{OK}$ intensity ratio of 3.5% (see section 4.3.2). However,

considering the total error obtained for the Nb-$M_{4,5}$ edges (± 2.1%) in the present work, the effects of these uncertainties seem to remain reasonably low when a 70 eV wide integration window is employed (the standard deviation even falls to ±1.4% after a reduction of the thickness-related errors – see above).

Comparison between the precisions achieved for different materials: correlation with background subtraction, signal intensity, Nb-M_1, and TEM-sample preparation

The precision of EELS quantification also depends on the investigated material. Comparing the three reference oxides, the standard deviation of the I_{NbM}/I_{OK} intensity ratios (which is equivalent to that of the corresponding *k*-factors) becomes larger with increasing C_{Nb}/C_O atomic concentration ratio from Nb_2O_5, NbO_2 to NbO. This was observed by using 70 eV wide integration windows to analyze the 12 NbO, 12 NbO_2, and 12 Nb_2O_5 spectra taken at the LEO microscope (see section 4.3.2). When using the Nb-$M_{2,3}$ edges the standard deviation amounts to ±3.3% in the case of Nb_2O_5, but ±4.4% for NbO_2 and ±5.5% for NbO. Quantification on the basis of the Nb-$M_{4,5}$ edges yields a standard deviation of ±1.6%, ±1.9%, and ±2.6% for Nb_2O_5, NbO_2 and NbO, respectively.

The difference in the standard deviation between NbO_2 and Nb_2O_5 is more pronounced when Nb-$M_{2,3}$ edges are used (relative deviation of 29% using the Nb-$M_{2,3}$ edges, 17% in the case of the Nb-$M_{4,5}$ edges). This can partly be explained by the errors in background subtraction under the Nb-$M_{2,3}$ edges, which are particularly important in the case of NbO_2 owing to the specific shape of the energy-loss region preceding the Nb-$M_{2,3}$ onset (see Fig. 4.2.6a and section 4.4.7). The errors in the background subtraction under the Nb-$M_{2,3}$ edges are also expected to be higher for NbO compared to Nb_2O_5 because of the more intense preceding Nb-$M_{4,5}$ edges due to the element ratio $C_{Nb}/C_O = 1$. Hence, these errors can also contribute to the large standard deviation obtained for $I_{NbM2,3}/I_{OK}$ in the case of NbO.

More generally, using either the Nb-$M_{4,5}$ or the Nb-$M_{2,3}$ edges, the differences observed in the standard deviation of the different oxides are mainly attributed to the comparably weak O-K intensity. If the Nb-$M_{4,5}$ edges and the O-K edge are used for quantification, the latter has to be recorded simultaneously with the intense Nb-$M_{4,5}$ edges which limits the absolute O-K edge signal, especially in the case of NbO. The relatively weak O-K signal thus degrades the counting statistics for increasing C_{Nb}/C_O. In addition, compared to the NbO_2 and Nb_2O_5 spectra, those of NbO were on an average acquired from specimen regions with larger relative thicknesses in the range of 0.4 to 0.6, which limits even more the measured O-K intensity. In the present case, the same spectra quantified using the Nb-$M_{4,5}$ edges were also analyzed by means of the Nb-$M_{2,3}$ edges, leading to the same influence of the intensity of the O-K edge on the precision of the $I_{NbM2,3}/I_{OK}$ intensity ratios. However, even if investigations by means of Nb-$M_{2,3}$ edges were performed on spectra acquired at a higher energy loss above the Nb-$M_{4,5}$ onset, the fact that the Nb-$M_{2,3}$ edges directly lie on the intense tail of the Nb-$M_{4,5}$ edges would also limit the maximum measurable O-K edge intensity and thus affect the quantification precision.

Moreover, errors related to the O-K signal at a high C_{Nb}/C_O ratio may be amplified by background-subtraction errors due to the presence of the Nb-M_1 edge in front of the O-K edge. However, even in the case of a high $C_{Nb}/C_O = 1$ the error induced by the M_1 edge

remains relatively small as shown in section 4.3.2 by varying the size and the position of the fitting window for background extrapolation under the O-K edge of one NbO spectrum (Tables 4.3.1 and 4.3.2). Nevertheless, it should be noted that the tested NbO spectrum was recorded on a specimen region with a relative thickness around 0.49. The random errors of the background subtraction under a weak edge may increase dramatically at larger thicknesses.
Hence, when using the Nb-$M_{2,3}$ edges to determine *k*-factors, the four Nb_2O_5 and four NbO spectra taken at the JEOL microscope led to standard deviations around ±2.9% and ±8.9%, respectively (see section 4.3.6). In that case, the very high error obtained for NbO can partly be attributed to the combination of the weak O-K signal with the effects of large specimen thicknesses, resulting in low signal-to-background and signal-to-noise ratios. Indeed, the spectra acquired by means of the JEOL microscope results from large relative thicknesses ranging from 0.46 to 1.40.
Finally, local concentration fluctuations can be a further contribution to a larger EELS quantification error for NbO. Generally, some deviation from the nominal chemical composition caused by differential sputtering accompanied by amorphization during the final ion-thinning stage of the TEM-sample preparation cannot be excluded completely. In the investigated samples a few amorphous regions were observed, especially in thinnest zones of NbO. Of course, before EELS the regions chosen for analysis were checked by electron diffraction with respect to the degree of amorphization. However, the contribution of some remaining amorphous material in surface-near zones to the recorded EELS signal is still possible. Moreover, the sample orientation may also influence the EELS quantification, one effect which was not considered here.

4.4.7 Accuracy of quantitative EELS

EELS quantification is based on the assumption that the number of counts under an inner-shell ionization edge is proportional to the number of atoms presents (Egerton, 1986). Hence, two main factors can strongly influence the accuracy of EELS quantification: the pertinence of the assumption and the ability to measure the exact intensity under an ionization edge. The rightness of the assumption depends on the strength of the ELNES, whose related intensity is not a function of only the element content in the specimen but, in the first instance, determined by the structural and chemical environment of the ionized atom. The possibility of extracting correctly the signal of interest from the spectrum is correlated to the accuracy of the background-subtraction procedure (in fact, in order to perform accurate EELS quantification, it is not even necessary to apply a perfectly accurate background-subtraction procedure; it would be sufficient if the systematic errors of the background subtraction had similar effects on the intensities measured under a given edge for the different investigated materials). On the one hand, the fine-structure effects are usually only significant in a 30 to 50 eV wide region beyond the edge onset. On the other hand, the background-extrapolation errors generally increase with increasing energy loss well above the edge onset (Egerton, 1978). Hence, depending on the analyzed material system and on the edges used for quantification, the pertinent choice of the integration windows used to measure the intensities of the edges

may lead the systematic errors related to the ELNES to compensate for those resulting from the background subtraction when different stoichiometries are investigated. Thus, in spite of the different errors, the quantification procedure could be accurate.

Background-related vs. ELNES-related errors: correlation with the integration-window width resulting in accurate quantification by means of the Nb-$M_{4,5}$ edges

In the present work, the very edge onset was systematically chosen as the lower limit of the integration window under each edge. This choice was made in order to maximize the number of counts collected in the case of the O-K and Nb-$M_{2,3}$ edges, to take the chemical shifts into account, and to avoid large background-subtraction errors at high energy losses above the edge onset. Moreover, in this way, the multiple-scattering effects on the measured intensities can roughly compensate for each other while calculating intensity ratios (see section 4.4.5). In order to find a compromise between the solid-state effects and the backgrounds-related errors, *k*-factors were derived from 12 NbO and 12 Nb_2O_5 spectra for different widths of the integration window ΔE (LEO microscope - see section 4.3.3). For accurate quantification, the analysis of different reference oxides should results in similar *k*-factors. Thus, by means of Nb-$M_{4,5}$ edges for quantification, the use of a 70 eV wide integration window appears to be pertinent (see Fig. 4.3.4b): the relative deviation between the mean *k*-factor determined from NbO and that found for Nb_2O_5 amounts to only 0.6%. Of course, this good agreement does not mean that the backgrounds under the different edges were properly fitted and removed. In particular, the background subtraction under the O-K edge can be disturbed by the presence of the preceding Nb-M_1 edge (see Fig. 4.2.9). It was already discussed that the Nb-M_1 edge does not dramatically affect the precision of the intensity ratios measured for the different reference materials (see sections 4.3.2 and 4.4.6). Nevertheless, systematic errors in the background subtraction under the O-K edge may still be a problem while comparing quantitative results from different oxides, if their effects differ in strength as a function of the stoichiometry. In fact, the difference between the O-K ELNES of NbO and Nb_2O_5 is so strong (see Fig. 4.2.10 and 4.2.11b) that it probably introduces a non-negligible error in the quantification procedure. Hence, the fact that the *k*-factors derived from NbO and Nb_2O_5 coincide well at ΔE = 70 eV - in contrast to the poorer agreement at smaller and larger ΔE values (see Fig. 4.3.4b) - implies that there must be errors in the background-subtraction procedure which cancel those related to ELNES for this particular ΔE. As discussed above, these errors are expected to concern principally the background extrapolation under the O-K edge. Nonetheless, they can also partly result from the modelling of the background under the Nb-$M_{4,5}$ edges. In addition, the strong divergence observed between the *k*-factors of the two reference oxides with increasing integration-window width above 70 eV (see Fig. 4.3.4b) indicates that at high energy losses above the onsets of the edges the systematic errors of the background-subtraction procedures are not of the same order of magnitude for NbO and Nb_2O_5.

In any case, the analysis of a third reference niobium oxide, namely NbO_2, enables to further test the accuracy of the quantification procedure. Using ΔE = 70 eV, 12 NbO_2 reference spectra were quantified by means of the *k*-factor averaged from all the 24 NbO and Nb_2O_5 spectra, yielding a relative deviation between the resulting C_{Nb}/C_O atomic concentration ratio (~ 0.503) and the expected nominal value (0.500) for NbO_2 of only 0.6% (see section 4.3.4).

Hence, in spite of the ELNES- and background-related errors, the very good agreement between the quantitative results obtained from the three reference oxides demonstrates that the EELS quantification procedure works in that case accurately by means of a 70 eV wide integration window. Moreover, the three reference oxides strongly differ in stoichiometry. In spite of these differences, each edge (Nb-$M_{4,5}$ or O-K) could be analyzed by means of background-fitting windows, which were similar in width and in position for all the three reference oxides (see section 4.3.2). Thus, no erratic variation of the shape of the energy-loss regions where the backgrounds are fitted is expected for stoichiometries between those of the reference oxides, and the same background fitting windows should be applicable. Hence, using ΔE = 70 eV, accurate results are expected for the quantification of any niobium oxide whose C_{Nb}/C_O atomic concentration ratio is in the large range from 0.4 (Nb_2O_5) to 1 (NbO).
A quantification test performed on NbO_2 by means of *k*-factors derived from NbO and Nb_2O_5 even led to more accurate results when only spectra taken from specimen regions with t/λ in the range of 0.3 to 0.5 were analyzed: the relative deviation between the measured (0.502) and nominal (0.500) C_{Nb}/C_O atomic concentration ratios is in that case only 0.4% (see section 4.3.5). However, the very low difference between the value (0.502) found here for C_{Nb}/C_O and that (0.503) achieved without taking care of the specimen thickness is not enough significant to be interpreted as an effect of the thickness. In addition, the effects of the systematic errors related to the specimen thickness are expected to be of similar importance for all the oxides (except for the effects on the O-K intensity of NbO at a large relative thickness above 0.5, which may differ from those occurring for the O-K signal of NbO_2 and Nb_2O_5 – see section 4.4.5). Thus, if one uses *k*-factors determined for a particular relative- thickness range to quantify spectra taken in that range, the width of the range and the magnitude of its limits should influence the precision of the quantification (see section 4.4.6), but not necessarily its accuracy.
Some of the reference spectra taken at the LEO microscope were also analyzed to determine k-factors after a correction of the Nb-$M_{4,5}$ and O-K edges for multiple scattering (see section 4.3.5). No quantification test could be performed on the deconvoluted data to check whether a 70 eV wide integration window still enables an optimum quantification accuracy in that case. However, ΔE = 70 eV was found to deliver accurate EELS quantification by analyzing spectra that were recorded at strongly different relative-thicknesses in the range from 0.21 to 0.57 and had thus suffered multiple-scattering effects of different strength. Hence, in the present work it is assumed that ΔE = 70 eV is still a good choice to quantify spectra corrected for the effects of multiple scattering.
Even if all the errors cannot clearly be identified and evaluated, obviously, ΔE = 70 eV is a good compromise between these errors, and can pragmatically be employed to analyze unknown niobium oxides by means of the Nb-$M_{4,5}$ edges at the LEO microscope.

Alternative quantification formalism

However, depending on the investigated material system and on the used edges, there is no assurance for the existence of an optimum integration window leading to a good agreement between the *k*-factors derived from two reference materials differing in stoichiometry. More generally, it is also possible that for one reason or another the maximum width of the

integration window under one of the edges is limited (for instance due to the presence of an other edge at a higher energy loss or due to a too small energy dispersion of the recording system), so that the optimum ΔE cannot be reached. Nonetheless, in such cases one can still try to use the data obtained from two reference materials to perform accurate quantification, and the investigation of the niobium oxides by means of the O-K and Nb-$M_{4,5}$ edges provides an interesting example of what can be done. In the case of 40 eV wide integration windows, the *k*-factors derived from the 12 NbO and 12 Nb_2O_5 spectra were not consistent with one another (see Fig. 4.3.4b): $k_{NbM4,5\text{-}OK} = 4.50 \pm 0.17$ for NbO and $k_{NbM4,5\text{-}OK} = 5.00 \pm 0.08$ in the case of Nb_2O_5 (corresponding to a relative deviation of 10.5% mainly attributed to ELNES-related errors). Thus, the *k*-factor obtained by analyzing Nb_2O_5 cannot be used to quantify NbO and vice versa. There is no direct proportionality between the measured $I_{NbM4,5}/I_{OK}$ intensity ratios and the C_{Nb}/C_O atomic concentration ratios. Nonetheless, some distinctive trends were observed in the evolution of the ELNES of the Nb-$M_{4,5}$ and O-K edges with increasing niobium oxidation state from +2 by NbO to +5 by Nb_2O_5 (see sections 4.2.3, 4.2.6, and 4.4.2) as well as in the evolution of the intensity of the Nb-M_1 edge which may influence the slope of the background preceding the O-K edge onset (see sections 4.2.5, 4.3.2 and the discussion above). Thus, in a first approximation it can be supposed that for C_{Nb}/C_O in the range of 0.4 (Nb_2O_5) to 1 (NbO) the strength of the systematic errors being responsible for the inaccuracy of the quantification varies quite linearly with stoichiometry, and consequently that there is still some kind of linear relationship between $I_{NbM4,5}/I_{OK}$ and C_{Nb}/C_O. The error-free quantification equation (4.3.1) can then be adapted by replacing the ideal *k*-factor by a constant K_{Er} and by introducing an error parameter *Er*:

$$\frac{C_{Nb}}{C_O} = \frac{1}{K_{Er}(E_0,\beta,\alpha,\Delta E)} \cdot \frac{I_{NbM4,5}(E_0,\beta,\alpha,\Delta E)}{I_{OK}(E_0,\beta,\alpha,\Delta E)} + Er(E_0,\beta,\alpha,\Delta E) \qquad (4.4.1).$$

Leaving the precision aside to focus on the accuracy, the averaged intensity ratios derived from the 12 NbO (4.50) and 12 Nb_2O_5 (2.00) reference spectra are used to determine the two unknown constants, leading to $K_{Er} \sim 4.17$ and $Er \sim -0.080$ for the used experimental parameters (LEO 922 microscope: $E_0 = 200$ keV, $\beta = 12.3$ mrad, $\alpha = 11.2$ mrad, ΔE = 40 eV). A quantification test can now be performed on NbO_2. The quantification of 12 NbO_2 spectra resulting in a mean $I_{NbM4,5}/I_{OK}$ intensity ratio of 2.42 yields $C_{Nb}/C_O \sim 0.538$ by means of the *k*-factor derived from NbO (4.50). For the *k*-factor obtained from Nb_2O_5 (5.00) $C_{Nb}/C_O \sim 0.484$ is found, whereas C_{Nb}/C_O amounts to about 0.509 when the *k*-factor averaged from all the 24 NbO and Nb_2O_5 spectra (4.75) is used. Finally, $C_{Nb}/C_O \sim 0.500$ is found using Eqn. (4.4.1). Since the nominal value for NbO_2 is $C_{Nb}/C_O = 0.500$, the use of Eqn. (4.4.1) clearly allows a much better accuracy in that case than quantification by means of classical *k*-factors derived from Eqn. (4.3.1). The value found with the mean *k*-factor resulting from both NbO and Nb_2O_5 reference spectra is not very distant from the nominal one (relative deviation of about 1.8% between 0.509 and 0.500), but this *k*-factor can neither be used to accurately quantify NbO (yields $C_{Nb}/C_O \sim 0.947$ instead of 1.000) nor to analyse Nb_2O_5 (yields $C_{Nb}/C_O \sim 0.421$ instead of 0.400) whereas the use of Eqn. (4.4.1) with $K_{Er} \sim 4.17$ and $Er \sim -0.080$ should enable a quite accurate quantification for C_{Nb}/C_O in the whole range of 0.4 to 1. Hence, this pragmatic adaptation of the classical EELS quantification procedure gives

very good results in the present case and may be useful to investigate other material system for which no optimum ΔE can be found.

Limitation of the accuracy achieved using the Nb-$M_{2,3}$ edges

The fact that the *k*-factors derived from two different reference oxides are found to be in good agreement does not mean that they can be used to quantify accurately any oxide with an in-between stoichiometry. The *k*-factors derived from the 12 NbO and the 12 Nb_2O_5 spectra by means of the Nb-$M_{2,3}$ edges are quite consistent with each other when a 50 eV wide integration window is used (LEO microscope, see Fig. 4.3.4a): a relative deviation of only 1.5% is achieved between the two mean *k*-factors. Nevertheless, while using the *k*-factor averaged from all the 24 NbO and Nb_2O_5 spectra to quantify 12 NbO_2 spectra, the relative deviation between the calculated C_{Nb}/C_O value (0.517) and the nominal value of 0.500 is as high as 3.3% (see section 4.3.4). Obviously, the compromise regarding errors arising from fine-structure and background contributions that was achieved with a 50 eV wide integration window for NbO and Nb_2O_5 is not optimal in the case of NbO_2. This is probably related to the errors of the background subtraction under the Nb-$M_{2,3}$ edges. It was already noticed that the method used to extrapolate the background under the Nb-$M_{2,3}$ edges presumably introduces some systematic errors in the intensities measured after background subtraction (see section 4.3.2). Unfortunately, the shape of the background preceding the Nb-$M_{2,3}$ edges onset is strongly different for NbO, NbO_2 and Nb_2O_5 (see Fig. 4.2.6a), so that the conditions under which the background subtraction under the Nb-$M_{2,3}$ edges can be performed for NbO and Nb_2O_5 differ from those existing for NbO_2. This probably leads to systematic errors of slightly different strength for NbO_2 in comparison to NbO and Nb_2O_5. In order to get an intensity close to zero in front of the O-K edge onset after background subtraction under the Nb-$M_{2,3}$ edges (see section 4.3.2), the background-fitting window applied for NbO_2 was typically 5 to 10 eV wide and ended 10 to 12 eV prior to the Nb-$M_{2,3}$ onset. The range of 10 eV that precedes the Nb-$M_{2,3}$ edges onset belongs to the background. However, after background subtraction, a positive intensity is observed in that range (see for instance the NbO_2 spectrum in Fig. 4.3.3). Hence, the intensity integrated under the Nb-$M_{2,3}$ edges was probably overestimated in comparison to that measured after different background subtraction for NbO and Nb_2O_5, yielding a higher C_{Nb}/C_O atomic concentration ratio than expected when NbO_2 is quantified by a *k*-factor resulting from NbO and Nb_2O_5. However, considering the precision of the quantification, the value achieved in that case for C_{Nb}/C_O (0.517 ± 0.029) is still consistent with NbO_2 (nominal $C_{Nb}/C_O = 0.5$).

Limitation of the accuracy by the precision in case of poor statistic

In addition, it can also be noted that the accuracy obviously depends on the precision of the quantification procedure when a single spectrum is analyzed. This was illustrated in section 4.3.4 by the quantification test performed on NbO_2 using the *k*-factor determined from 24 NbO and Nb_2O_5 spectra by means of the Nb-$M_{2,3}$ edges. A single NbO_2 spectrum was firstly investigated, leading to an atomic concentration ratio C_{Nb}/C_O of 0.541 ± 0.021, i.e. to a large relative deviation of 7.9% with respect to the nominal value (0.500). Nevertheless, in that case this spectrum was not particularly representative for the 11 further analyzed NbO_2 spectra.

The quantification of all the 12 NbO_2 spectra resulted in $C_{Nb}/C_O = 0.517 \pm 0.029$, which shows a much smaller relative deviation of about 3.3% from the nominal value. This demonstrates the importance of investigating numerous spectra (as much as possible) to achieve the highest accuracy of the quantification procedure. Even by means of the Nb-$M_{4,5}$ edges, which led to particularly accurate results (see above), the good but not perfect precision of ± 2.8% achieved by quantifying 12 NbO_2 spectra via a *k*-factor derived from 24 NbO and Nb_2O_5 spectra implies that all the individual measurements are not identically accurate (see section 4.3.4).

Quantification by calculated partial cross-sections

The above discussion showed that depending on the investigated material system, there may be several accurate ways to pragmatically perform experimental EELS quantification. The different tests also showed the great advantage of analyzing several reference materials to investigate and optimize the accuracy. In the present case, the use of experimental *k*-factors derived by means of the Nb-$M_{4,5}$ edges yielded a very good accuracy. In contrast, the use of theoretical cross sections gave strongly inaccurate results for EELS quantification by means of the O-K and Nb-$M_{4,5}$ edges (see section 4.3.4). One NbO_2 spectrum, yielding a representative $I_{NbM4,5}/I_{OK}$ intensity ratio, was analyzed by the *Hartree-Slater* model (Leapman et al., 1980; Rez, 1982; Ahn & Rez, 1985) using different widths of the integration window ΔE. This resulted in strongly underestimated C_{Nb}/C_O atomic concentration ratios. Nonetheless, with increasing ΔE the obtained values were found to get closer to the nominal one (see Fig. 4.3.5). Hence, in that case the increase of the background-extrapolation errors at large ΔE seems to be compensated by a decrease of the very intense errors related to the calculation of theoretical cross-sections. Indeed, Rez (1982) and Ahn & Rez (1985) showed that the intensity of the $M_{4,5}$ edges of the elements with an atomic number *Z* in the range of 37 to 53 is strongly overestimated by the *Hartree-Slater* model. But this overestimation of the experimental value tends to decrease with increasing ΔE. However, in the present case, even for an integration window as large as 125 eV, the relative deviation between the determined C_{Nb}/C_O (0.341) and its nominal value for NbO_2 (0.500) remained very high at 37.8%. This difference reflects a large overestimation of the theoretical *k*-factor given by the calculated $\sigma_{NbM4,5}/\sigma_{OK}$ partial cross-section ratio in comparison to the experimental *k*-factor resulting from the measured $I_{NbM4,5}/I_{OK}$ intensity ratio. Such distinct discrepancies were already reported in the literature (Hofer, 1991; Hofer & Kothleitner, 1993; Hofer & Kothleitner, 1996; Fix et al., 2007), so that compared to standardless analysis based on theoretical cross sections the use of reference materials is recommended for accurate quantification, particularly when M edges have to be quantified. For instance, the theoretical ratios between L or M cross sections and the O-K cross section were compared by Auerhammer et al. (1989) with experimental ratios. The experimental ratios were available for $L_{2,3}$ edges of elements $13 \leq Z \leq 30$ and for $M_{4,5}$ edges of elements $38 \leq Z \leq 74$ from Hofer et al (Hofer et al., 1988; Hofer & Golob, 1988). The theoretical ratios were taken from Ahn and Rez (1985). Auerhammer et al. (1989) noticed that the theoretical cross-section ratios, which were calculated via the *Hartree-Slater* model, exceed the experimental ratios in almost all cases by

5% to 50%, but that both ratios approach each other for larger integration windows. In particular, an experimental *k*-factor of ~ 8.35 was measured for Nb_2O_5 for ΔE = 50 eV by Hofer et al. (1988) for E_0 = 120 keV, β = 5.9 mrad, α = 2.4 mrad, yielding a relative deviation of about 70 % from the theoretical value $\sigma_{NbM4,5}/\sigma_{OK}$ = 17.3 given by Ahn and Rez (1985). For ΔE = 100 eV, the experimental and theoretical ratios amount to about 17.9 and 28.3, respectively, resulting in a relative deviation of 45%. Hence, these observations are in agreement with the results obtained from NbO_2 in the present work. In contrast, Olszta et al. (2006) found a reasonable agreement between experimental and theoretical *k*-factors for Nb oxides if cross-sections of the O-K edge are computed by the hydrogenic model (Egerton, 1979; Egerton, 1986) (the Nb-$M_{4,5}$ cross section is still calculated using the *Hartree-Slater* model). Their experimental *k*-factor (E_0 = 200 keV, β = 6.9 mrad, α = 2.5 mrad) was found to deviate by only 6 % from the theoretical one for ΔE =150 eV. In the present work, the energy dispersion used to acquire the analyzed NbO_2 spectrum limits the maximum width of the integration window to 125 eV (see section 4.3.4). Nonetheless, one representative Nb_2O_5 spectrum taken via a larger energy dispersion could be analyzed with ΔE = 150 eV (LEO 922 microscope: E_0 = 200 keV, β = 12.3 mrad, α = 11.2 mrad). Even when the O-K cross section is determined by the hydrogenic model, the relative deviation between the theoretical and experimental *k*-factors is still larger than 22%. The discrepancy observed with the results of Olszta et al. (2006) may partly result from the different experimental parameters α and β used. It may also be related to the method that the authors employed to extrapolate the background under the O-K edge. Under the assumption that the O-K edge can accurately be modelled by the hydrogenic model at energies far past the ELNES, they chose the background-fitting window so that the experimental spectrum matched the theoretical cross-section in the region ~750-800 eV. In any case, even with differences between theoretical and experimental *k*-factors as low as 6% (leading to 6% discrepancy between nominal and measured C_{Nb}/C_O while quantifying niobium-oxide spectra), quantification by means of theoretical cross sections is still much less accurate than the use of experimental *k*-factors. In the present work a relative deviation of only 0.6% was achieved between the *k*-factors derived from NbO and Nb_2O_5, and the use of the *k*-factor averaged from measurements on both NbO and Nb_2O_5 to quantify NbO_2 spectra also led to a 0.6% relative deviation between the measured C_{Nb}/C_O and its nominal value (see above and sections 4.3.3 and 4.3.4).

In the present work, some attempts were also made to quantify reference niobium-oxide spectra by means of the EELSMODEL software developed by J. Verbeeck (Verbeeck, 2002; Verbeeck & Van Aert, 2004). However, this analysis, when it is done without the use of oxidic standards, also requires theoretical cross sections for M-edges, leading in the present case to inaccurate atomic concentration ratios. However, more generally, the model-based quantification approach implemented in the program EELSMODEL enables a more accurate quantification by means of K- and L-edges than conventional quantification procedures making use of theoretical cross-sections (Bertoni & Verbeeck, 2008).

Influence of the specimen orientation

Finally, it should be noted that the specimen orientation may also affect the accuracy of EELS quantification by introducing systematic errors if crystalline material is analyzed (Egerton 1978; Egerton, 1986; Bertoni & Verbeeck 2008). Hence, the averaging of random orientations could also affect the precision. This effect was not investigated in the present work. However, the specimens were preferably oriented far away from zone axes, which should minimize the influence of the orientation. By doing so, the good precision and accuracy achieved in the present work indicates that the effects of orientation-related errors remain reasonably low.

4.4.8 The use of the experimentally determined *k*-factors for the quantification of unknown niobium oxide phases

As discussed in the previous section (4.4.7), for the quantitative analysis of niobium oxides by means of M-edges the use of empirical *k*-factors should be strongly preferred to that of theoretical cross sections. Moreover, the use of *k*-factors derived from Nb-$M_{4,5}$ instead of Nb-$M_{2,3}$ edges is clearly recommended because of the better obtainable reliability (see the results obtained in sections 4.3.2, 4.3.3, and 4.3.4 and the discussion above in sections 4.4.6 and 4.4.7). However, depending on the accuracy and precision needed, a quantification by means of Nb-$M_{2,3}$ edges can also give satisfying results.

It is known that the *k*-factors differ for a particular set of experimental parameters (E_0, β, α, ΔE) and should only be used to quantify spectra acquired and analyzed by means of the same set of parameters (see, e.g., Brydson 2001). Indeed, the strong influence of the integration window ΔE on the *k*-factors determined from Nb-$M_{4,5}$ edges can for instance be observed in Fig. 4.3.4b. By analyzing reference spectra taken from NbO, the averaged *k*-factor using ΔE = 130 eV is 4.5 times higher than the value found for ΔE = 40 eV. Since in that case the *k*-factor is equivalent to the $I_{NbM4,5}/I_{OK}$ intensity ratio, this dependence on ΔE is a trivial consequence of the differences in the basic shapes of the two edges: the Nb-$M_{4,5}$ edges are characterized by a delayed-maximum, whereas the O-K edge presents an abrupt onset followed by a smooth intensity decrease (so-called "sawtooth" shape).

The influence of the parameters E_0, β, and α is for instance shown by the different $k_{NbM4,5\text{-}OK}$ values determined in this study for constant ΔE (70 eV) at the LEO and VG microscopes (see Table 4.3.3). For example, $k_{NbM4,5\text{-}OK} = 9.45 \pm 0.20$ was derived from 53 reference spectra taken at the LEO (E_0 = 200 keV, β = 12.3 mrad, α = 11.2 mrad) whereas in the case of the VG (E_0 = 100 keV, β = 6.5 mrad, $\alpha \approx$ 10 mrad) $k_{NbM4,5\text{-}OK} = 13.57 \pm 0.77$ was averaged from 6 reference spectra. The observed discrepancy can be interpreted by considering the β_{eff}/θ_E ratios for the two edges (see section 4.4.1). For each edge, the recording parameters (E_0, β and α) used at the VG microscope lead to a lower β_{eff}/θ_E ratio than the parameters of the LEO microscope. For the Nb-$M_{4,5}$ edges, theβ_{eff}/θ_E ratio is found around 9.1 at the VG and 23.8 at the LEO when a "mean" energy loss E = 240 eV is chosen to represent the 70 eV wide integration window. In the case of the O-K edge, β_{eff}/θ_E amounts to about 3.9 at the VG and

10.1 at the LEO for E = 565 eV. The amount of signal collected for a given edge increases with rising β_{eff}/θ_E. However, this increase is generally more pronounced within low β_{eff}/θ_E ranges. Hence, since for given E_0, β, and α the β_{eff}/θ_E ratios are lower for the O-K edge than in the case of the Nb-$M_{4,5}$ edges (due to higher E), the O-K intensity increases faster than the Nb-$M_{4,5}$ intensity when β_{eff}/θ_E increases similarly for both edges. Since the k-factors are proportional to the measured $I_{NbM4,5}/I_{OK}$ intensity ratios, this can explain the smaller k-factors obtained for the recording parameters of the LEO compared to those achieved at the VG.

The k-factors can also be sensitive to the post-acquisition procedures used to analyze the spectra. Hence, for $k_{NbM4,5\text{-}OK}$ the LEO and VG data reveal the influence of *Fourier*-ratio deconvolution at constant E_0, β, α, and ΔE (see Fig. 4.3.8a, the LEO data in Table 4.3.3). This sensitivity of $k_{NbM4,5\text{-}OK}$ over deconvolution is related to the different shapes of the O-K and Nb-$M_{4,5}$ edges (see section 4.4.5). Moreover, whereas in this study ΔE = 70 eV is found to be optimum in terms of agreement between the $k_{NbM4,5\text{-}OK}$-data derived from NbO, NbO_2, and Nb_2O_5 (see sections 4.3.3 and 4.3.4, see also below), Olszta et al. (2006) observed a different behavior of the k-factors ($k_{NbM4,5\text{-}OK}$) as a function of ΔE. Their k-factors start converging at ΔE = 75 eV with a good agreement for the k-factors of all three reference oxides (NbO, NbO_2 and Nb_2O_5) at higher ΔE (optimum around 100-125 eV, see Table 4.3.4). In addition to possible effects of different β and α, this distinct behavior is mainly attributed to the specific method that Olszta et al. (2006) employed to extrapolate the background under the O-K edge. Assuming that the O-K edge can accurately be modelled by the hydrogenic model (see, e.g., Egerton, 1979) at energies far past the ELNES, they chose the background-fitting window to achieve a match of the experimental spectrum and the theoretical cross-section at energy losses of ~750-800 eV.

The importance of the choice of the integration window ΔE was already demonstrated in section 4.3.3 and discussed in section 4.4.7. By analyzing different reference oxides at the LEO microscope, for the used recording parameters (E_0 = 200 keV, β = 12.3 mrad, α = 11.2 mrad) a 70 eV wide integration window was found to enable accurate quantification by means of Nb-$M_{4,5}$ edges. In the next chapter (5), the resulting k-factors will be applied to investigate Nb-based capacitor structures. For this purpose other k-factors will also be used, obtained at the VG microscope as well as by means of deconvolution at the LEO machine. However, the VG data and the deconvoluted LEO data could not be tested to determine an optimum ΔE. Nevertheless, it was shown in the previous section (4.4.7) that ΔE = 70 eV should be a good choice to quantify deconvoluted LEO spectra with accuracy. For the quantitative analyses at the VG, the k-factors were derived from only one reference oxide, namely Nb_2O_5. It was already discussed in section 4.4.1 that the general shape of the spectra observed in the present work at the different microscopes were quite independent of the used recording parameters E_0, β, and α. Moreover, for each edge (O-K and Nb-$M_{4,5}$) background fitting-windows similar in width and positions can generally be used at the LEO and VG microscopes. Hence, the effects of the systematic errors related to ELNES and background extrapolation are expected to be of approximately similar strength on the $I_{NbM4,5}/I_{OK}$ intensity

ratios measured at the VG and on those obtained using the LEO. Consequently, a quite equivalent accuracy can also be expected for quantification by means of the same ΔE at both microscopes. Since the dependence of the accuracy on ΔE could not specifically be checked for the VG data (only one reference oxide was quantitatively investigated), for the VG microscope there is thus no reason not to use the optimum value ΔE = 70 eV found for the LEO. In addition, the stoichiometry of the oxide layers in the capacitor structures is expected to be close to Nb_2O_5. Thus, Nb_2O_5, which was analyzed at the VG, seems to be the most natural and efficient reference oxide to determine *k*-factors for the accurate investigation of these layers. In that case, ΔE should not have a strong influence on the accuracy, making its choice less critical. Moreover, Nb_2O_5 is the reference material that enables the best quantitative precision (see section 4.4.6), hence its use for the analysis of the oxide layers is even more pertinent.

Chapter 5

Application of the results obtained from the reference materials: EELS investigations of Nb-based capacitor structures

After the formation of niobium-oxide layers, Nb-based capacitors undergo different kinds of annealing during their fabrication process (see section 2.3.2). In order to check the influence of the annealing on the stoichiometry of the oxide layers (OL) capacitor structures (Cap) achieved after different annealing steps were investigated: I) without annealing (Cap_{No_Anneal}) and after an annealing of II) 5 h at 300°C ($Cap_{300°C\text{-}5h}$), III) 1 h at 320°C ($Cap_{320°C\text{-}1h}$), and IV) 1h at 350°C ($Cap_{350°C\text{-}1h}$). EELS analyses were performed at the LEO 922 microscope (on Cap_{No_Anneal}, $Cap_{300°C\text{-}5h}$ and $Cap_{350°C\text{-}1h}$), at the ZEISS Libra FE microscope (on Cap_{No_Anneal} and $Cap_{320°C\text{-}1h}$) as well as by means of the VG HB501UX microscope (on Cap_{No_Anneal}, $Cap_{300°C\text{-}5h}$ and $Cap_{350°C\text{-}1h}$). At the LEO microscope, the core-loss spectra were generally recorded using a spot size of about 25 nm in diameter. At the Libra instrument, the specimen regions selected to contribute to the EELS spectra had diameters of a few ten nm. Hence, in both cases the recorded spectra resulted from quite large specimen areas. In particular, one spectrum acquired within one oxide layer can be considered to be a global spectrum representing the oxide layer away from its interface to the anode. In contrast, a 0.5 nm sized electron probe was used for the local investigation of the capacitor structures at a nanometer scale by means of the VG scanning transmission electron microscope. EELS linescans were performed across the interface between the niobium anode and the oxide layer (typically, one spectrum was taken each 2 nm). However, spectra gathered during the linescan within one oxide layer can be averaged to obtain mean data. In addition, some averaged spectra were also recorded by scanning quadratic specimen regions within the oxide layers (typically areas of a few 100 nm^2).

In the following subchapters 5.1 and 5.2, global ELNES and quantitative EELS results obtained from large specimen areas in the capacitor structures are presented, whereas subchapter 5.3 focuses on the local investigation of stoichiometry gradients and inhomogeneities within the oxide layers as well as on the study of the anode - dielectric layer interfaces.

5.1 Low-loss fingerprinting and ELNES results

EELS spectra were recorded from the oxide layers of the four different types of capacitor structures ($Cap_{No\text{-}Anneal}$, $Cap_{300°C\text{-}5h}$, $Cap_{320°C\text{-}1h}$ and $Cap_{350°C\text{-}1h}$). The resulting ELNES of the O-K edge and of the Nb-$N_{2,3}$, -$M_{4,5}$, –$M_{2,3}$ and – $L_{2,3}$ edges as well as the obtained plasmon fingerprints are presented in the following sections and compared to the data achieved by the analysis of the reference materials (see subchapter 4.2).
It will be shown that the shapes of all the different EELS features show close similarities to those taken from the reference Nb_2O_5. Moreover, as it will be discussed in section 5.4.1, the small discrepancies observed between the OL and Nb_2O_5 spectra can partly result from the fact that the capacitor oxide layers are amorphous, whereas the Nb_2O_5 reference material is crystalline.
In addition, it can already be noted that no clear distinction could be made between the different capacitor structures by investigating their oxide layers via low-loss fingerprinting or ELNES. Thus, for one given EELS feature (plasmon or edge) acquired at one given microscope, only one OL spectrum being representative for the different investigated capacitor structures will generally be presented.
In the case of the crystalline anodes (An) in the capacitor structures, the shapes of the recorded EELS edges cannot clearly be distinguished from those of the Nb reference. The ELNES of the Nb-$M_{2,3}$ edges will be presented as one example. However, it will be shown that the O-K signal recorded from the anodes appears more intense after annealing than before.

5.1.1 Low-loss fingerprinting

Low-loss spectra were taken from the oxide layers of $Cap_{No\text{-}Anneal}$, $Cap_{300°C\text{-}5h}$, and $Cap_{350°C\text{-}1h}$ by means of the LEO microscope. Their shapes do not allow to differentiate between the three types of capacitor structures. One representative spectrum recorded on one oxide layer produced without annealing ($OL_{No\text{-}Anneal}$) is shown as an example in Fig. 5.1.1a together with the reference low-loss spectra acquired for NbO_2 and Nb_2O_5 (cf. Fig. 4.2.2a). The spectra were corrected for ZLP and multiple scattering. Compared to the reference data, the second peak (b) of the OL plasmon is not anymore clearly visible. The peaks (a) and (c) appear around 14.4 eV and 25.8 eV, respectively, and the full width at 60% of the intensity maximum of the plasmon amounts to about 21.5 eV, which is even more than the value found for Nb_2O_5 (20.3 eV, i.e. the highest value measured from the reference materials - cf. section 4.2.1). Hence, none of the reference plasmon fingerprints perfectly match the shape of the OL plasmon. However, considering the relative height of the peaks (a) and (c), the Nb_2O_5 plasmon is most similar to that taken from the capacitor oxide layer.

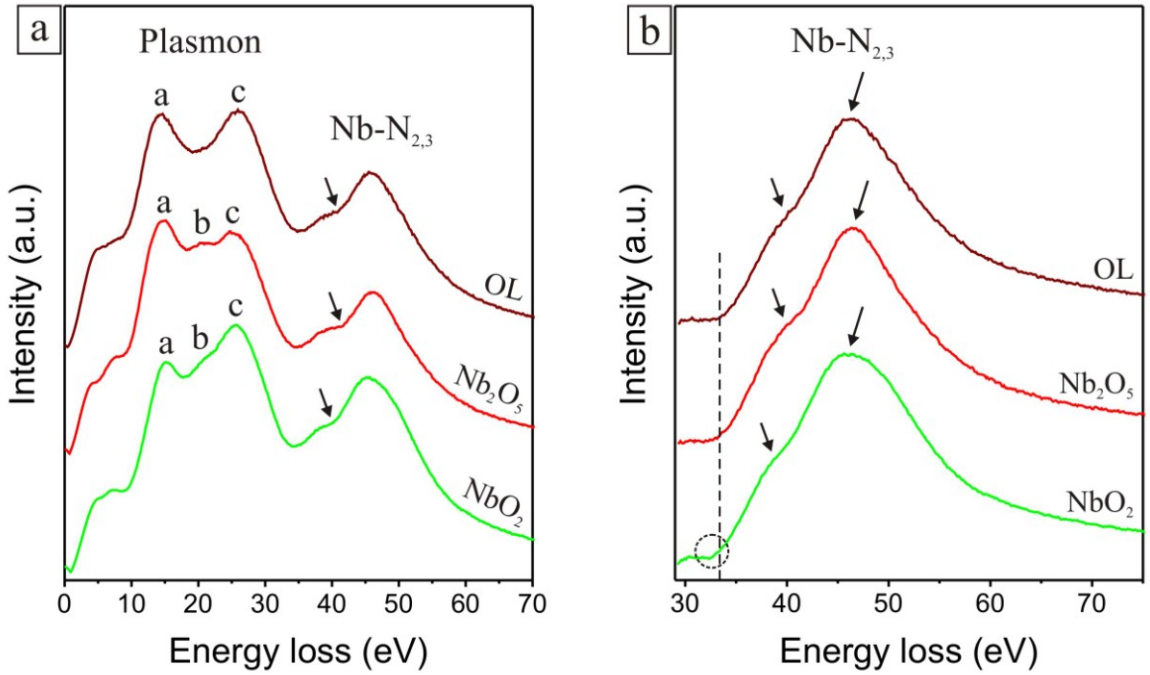

Fig. 5.1.1. EEL low-loss spectra **(a)** and corresponding Nb-$N_{2,3}$ edges **(b)** recorded from NbO_2, Nb_2O_5, and $OL_{No\text{-}Anneal}$ by means of the LEO 922 microscope (dE ~ 2.1 eV, E_0 = 200 keV, β = 12.3 mrad, α = 11.2 mrad). The ZLP was subtracted and the multiple scattering removed from the spectra. An additional background subtraction was performed to achieve the Nb-$N_{2,3}$ data shown in (b).

5.1.2 Nb-$N_{2,3}$ ELNES

In Fig. 5.1.1b the Nb-$N_{2,3}$ edges corresponding to the low-loss spectra (cf. Fig. 5.1.1a) are presented after an additional background-subtraction procedure (see section 4.2.2 for more information on the background extrapolation under the Nb-$N_{2,3}$ edges). The general shape of the Nb-$N_{2,3}$ edges of OL shows close similarities to the ELNES measured for Nb_2O_5. It is characterized by a bump preceded by a shoulder at the lower energy side (arrows in Fig. 5.1.1b). The shoulder is not as well defined and the top of the bump not as sharp as in the case of Nb_2O_5. However, like for Nb_2O_5 the top of the bump is sharper, more rounded and more symmetric than that observed for NbO_2. Moreover, the shoulder measured for OL resembles more that taken from Nb_2O_5 than that of NbO_2. This is particularly visible before background subtraction (see Fig. 5.1.1a). The upper bend of the shoulder appears at higher energy loss for OL and Nb_2O_5 than in the case of NbO_2 (arrows in Fig. 5.1.1a).
Finally, it can be noticed that the edge-onset position of Nb-$N_{2,3}$ is identical for OL and Nb_2O_5 and corresponds to a chemical shift by about 4-5 eV to higher energy with respect to the Nb standard (cf. Fig. 4.2.3). In comparison, the Nb-$N_{2,3}$ onset of NbO_2 seems to occur at a slightly lower energy loss (see the dashed line and circle in Fig. 5.1.1b).

5.1.3 Nb-$M_{4,5}$ ELNES

Spectra showing the Nb-$M_{4,5}$ edges were recorded from $OL_{No\text{-}Anneal}$, $OL_{300°C\text{-}5h}$ and $OL_{350°C\text{-}1h}$ at the LEO microscope. Here again, the three different types of capacitors cannot be distinguished by the ELNES investigation of these edges. Fig. 5.1.2 presents one representative $OL_{No\text{-}Anneal}$ spectrum as well as reference NbO_2 and Nb_2O_5 spectra after background and multiple-scattering corrections. Compared to the Nb-$M_{4,5}$ ELNES of the four reference materials (see Fig. 4.2.4a), the general shape of the Nb-$M_{4,5}$ edges taken from OL shows strong similarities to those of NbO_2 and Nb_2O_5. Indeed, like the NbO_2 and Nb_2O_5 data, the OL spectrum is characterized by well-defined peaks (a) and (c). Considering the width of the peak (c) and the slope of its high-energy side (arrows in Fig. 5.1.2), the OL ELNES is more comparable to that of NbO_2. However, the concave shape of the shoulder observed for OL between the Nb-$M_{4,5}$ onset and the peak (a) is more similar to the structure measured from Nb_2O_5 than to the almost linear slope achieved in the case of NbO_2 (arrows in Fig. 5.1.2). Finally, the bump (d) appears wider for OL than for both NbO_2 and Nb_2O_5, but the position of its intensity maximum matches better with that observed on NbO_2.

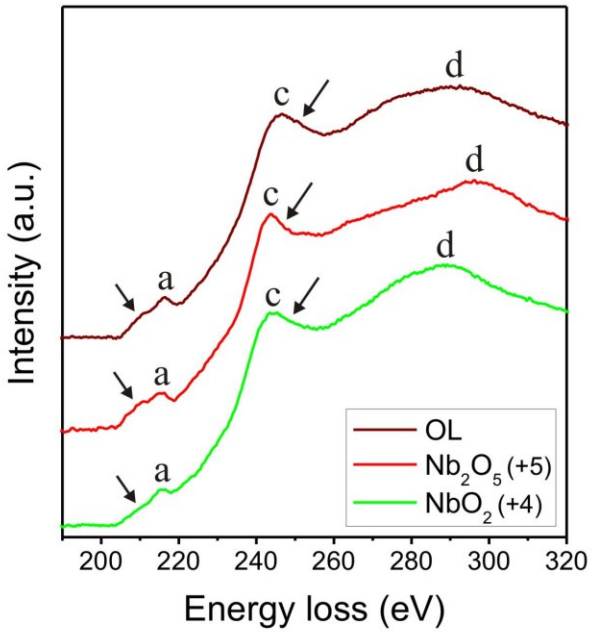

Fig. 5.1.2. EEL spectra showing the Nb-$M_{4,5}$ edges recorded from NbO_2, Nb_2O_5, and $OL_{No\text{-}Anneal}$ by means of the LEO 922 microscope (dE ~ 2.1 eV, E_0 = 200 keV, β = 12.3 mrad, α = 11.2 mrad). The spectra were corrected for background and multiple scattering.

In addition, no distinction could be made between $OL_{No\text{-}Anneal}$, $OL_{300°C\text{-}5h}$, and $OL_{350°C\text{-}1h}$ by investigating the position of the onset of the Nb-$M_{4,5}$ edges. Analyses performed on four Nb reference spectra and nine OL spectra (three spectra for each type of capacitor structure) indicate that the Nb-$M_{4,5}$ onset of OL is shifted by about 4.5 ± 0.6 eV to higher energies with respect to that of Nb (see sections 4.2.3 and 4.4.3 for more information on the procedure used to determine chemical shifts). This is larger than the chemical shifts found for NbO_2 and

Nb_2O_5 (2.8 ± 0.8 eV and 3.8 ± 0.8 eV, respectively - cf. Fig. 4.2.5). However, considering the imprecision of the measurements (± 0.8 eV for NbO_2 and Nb_2O_5, ± 0.6 eV in the case of OL) the value achieved for OL is still roughly consistent with that measured from Nb_2O_5 but does not correspond to NbO_2.

5.1.4 Nb-$M_{2,3}$ ELNES

Nb-$M_{2,3}$ edges were measured at the LEO microscope for $OL_{No\text{-}Anneal}$, $OL_{300°C\text{-}5h}$, and $OL_{350°C\text{-}1h}$. Their shape is identical for the three types of capacitors. Representative spectra recorded from $OL_{No\text{-}Anneal}$, NbO_2, and Nb_2O_5 are visible in Fig. 5.1.3a. The spectra were corrected for background and multiple scattering (for more information concerning the background extrapolation under the Nb-$M_{2,3}$ edges see sections 4.2.4, 4.3.2, and 4.4.6). At an energy resolution dE ~ 2.1 eV the three different materials present a quite similar Nb-$M_{2,3}$ ELNES. It can just be noticed that like in the case of the reference niobium oxides no peak is observed between the M_3 and M_2 white lines of OL, which differentiates the OL spectrum from that taken from the Nb reference (cf. Fig. 4.2.6b).

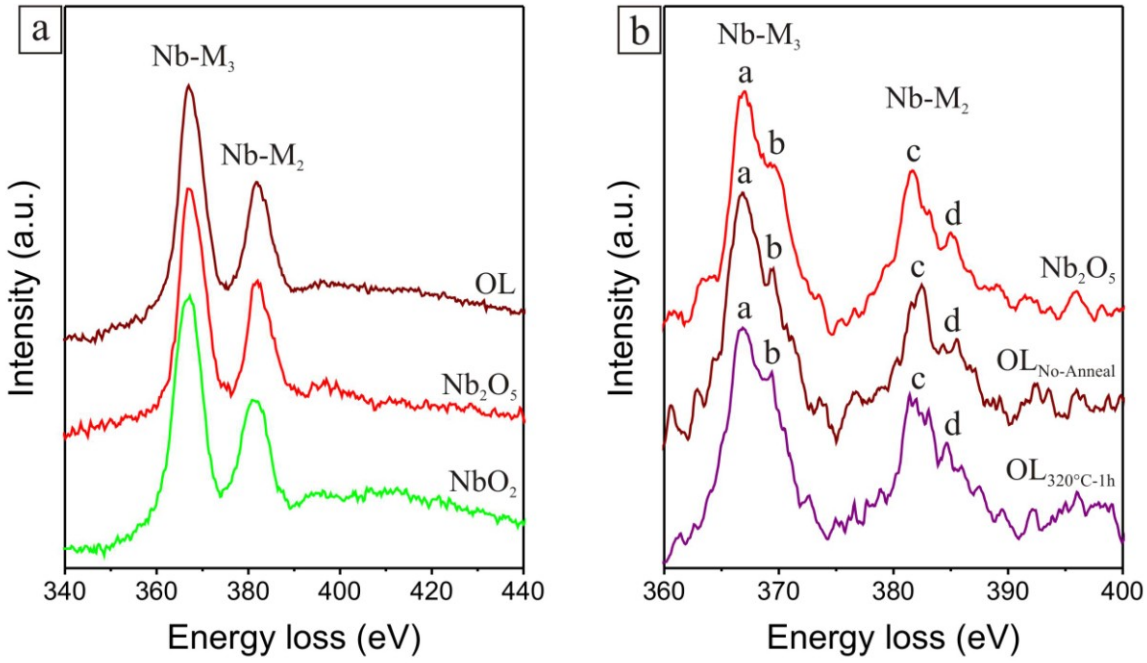

Fig. 5.1.3. EEL spectra showing the Nb-$M_{2,3}$ edges recorded from: **a)** NbO_2, Nb_2O_5, and $OL_{No\text{-}Anneal}$ by means of the LEO 922 microscope (dE ~ 2.1 eV, E_0 = 200 keV, β = 12.3 mrad, α = 11.2 mrad); **b)** Nb_2O_5, $OL_{No\text{-}Anneal}$, and $OL_{320°C\text{-}1h}$ using the ZEISS Libra FE microscope (dE ~ 0.3 eV, E_0 = 200 keV, β = 2.3 mrad, α ~ 0.4 mrad). The spectra were corrected for background and multiple scattering. The spectra in b) were smoothed with respect to the noise.

In relation to the Nb-$M_{2,3}$ edges of reference Nb, a chemical shift similar to that detected for Nb_2O_5 is measured in the case of the Nb-$M_{2,3}$ signal of OL: the position of the edges,

measured at the front half maximum of the M_3 white line, is shifted by approximately 4 eV to higher energies.

The relative position of the Nb-$M_{2,3}$ edges with respect to that of the O-K edge, i.e. $E_{NbM2,3} - E_{OK}$, was also investigated. By analyzing the reference oxides at the LEO microscope, a correlation could be established between $E_{NbM2,3} - E_{OK}$ and the oxidation state of niobium (cf. Fig. 4.4.2a in section 4.4.3). In the case of the capacitor structures, measurements were performed on six $OL_{No\text{-}Anneal}$, six $OL_{300°C\text{-}5h}$, and six $OL_{350°C\text{-}1h}$ spectra. The spectra were recorded by the same region of the detector system as that used to measure the relative edge positions shown in Fig. 4.4.2a for NbO, NbO_2, and Nb_2O_5. The energy-loss positions of Nb-$M_{2,3}$ and O-K were determined at the respective front half maxima of the edges (see section 4.4.3 for more details regarding the position analysis of the edges). Quite equivalent $E_{NbM2,3} - E_{OK}$ values were achieved for the three different types of capacitors, so that no trend in the relative position of the edges could be identified as a function of annealing. Averaging all the 18 OL spectra yields $E_{NbM2,3} - E_{OK}$ = -165.3 ± 0.1 eV, which is perfectly concordant with the value found for reference Nb_2O_5 (-165.3 ± 0.2 eV, cf. section 4.4.3). For comparison, $E_{NbM2,3} - E_{OK}$ = -166.7 ± 0.1 eV was determined for NbO_2. Hence, by means of the above-mentioned correlation between $E_{NbM2,3} - E_{OK}$ and the oxidation state of niobium, the latter is found to be around +5 in OL (cf. Fig. 4.4.2a). In addition, the relative chemical shift of the Nb-$M_{2,3}$ edges in relation to the O-K edge was derived from the $E_{NbM2,3} - E_{OK}$ measurements (see section 4.4.3). It amounts to about +2.6 ± 0.3 eV between NbO and OL.

By means of the Libra microscope, the Nb-$M_{2,3}$ ELNES was also examined for $OL_{No\text{-}Anneal}$ and $OL_{320°C\text{-}1h}$ at a high energy resolution of around 0.3 eV. Representative spectra (after background removal and multiple-scattering correction) measured from the two different types of OL are shown in Fig. 5.1.3b together with a reference spectrum taken from Nb_2O_5. Since the raw-data achieved at the Libra are particularly noisy (cf. Fig. 4.2.7b), the spectra were slightly smoothed. Characteristic fine structures becomes apparent at dE ~ 0.3 eV. Double-peak structures similar to those observed for Nb_2O_5 are also obtained on the Nb-M_3 and M_2 white lines of the OL spectra (letters a and b for Nb-M_3, c and d for Nb-M_2 in Fig. 5.1.3b). Considering the high noise level affecting the data, no significant discrepancies enable to distinguish between the $OL_{No\text{-}Anneal}$ and $OL_{320°C\text{-}1h}$ spectra. At the same energy resolution and using the same smoothing procedure, double-peak structures could not clearly be demonstrated in the case of NbO (cf. Fig. 4.2.7b and the corresponding text in section 4.2.4). In contrast, for NbO_2 double-peak structures were obtained by means of the VG microscope at dE ~ 0.6 eV (see Fig. 4.2.8). Different experimental parameters E_0, α, and β were used at the Libra and VG microscopes to acquire the spectra. However, for the chosen range of E_0, α and β, the combination of these three parameters is expected to have little influence on the shape of the recorded spectra (see the discussion on the influence of the experimental parameters on ELNES in section 4.4.1). In addition, it was shown for Nb_2O_5 that the general shape of the Nb-$M_{2,3}$ double-peak structures and more particularly the relative height of the different peaks remains approximately unchanged when the energy resolution dE varies from 0.3 eV at the Libra to 1.2 eV at the JEOL microscope (see Fig. 4.2.7). Since by

means of the same experimental conditions the relative height and the energy splitting of the peaks appear quite similar for Nb_2O_5 and for OL (Fig 5.1.3b), it can be assumed that the general shape of the OL white lines also stays uniform for dE in the range of 0.3 eV to 1.2 eV. Thus, the fact that for each white line at dE ~ 0.6 eV the two peaks have similar height in the case of NbO_2 (Fig. 4.2.8) clearly differentiates NbO_2 from OL. Indeed, for OL the second peak is always less intense than the first one (Fig. 5.1.3b). Hence, the Nb-$M_{2,3}$ edges of OL show Nb_2O_5 distinct character.

The anodes (An) in the capacitor structures were also analyzed by means of the Nb-$M_{2,3}$ ELNES at the LEO microscope. The shape of the spectra taken from $An_{No\text{-}Anneal}$, $An_{300°C\text{-}5h}$ and $An_{350°C\text{-}1h}$ does not allow the differentiation between the three types of capacitor structures. Fig. 5.1.4 presents one typical spectrum of $An_{300°C\text{-}5h}$ as well as two reference spectra acquired from Nb and NbO. The spectra are background-subtracted and corrected for multiple scattering. Like reference Nb, the anodes are characterized by a little peak occurring between the Nb-M_3 and –M_2 white lines (arrows in Fig. 5.1.4), whereas such a structure was not detected for NbO and for the other reference niobium oxides (cf. Fig. 4.2.6b or Fig. 5.1.3a).

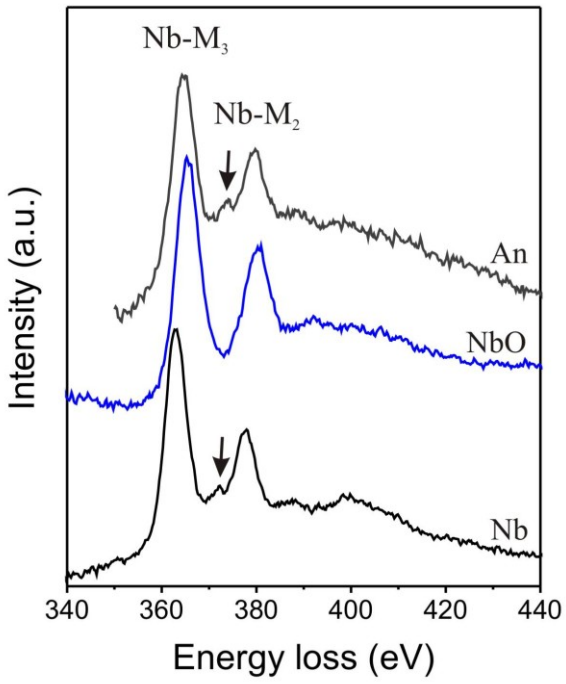

Fig. 5.1.4. EEL spectra showing the Nb-$M_{2,3}$ edges recorded from Nb, NbO, and $An_{300°C\text{-}5h}$ using the LEO 922 microscope (dE ~ 2.1-2.6 eV, E_0 = 200 keV, β = 12.3 mrad, α = 11.2 mrad. The spectra were corrected for background and multiple scattering.

5.1.5 O-K ELNES

Oxide layers

The O-K edges of $OL_{No\text{-}Anneal}$, $OL_{300°C\text{-}5h}$, and $OL_{350°C\text{-}1h}$ were investigated at the LEO microscope. The three types of capacitors present a similar O-K ELNES. One representative background-subtracted spectrum of $OL_{No\text{-}Anneal}$ is shown after multiple-scattering correction in Fig. 5.1.5a together with spectra of Nb_2O_5 and NbO_2. The general shape of the O-K edge of OL does not correspond to that of NbO_2 but is more or less in agreement with the O-K ELNES of Nb_2O_5. Like the reference oxides (cf. Fig. 4.2.10a), OL exhibits a characteristic double-peak structure just above the O-K ionization threshold (letters a and b in Fig. 5.1.5a). In the case of OL, the relative height of the two peaks is roughly similar to that observed for Nb_2O_5 but strongly differs from those of NbO and NbO_2. However, the energy splitting E_b - E_a of OL appears clearly smaller than that determined from the Nb_2O_5 reference. At dE ~ 2.1 eV it is hardly measurable and amounts to about 2.8 eV, whereas a value around 3.8 eV was found for Nb_2O_5 (cf. section 4.2.6). The splitting of OL (~ 2.8 eV) is even lower than that measured from NbO_2 (~ 3.0 eV). In addition, the further peaks and bumps above the double-peak structure appear less pronounced and more spread out for OL than in the case of Nb_2O_5 (letters c, d and e in Fig. 5.1.5a). Particularly the peak (d) in the ELNES of Nb_2O_5 is not any more detected for OL.

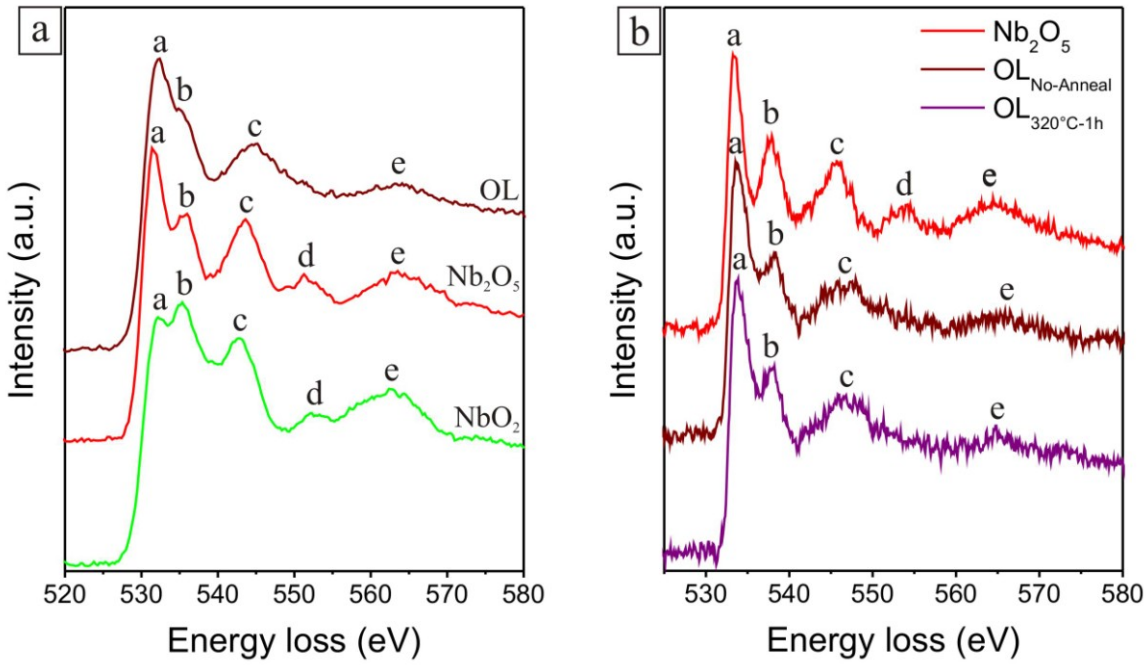

Fig. 5.1.5. O-K edges recorded from: **a)** NbO_2, Nb_2O_5, and $OL_{No\text{-}Anneal}$ using the LEO 922 microscope (dE ~ 2.1 eV, E_0 = 200 keV, β = 12.3 mrad, α = 11.2 mrad), **b)** Nb_2O_5, $OL_{No\text{-}Anneal}$, and $OL_{320°C\text{-}1h}$ using the ZEISS Libra FE microscope (dE ~ 0.3 eV, E_0 = 200 keV, β = 2.3 mrad, α ~ 0.4 mrad). The spectra were corrected for background and multiple scattering.

The O-K edges of $OL_{No\text{-}Anneal}$ and $OL_{320°C\text{-}1h}$ were also measured at dE ~ 0.3 eV by means of the Libra microscope. Representative background-subtracted and multiple-scattering corrected spectra are shown in Fig. 5.1.5b for the two types of capacitors as well as for reference Nb_2O_5. No clear distinction is possible between $OL_{No\text{-}Anneal}$ and $OL_{320°C\text{-}1h}$ by investigating the O-K ELNES. Using the Libra, the similarities in the O-K double-peak structures of OL and Nb_2O_5 appear more obvious than at the LEO microscope. Indeed, the double-peak structure measured for OL is much better defined at dE ~ 0.3 eV (Libra) than at dE ~ 2.1 eV (LEO). The relative height of the two peaks is in good agreement with that obtained from Nb_2O_5. The energy splitting $E_b - E_a$ is found around 4.1 eV for both $OL_{No\text{-}Anneal}$ and $OL_{320°C\text{-}1h}$. This is still lower than the value measured in the case of Nb_2O_5 (~ 4.4 eV, cf section 4.2.6), but compared to the results achieved at the LEO microscope, the relative discrepancy between the $E_b - E_a$ splittings of OL and Nb_2O_5 is strongly reduced. Nevertheless, similarly to the observations performed at the LEO, the structure occurring above the peak (b) is still more blurred for OL than in the case of Nb_2O_5 and no peak (d) can clearly be recognized.

Anodes

Despite being supposed to consist originally of pure Nb, the anodes (An) in capacitor structures present an O-K edge in their EEL spectra. Similarly to what is observed for reference Nb (cf. section 4.2.6), the relative intensity of the O-K edge with respect to the Nb-$M_{2,3}$ intensity decreases with increasing specimen thickness, so that at least a part of the O-K signal is expected to result from surface oxide layers whose thickness is independent of the total specimen thickness. Moreover, in the case of the anodes it can also be observed that at a constant relative thickness the O-K signal increases with annealing. Raw spectra recorded from $An_{No\text{-}Anneal}$, $An_{300°C\text{-}5h}$ and $An_{350°C\text{-}1h}$ by means of the LEO microscope are for instance shown in Fig. 5.1.6a without background subtraction and multiple-scattering correction. All the data were taken from specimen regions with similar relative thicknesses in the range of 0.66 to 0.69. The three spectra were adjusted so that their Nb-M_3 white-lines (not shown in Fig. 5.1.6a) are equal in intensity. Without annealing ($An_{No\text{-}Anneal}$), the O-K edge is not clearly recognizable, which is consistent with the results presented in section 4.2.6 for reference Nb: at t/Λ = 0.51 a very low O-K signal was observed, whereas the edge was not any more detected at t/Λ = 0.80 (cf. Fig. 4.2.12b). In contrast, well-defined O-K edges are measured from $An_{300°C\text{-}5h}$ and $An_{350°C\text{-}1h}$. In the case of the spectra shown in Fig. 5.1.6a, the O-K intensity is quite equivalent for both types of annealed capacitors. However, by considering other spectra taken at an another relative thickness, the O-K signal of $An_{350°C\text{-}1h}$ seems sometimes to be slightly more intense than that of $An_{300°C\text{-}5h}$, but the differences remain small and thus not particularly significant.

The passive oxide layer measured at the surface of reference Nb (cf. sections 4.2.6 and 4.3.7) is assumed to originate from an oxidation process taking place in the ambient atmosphere after the TEM-sample preparation is finished. Indeed, the sample preparation involves mechanical grinding, dimpling, and ion (Ar^+ or Xe^+) thinning, so that a pre-existing surface oxide layer is expected to be removed during this procedure. Also in the case of the capacitor structures, the investigated TEM samples were prepared in an analogous manner. Hence, the

additional O-K signal measured from $An_{300°C\text{-}5h}$ and $An_{350°C\text{-}1h}$ compared to $An_{No\text{-}Anneal}$ cannot result from a surface layer which could have grown during annealing. Thus, this strong signal is probably induced by oxygen atoms which diffuse into the anode material due to annealing. Although the O-K edge of the annealed anodes is more intense than that of reference Nb, the O-K ELNES is quite similar for both types of materials. Representative spectra taken from $An_{350°C\text{-}1h}$ and reference Nb and NbO at the LEO microscope are presented in Fig. 5.1.6b after background and multiple-scattering correction (cf. Fig. 4.2.13). It should be noted that the Nb spectrum was acquired from a specimen region with $t/\Lambda \sim 0.25$, whereas the spectrum taken from the anode results from a higher t/Λ of around 0.64 that minimizes the influence of the surface oxide layers on the observed O-K ELNES. Nonetheless, like reference Nb the anode is most similar to NbO when its O-K ELNES is compared to those of the reference oxides (cf. Fig. 4.2.10a and more generally section 4.2.6).

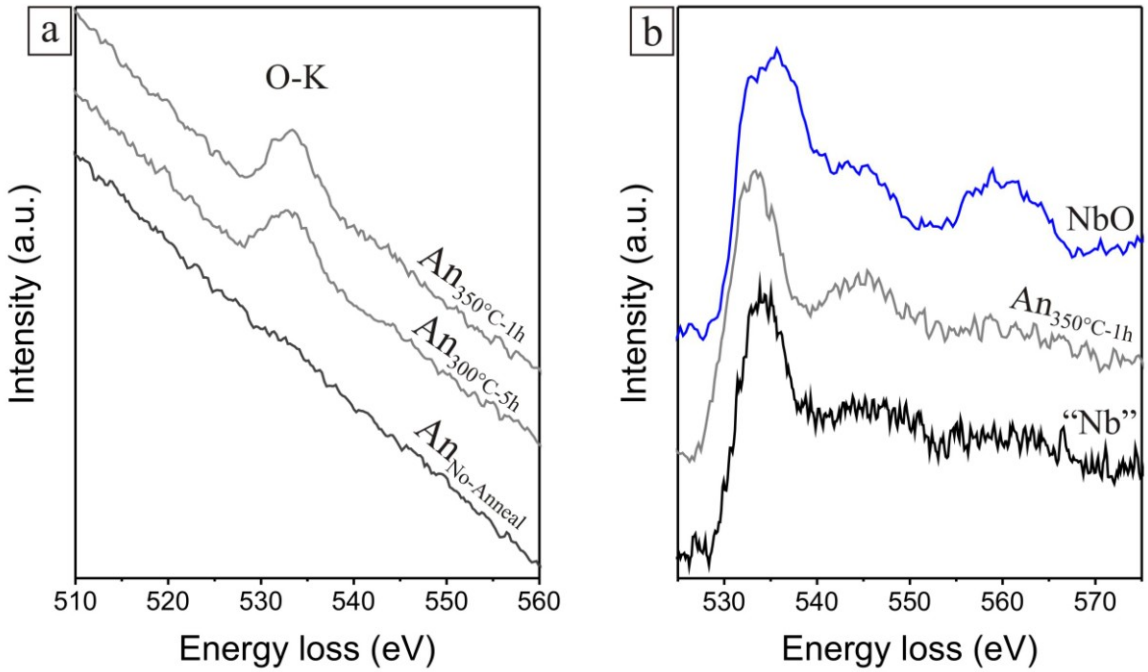

Fig. 5.1.6. EEL spectra recorded at the LEO 922 microscope (dE ~ 2.1 eV, E_0 = 200 keV, β = 12.3 mrad, α = 11.2 mrad) and showing the O-K edges of **a)** $An_{No\text{-}Anneal}$, $An_{300°C\text{-}5h}$ and $An_{350°C\text{-}1h}$, **b)** reference Nb, $An_{350°C\text{-}1h}$ and NbO. The three raw spectra shown in a) were taken from specimen regions with a similar relative thickness in the range from 0.66 to 0.69 and their Nb-M_3 white-lines were equalized in intensity (the Nb-$M_{2,3}$ edges are not visible in the energy range presented here). The spectra shown in b) were corrected for background and multiple scattering.

5.1.6 Nb-$L_{2,3}$ ELNES

High-loss spectra showing the Nb-$L_{2,3}$ edges were taken at the LEO microscope from $OL_{No\text{-}Anneal}$ and $OL_{300°C\text{-}5h}$. Here again, the two different types of capacitors cannot be distinguished by means of ELNES. Representative spectra acquired from NbO_2, Nb_2O_5, and $OL_{No\text{-}Anneal}$ are presented after background and multiple-scattering correction in Fig. 5.1.7.

Compared to the Nb-$L_{2,3}$ ELNES of the reference materials (cf. Fig. 4.2.14), the general shape of the Nb-$L_{2,3}$ edges recorded from OL is most similar to the spectrum taken from Nb_2O_5. For example, whereas Nb and NbO are characterized by a smooth intensity decrease at the bottom of the L_3 white line, OL, just like Nb_2O_5, shows a more abrupt drop followed by a little bump (cf. arrows in Fig. 4.2.14). Moreover, the bump marked by arrows in Fig. 5.1.7 appears similarly broad for OL and Nb_2O_5, whereas it is sharper in the case of NbO_2.

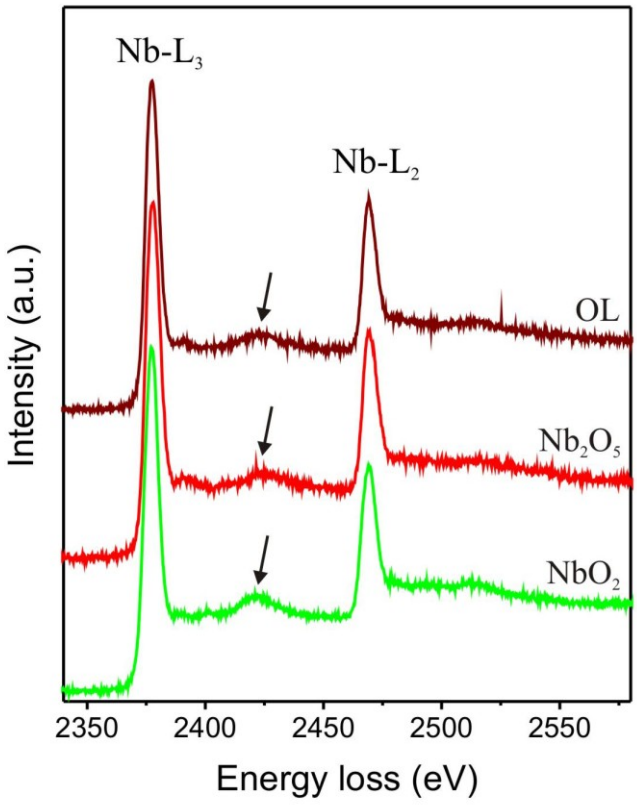

Fig. 5.1.7. Nb-$L_{2,3}$ edges of NbO_2, Nb_2O_5, and $OL_{No\text{-}Anneal}$ recorded with the LEO 922 microscope (dE ~ 2.4 eV, E_0 = 200 keV, β = 18 mrad, α = 12.6 mrad). The spectra were corrected for background and multiple scattering.

The chemical shift of the Nb-$L_{2,3}$ edges does not allow to clearly differentiate $OL_{No\text{-}Anneal}$ from $OL_{300°C\text{-}5h}$. Analyses performed on both types of capacitors yield a chemical shift by approximately 4.2 ± 0.9 eV to higher energies with respect to the Nb-$L_{2,3}$ edges of reference Nb when the position of the edges is measured at the front half maximum of the L_3 white line (see section 4.2.7 for more information on the method employed to determine the chemical shift). This is consistent with the chemical shift of about 4.1 ± 0.7 eV measured from Nb_2O_5, but in poorer agreement with the value of 3.6 ± 0.6 eV found for NbO_2 (cf. Fig. 4.2.15).

Normalized Nb-$L_{2,3}$ white-line intensities I_{L3+L2} were determined from the spectrum shown in Fig. 5.1.7 for $OL_{No\text{-}Anneal}$ as well as from one representative spectrum taken from $OL_{300°C\text{-}5h}$. These analyses were performed by the method described in section 4.2.7 and discussed in section 4.4.4. Similar values were achieved for both types of capacitors: I_{L3+L2} ~ 0.77 for

$OL_{No\text{-}Anneal}$ and $I_{L3+L2} \sim 0.80$ in the case of $OL_{300°C\text{-}5h}$. The niobium 4d state occupancy n_{4d} of the oxide layers can be determined via the linear relationship found between I_{L3+L2} and n_{4d} by investigating the four reference materials ($I_{L3+L2} = 0.75 - 0.069n_{4d}$ – cf. section 4.2.7). Negative values were obtained, viz. $n_{4d} \sim -0.29$ for $OL_{No\text{-}Anneal}$ and –0.72 for $OL_{300°C\text{-}5h}$. Nevertheless, these values are still relatively close to zero. Moreover, by means of the linear function connecting I_{L3+L2} and n_{4d}, the normalized intensity measured from Nb_2O_5 ($I_{L3+L2} \sim 0.78$, cf. Fig. 4.2.16b) also corresponds to a negative Nb 4d occupancy of about -0.43, whereas the nominal value is $n_{4d} = 0$. Indeed, the I_{L3+L2} normalized intensities measured for the oxide layers are in good agreement with that determined from Nb_2O_5. The relative deviations between the normalized intensity of Nb_2O_5 and those of $OL_{No\text{-}Anneal}$ and $OL_{300°C\text{-}5h}$ amount to about 1.3% and 2.5%, respectively. For comparison, the relative deviations with respect to NbO_2 ($I_{L3+L2} \sim 0.65$, cf. Fig. 4.2.16b) are around 17% for $OL_{No\text{-}Anneal}$ and 21% in the case of $OL_{300°C\text{-}5h}$. In addition, by considering only the normalized Nb-$L_{2,3}$ intensities determined from NbO_2 (nominal $n_{4d} = 1$) and Nb_2O_5 (nominal $n_{4d} = 0$) the following relationship can be derived between I_{L3+L2} and n_{4d}: $I_{L3+L2} = 0.78 - 0.13n_{4d}$. By applying this relationship to the I_{L3+L2} normalized intensities of the oxide layers, n_{4d} is found around 0.077 for $OL_{No\text{-}Anneal}$ and –0.15 for $OL_{300°C\text{-}5h}$. These values are very close to zero, and thus in good agreement with a niobium oxidation state of +5, i.e. with Nb_2O_5.
However, it should be emphasized that no statistics was performed on the normalized Nb-$L_{2,3}$ white-line intensities. For each investigated material (Nb, NbO, NbO_2, Nb_2O_5, $OL_{No\text{-}Anneal}$, and $OL_{300°C\text{-}5h}$), only one spectrum was analyzed, so that no information is available on the precision of the quantitative results achieved by means of normalized Nb-$L_{2,3}$ intensities. As a test, the spectrum taken from $OL_{300°C\text{-}5h}$ was re-analyzed. Compared to the first analysis, strongly different but still acceptable delimiting lines between bound-state and continuum contributions as well as different integration windows under the L_3 and L_2 white lines were chosen, yielding a I_{L3+L2} normalized intensity of about 0.76. Moreover, a second $OL_{300°C\text{-}5h}$ spectrum was analyzed, resulting in $I_{L3+L2} \sim 0.83$. The relative deviation between these two extreme values (0.76 and 0.83) amounts to approximately 8.8%. Thus, this important discrepancy indicates the necessity to perform statistics to get more reliable results. Nonetheless, it can be concluded that the different I_{L3+L2} values obtained from $OL_{300°C\text{-}5h}$ are in a much better agreement with Nb_2O_5 (0.78) than with NbO_2 (0.65).

5.2 Quantitative EELS results

$OL_{No\text{-}Anneal}$, $OL_{300°C\text{-}5h}$, and $OL_{350°C\text{-}1h}$ were quantitatively investigated by means of the Nb-$M_{4,5}$ edges. In chapter 4 it was shown that the use of Nb-$M_{4,5}$ edges and 70 eV wide integration windows yields accurate EELS quantification. However, minimal variations in the chemical composition of the OL can result in a significant deterioration of the capacitor performance. The quantitative EELS results presented here will show some trends as a

function of annealing. To better interpret these trends and discuss whether they are real or just apparent as a consequence of statistical errors, different procedures were applied for EELS quantification. Quantitative investigations were performed at the LEO microscope with or without deconvolution of the spectra regarding multiple scattering. At the VG microscope, different *k*-factors derived without deconvolution were used to determine the OL stoichiometry. Discrepancies in the results of the different procedures will allow to roughly evaluate how sensitive EELS quantification is with respect to changes of the C_{Nb}/C_O atomic concentration ratio within the oxide layers (see section 5.4.2 devoted to the discussion of the quantitative results).

5.2.1 Influence of the specimen thickness on the quantitative EELS results

By analyzing the reference oxides, a decrease of the *k*-factors derived from NbO_2 and Nb_2O_5 was observed with increasing relative thickness of the investigated specimen regions (see sections 4.3.5 and 4.3.6 as well as the related discussion in section 4.4.5). A similar trend is obtained for the $I_{NbM4,5}/I_{OK}$ intensity ratios measured from the capacitor oxide layers (see section 4.3.2 for more information on the determination of intensity ratios). As an example, Fig. 5.2.1 shows the individual intensity ratios derived from 36 $OL_{300°C\text{-}5h}$ spectra as a function of the relative thickness t/Λ. The spectra were taken from specimen regions with t/Λ in the range from 0.11 to 0.61 by means of the LEO microscope. A very clear decrease of $I_{NbM4,5}/I_{OK}$ is visible when t/Λ rises. This trend is even more pronounced than that achieved at the LEO microscope for the *k*-factors determined from NbO_2 and Nb_2O_5 (cf. Fig. 4.3.6). Hence, it again points out the importance of taking the specimen thickness into account to perform a reliable quantitative analysis of the oxide layers (cf. sections 4.4.6 and 4.4.7). For this purpose, at least one of the two approaches presented in section 4.3.5 was systematically applied: multiple-scattering correction of the spectra and/or limitation of the relative-thickness range used for quantification.

For instance, Fig. 5.2.2 reveals the $I_{NbM4,5}/I_{OK}$ intensity ratios determined with or without deconvolution from five spectra of one and the same oxide layer of $Cap_{No\text{-}Anneal}$ (LEO microscope: E_0 = 200 keV, β = 12.3 mrad, α = 11.2 mrad, ΔE = 70 eV). The investigated layer was not homogeneous in thickness and the intensity ratios are presented in dependence on the relative thickness in the range of 0.23 to 0.53. Without deconvolution, the averaging of all the spectra yields $I_{NbM4,5}/I_{OK} \sim 3.82 \pm 0.13$ (±3.4%). After deconvolution $I_{NbM4,5}/I_{OK} \sim 4.22 \pm 0.03$ (±0.7%) is found. The reduction of the standard deviation from ±3.4% to ±0.7% by deconvolution demonstrates the direct benefit of correcting the spectra for multiple scattering to quantify the oxide layers with high precision.

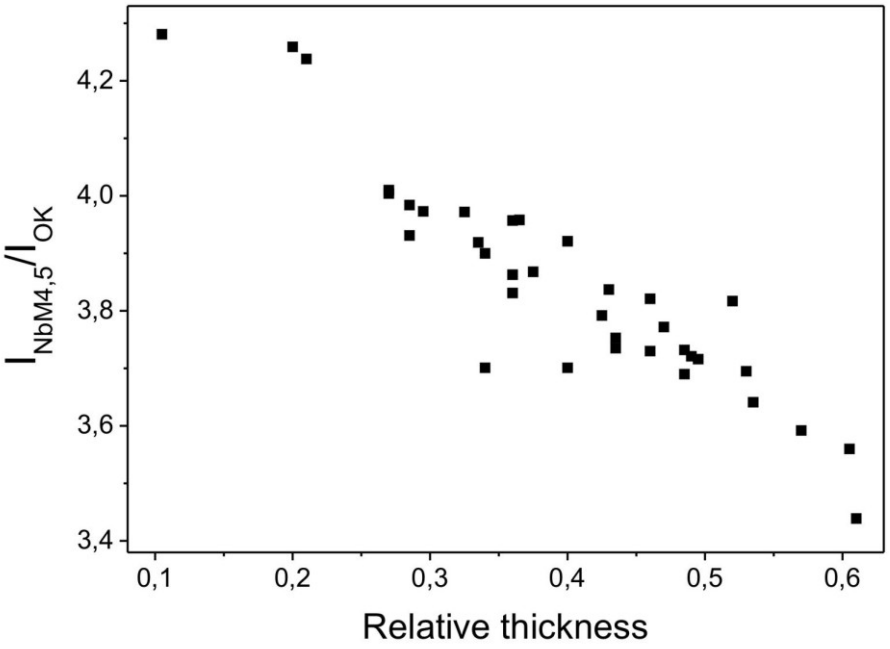

Fig. 5.2.1. $I_{NbM4,5}/I_{OK}$ intensity ratios determined from 36 spectra taken from $OL_{300°C\text{-}5h}$ as a function of the relative thickness of the measured specimen region (LEO 922 microscope: E_0 = 200 keV, β = 12.3 mrad, α = 11.2 mrad, ΔE = 70 eV).

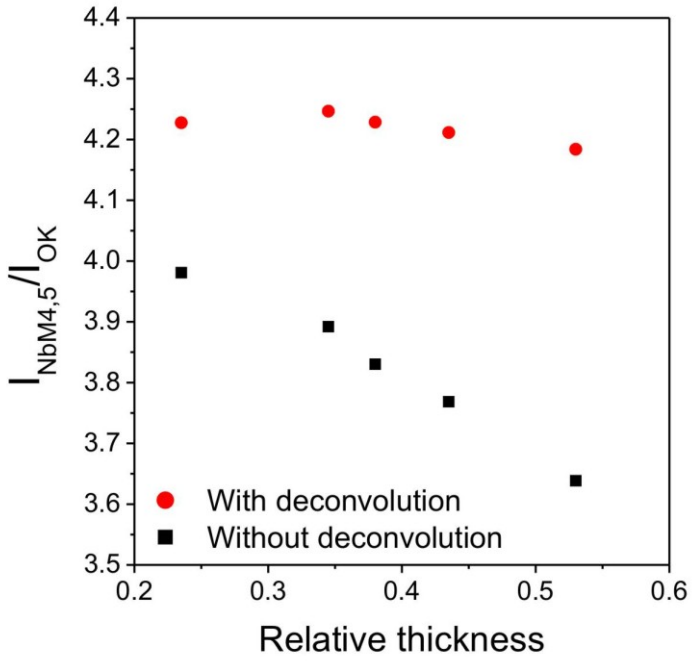

Fig. 5.2.2. $I_{NbM4,5}/I_{OK}$ intensity ratios determined with and without *Fourier*-ratio deconvolution from five $OL_{No\text{-}Anneal}$ spectra as a function of the relative thickness of the measured specimen region (LEO 922 microscope: E_0 = 200 keV, β = 12.3 mrad, α = 11.2 mrad, ΔE = 70 eV). The spectra were taken from regions of different thickness in one and the same oxide layer.

5.2.2 Determination of C_{Nb}/C_O atomic concentration ratios at the LEO microscope

Oxide layers

Spectra acquired from $OL_{No\text{-}Anneal}$, $OL_{300°C\text{-}5h}$, and $OL_{350°C\text{-}1h}$ at the LEO microscope ($E_0 = 200$ keV, $\beta = 12.3$ mrad, $\alpha = 11.2$ mrad) from specimen regions with t/Λ ranging from 0.30 to 0.50 were quantified via the Nb-$M_{4,5}$ edges ($\Delta E = 70$ eV). The investigations were firstly conducted without deconvolution by making use of the *k*-factor $k_{NbM4,5\text{-}OK} = 9.39 \pm 0.17$ (±1.8%) determined from 37 reference spectra with t/Λ in the same range of 0.30 to 0.50 for the same experimental parameters E_0, β, α, and ΔE (cf. section 4.3.5 and Table 4.3.3). The averaged relative thickness corresponding to all 37 reference spectra is $t/\Lambda = 0.42$.

The analysis of 13 $OL_{No\text{-}Anneal}$ spectra corresponding to an averaged relative thickness of about 0.39 led to a C_{Nb}/C_O atomic concentration ratio of 0.405 ± 0.011 (±2.7%). This stoichiometry can be represented by the chemical formula $Nb_2O_{4.94\pm0.13}$. A quite similar value, namely $C_{Nb}/C_O = 0.406 \pm 0.012$ (±3.0%), is found for 22 $OL_{300°C\text{-}5h}$ spectra, where the averaged relative thickness amounts to approximately 0.41. It corresponds to a stoichiometry $Nb_2O_{4.93\pm0.15}$. Compared to $OL_{No\text{-}Anneal}$ and $OL_{300°C\text{-}5h}$, a higher atomic concentration ratio $C_{Nb}/C_O = 0.411 \pm 0.012$ (±2.9%) is measured for $OL_{350°C\text{-}1h}$ that corresponds to $Nb_2O_{4.87\pm0.14}$. However, this value results from the investigation of only four spectra presenting an averaged relative thickness of 0.41. Unfortunately, massive defects put the LEO microscope out of order before more spectra with t/Λ in the range of 0.30 to 0.50 could be recorded from $OL_{350°C\text{-}1h}$. Thus, because of the poor statistics, the C_{Nb}/C_O ratio achieved for $OL_{350°C\text{-}1h}$ should be considered with more caution than those obtained for $OL_{No\text{-}Anneal}$ and $OL_{300°C\text{-}5h}$.

Therefore, according to the mean values found for C_{Nb}/C_O (0.405, 0.406, and 0.411 for $OL_{No\text{-}Anneal}$, $OL_{300°C\text{-}5h}$, and $OL_{350°C\text{-}1h}$, respectively) the oxide layers of all three different types of capacitor structures show an oxygen deficiency compared to stoichiometric Nb_2O_5 (nominal $C_{Nb}/C_O = 0.400$). Nevertheless, considering the corresponding standard deviations (0.11, 0.12, and 0.12 for $OL_{No\text{-}Anneal}$, $OL_{300°C\text{-}5h}$, and $OL_{350°C\text{-}1h}$, respectively) the stoichiometry in the oxide layers is in each case still statistically compatible with Nb_2O_5, but $OL_{350°C\text{-}1h}$ is particularly close to the acceptable limit.

The same OL spectra were reanalyzed by means of *Fourier*-ratio deconvolution using the *k*-factor $k_{NbM4,5\text{-}OK/deconv} = 10.41 \pm 0.15$ (±1.4%) determined from 28 reference spectra taken from specimen regions with t/Λ ranging from 0.30 to 0.50 (averaged relative thickness of about 0.40 – cf. section 4.3.5 and Table 4.3.3). Depending on how exactly the onset of the Nb-$M_{4,5}$ edges can be localized before and after deconvolution, the position of the integration window under the Nb-$M_{4,5}$ edges of each OL spectrum was not necessarily identical for both procedures. C_{Nb}/C_O atomic concentration ratios of 0.403 ± 0.006 (±1.5%), 0.406 ± 0.009 (±2.2%), and 0.408 ± 0.008 (±2.0%) were found for $OL_{No\text{-}Anneal}$, $OL_{300°C\text{-}5h}$, and $OL_{350°C\text{-}1h}$, respectively, corresponding to the chemical formula $Nb_2O_{4.96\pm0.07}$, $Nb_2O_{4.93\pm0.11}$, and $Nb_2O_{4.90\pm0.10}$, respectively.

For each type of capacitor, the C_{Nb}/C_O atomic concentration ratio determined after deconvolution of the OL spectra appears smaller or equal to that obtained without deconvolution. The standard deviation of the measurements is also reduced by the deconvolution (e.g., from ±2.7% to ±1.5% in the case of $OL_{No\text{-}Anneal}$), resulting in a more precise quantification. Nevertheless, the mean C_{Nb}/C_O values still indicate an oxygen deficiency in each type of oxide layer in comparison to stoichiometric Nb_2O_5, even if here again the measured stoichiometries are compatible with Nb_2O_5 when the standard deviations are taken into account. In addition, while comparing the different capacitor structures with each other, $OL_{No\text{-}Anneal}$ still presents the lowest C_{Nb}/C_O ratio whereas the highest value is found for $OL_{350°C\text{-}1h}$, similarly to what was observed without deconvolution.

The quantitative results achieved for the oxide layers at the LEO microscope are summarized in a graph (Fig. 5.2.3) showing the C_{Nb}/C_O atomic concentration ratios measured with or without deconvolution as a function of the annealing step endured by the oxide layers.

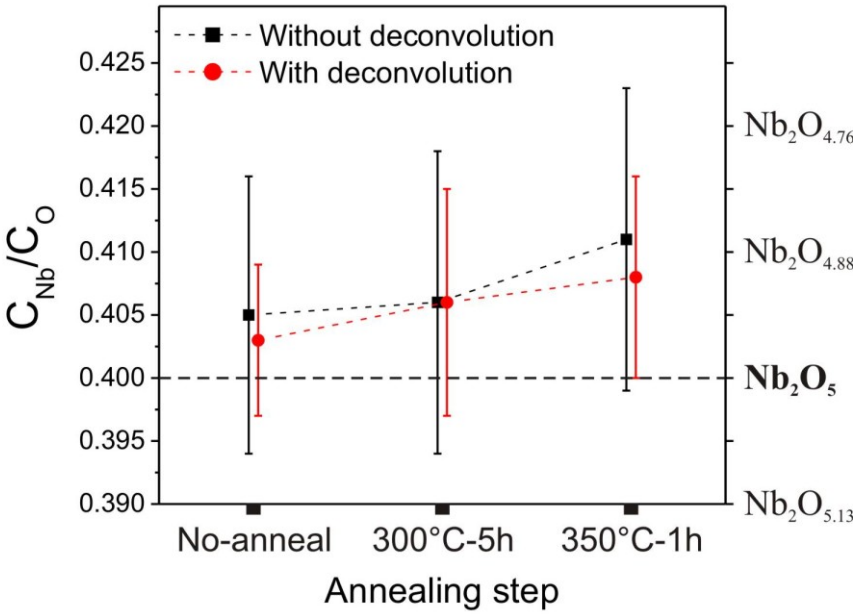

Fig. 5.2.3. C_{Nb}/C_O atomic concentration ratios determined with and without *Fourier*-ratio deconvolution from 13 $OL_{No\text{-}Anneal}$, 22 $OL_{300°C\text{-}5h}$, and four $OL_{350°C\text{-}1h}$ spectra taken from specimen regions with a relative thickness in the range of 0.30 to 0.50 (LEO 922 microscope: E_0 = 200 keV, β = 12.3 mrad, α = 11.2 mrad, ΔE = 70 eV).

Anodes

By investigating the shapes of the spectra taken from the anodes in the capacitor structures, it was shown in section 5.1.5 that $An_{No\text{-}Anneal}$ is consistent with reference Nb, whereas a more intense O-K edge was measured for $An_{300°C\text{-}5h}$ and $An_{350°C\text{-}1h}$ compared to reference Nb. This additional O-K signal is attributed to oxygen atoms which diffuse into the anode during annealing. For $An_{No\text{-}Anneal}$, only relatively thick specimen regions could be investigated by EELS. Hence, the O-K signal of the resulting spectra is too weak to enable quantitative EELS, and thus, reference Nb and $An_{No\text{-}Anneal}$ cannot be compared in a quantitative manner.

However, EELS quantification is possible for $An_{300°C\text{-}5h}$ and $An_{350°C\text{-}1h}$ due to their strong O-K signals.

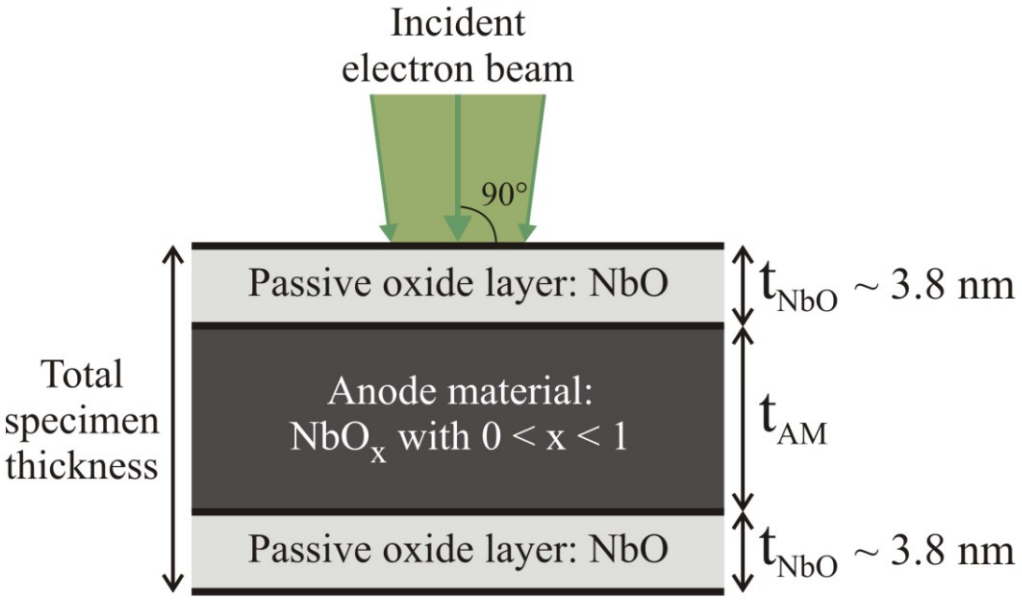

Fig. 5.2.4. Schema of the annealed capacitor anode showing the composition and geometry expected for the investigated specimen region and its assumed orientation with respect to the incident electron beam in the microscope.

One $An_{300°C\text{-}5h}$ and one $An_{350°C\text{-}1h}$ spectrum taken from specimen regions with relative thicknesses of about 0.40 and 0.46, respectively, were analyzed by means of the *k*-factor $k_{NbM4,5\text{-}OK} = 9.39 \pm 0.17$ applied above to the quantification of the oxide layers in capacitor structures (LEO 922 microscope: E_0 = 200 keV, β = 12.3 mrad, α = 11.2 mrad, ΔE = 70 eV). The resulting C_{Nb}/C_O atomic concentration ratios amount to approximately 2.71 and 2.66, respectively, for $An_{300°C\text{-}5h}$ and $An_{350°C\text{-}1h}$. In each case, the concentration ratio corresponds to the averaged stoichiometry of the total transmitted specimen volume. However, as pointed out in section 5.1.5, oxide layers are present at the surface of the anode material. The thickness of these surface layers is expected to be independent on the total specimen thickness. To calculate the stoichiometry inside the anode, it is assumed that, like for reference Nb (cf. Fig. 4.3.9), the anode material (AM) is sandwiched between two 3.8 nm thick NbO layers on its upper and lower surface as shown in Fig. 5.2.4. Indeed, passive oxide layers consisting probably of NbO were observed at the surface of reference Nb, and the total thickness of these layers ($2t_{NbO}$) was estimated to be around 7.6 nm (cf sections 4.2.6 and 4.3.7). In addition, the C_{Nb}/C_O ratios measured for the anodes (2.71 for $An_{300°C\text{-}5h}$ and 2.66 for $An_{350°C\text{-}1h}$) are higher than the nominal value of NbO (C_{Nb}/C_O = 1), indicating that the stoichiometries averaged in the total analyzed volumes are oxygen-deficient compared to stoichiometric NbO. Nevertheless, the ratios are lower than for reference Nb (C_{Nb}/C_O ~ 4.13, cf. section 4.3.7) from a thinner specimen region (t/Λ ~ 0.27) in comparison to those analyzed for $An_{300°C\text{-}5h}$ (t/Λ ~ 0.40) and $An_{350°C\text{-}1h}$ (t/Λ ~ 0.46). Thus, assuming identical NbO surface layers for the anode material and the original Nb reference material, the annealed anode must contain more

oxygen than the Nb reference. As a conclusion, it can already be recognized that the anode material should consist of NbO_x with $0 < x < 1$.

While investigating the passive oxide layers grown on reference Nb, it was possible to derive their thickness under the assumption that they have a certain stoichiometry (cf. section 4.3.7). In the present case, the reverse procedure is applied to determine the C_{Nb}/C_O atomic concentration ratio in the anode material while the layer thickness is known. The determination of the stoichiometry was performed iteratively. The effective inelastic mean free path Λ_{eff} of one electron going through the specimen is assumed to be given by $\Lambda_{eff} \sim (t_{AM}/t)\Lambda_{AM} + (2t_{NbO}/t)\Lambda_{NbO}$, where t is the total specimen thickness, t_{AM} and $2t_{NbO}$ (~ 7.6 nm, see section 4.3.7) are the thicknesses of the anode material and the surface oxide layers, respectively, and Λ_{AM} and Λ_{NbO} (~ 98 nm for the used experimental parameters, see section 4.3.7) are the inelastic mean free paths within the anode material and NbO. Λ_{eff} corresponds to the mean free path Λ that defines the relative thickness t/Λ measured from a low-loss spectrum. To start the iteration, Λ_{AM} is firstly assumed to be equal to the mean free path within pure Nb (Λ_{Nb} ~ 88 nm, see section 4.3.7). By means of the definition of Λ_{eff}, the thickness t_{AM} can then be derived from the measured relative thickness t/Λ. On the basis of the C_{Nb}/C_O atomic concentration ratio obtained for the total specimen by EELS quantification, the value found for t_{AM} is used to determine the C_{Nb}/C_O ratio in the anode material under the assumption that the molar volume V_{AM} of the anode material NbO_x is equal to that of Nb (V_{Nb} ~ 10.8 cm^3, see section 4.3.7). Hence, a first value is found for x. Using the empirical parameterization of Malis et al. (1988), a new Λ_{AM} value can be calculated from the found stoichiometry (see sections 3.2.4 and 4.3.7 for more details), yielding a new value for t_{AM}. In addition, the molar volume of the anode material NbO_x can now be assumed to be given by $V_{AM} = V_{Nb} + x(V_{NbO} - V_{Nb})$, where V_{NbO} is the molar volume of NbO (~ 15.0 cm^3, see section 4.3.7). The new t_{AM} and V_{AM} enable to recalculate x, and so on. This procedure is repeated until the relative deviation between two consecutively found x values is lower than 1%.
The resulting C_{Nb}/C_O atomic concentration ratios are of the same order of magnitude for both types of annealed anodes. For the anode material in $An_{300°C\text{-}5h}$ the C_{Nb}/C_O ratio amounts to about 4.2, corresponding to $NbO_{0.24}$. In the case of $An_{350°C\text{-}1h}$, a slightly lower value $C_{Nb}/C_O \sim 3.7$ is found, corresponding to $NbO_{0.27}$. In addition, for the specific specimen regions, where the two analyzed spectra were taken, a thickness of the anode material t_{AM} of about 29 nm and 35 nm was found for $An_{300°C\text{-}5h}$ and $An_{350°C\text{-}1h}$, respectively.
Like for the determination of the thickness of the surface oxide layers grown on reference Nb (cf. section 4.3.7), the calculation of the atomic concentration ratio of the anode material involves several assumptions whose validity could be discussed. For instance, as the stoichiometry of the annealed anode material differs from pure Nb, it is not certain that the passive oxide layers grown at the surface of the anodes are equivalent to those being present on reference Nb. In addition, the accuracy of the quantification procedure is not assured for C_{Nb}/C_O ratios greater than 1. Moreover, the accuracy of the thickness determination on the basis of the the parameterization of Malis et al. (1988) is also limited to ±20%. Thus, the results presented here for the stoichiometry of the annealed anodes can only be considered as rough estimates.

5.2.3 Determination of C_{Nb}/C_O atomic concentration ratios at the VG microscope

Three quantification procedures

At the VG microscope EELS linescans were performed across oxide layers in $Cap_{No\text{-}Anneal}$, $Cap_{300°C\text{-}5h}$, and $Cap_{350°C\text{-}1h}$ (E_0 = 100 keV, β = 6.5 mrad, α = 10 mrad, ΔE = 70 eV). The three types of oxide layers were quantitatively analyzed by means of the Nb-$M_{4,5}$ edges.

For each core-loss linescan a low-loss linescan was also taken. However, owing to specimen drift as well as carbon contamination during the acquisition, it is not assured that the individual spectra of a low-loss linescan were recorded exactly in the same specimen region as the corresponding core-loss spectra. Moreover, the analyzed oxide layers were frequently inhomogeneous in thickness. Hence, the true relative thickness of the specimen regions investigated by a core-loss linescan may sometimes differ from the value measured from the related low-loss spectra. For the same reasons, the use of the low-loss linescans for the *Fourier*-ratio deconvolution of the spectra of the core-loss linescans may also be problematic.

Regarding the reference materials, only seven spectra taken from Nb_2O_5 were available to determine *k*-factors (cf. section 4.3.6). In addition, the reference spectra were recorded form specimen regions with relative thicknesses in a wide range from 0.14 to 0.66, yielding strongly different *k*-factors (without deconvolution, cf. Fig. 4.3.8a). Thus, to take the effects of the specimen thickness into consideration, different combinations of the Nb_2O_5 spectra were used to determine averaged *k*-factors being representative for different relative thickness ranges (cf. Table 4.3.3). Nevertheless, each averaged *k*-factor results from the analysis of only four to six reference spectra. Hence, the statistics is relatively poor and a given *k*-factor will not necessarily enable accurate quantification of spectra taken from specimen regions with t/Λ in the range that it is supposed to represent.

Due to these different inconveniences, the determination of C_{Nb}/C_O atomic concentration ratios at the VG microscope may be uncertain. Thus, three different procedures were applied for quantification to check the sensitivity of the results with respect to the used *k*-factors. In a first procedure, the *k*-factor $k_{NbM4,5\text{-}OK} = 13.86 \pm 0.35$ (±2.5%) derived from five reference spectra taken from specimen regions in a relative-thickness range of 0.21 to 0.46 (corresponding to a mean t/Λ around 0.32, cf. Table 4.3.3) was used to quantify all OL spectra. The results were then averaged for each type of capacitor. In a second procedure, the slightly different *k*-factor $k_{NbM4,5\text{-}OK} = 13.97 \pm 0.30$ (±2.1%) resulting from four reference spectra in the relative-thickness range of 0.26 to 0.46 (mean t/Λ around 0.35, cf. Table 4.3.3) was applied for quantification. The third procedure consisted in using simultaneously the four *k*-factors given in Table 4.3.3 and is termed “mixed *k*-factors”. Here, for each individual oxide layer, the most adequate *k*-factor in terms of relative thickness was applied for quantification, before averaging the results for each type of capacitor. For instance, 25 spectra taken from one and the same oxide layer of $Cap_{No\text{-}Anneal}$ with t/Λ in the range of 0.24 to 0.28 were analyzed via the *k*-factor $k_{NbM4,5\text{-}OK} = 14.05 \pm 0.55$ corresponding to a mean t/Λ of about 0.29 (cf. Table 4.3.3). In contrast, 33 spectra from another region of $Cap_{No\text{-}Anneal}$ with t/Λ raging from 0.41 to 0.46 were quantified by means of the k-factor $k_{NbM4,5\text{-}OK} = 13.57 \pm 0.77$, whose related mean t/Λ amounts to approximately 0.38 (cf. Table 4.3.3).

Table 5.2.1. C_{Nb}/C_O atomic concentration ratios determined from $OL_{No\text{-}Anneal}$, $OL_{300°C\text{-}5h}$, and $OL_{350°C\text{-}1h}$ spectra by means of three procedures involving different *k*-factors (VG HB501UX microscope: E_0 = 100 keV, β = 6.5 mrad, α = 10 mrad, ΔE = 70 eV).

	$OL_{No\text{-}Anneal}$	$OL_{300°C\text{-}5h}$	$OL_{350°C\text{-}1h}$
Number of investigated oxide layers	5	5	4
Number of analyzed core-loss spectra	144	151	130
t/Λ – range $\Rightarrow$ mean t/Λ	0.24 – 0.50 $\Rightarrow$ 0.38	0.32 – 0.65 $\Rightarrow$ 0.43	0.23 – 0.54 $\Rightarrow$ 0.36
C_{Nb}/C_O Quantified by $k_{NbM4,5\text{-}OK}$ = 13.86 ± 0.35 $\Rightarrow Nb_2O_y$	0.405 ± 0.019 (±4.7%) $\Rightarrow Nb_2O_{4.94\pm0.23}$	0.403 ± 0.016 (±4.0%) $\Rightarrow Nb_2O_{4.96\pm0.20}$	0.415 ± 0.024 (±5.8%) $\Rightarrow Nb_2O_{4.82\pm0.28}$
C_{Nb}/C_O Quantified by $k_{NbM4,5\text{-}OK}$ = 13.97 ± 0.30 $\Rightarrow Nb_2O_y$	0.402 ± 0.018 (±4.5%) $\Rightarrow Nb_2O_{4.98\pm0.22}$	0.400 ± 0.015 (±3.8%) $\Rightarrow Nb_2O_{5.00\pm0.19}$	0.412 ± 0.023 (±5.6%) $\Rightarrow Nb_2O_{4.85\pm0.27}$
C_{Nb}/C_O Quantified by mixed *k*-factors $\Rightarrow Nb_2O_y$	0.406 ± 0.021 (±5.2%) $\Rightarrow Nb_2O_{4.93\pm0.25}$	0.406 ± 0.022 (±5.4%) $\Rightarrow Nb_2O_{4.93\pm0.27}$	0.412 ± 0.027 (±6.6%) $\Rightarrow Nb_2O_{4.85\pm0.32}$
Relative deviation between minimal and maximal C_{Nb}/C_O	1.0%	1.5%	0.7%

Results of the quantifications

The quantitative results obtained that way from $OL_{No\text{-}Anneal}$, $OL_{300°C\text{-}5h}$, and $OL_{350°C\text{-}1h}$ are presented in Table 5.2.1. The number of individual oxide layers investigated for each type of capacitor structure is given, as well as the total number of investigated core-loss spectra, the estimated relative-thickness range of the analyzed specimen regions and the corresponding mean relative thickness, the resulting C_{Nb}/C_O atomic concentration ratios determined by the three different procedures together with the corresponding chemical formulas, and finally the relative deviation between the minimum and maximum values found for the C_{Nb}/C_O ratio.

These results are also summarized in a graph (Fig. 5.2.5) showing the C_{Nb}/C_O ratios measured by the three different procedures as a function of the annealing step endured by the oxide layers.

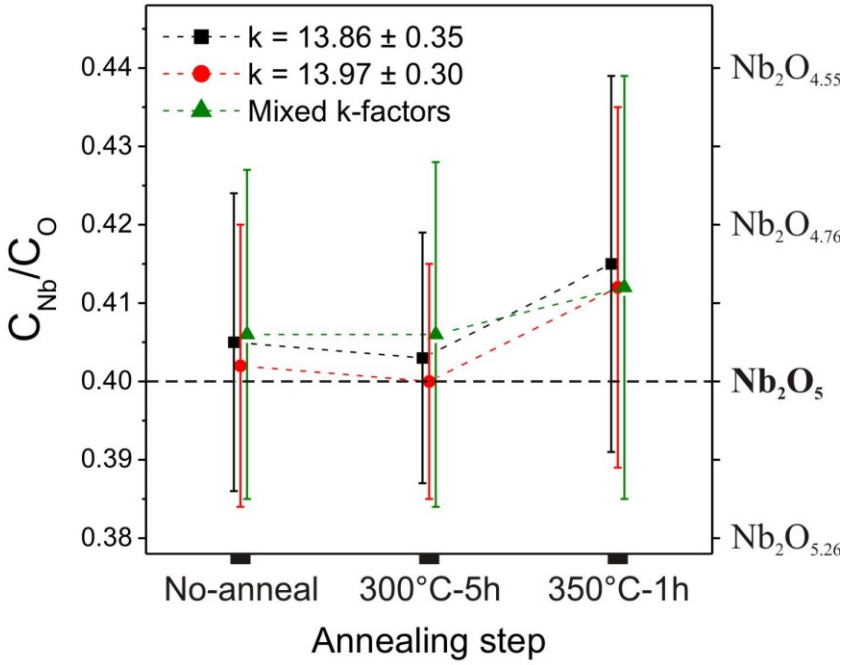

Fig. 5.2.3. C_{Nb}/C_O atomic concentration ratios determined from 144 $OL_{No\text{-}Anneal}$, 151 $OL_{300°C\text{-}5h}$, and 130 $OL_{350°C\text{-}1h}$ spectra by means of three procedures involving different *k*-factors (cf. Table 5.2.1; VG HB501UX microscope: E_0 = 100 keV, β = 6.5 mrad, α = 10 mrad, ΔE = 70 eV).

For each type of oxide layer the mean C_{Nb}/C_O value determined via each procedure indicates an oxygen deficiency with respect to stoichiometric Nb_2O_5 (nominal C_{Nb}/C_O = 0.400), except for $OL_{300°C\text{-}5h}$ whose mean C_{Nb}/C_O ratio is found around 0.400 in agreement with Nb_2O_5 if the quantification is carried out with $k_{NbM4,5\text{-}OK}$ = 13.97 ± 0.30. Taking the standard deviations of the measured C_{Nb}/C_O ratios into consideration, the results obtained for all three types of oxide layer are still compatible with Nb_2O_5 but with a clear trend towards an oxygen deficiency.
Compared to $OL_{No\text{-}Anneal}$ and $OL_{350°C\text{-}1h}$, the results achieved for $OL_{300°C\text{-}5h}$ seem to be more sensitive to the particular quantification procedure. The relative deviation between the maximum value found for the mean C_{Nb}/C_O ratio (0.406 using mixed *k*-factors) and the minimum one (0.400 using $k_{NbM4,5\text{-}OK}$ = 13.97 ± 0.30) amounts to about 1.5%, whereas it is only 1.0% and 0.7% for $OL_{No\text{-}Anneal}$ and $OL_{350°C\text{-}1h}$, respectively. This large relative deviation is due to the strong variation of relative thicknesses related to the $OL_{300°C\text{-}5h}$ spectra (t/Λ up to 0.65, mean $t/\Lambda \sim 0.43$) compared to the Nb_2O_5 specimen regions whose EELS analysis resulted in the *k*-factors $k_{NbM4,5\text{-}OK}$ = 13.86 ± 0.35 (t/Λ up to 0.46, mean $t/\Lambda \sim 0.32$) and $k_{NbM4,5\text{-}OK}$ = 13.97 ± 0.30 (t/Λ up to 0.46, mean $t/\Lambda \sim 0.35$). Hence, the *k*-factor $k_{NbM4,5\text{-}OK}$ = 13.57 ± 0.77, whose determination involved one Nb_2O_5 spectrum recorded at t/Λ = 0.66, is often used to quantify the $OL_{300°C\text{-}5h}$ spectra by the mixed *k*-factors procedure. This leads to quite different results than the use of solely $k_{NbM4,5\text{-}OK}$ = 13.86 ± 0.35 or

$k_{NbM4,5\text{-}OK} = 13.97 \pm 0.30$ for quantification, yielding the large relative deviation observed. It could be expected that the use of an averaged *k*-factor including the Nb_2O_5 spectrum with $t/\Lambda = 0.66$ to quantify $OL_{300°C\text{-}5h}$ would lead to valid results. Nevertheless, the individual *k*-factor resulting from this spectrum is strongly different from those achieved with the other Nb_2O_5 spectra (see Fig. 4.3.8a). Hence, its inclusion to the statistics determining an averaged *k*-factor results in a low precision (e.g. ± 5.7% for $k_{NbM4,5\text{-}OK} = 13.57 \pm 0.77$) and probably also in a poor quantitative accuracy. Thus, the large relative deviation found for the C_{Nb}/C_O ratio of $OL_{300°C\text{-}5h}$ indicates that the results may be inaccurate.

The relative thicknesses measured for the spectra of $OL_{No\text{-}Anneal}$ (t/Λ up to 0.50, mean $t/\Lambda \sim 0.38$) and $OL_{350°C\text{-}1h}$ (t/Λ up to 0.54, mean $t/\Lambda \sim 0.36$) are also slightly higher than those corresponding to $k_{NbM4,5\text{-}OK} = 13.86 \pm 0.35$ (t/Λ up to 0.46, mean $t/\Lambda \sim 0.32$). The agreement in terms of thickness is better with $k_{NbM4,5\text{-}OK} = 13.97 \pm 0.30$ (t/Λ up to 0.46, mean $t/\Lambda \sim 0.35$). However, due to the low statistics (few reference spectra) yielding the averaged *k*-factors and the uncertainties of the relative-thickness measurements, the *k*-factor $k_{NbM4,5\text{-}OK} = 13.97 \pm 0.30$ is not necessarily better than $k_{NbM4,5\text{-}OK} = 13.86 \pm 0.35$ to quantify $OL_{No\text{-}Anneal}$ and $OL_{350°C\text{-}1h}$.

No clear trend is observed in the evolution of the C_{Nb}/C_O ratio of the oxide layers if an annealing step at 300°C for 5 h is applied to the capacitor structures. Quantification using mixed *k*-factors indicates the same C_{Nb}/C_O ratio for $OL_{No\text{-}Anneal}$ as for $OL_{300°C\text{-}5h}$ ($C_{Nb}/C_O \sim 0.406$), whereas a very slight decrease of the C_{Nb}/C_O ratio with annealing is suggested for $k_{NbM4,5\text{-}OK} = 13.86 \pm 0.35$ (from 0.405 to 0.403) and $k_{NbM4,5\text{-}OK} = 13.97 \pm 0.30$ (from 0.402 to 0.400). However, this apparent decrease could result from quantification errors related to the difference in thickness between $OL_{No\text{-}Anneal}$ and $OL_{300°C\text{-}5h}$ (see above). In contrast, a clear increase of C_{Nb}/C_O is observed if the oxide layers are annealed at 350°C for 1 h (see Table 5.2.1 and Fig. 5.2.5). As the relative thicknesses of the specimen regions investigated for $OL_{No\text{-}Anneal}$ (t/Λ in the range of 0.24 to 0.50, mean $t/\Lambda \sim 0.38$) are quite similar to those of $OL_{350°C\text{-}1h}$ (t/Λ in the range of 0.23 to 0.54, mean $t/\Lambda \sim 0.36$), the comparison between the resulting C_{Nb}/C_O ratios is significant. By averaging the results of the three procedures, mean C_{Nb}/C_O ratios of about 0.404 and 0.413 are found for $OL_{No\text{-}Anneal}$ and $OL_{350°C\text{-}1h}$, respectively, corresponding to a relative deviation of approximately 2.2%.

Non-uniformity of the results of one and the same type of capacitor structure

By investigating one and the same type of capacitor structure, quite significant discrepancies are sometimes achieved for the C_{Nb}/C_O ratios averaged from two different oxide layers. This effect appears independent of the specimen thickness and could be observed for all three types of capacitor structures, i.e. with or without annealing. The analysis of two oxide layers anodically grown on two different niobium grains (anode) of one capacitor is presented as an example. The two oxide layers were investigated in one and the same $Cap_{No\text{-}Anneal}$ TEM sample on the same day. For each oxide layer, 28 spectra were taken. The relative thicknesses of the measured specimen regions in the first layer range from 0.33 to 0.42 (mean $t/\Lambda \sim 0.36$) and are almost identical to the relative thicknesses within the second layer, which are estimated to be between 0.35 and 0.40 (mean $t/\Lambda \sim 0.38$). The two oxide layers were quantified by means of the same *k*-factor $k_{NbM4,5\text{-}OK} = 13.97 \pm 0.30$, yielding

$C_{Nb}/C_O = 0.412 \pm 0.023$ (±5.6%) in the first case and $C_{Nb}/C_O = 0.396 \pm 0.014$ (±3.5%) in the second. The relative deviation between the mean C_{Nb}/C_O values of the two layers amounts to about 4.0%. This is more than the standard deviation achieved from the analysis of the 28 spectra of the second layer (~3.5%), which seems to exclude random statistical errors occurring during the acquisition and the quantitative investigation of each individual spectrum as the origin of this strong discrepancy measured for the two layers.

Besides the specimen thickness, further experimental factors can influence the mean C_{Nb}/C_O value found for one layer. For both investigated layers, a large dispersion of 0.5 eV per channel was used to record the EEL spectra. Thus, the intensity measured under the delayed-maximum Nb-$M_{4,5}$ edges is particularly sensitive to the positioning of the integration window (see section 4.4.6). In addition, for each layer one and the same integration window under the Nb-$M_{4,5}$ edges is applied to analyze all the spectra of the linescan. Hence, an inappropriate positioning of this integration window can similarly affect the $I_{NbM4,5}/I_{OK}$ intensity ratios measured from all the different spectra and thus the resulting mean C_{Nb}/C_O ratio. As a test, the second layer was reanalyzed. The 70 eV wide integration window under the Nb-$M_{4,5}$ edges was shifted by one channel (0.5 eV) to higher energies, yielding $C_{Nb}/C_O = 0.401 \pm 0.014$. A shift by one channel to lower energies resulted in $C_{Nb}/C_O = 0.391 \pm 0.014$. Thus, a total difference of two channels (1 eV) in the positioning of the window corresponds to a relative deviation of 2.5 % between the two resulting mean C_{Nb}/C_O ratios (0.401 and 0.391). This is lower than the relative deviation of the mean C_{Nb}/C_O ratios of the two layers (4.0%). Moreover, for one given layer several spectra of the linescan were checked in order to position the integration window, and in case of doubt the position was chosen in such a way that the discrepancy between the two layers is reduced. Hence, an error of two channels or more in the positioning of the integration window is improbable, and the uncertainties related to the choice of the position cannot alone explain the stoichiometry difference measured for the two layers.

Carbon contamination can lead to an overestimation of the relative thickness of the oxide layers. Thus, discrepancies in the determined C_{Nb}/C_O ratios could also result from different thicknesses. However, in the present case, for both investigated oxide layers the effects of carbon contamination were negligible.

Hence, the different mean C_{Nb}/C_O ratios measured from the two oxide layers suggest that there may be stoichiometry inhomogeneities from one oxide layer to another within the same capacitor structure. Nevertheless, as will be discussed in section 5.4.4, argon contamination occurring during the preparation of TEM samples can induce an overestimation of the C_{Nb}/C_O ratio measured by EELS and could thus contribute to apparent differences in the stoichiometry of the two oxide layers.

Furthermore, it can be noticed that the standard deviation found for the C_{Nb}/C_O ratio of the first layer amounts to ±5.6% in contrast to only ±3.5% for the second layer. Hence, this suggests that the first nanoscale oxide layer may be more inhomogeneous in stoichiometry than the second one. The results of the investigation of the capacitor structures at a nanometer scale by means of the VG microscope are presented in more detail in the following subchapter.

5.3 The nanochemistry of capacitor structures

Stoichiometry gradients and inhomogeneities within the capacitor oxide layers as well as at the interfaces between the "niobium" anodes (An, may in fact consist of NbO_x with $0 < x < 1$, see section 5.2.2) and the oxide layers (OL) were quantitatively examined at nanometer scale for $Cap_{No\text{-}Anneal}$, $Cap_{300°C\text{-}5h}$, and $Cap_{350°C\text{-}1h}$ using the VG HB501UX scanning transmission electron microscope. EELS linescans were performed across the interfaces and within the oxide layers. The electron probe was about 0.5 nm in diameter and during one given linescan either low-loss or core-loss spectra were taken with a spatial frequency of typically one spectrum per 2 or 2.5 nm. As an example, the results achieved from one core-loss linescan and corresponding low-loss linescan across one and the same An-OL interface of $Cap_{No\text{-}Anneal}$ are presented in Fig. 5.3.1. Fig. 5.3.1a shows a scanning transmission electron microscopy (STEM) dark-field (DF) image of the investigated specimen region. The contrast in such an image is amongst others related to the structure of the investigated material, allowing a clear distinction between the crystalline anode and the amorphous oxide layer. Indeed, whereas an amorphous specimen region is characterized (at constant thickness) by a homogeneous gray-scale value, a crystalline material presents strong contrast fluctuations with coexistent white and dark areas. In addition, the contrast in crystalline specimen regions is strongly dependent on the orientation of the material with respect to the incident electron beam. Furthermore, it can be noted that vacuum regions (holes in the specimen) appear black. For each linescan, a series of 50 spectra was acquired along a 120 nm long line represented by an arrow in Fig. 5.3.1a. The two linescans were performed side by side at slightly different positions within the specimen. The 50 core-loss spectra are visible in Fig. 5.3.1b as a function of the position of the electron probe during the scan. They were recorded at a dispersion of 0.3 eV per channel in the energy range of approximately 180 eV to 580 eV so that the Nb-$M_{4,5}$ and the O-K edges could be taken in one and the same run. The occurrence of oxygen in the Nb anode is attributed to native oxide layers (see sections 5.1.5 and 5.2.2). In order to investigate stoichiometry gradients or inhomogeneities within one oxide layer, the determination of the absolute values of the C_{Nb}/C_O atomic concentration ratios is not systematically required. The $I_{NbM4,5}/I_{OK}$ intensity ratios, which are directly proportional to the C_{Nb}/C_O ratios, may be sufficient (see section 4.3.2). In fact, the analysis of the $I_{NbM4,5}/I_{OK}$ ratios allows a more precise characterization of the homogeneity of the layer. While averaging the results from several OL spectra, the standard deviation achieved for the C_{Nb}/C_O ratio is artificially amplified compared to that of the $I_{NbM4,5}/I_{OK}$ ratio owing to the imprecision of the *k*-factor used to determine C_{Nb}/C_O from $I_{NbM4,5}/I_{OK}$. The $I_{NbM4,5}/I_{OK}$ intensity ratios derived from the 50 core-loss spectra are given in Fig. 5.3.1c. Since the spectra end at an energy loss of about 580 eV, integration windows of only 40 eV in width were used in that particular case to measure the intensities under the Nb-$M_{4,5}$ and O-K edges (70 eV wide windows are generally used, but this requires spectra ending above 600 eV to integrate the O-K intensity). The relative thickness t/Λ determined from the low-loss spectra is shown in Fig. 5.3.1d. The investigated layer appears homogeneous in thickness. The analysis of 32 spectra taken within

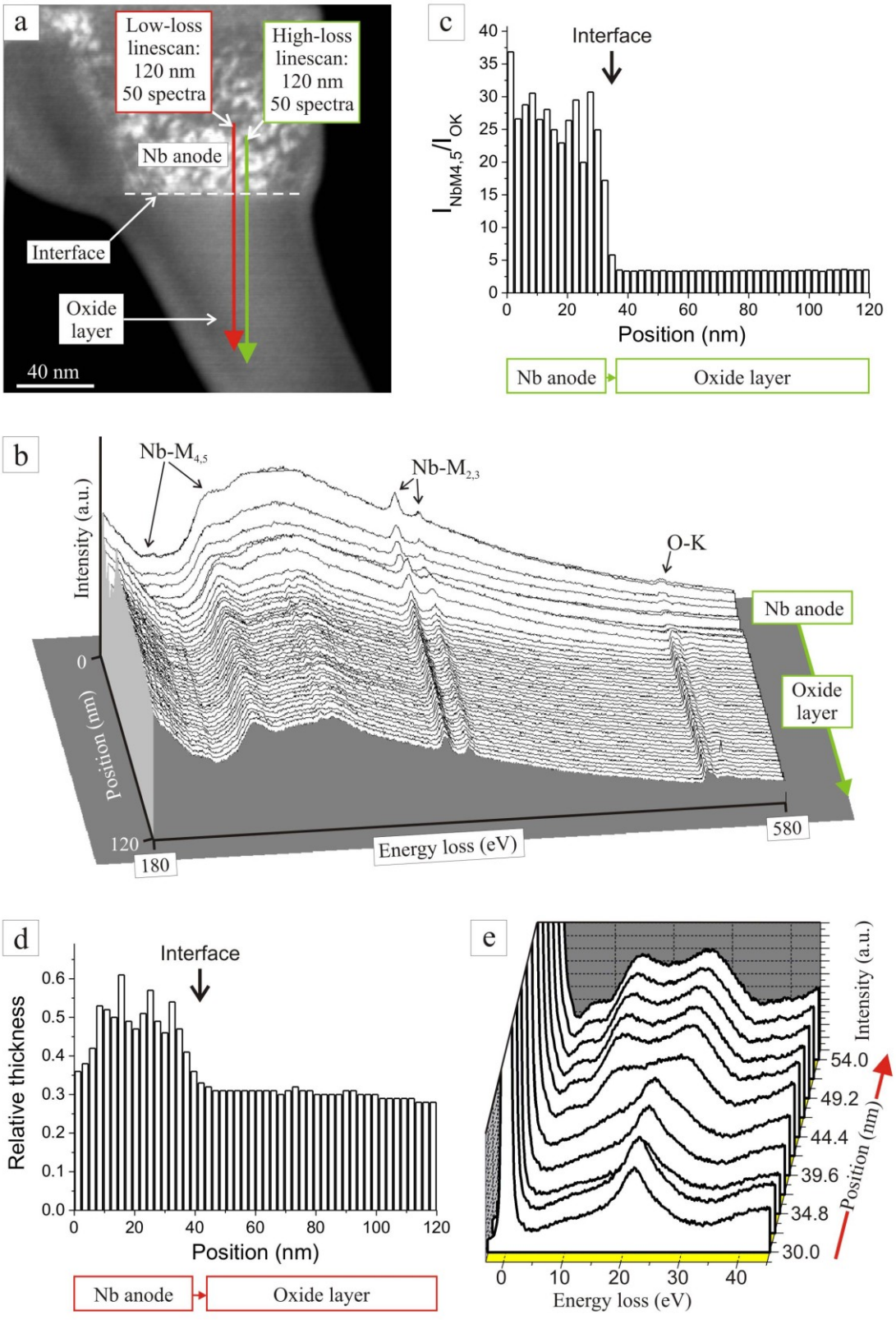

Fig. 5.3.1. EELS linescans performed across one An-OL interface of $Cap_{No\text{-}Anneal}$ (VG HB501UX microscope: $E_0 = 100$ keV, $\beta = 6.5$ mrad, $\alpha = 10$ mrad): **a)** STEM-DF image, **b)** series of 50 core-loss spectra taken along a line of about 120 nm (cf. arrow in Fig. 5.3.1a), **c)** $I_{NbM4,5}/I_{OK}$ intensity ratios derived from the 50 core-loss spectra ($\Delta E = 40$ eV), **d)** relative thickness determined from a series of 50 low-loss spectra taken along a line of about 120 nm (cf. arrow in Fig. 5.3.1a), **e)** 11 spectra from the low-loss series showing the transition between the anode and the oxide layer.

a 77 nm long path yields a relative thickness in the range of 0.28 to 0.32 corresponding to a mean t/Λ around 0.30. No significant stoichiometry gradient is observed in the oxide layer. A $I_{NbM4,5}/I_{OK}$ ratio of 3.36 ± 0.07 (±2.1%) is achieved by averaging 34 spectra acquired along a 82 nm line. The standard deviation (±2.1%) is quite low and indicates that the chemical composition of the oxide layer is homogeneous at a nanometer scale. The sharpness of the interface between the Nb anode and the oxide layer can be analyzed by considering the evolution of the measured $I_{NbM4,5}/I_{OK}$ intensity ratios as well as by investigating the fingerprints of the EELS features. Particularly the plasmons are appropriate to distinguish Nb from the oxide layer (cf. Fig. 4.2.2a and Fig. 5.1.1a). In the present case, only one core-loss spectrum (taken about 34 nm from the starting point during the core-loss scan) clearly yields an intermediate $I_{NbM4,5}/I_{OK}$ value (~ 5.81) between those typically achieved for the anode (around 20-25, the imprecision is due do thickness effects and the low signal-to-noise ratio of the O-K edge) and the oxide layer (around 3.36). Fig. 5.3.1e reveals 11 spectra from the low-loss series showing the plasmon energy range and taken along a line of about 24 nm across the interface. The transition from a Nb character of the plasmon to an OL one occurs within two spectra taken at around 39.6 nm and 42 nm in the low-loss scan. Hence, the observation of both the $I_{NbM4,5}/I_{OK}$ intensity ratio and the plasmon fingerprint indicates a sharp interface of less than about 5 nm in width.
The results from the investigations of other oxide layers and An-OL interfaces in $Cap_{No\text{-}Anneal}$, $Cap_{300°C\text{-}5h}$, and $Cap_{350°C\text{-}1h}$ are presented in the following.

5.3.1 Stoichiometry gradients and inhomogeneities within the capacitor oxide layers

Stoichiometry gradients

While analyzing a core-loss linescan performed perpendicularly to an An-OL interface, the $I_{NbM4,5}/I_{OK}$ ratios measured within the oxide layer sometimes present a slight gradient as a function of the distance to the interface. This is observed for the three types of capacitors. However, several experimental effects independent of the true stoichiometry in the oxide layer can explain these variations.
The investigated oxide layers were often affected by thickness gradients, i.e. the relative thickness decreases generally as the distance from the An-OL interface increases. Such a gradient can induce lower $I_{NbM4,5}/I_{OK}$ ratios at the interface in comparison to those measured inside the oxide layer (cf. section 5.2.1 and Fig. 5.2.1). As an example, Fig. 5.3.2 shows the relative thickness and the $I_{NbM4,5}/I_{OK}$ ratios determined within an oxide layer of $Cap_{350°C\text{-}1h}$ as a function of the approximate distance to the An-OL interface. In this quite extreme case, a strong gradient of the relative thickness from about 0.51 at the interface to 0.25 at approximately 63 nm inside the layer is measured from a low-loss linescan. As a consequence, with rising distance from the interface a clear increase of the $I_{NbM4,5}/I_{OK}$ ratio is indicated by the linear fit to the experimental data resulting from the quantitative analysis of a core-loss linescan. Nevertheless, it should be noticed that the two series of spectra (low-loss and core-loss) were not taken exactly along the same line within the oxide layer, so that the

specimen positions where the relative thickness was measured are not one-to-one identical to those checked for stoichiometry.

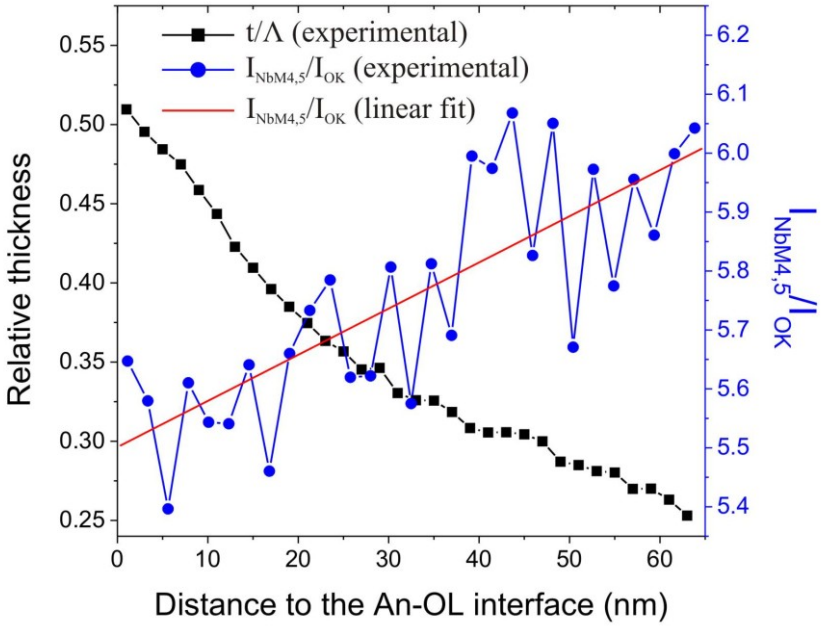

Fig. 5.3.2. Relative thickness t/Λ and $I_{NbM4,5}/I_{OK}$ intensity ratio measured within an oxide layer of $Cap_{350°C\text{-}1h}$ (VG HB501UX microscope: E_0 = 100 keV, β = 6.5 mrad, α = 10 mrad). The t/Λ and $I_{NbM4,5}/I_{OK}$ ratios were determined from one low-loss and one core-loss linescan, respectively. 70 eV wide integration windows were used to measure the $I_{NbM4,5}/I_{OK}$ intensity ratios. The results are presented as a function of the approximate distance to the An-OL interface. The experimental $I_{NbM4,5}/I_{OK}$ data were fitted by means of a linear function.

An $I_{NbM4,5}/I_{OK}$ gradient can also result from a spectrum drift occurring in the energy-dispersive axis of the detector system during the collection of a series of EEL spectra. Indeed, for the analysis of a given core-loss linescan, one and the same position of the integration window under the Nb-$M_{4,5}$ edges was chosen to quantify all the acquired spectra. Hence, a spectrum drift acts like a shift of the integration window, yielding an artificial variation of the measured $I_{NbM4,5}/I_{OK}$ ratios (cf. sections 4.4.6 and 5.2.3 for more information concerning the influence of the position of the integration window under the Nb-$M_{4,5}$ on $I_{NbM4,5}/I_{OK}$).
In addition, an inhomogeneous carbon contamination during the recording of a series of EEL spectra can also perturb the resulting $I_{NbM4,5}/I_{OK}$ ratios.
All the $I_{NbM4,5}/I_{OK}$ gradients detected in the oxide layers of $Cap_{No\text{-}Anneal}$, $Cap_{300°C\text{-}5h}$, and $Cap_{350°C\text{-}1h}$ could be correlated with at least one of the above-mentioned experimental effects. Hence, none of these gradients could clearly be related to a true variation of the chemical composition in the capacitor oxide layer.

Stoichiometry inhomogeneities within one and the same oxide layer

In section 5.2.3 it was already mentioned that one oxide layer may appear more inhomogeneous in stoichiometry than another one. As an example, the quantitative results of the core-loss linescans performed within two different oxide layers of $Cap_{No\text{-}Anneal}$ are given in

Fig. 5.3.3. The measured $I_{NbM4,5}/I_{OK}$ intensity ratios are presented as a function of the approximate distance to the An-OL interface.

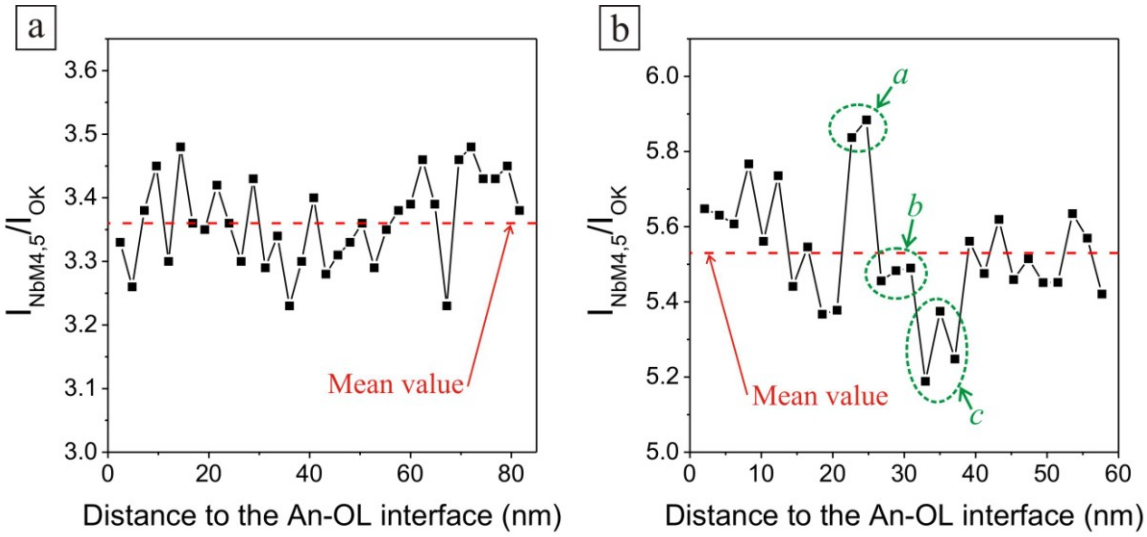

Fig. 5.3.3. $I_{NbM4,5}/I_{OK}$ intensity ratio measured within two oxide layers of $Cap_{No\text{-}Anneal}$ as a function of the approximate distance to the An-OL interface (core-loss linescans at the VG HB501UX microscope: $E_0 = 100$ keV, $\beta = 6.5$ mrad, $\alpha = 10$ mrad). **(a)** A 40 eV wide integration window was used to determine the $I_{NbM4,5}/I_{OK}$ intensity ratios within the first layer whereas it amounted to 70 eV for the second layer **(b)**. The red dashed lines represent the $I_{NbM4,5}/I_{OK}$ mean values of the two layers. The oxide layer shown in **(a)** appears quite homogeneous, but that visible in **(b)** exhibits inhomogeneities (letters *a*, *b*, and *c*).

Fig. 5.3.3a corresponds to the oxide layer whose investigation resulted in the data shown in Fig. 5.3.1. The relative thickness of the layer was found to be relatively constant, ranging from 0.28 to 0.32. A series of 34 spectra taken along a line of about 77 nm yields on average $I_{NbM4,5}/I_{OK} = 3.36 \pm 0.07$ (±2.1%) by using 40 eV wide integration windows for quantification. The individual $I_{NbM4,5}/I_{OK}$ values achieved by analyzing the spectra one by one appear as statistical noise around the mean value. Such a statistical dispersion of the quantitative results is the most common behavior observed when investigating an oxide layer. It was already mentioned that the standard deviation achieved from the averaging of all the individually determined $I_{NbM4,5}/I_{OK}$ ratios can be regarded as a measure for the stoichiometric homogeneity of a layer. In the present case it is relatively low and amounts to 2.1%. This is for instance comparable with the standard deviation obtained for the *k*-factor $k_{NbM4,5\text{-}OK} = 13.97 \pm 0.30$ (±2.1%) determined from four reference Nb_2O_5 spectra taken from specimen regions with t/Λ in the range of 0.26 to 0.46 at the VG microscope (see Table 4.3.3). Hence, the oxide layer seems to have a homogeneous stoichiometry. However, the analysis of other layers often led to larger fluctuations of the individual $I_{NbM4,5}/I_{OK}$ ratios around their mean value. Fig. 5.3.3b shows the results gained from an oxide layer having a relative thickness ranging from about 0.35 to 0.40. A series of 28 spectra was acquired along a line of about 58 nm within the oxide layer, resulting in $I_{NbM4,5}/I_{OK} = 5.53 \pm 0.16$ (±2.9%) by means of 70 eV wide integration windows. In that particular case, the distribution of the individually measured $I_{NbM4,5}/I_{OK}$

values does not seem to be purely statistical. Indeed, small groups of consecutive spectra are visible showing similar $I_{NbM4,5}/I_{OK}$ ratios. In Fig. 5.3.3b three groups are for instance marked by the letters *a*, *b*, and *c*. The relative deviation between the minimum and maximum $I_{NbM4,5}/I_{OK}$ ratios measured within a given group amounts to 0.8%, 0.6%, and 3.5% for the groups *a*, *b*, and *c*, respectively. In contrast, the relative deviation between the mean $I_{NbM4,5}/I_{OK}$ value of group *a* (~ 5.86) and that of group *c* (~ 5.27) is as high as 10.6%. This suggests that the discrepancies observed between the $I_{NbM4,5}/I_{OK}$ values of the different groups could be related to true stoichiometry inhomogeneities in the oxide layer and not only to random errors affecting the EELS quantification procedure. However, it should be noted that the investigation of the O-K ELNES did not allow to clearly distinguish the different groups. Such a behavior of the individual $I_{NbM4,5}/I_{OK}$ ratios determined across a layer was not frequently observed. However, similar effects could also be measured for a few oxide layers in the annealed capacitor structures.

In order to examine the influence of the annealing on the stoichiometry of the oxide layers, the standard deviations of the $I_{NbM4,5}/I_{OK}$ ratios resulting from the linescan investigation of different oxide layers were averaged. Eight, six, and eight oxide layers were analyzed for $Cap_{No\text{-}Anneal}$, $Cap_{300°C\text{-}5h}$, and $Cap_{350°C\text{-}1h}$, respectively. The relative thickness of the investigated specimen regions was found to range from 0.22 to 0.70. For each layer, 14 to 37 core-loss spectra were taken along lines of about 22 nm to 83nm. Each spectrum was recorded at a dispersion of 0.5 eV per channel and quantified by means of 70 eV wide integration windows to determine $I_{NbM4,5}/I_{OK}$. The resulting intensity ratios were averaged for each layer, yielding a mean $I_{NbM4,5}/I_{OK}$ value and a corresponding standard deviation. Hence, eight, six, and eight different standard deviations were determined for $Cap_{No\text{-}Anneal}$, $Cap_{300°C\text{-}5h}$, and $Cap_{350°C\text{-}1h}$, respectively. These standard deviations were averaged for each type of capacitor structure, resulting in a mean standard deviation of about 3.21% for the oxide layers of $Cap_{No\text{-}Anneal}$, 3.11% for $Cap_{300°C\text{-}5h}$, and 3.46% in the case of $Cap_{350°C\text{-}1h}$. It should mentioned that the reliability of the quantitative analysis of some of the linescans implemented in this statistics was deteriorated by an inhomogeneous specimen thickness, spectrum drift or carbon contamination. All these experimental drawbacks have the tendency to artificially amplify the achieved standard deviation. Hence, the here obtained standard deviations are not necessarily comparable with those derived by averaging quantitative results from reference oxides (for instance while determining *k*-factors, see Table 4.3.3). In addition, during the analysis it was observed that the size and position of the windows used for background extrapolation under the Nb-$M_{4,5}$ and O-K edges can also influence the standard deviation resulting from a series of spectra. However, the three types of capacitor structures are expected to suffer in equal measure from these spectrum-processing artefacts, so that the comparison between the mean standard deviations (MSD) resulting from the different capacitors should still make sense. These mean standard deviations are close to each other. The MSD of $Cap_{350°C\text{-}1h}$ (3.46%) appears slightly higher than that found for $Cap_{No\text{-}Anneal}$ (3.21%), however, the discrepancy is small and considering the uncertainties of the estimation procedure of the mean standard deviations no clear conclusion can be drawn concerning an eventual deterioration of the

stoichiometric homogeneity of the oxide layers at a nanometer scale owing to an annealing step of 1 h at 350°C.

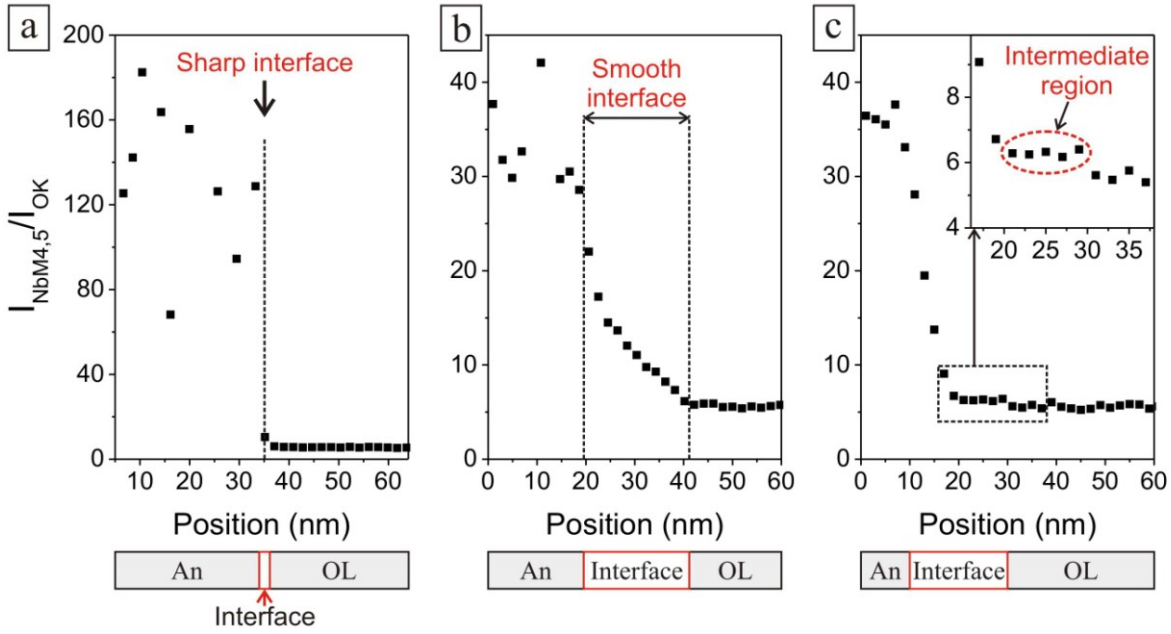

Fig. 5.3.4. $I_{NbM4,5}/I_{OK}$ intensity ratio as a function of the position of the electron probe during three core-loss linescans across different An-OL interfaces of $Cap_{No\text{-}Anneal}$ (a) and $Cap_{300°C\text{-}5h}$ (b and c). The linescans were performed at the VG HB501UX microscope ($E_0 = 100$ keV, $\beta = 6.5$ mrad, $\alpha = 10$ mrad) and 70 eV wide integration windows were used to determine the $I_{NbM4,5}/I_{OK}$ ratios. These quantitative results illustrate the three categories of An-OL interfaces: **(a)** sharp interface, **(b)** smooth interface, and **(c)** interface with intermediate region.

5.3.2 The nanochemistry of the interface between Nb anode and oxide layer

The An-OL interfaces were classified into three different categories depending on their apparent sharpness when investigated by means of EELS linescans. For each category, the quantitative results of a core-loss linescan across a representative interface are shown as an example in Fig. 5.3.4. The interface is said to be sharp when only one or two spectra taken along a line of less than 5 nm present intermediate characteristics between those typical for the anode and the oxide layer (see Fig. 5.3.4a or Fig. 5.3.1c and Fig. 5.3.1e). It is described as smooth when the transition between anode and oxide layer seems to take place within more than 5 nm and the characteristics of the corresponding spectra vary continuously. For instance, in the quite extreme case shown in Fig. 5.3.4b the An-OL interface presents an $I_{NbM4,5}/I_{OK}$ gradient of about –0.8 per nm measured from 11 spectra taken along a line of approximately 20 nm. Finally, the third category of interface is characterized by the presence of an intermediate region, where at least three spectra taken along a line of more than 5 nm show similar characteristics being intermediate relative to those of the anode and the oxide layer. Quantitative results of the investigation of anodes are also visible in Fig. 5.3.4. To understand these results it should be recalled here that the absolute value measured for

$I_{NbM4,5}/I_{OK}$ within the "Nb" anode strongly depends on the specimen thickness and on the annealing step suffered by the capacitor structure (cf. sections 4.3.7 and 5.2.2). In addition, as the signal-to-noise and signal-to-background ratios of the O-K edge decrease the error related to the measurements of I_{OK} becomes very large. Hence, the standard deviation of several $I_{NbM4,5}/I_{OK}$ measurements within one and the same anode can be particularly high, especially when the mean $I_{NbM4,5}/I_{OK}$ value is large (as for instance in Fig. 5.3.4a).

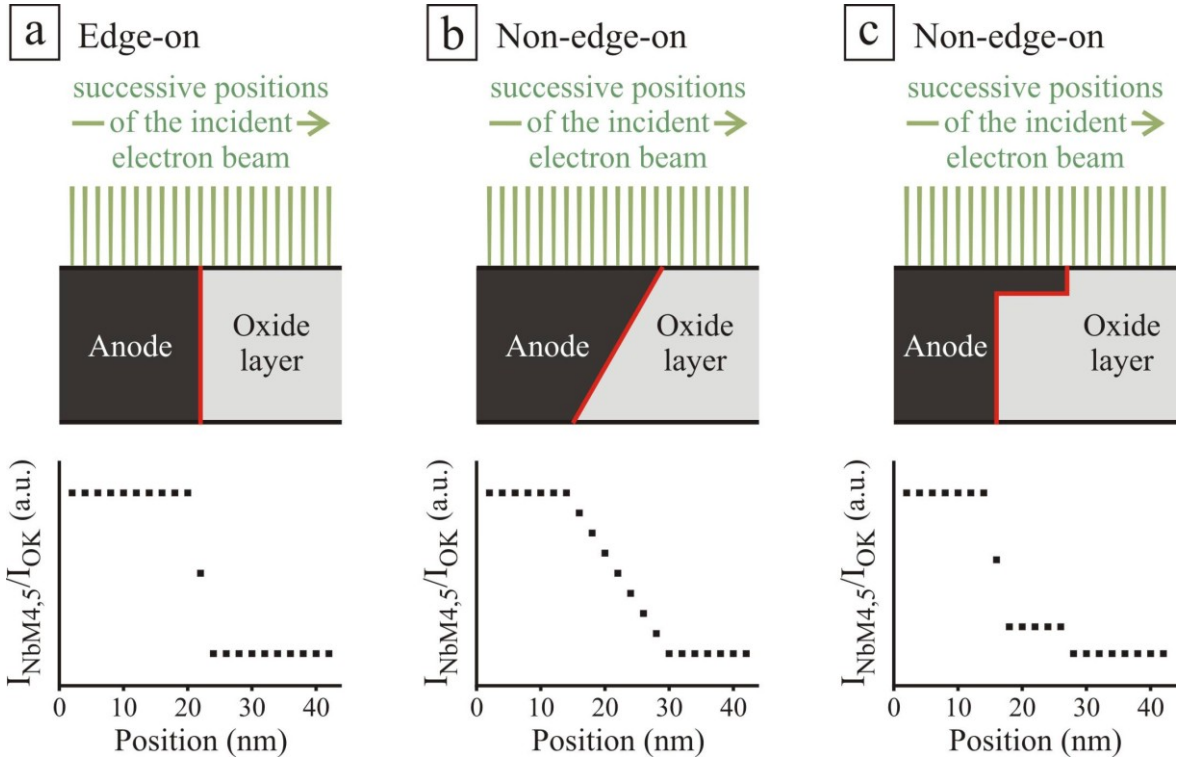

Fig. 5.3.5. Schemas of three ideally sharp An-OL interfaces (red lines) and of the $I_{NbM4,5}/I_{OK}$ intensity ratios expected from three series of 21 core-loss spectra taken along lines of 40 nm across the interfaces (probe size of 0.5 nm in diameter). Three different orientations of the interfaces with respect to the incident electron beam are represented: **(a)** edge-on, **(b)** and **(c)** non-edge-on.

Sharp interfaces as defined above were only observed while investigating $Cap_{No\text{-}Anneal}$. However, for $Cap_{No\text{-}Anneal}$ just as well as in the case of $Cap_{300°C\text{-}5h}$ and $Cap_{350°C\text{-}1h}$, most of the investigated interfaces appeared to be smooth. Hence, under the assumption that EELS linescan analyses allow an accurate measurement of the width of the interfaces, the fact that both sharp and smooth interfaces were detected in $Cap_{No\text{-}Anneal}$ would signify that from the beginning, i.e. already before annealing, the An-OL interfaces were not identical within the capacitor structures. Nevertheless, a smooth appearance can also be interpreted as being an effect of the orientation of a sharp interface with respect to the incident electron beam. Fig. 5.3.5 schematically shows the expected $I_{NbM4,5}/I_{OK}$ intensity ratios as a function of the position of the incident electron beam during a core-loss linescan in the case of an ideally sharp An-OL interface. Fig. 5.3.5a corresponds to an edge-on orientation of the interface in

relation to the incident electrons, i.e. the electron beam is parallel to the interface, whereas Fig. 5.3.5b and Fig. 5.3.5c present different non-edge-on orientations. Particularly the orientation illustrated in Fig. 5.3.5b would lead to the measurement of an $I_{NbM4,5}/I_{OK}$ gradient, i.e. to an apparently smooth interface. Thus, the fact that no sharp An-OL interface could be detected in $Cap_{300°C\text{-}5h}$ and $Cap_{350°C\text{-}1h}$ does not necessarily imply that the investigated interfaces are not sharp.

However, besides this consideration, the results as a whole seem to indicate that annealing yields a broadening of the An-OL interfaces. EELS linescans were performed across eight, seven, and nine An-OL interfaces of $Cap_{No\text{-}Anneal}$, $Cap_{300°C\text{-}5h}$, and $Cap_{350°C\text{-}1h}$, respectively. For each interface, two series of 50 low-loss and 50 core-loss spectra, respectively, were taken along two lines of about 100 nm crossing the interface at slightly different positions. Hence, the sharpness of each interface can be estimated by investigating both the $I_{NbM4,5}/I_{OK}$ intensity ratio and the plasmon fingerprint (cf. the introduction to subchapter 5.3). All the core-loss spectra were analyzed using 70 eV wide integration windows to determine $I_{NbM4,5}/I_{OK}$. For the three types of capacitor structures the investigated interfaces were selected in the TEM samples according to one and the same criterion: interfaces were searched which appeared sharp by means of STEM-DF imaging, namely with a strong contrast between anode and oxide layer (like for instance the interface visible in Fig. 5.3.1a) so as to enhance the chances to be in an edge-on configuration. Thus, under the assumption that the proportion of edge-on interfaces is the same in each capacitor TEM sample (without tilting the sample, i.e. when the sample plane is perpendicular to the incident electron beam), the probability that any investigated interface is effectively edge-on oriented should be the same for the three types of capacitor structures. Hence, for each type of capacitor structure averaging the results from the linescan analyses of all the investigated An-OL interfaces is expected to yield a measure for the interface sharpness which should allow to compare $Cap_{No\text{-}Anneal}$, $Cap_{300°C\text{-}5h}$, and $Cap_{350°C\text{-}1h}$ with each other. The low-loss and core-loss analyses of the eight, seven, and nine An-OL interfaces of $Cap_{No\text{-}Anneal}$, $Cap_{300°C\text{-}5h}$, and $Cap_{350°C\text{-}1h}$, respectively, result in averaged interfaces widths of 11.0 ± 8.2 nm, 14.3 ± 6.8 nm, and 15.5 ± 9.4 nm, respectively. Thus, by considering the found mean values (11.0 nm, 14.3 nm, and 15.5 nm for $Cap_{No\text{-}Anneal}$, $Cap_{300°C\text{-}5h}$, and $Cap_{350°C\text{-}1h}$) the annealing seems to have a non-negligible influence on the sharpness of the An-OL interfaces. In this perspective, it would mean that the smooth interfaces observed in the annealed capacitor structures cannot only be a result of the non-edge-on orientations of actually sharp interfaces, but are also related to true smooth stoichiometry gradients at the An-OL interfaces. Nevertheless, these results should be considered with caution. Indeed, for a given type of capacitor structure the different values measured for the interface width show a very large variation. As an example, the widths measured for $Cap_{350°C\text{-}1h}$ range from 6 nm to 36 nm, yielding a large standard deviation of 9.4 nm while averaging all the results. This wide distribution of the results together with the low number of investigated interfaces make the present statistics particularly instable: adding (removing) the result of only one linescan to (from) the statistics of one given capacitor structures can lead to a significant variation of the averaged value obtained for the width of the An-OL interface.

The third category of interfaces (characterized by an intermediate region, see Fig. 5.3.4c) was not clearly observed in $Cap_{No\text{-}Anneal}$. It was measured once in $Cap_{300°C\text{-}5h}$ (cf. Fig. 5.3.4c). Nevertheless, the observation of such an interface can be interpreted by the superposition of the anode material with the oxide layer in the axis of incident electron beam, as schematized in Fig. 5.3.5c for an ideally sharp An-OL interface. Only in $Cap_{350°C\text{-}1h}$, intermediate regions in the $I_{NbM4,5}/I_{OK}$ profiles resulting from core-loss linescans could be correlated with STEM-DF and –high angle annular dark-field (HAADF) observations as well as with plasmon-fingerprint and OK-ELNES results. They clearly indicate the presence of an intermediate niobium-oxide phase at the An-OL interface. Such consistent results were not obtained for $Cap_{No\text{-}Anneal}$ and $Cap_{300°C\text{-}5h}$, suggesting an influence of the annealing step of 1 h at 350°C on the An-OL interfaces. The analysis of this intermediate phase in $Cap_{350°C\text{-}1h}$ is presented in more detail in the following section.

5.3.3 Crystallites at the An-OL interface of $Cap_{350°C\text{-}1h}$

Fig. 5.3.6a presents a STEM-DF image of an An-OL interface of $Cap_{350°C\text{-}1h}$ characterized by an apparent crystalline intermediate region. One distinct crystallite showing a strong contrast with the surrounding anode and the oxide layer is for instance marked by a dashed black oval (label "Crystallite" in Fig. 5.3.6a). This intermediate region can also be observed by means of STEM-HAADF imaging (Fig. 5.3.6b). At constant specimen thickness, the contrast in a STEM-HAADF image is directly related to the atomic numbers of the chemical elements in the investigated material i.e. to spatial fluctuations of the chemical composition (cf. section 3.1.2). Heavy elements yield a higher number of counts, i.e. a lighter shade of gray, than elements with a lower atomic number which appear darker in the image. Assuming that the

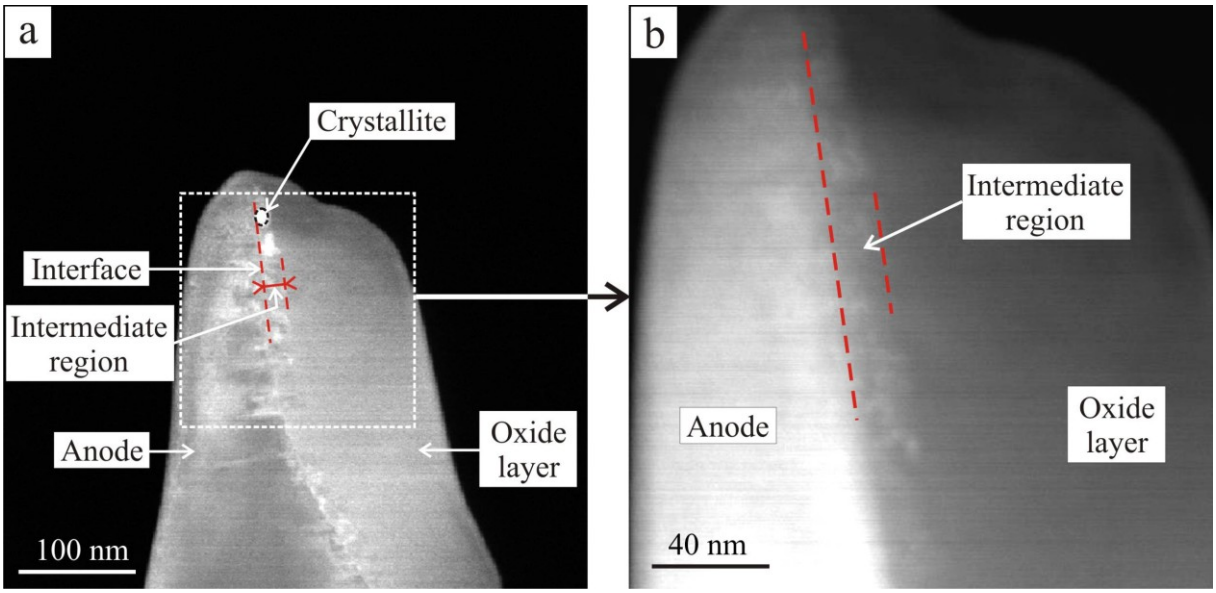

Fig. 5.3.6. STEM-DF **(a)** and STEM-HAADF **(b)** images of the interface between one anode and one oxide layer of $Cap_{350°C\text{-}1h}$ (VG HB501UX microscope). On both images an intermediate region is visible.

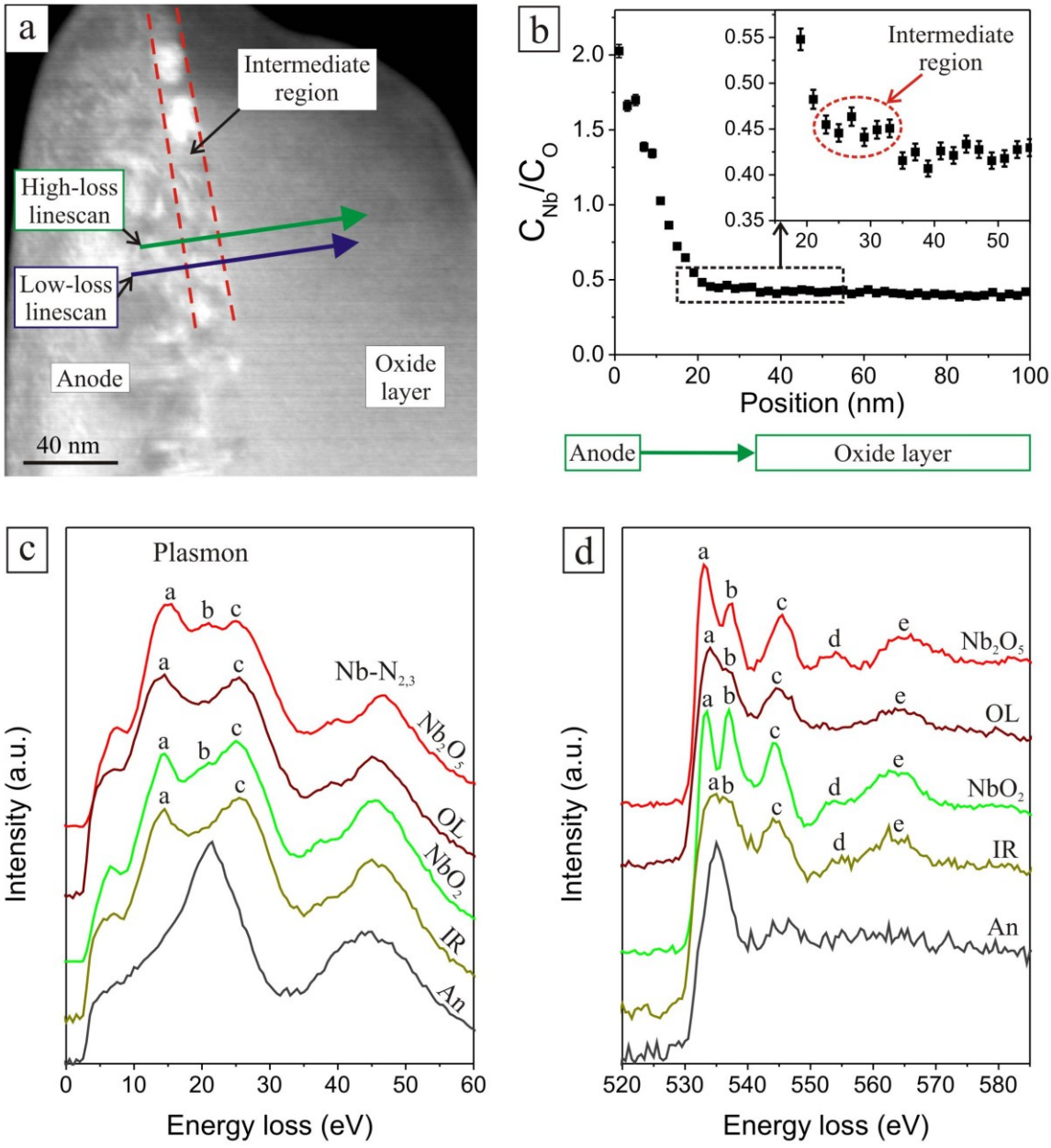

Fig. 5.3.7. EELS investigation of the intermediate region observed in $Cap_{350°C\text{-}1h}$ (cf. Fig. 5.3.6). **a)** STEM-DF image of the investigated An-OL interface. The arrows indicate the position of the performed low-loss and core loss linescans (VG HB501UX microscope: dE ~ 1-1.5 eV, E_0 = 100 keV, β = 6.5 mrad, α = 10 mrad). **b)** C_{Nb}/C_O atomic concentration ratios derived from the core-loss spectra (using $k_{NbM4,5\text{-}OK} = 13.97 \pm 0.30$) and shown as function of the position of the electron beam during the corresponding linescan. **c)** Representative low-loss spectra resulting from the linescan across the anode (An), the intermediate region (IR), and the oxide layer (OL) as well as from the investigation of reference NbO_2 and Nb_2O_5. The ZLP was subtracted and the multiple scattering removed from the spectra. **d)** EEL spectra showing the O-K edges recorded from An, IR, an OL (core-loss linescan) as well as from reference NbO_2 and Nb_2O_5. The spectra were corrected for background but not for multiple scattering. The reference spectra (NbO_2 and Nb_2O_5) shown in c) and d) were also taken at the VG HB501UX microscope.

anodes in $Cap_{350°C\text{-}1h}$ contain a significant amount of oxygen, e.g. $NbO_{0.27}$ (see section 5.2.2), and considering that the stoichiometry of the oxide layers is relatively close to Nb_2O_5, the mean atomic number in the anodes is expected to be around 34.0, whereas that of the oxide layers amounts to approximately 17.4. As a result, the anode appears brighter than the oxide layer in Fig. 5.3.6b. In contrast, the intermediate region exhibits an intermediate shade of gray indicating a stoichiometry between those of the anode and the oxide layer (under the assumption that there is no dramatic thickness variation at the interface). This could be explained by the superposition of anode and oxide-layer materials in the axis of the incident electron beam; however, the below-presented EELS results will show that it is more likely correlated with the presence at the An-OL interface of an independent niobium oxide phase differing from those composing the anode and the oxide layer.

One low-loss linescan and one core-loss linescan were performed across the An-OL interface. For each linescan, a series of 50 spectra was acquired along a 100 nm long line represented by an arrow in the STEM-DF image shown in Fig. 5.3.7a. From the low-loss linescan the relative thickness t/Λ in the immediate vicinity of the intermediate region was estimated to be around 0.48 in the anode and 0.34 in the oxide layer, whereas $t/\Lambda \sim 0.37$ was measured within the intermediate region. However, for the experimental parameters of the VG microscope ($E_0 = 100$ keV, $\beta = 6.5$ mrad, $\alpha = 10$ mrad), the inelastic mean free path Λ is estimated at approximately 62 nm in the anode and 73 nm in the oxide layer (considering stoichiometries around $NbO_{0.27}$ and Nb_2O_5 for the anode and the oxide layer, respectively – see above). These estimations were performed using a routine implemented in the digital micrograph software and adapted from the parameterization of Malis et al. (1988) (see section 3.2.4) to take the convergence semi-angle α into consideration when it is greater than the collection semi-angle β. Hence, the measured relative thicknesses yield absolute specimen thicknesses near the intermediate region of approximately 30 nm for the anode and 25 nm for the oxide layer. Thus, the variation of the absolute thickness at the An-OL interface (relative deviation of about 18% between 30 nm and 25 nm) is not as dramatic as the measured relative thicknesses suggest (relative deviation of about 34% between 0.48 and 0.34).

The C_{Nb}/C_O atomic concentration ratios determined from the core-loss spectra by means of the k-factor $k_{NbM4,5\text{-}OK} = 13.97 \pm 0.30$ (corresponding to a mean t/Λ of about 0.35 – cf. Table 4.3.3) are shown in Fig. 5.3.7b as function of the position of the electron beam during the linescan. The EELS quantification enables a clear observation of the intermediate region. Six spectra taken along a 12 nm line within the intermediate region result in a C_{Nb}/C_O ratio of 0.451 ± 0.008 ($\pm 1.8\%$), whereas $C_{Nb}/C_O \sim 0.410 \pm 0.014$ ($\pm 3.4\%$) is found by averaging 31 spectra acquired within the oxide layer. These ratios correspond to two distinct chemical formulas, namely $Nb_2O_{4.43\pm0.08}$ for the intermediate region and $Nb_2O_{4.88\pm0.17}$ in the oxide layer. Hence, these results suggest a stoichiometry closer to NbO_2 than to Nb_2O_5 in the intermediate region but could still be interpreted by the overlapping of oxide-layer and anode materials. However there should be 8.6 times more $Nb_2O_{4.88}$ oxide-layer material than $NbO_{0.27}$ anode material in the intermediate region to yield the averaged stoichiometry $Nb_2O_{4.43}$. Thus, since the oxide-layer material is amorphous, this interpretation is hardly compatible with the very strong crystalline contrast observed in the intermediate region by means of STEM-DF

imaging (cf. Fig. 5.3.7a and Fig. 5.3.6a). In addition, the investigation of the plasmon fingerprint and of the O-K-ELNES provides further evidence allowing to conclude that another niobium-oxide phase is present in the intermediate region.

Fig. 5.3.7c shows representative ZLP-subtracted low-loss spectra resulting from the linescan in the oxide layer (OL), the intermediate region (IR), and the anode (An) together with crystalline Nb_2O_5 and crystalline NbO_2 reference spectra (also taken at the VG microscope). The spectra were corrected for multiple scattering via *Fourier*-log deconvolution. The plasmon fingerprint of the intermediate region differs from that taken in the oxide layer but shows close similarities with the NbO_2 one. Especially the relative height and width of the peaks (a) and (c) measured from the intermediate region are in good agreement with the NbO_2 features, whereas the oxide layer spectrum shows intermediate characteristics between those of NbO_2 and Nb_2O_5. In addition, the IR fingerprint cannot be explained by a linear combination of those observed for the anode and the oxide layer, indicating that the intermediate region is constituted by an additional phase differing from those of the anode and the oxide layer (when the eventual effects of surface and interface plasmons are neglected).

Fig. 5.3.7d presents representative O-K edges resulting from the core-loss linescan across the anode, the intermediate region and the oxide layer as well as from the investigation of crystalline NbO_2 and Nb_2O_5 reference materials. The spectra were corrected for background but not for multiple scattering. Nevertheless, except for the An spectrum taken at a specimen region with t/Λ around 0.50, the spectra result from quite similar relative thicknesses in the range of approximately 0.29 to 0.38 so that a comparison between the corresponding OK-ELNES should still be relevant. By comparing the ELNES results achieved for OL with those obtained from the different reference materials, it was already shown in section 5.1.5 that the general shape of the O-K edge measured from OL is the most similar to the O-K ELNES of Nb_2O_5. In contrast, the shape of the IR spectrum (corresponding to t/Λ around 0.37) matches well with the NbO_2 spectrum ($t/\Lambda \sim 0.38$). Like NbO_2, IR is characterized by two peaks of similar height just above the O-K ionization threshold (letters a and b in Fig. 5.3.7d). Moreover, the relative heights and widths of the further EELS features marked by the letters (c), (d), and (e) demonstrate a very good agreement between the two materials. Here again, the well-pronounced O-K ELNES of IR cannot be the result of a linear combination of the An and OL spectra. Furthermore, the bump (d), which is characteristic for the crystalline NbO_2 and Nb_2O_5 reference phases is not visible in the case of the amorphous oxide layer. Hence, its occurrence in the OK-ELNES of the intermediate region seems to confirm the presence of a crystalline niobium-oxide phase at the An-OL interface.

Thus, the results as a whole indicate that the intermediate region is independent of the anode and the oxide layer and is composed of a crystalline niobium-oxide phase having a stoichiometry close to NbO_2 (or at least strongly oxygen deficient with respect to Nb_2O_5). Since this intermediate region was only measured in $Cap_{350°C\text{-}1h}$ and not in $Cap_{No\text{-}Anneal}$ or $Cap_{300°C\text{-}5h}$, its formation may be correlated with the annealing step of 1 h at 350°C. However, regions exhibiting such crystallites were not systematically observed at all An-OL interfaces of $Cap_{350°C\text{-}1h}$, neither by means of STEM-DF or -HAADF nor via EELS. In fact, like for $Cap_{No\text{-}Anneal}$ and $Cap_{300°C\text{-}5h}$, most of the investigated interfaces appeared smooth (cf. previous

section), the thinnest having an apparent width of only 6 nm. Hence, this clearly shows that the capacitor structures annealed for 1 hour at 350°C are not homogeneous.

5.4 Discussion

Capacitor structures achieved after different annealing steps were investigated by means of ELNES as well as quantitative EELS. The results were analyzed using the data gathered by studying reference materials. Both the ELNES and the quantitative EELS results agree to indicate that the chemical composition of the oxide layers in capacitor structures is close to Nb_2O_5. The homogeneity of the oxide layers and the interfaces between anodes and oxide layers were also inspected at a nanometer scale. In the following sections, different aspects of the EELS investigation techniques are discussed, as well as the pertinence of the results. The significance of these results with regard to the influence of annealing on the capacitors is also examined in more detail.

5.4.1 Low-loss fingerprinting and ELNES

Influence of the amorphous/crystalline structure

It was shown in Subchapter 5.1 that the ELNES of the different edges taken from the oxide layers (OL) in capacitor structures present generally more similarities with the data obtained from Nb_2O_5 than with those achieved by investigating the other reference materials (Nb, NbO and NbO_2). However, significant ELNES discrepancies were still observed between OL and Nb_2O_5. For instance, the double-peak structure of the O-K edge of OL is characterized by a lower energy splitting $E_b - E_a$ than that measured for Nb_2O_5 (cf. section 5.1.5). Moreover, the O-K ELNES as a whole appears less pronounced and more blurred for OL than in the case of Nb_2O_5 (cf. Fig. 5.1.5). Especially the peak (d) in the ELNES of Nb_2O_5 is not any more detected for OL. Nevertheless, the quantitative EELS results showed that the stoichiometry within the oxide layers is very close to Nb_2O_5 (see sections 5.2.2 and 5.2.3). Even at a precision as good as about ± 2% (standard deviations of the measured C_{Nb}/C_O atomic concentration ratios), it could not be excluded that the oxide layers are composed of stoichiometric Nb_2O_5 (cf. in Fig. 5.2.3 the data achieved with deconvolution). Hence, the discrepancies between the ELNES of OL and Nb_2O_5 are mainly attributed to the fact that the capacitor oxide layers are amorphous whereas the Nb_2O_5 reference material is crystalline. Indeed, the ELNES of a given edge directly reflects the density of the possible final states of the electronic transitions responsible for the edge (cf. section 3.4.6). Therefore, since the structure (crystalline or amorphous) of a solid strongly affects the electronic band structure, it also influences the corresponding ELNES data. Thus, the present example of the O-K edge demonstrates the limit of the ELNES method to determine the stoichiometry of a material by

means of reference spectra: one reference spectrum per stoichiometry is not always sufficient, since materials with similar stoichiometries can present different ELNES features. Concurrently, it proves the force of ELNES for the identification of phases: two different phases, even if they are characterized by the same stoichiometry, can principally be distinguished by ELNES investigations. This was already observed, e.g., for carbon: amorphous carbon, graphite, and diamond - in spite of being composed of pure carbon - strongly differ in the C-K ELNES owing to the different crystal structures and associated chemical-bonding types (see, e.g., Bruley et al., 1995).
Similarly, the plasmon fingerprint of OL is not identical to that measured from reference Nb_2O_5 (see Fig. 5.1.1a). Particularly the peak (b) detected for Nb_2O_5 is not visible in the case of OL. Here again, the fingerprint discrepancies can be attributed to the different structures of the two materials (amorphous OL, crystalline Nb_2O_5). Indeed, the plasma oscillations in a material are damped by scattering with the ion-core lattice. The strength of this damping strongly affects the shape of the plasmon peak measured by EELS and depends on the band structure of the material, i.e. on the crystal structure (Egerton, 1986).
Nonetheless, different EELS features sensitive to the niobium oxidation state can be quantified and give values in good agreement for OL and Nb_2O_5. This is for instance the case for the normalized Nb-$L_{2,3}$ white-lines intensity (see section 5.1.6). Particularly the relative position of the Nb-$M_{2,3}$ edges with respect to that of the O-K edge $E_{NbM2,3} - E_{OK}$ was found to be perfectly identical for OL and Nb_2O_5 (-165.3 eV at the LEO 922 microscope, see section 5.1.4), yielding identical relative chemical shifts. Hence, contrary to the energy splitting E_b - E_a of the O-K double-peak structure (also sensitive to the niobium oxidation state – see Fig. 4.4.1 and section 4.4.2), these features seems to have a low dependence on the crystalline or amorphous structure of the niobium-oxide material and they can directly be analyzed to make a statement on the stoichiometry of an unknown niobium-oxide phase.

Comparison with quantitative EELS in terms of sensitivity

No clear distinction could be made between the different types of capacitor structures by investigating the fingerprints of the plasmons and edges taken from the oxide layers (see subchapter 5.1). However, as discussed in the following section, the quantitative results seem to indicate some significant discrepancies between $OL_{No\text{-}Anneal}$ and $OL_{350°C\text{-}1h}$. Hence, in the present case, quantitative EELS appears to be a more sensitive method than ELNES to analyze the chemical variations presented by the oxide layers.

Spatial resolution of the plasmon-fingerprint analysis

In subchapter 5.3, the variations of the plasmon fingerprints taken during low-loss linescans were investigated to estimate the sharpness of An-OL interfaces. The precision of such measurements may be limited by the delocalization of plasmon scattering (Egerton, 1986). Indeed, whereas inelastic scattering at high energy losses (E > 100eV) is strongly localized, the inelastic scattering at low energy losses does not necessarily occur at a sharp predictable point (Egerton 2003, Erni & Browning, 2005). However, spatial resolutions better than 1-2 nm have been demonstrated while investigating material/material interfaces by means of plasmon fingerprinting. For instance, Pokrant et al. (2005) report the analysis of a

$Si/SiO_2/HfO_2/Si$ model sample at a spatial resolution of nearly one monolayer. Using reference low-loss spectra, the authors successfully identified the presence of an independent $HfSi_xO_y$ phase extending over about only three-four atomic planes at the interface between a HfO2 layer and polycrystalline Si. During the low-loss linescans performed in the present work, the successive spectra were typically taken with a spatial frequency of only one spectrum each 2 nm (using an 0.5 nm sized electron probe). Hence, the effects of the delocalization are not expected to particularly affect the spatial resolution in the present case. This is confirmed by the fact that sharp interfaces (as defined in section 5.3.2) could be detected from plasmon-fingerprint investigations as well as by analyzing $I_{NbM4,5}/I_{OK}$ intensity ratios resulting from strongly localized core-loss excitations. In addition, even if delocalization would prevent the absolute measurement of the width of the interfaces, the estimations given by the plasmon fingerprint would still be a relevant criterion allowing to compare interfaces with each other in terms of sharpness.

5.4.2 Quantitative EELS

Whereas the ELNES investigation of niobium oxides allows only a rough estimation of the stoichiometry (see previous section), the accuracy and the precision of EELS quantification by means of experimental *k*-factors was already demonstrated in chapter 4 (see sections 4.3.4, 4.4.6, and 4.4.7). The accuracy was checked via the analysis of NbO_2 spectra by means of *k*-factors derived from the study of NbO and Nb_2O_5 (LEO microscope) and was found in that case to be around 0.4-0.6% (relative deviation between the measured C_{Nb}/C_O atomic concentration ratio and its nominal value – cf. sections 4.3.4 and 4.3.5). Discrepancies in the same order of magnitude were obtained between the C_{Nb}/C_O ratios determined for the oxide layers of the different types of capacitors (see sections 5.2.2 and 5.2.3). In order to evaluate the significance of the trends observed as a function of the annealing step suffered by the capacitors, different quantification procedures were applied to the oxide layers. By checking whether the different procedures give similar trends or not, more information is gained on the sensitivity of the EELS quantification and the pertinence of the results can be discussed.

Accuracy of the quantification / Oxygen deficiency in the oxide layers

Five different analysis procedures based on the use of experimental *k*-factors (all determined for 70 eV wide integration windows) were employed: two at the LEO microscope (with or without deconvolution of the data - see section 5.2.2), and three at the VG microscope (using different individual or "mixed" *k*-factors – see section 5.2.3). Depending on the applied procedure, slightly different quantitative results were achieved. Nonetheless, when the stoichiometries measured for the oxide layers are compared to Nb_2O_5, the different results are still quite consistent with each other. For each type of capacitor structures, every procedure yields a mean C_{Nb}/C_O ratio indicating a small oxygen deficiency in the oxide layers with respect to stoichiometric Nb_2O_5 (except for $Cap_{300°C\text{-}5h}$ when analyzed at the VG microscope by means of $k_{NbM4,5\text{-}OK} = 13.97 \pm 0.30$ – see Fig. 5.2.3 and Fig. 5.2.5). But in all cases,

considering the standard deviations of the averaged C_{Nb}/C_O ratios, the results are still compatible with oxide layers composed of Nb_2O_5.

The procedure allowing the most accurate determination of the absolute chemical composition (C_{Nb}/C_O) in the oxide layers is expected to be the one performed at the LEO microscope without deconvolution. Indeed, for this procedure it has been clearly demonstrated that the use of 70 eV wide integration windows ΔE enables to optimize the accuracy of the quantification (see section 4.3.3). This could not directly be proven in the case of the other quantification procedures, even if as already discussed in sections 4.4.7 and 4.4.8, the choice of $\Delta E = 70$ eV should also be pertinent for the accurate analysis of both the data achieved with deconvolution at the LEO microscope and those gathered at the VG microscope. Moreover, compared to the LEO procedure without deconvolution, the accuracy of the other procedures may be degraded by the number and the quality of the reference spectra yielding the *k*-factors employed for quantification. At the LEO microscope, owing to an artefact occurring in the low-loss spectra, fewer spectra were analyzed to determine the *k*-factor with deconvolution than to derive the *k*-factor without deconvolution (see section 4.3.5 and Table 4.3.3). Furthermore, a large majority of the deconvoluted spectra were taken from one and the same reference material, namely NbO_2 (whereas more NbO and Nb_2O_5 spectra were treated without deconvolution), and some of the few Nb_2O_5 spectra implemented in the statistics may be affected by slight deconvolution errors resulting from the artefacts of the low-loss spectra. At the VG microscope, only seven Nb_2O_5 reference spectra were available to determine the *k*-factors employed in the different procedures, resulting in poor statistics. As a whole, these different aspects make the accuracy of the LEO procedure with deconvolution and of the VG procedures relatively uncertain compared to the LEO quantification without deconvolution that is the only procedure whose accuracy could be directly evaluated by a quantification test (performed on NbO_2 – see above and section 4.3.5).

Using the *k*-factor derived without deconvolution at the LEO microscope (for t/Λ in the range of 0.30 to 0.50), $Cap_{No\text{-}Anneal}$ presents the oxide layers whose measured stoichiometry is the closest to Nb_2O_5 (see section 5.2.2). The mean C_{Nb}/C_O ratio averaged from the $OL_{No\text{-}Anneal}$ spectra is determined around 0.405, i.e. at a relative deviation of 1.2% with the nominal value of Nb_2O_5 (0.400). Furthermore, an accuracy as good as 0.4% was found to be possible when EELS quantification is performed without deconvolution at the LEO microscope (see above and section 4.3.5). Hence the relatively large deviation measured between $OL_{No\text{-}Anneal}$ and Nb_2O_5 (1.2%) suggests that the apparent oxygen deficiency detected with respect to Nb_2O_5 in the oxide layers of the different types of capacitors is true (the influence of an eventual Ar contamination is discussed below). This is confirmed by the fact that such oxygen deficiencies were also indicated by all the other quantification procedures (see above and Figs. 5.2.3 and 5.2.5).

Sensitivity of the quantification / Variation of the oxygen deficiency with annealing

Even if the accuracy of the determination of the absolute stoichiometry in the oxide layers is not proven when it is preformed at the VG microscope or by means of deconvolution at the LEO microscope, the results obtained from these quantification procedures are relevant to compare the different types of capacitors with each other. Indeed, for the estimation of

relative stoichiometry variations, the original $I_{NbM4,5}/I_{OK}$ intensity ratios are of main interest, whereas the accuracy of the determination of C_{Nb}/C_O ratios via the different *k*-factors is less important. However, to interpret the results, the question of the sensitivity of the quantification procedures needs to be answered. Are the discrepancies observed between the different capacitor structures significant?

At the LEO microscope, the largest discrepancy observed between the mean C_{Nb}/C_O ratios determined with or without deconvolution for one and the same type of capacitor is of about 0.7% in the case of $OL_{350°C\text{-}1h}$ ($C_{Nb}/C_O \sim 0.408$ with deconvolution, ~ 0.411 without – see section 5.2.2). But using the same quantification procedures, no discrepancy was measured for $OL_{300°C\text{-}5h}$ ($C_{Nb}/C_O \sim 0.406$ with or without deconvolution). This means that the observation of a relative variation of 0.7% between the stoichiometries measured for two different types of capacitors is not necessarily relevant (with other words, the sensitivity is worse than 0.7%). This is comparable with the quantification accuracy of 0.4-0.6% achieved at the LEO microscope (see above and sections 4.3.4 and 4.3.5). The relative deviation between the C_{Nb}/C_O ratios measured for $OL_{No\text{-}Anneal}$ and $OL_{300°C\text{-}5h}$ is of 0.2% without deconvolution and 0.7% with deconvolution. Hence, this is not significant enough to draw any conclusion concerning an eventual influence of an annealing step of 5 h at 300°C on the stoichiometry within the oxide layers. In contrast, the relative increase of the C_{Nb}/C_O ratio observed between $OL_{No\text{-}Anneal}$ and $OL_{350°C\text{-}1h}$ amounts to about 1.5% without deconvolution and 1.2% with deconvolution. Thus, these relatively large discrepancies seem to indicate a true effect of 1 h annealing at 350°C. However, in the present case, the uncertainty lies in the fact that only four $OL_{350°C\text{-}1h}$ spectra could be analyzed, leading to a poor statistics (see section 5.2.2). Hence, these results should first be considered with caution.

It was already mentioned in section 5.2.3 that the large deviation observed in the case of $OL_{300°C\text{-}5h}$ between the C_{Nb}/C_O ratios resulting from the three VG procedures can be attributed to the large thickness of the investigated specimen regions. Letting the $OL_{300°C\text{-}5h}$ results aside, the largest discrepancy measured between the mean C_{Nb}/C_O ratios determined at the VG microscope for one and the same type of capacitor is of 1.0% in the case of $OL_{No\text{-}Anneal}$ ($C_{Nb}/C_O \sim 0.402$ using $k_{NbM4,5\text{-}OK} = 13.97 \pm 0.30$, ~ 0.406 by means of mixed *k*-factors – see Table 5.2.1). Contrary, using the two same quantification procedures ($k_{NbM4,5\text{-}OK} = 13.97 \pm 0.30$ and mixed *k*-factors), no discrepancy was observed for $OL_{350°C\text{-}1h}$ ($C_{Nb}/C_O \sim 0.412$), implying that a relative variation of 1.0% is not necessarily significant when the stoichiometry of two different types of oxide layers is measured at the VG microscope. But as showed in section 5.2.3, a relative increase as large as 2.2% is found between the C_{Nb}/C_O ratios of $OL_{No\text{-}Anneal}$ and $OL_{350°C\text{-}1h}$ by averaging the results of the three VG procedures. Hence, this relatively large deviation suggests that the stoichiometry within $OL_{No\text{-}Anneal}$ is truly different from that of $OL_{350°C\text{-}1h}$ and confirms the measurements performed at the LEO microscope. Thus, the results of all the five different quantification procedures (conducted both at the LEO and the VG microscopes) are consistent to indicate that 1 h annealing at 350°C yields a significant increase of the C_{Nb}/C_O ratio in the oxide layers of the capacitor structures (i.e. a relative decrease of the O content when compared to the Nb content).

Conclusion

The analysis of the quantitative EELS results revealed some clear trends: oxygen deficiency in the oxide layers with respect to Nb_2O_5, oxygen deficiency worsened by an annealing step of 1h at 350°C. Nevertheless three aspects related to the accuracy of EELS quantifications were not specifically considered yet in the present work and need to be discussed to confirm the reliability of these trends. These eventual problems concern the difference in structure between the oxide layers (amorphous) and the reference oxides (crystalline), argon contamination, and the possible homogeneity ranges of the reference oxides.

5.4.3 Quantitative efficiency vs. structure differences (amorphous/crystalline)

One of the questions related to the accuracy of EELS quantification and which was not considered yet during the analyses of the reference materials is discussed here. The reference materials are all crystalline whereas the capacitor oxide layers are amorphous. Can this structure difference affect the accuracy of the quantitative investigation of the oxide layers by means of experimental *k*-factors resulting from the reference materials? Whether the investigated material is crystalline or amorphous, EELS quantification is based on the same principle assuming that the number of counts under an inner-shell ionization is proportional to the number of atoms present. Hence, as already discussed in section 4.4.7, the quantification accuracy is mainly limited by the same two factors, namely the impact of the ELNES and the accuracy of the background-subtraction procedures. Concerning the shape of the backgrounds on which the Nb-$M_{4,5}$ and O-K edges lie, no particular differences could be noticed between the reference oxides and the oxide layers. Fitting windows similar in width and positions were used in both cases to extrapolate and remove the backgrounds (cf. sections 4.3.2 and 4.4.7). Thus, quite equivalent systematic errors can be expected and the quantitative accuracy should not especially be more affected by the background-subtraction procedures when the oxide layers are analyzed using reference materials than in the case where one reference material is analyzed by means of another one. In contrast, it was discussed in section 5.4.1 that the crystalline or amorphous structure of a material influences significantly the ELNES. However, in spite of the strongly different O-K ELNES of NbO, NbO_2, and Nb_2O_5 (see Fig. 4.2.10 and Fig. 4.2.11), the analysis of the different reference oxides resulted in a good quantitative accuracy (around 0.4-0.6%) when 70 eV wide integration windows were used to determine $I_{NbM4,5}/I_{OK}$ intensity ratios (see above and sections 4.3.3, 4.3.4, and 4.3.5). In the case of the oxide layers, the O-K ELNES is clearly different from those achieved from NbO and NbO_2, but shows close similarities to that of Nb_2O_5 (see Fig. 5.1.5). Hence, the ELNES discrepancies are not expected to particularly reduce the accuracy of the quantitative analysis of the oxide layers. In addition, another effect related to the crystal structure of the investigated material may influence the accuracy of EELS quantification, namely the specimen orientation (Egerton 1978; Egerton, 1986; Bertoni & Verbeeck 2008). Indeed, for a crystalline material, the partial cross-section for a particular inner-shell excitation $\sigma(E_0, \beta, \alpha, \Delta E)$ and thus the corresponding collected intensity $I(E_0, \beta, \alpha, \Delta E)$ can become a function of

the orientation of the crystal with respect to the incident electron beam. This effect results from changes (depending on the orientation) in the relative intensity of the *Bloch* waves corresponding to the movement of electrons in the periodic potential of the crystal, and from the probabilities with which these different *Bloch* waves can inelastically excite electrons out of given inner atomic shells. Particularly, in the present case, the orientation of one and the same reference oxide along different zone-axes may yield different $I_{NbM4,5}/I_{OK}$ intensity ratios (the influence of the sample orientation is especially strong along zone-axes). However, for each reference material, spectra taken from different random orientations far away from zone-axes were averaged to determine intensity ratios and *k*-factors, which should minimize the orientation effects. Hence, at the end, the resulting *k*-factors are expected to be equivalent to that which would have been obtained by analyzing an amorphous reference oxide. This is confirmed by the good quantitative precision and accuracy achieved in the present work by studying the crystalline reference oxides (see sections 4.4.6 and 4.4.7), indicating that like in the case of an amorphous material the different investigated sample orientations had apparently no significant influence on the final quantitative results. Thus, on the whole, the different crystalline and amorphous structures of the reference oxides and capacitor oxide layers are not expected to significantly affect the accuracy of the different EELS quantification procedures applied to investigate the oxide layers. Moreover, if there was an influence of the different crystal structures, it would introduce the same systematic error for all the different types of capacitors (the oxide layers are in each case amorphous). Hence, the absolute values determined for the C_{Nb}/C_O ratios in the oxide layers would be affected, but the investigation of the trends observed as a function of the annealing would still be relevant. Finally, it will be discussed below that argon contamination occurring during the TEM-sample preparation can disturb the accuracy of the analysis of the oxide layers. Both the reference-oxides samples and the capacitor samples were etched by means of Ar^+ ions. Nevertheless, whereas contamination could be measured in some capacitor oxide layers, no clear contamination was detected in the reference oxides. This may result from an easier implantation of the argon ions in an amorphous niobium oxide than in a crystalline one. Thus, there is a slight chance that the quantification accuracy could be indirectly influenced by the different type of structure of the oxide layers (amorphous) compared to the reference oxides (crystalline).

5.4.4 Quantitative efficiency vs. argon contamination

No stoichiometry gradients were clearly detected at a nanometer scale within the oxide layers (see section 5.3.1). Nonetheless, inhomogeneities were sometimes observed. Particularly, apparent stoichiometry discrepancies were measured between different oxide layers of one and the same capacitor type (see section 5.2.3). As briefly mentioned in section 5.2.3, argon contamination could contribute to this effect. Indeed, the TEM samples were generally etched by means of Ar^+ ions during the final thinning stage of their preparation. Hence, depending on the intensity and the duration of the etching, some Ar atoms may remain in the finished sample. Fig. 5.4.1 shows two EEL spectra taken from a contaminated oxide layer and a

regular layer in which no contamination could be detected (LEO microscope). The spectra are presented after background subtraction under the Nb-$M_{4,5}$ edges and correction for multiple scattering. A background-subtracted reference spectra of the Ar-$L_{2,3}$ edges is also visible in Fig. 5.4.1. The original data of the latter spectrum (without background subtraction) come from the EELS atlas implemented in the Gatan Digital Micrograph software. Argon contamination in the capacitor oxide layers is observable by EELS in the form of a bump superimposed on the Nb-$M_{4,5}$ edges (arrow in Fig. 5.4.1) and corresponding to the Ar-$L_{2,3}$ edges. The presence of Argon in the layers exhibiting such a characteristic bump could be confirmed by EDXS investigations (also performed at the LEO 922 microscope). This contamination is especially problematic for EELS quantification due to the position of the Ar-$L_{2,3}$ edges, whose onset occurs at about 245 eV. Indeed, in the case of a contaminated layer, the Ar signal also contributes to the measured intensity within the 70 eV wide integration window ΔE used to determine the intensity under the Nb-$M_{4,5}$ edges, resulting in an overestimation of the C_{Nb}/C_O ratio. The contamination was particularly strong in the $Cap_{No\text{-}Anneal}$ samples investigated at the LEO microscope. However, it was not homogeneous within one and the same sample (all the regions of a sample are not equivalently exposed to the Ar^+ beam during the etching procedure). Most of the analyzed layers still appeared free of contamination (no Ar-$L_{2,3}$ edges detected). Of course, the spectra showing a clear contamination or suspected of contamination were not considered in the ELNES and quantitative analyses reported in the present work (subchapters 5.1 and 5.2). By doing so, the analysis of 13 $OL_{No\text{-}Anneal}$ spectra (with t/Λ in the range of 0.30 to 0.50) resulted in a C_{Nb}/C_O atomic concentration ratio around 0.405 ± 0.011 (LEO microscope, see section 5.2.2). However, the fact that no Ar signal is clearly detected by investigating the Nb-$M_{4,5}$ ELNES does not necessarily imply that there is no Ar atom in the specimen (some signal can be hidden by the noise), and that Ar contamination cannot significantly affect the EELS quantification. In order to check the validity of the quantitative results presented in the subchapter 5.2, TEM samples of $Cap_{No\text{-}Anneal}$ were prepared using Xenon instead of Argon during the ion-thinning stage. The different EELS edges which can result from an eventual Xe contamination are not expected to disturb the quantification of niobium oxides. The Xe-prepared samples were investigated at the LEO microscope by making use of the same *k*-factor $k_{NbM4,5\text{-}OK} = 9.39 \pm 0.17$ (±1.8%) than that previously employed in section 5.2.2 to quantify the Ar-prepared ones. The averaging of 25 $OL_{No\text{-}Anneal}$ spectra taken from specimen regions with t/Λ in the range of 0.30 to 0.50 yielded $C_{Nb}/C_O \sim 0.406 \pm 0.010$. This is in very good agreement with the results achieved from the Ar-prepared samples (see above). Hence, Ar contamination does not seem to have a significant effect on the quantitative EELS results when the spectra showing contamination by means of ELNES are excluded from the quantification statistic. Particularly, the oxygen deficiency with respect to Nb_2O_5 ($C_{Nb}/C_O = 0.400$) that is measured in the capacitor oxide layers cannot be attributed to Ar contamination. Nevertheless, compared to the thinning procedure using Ar^+ ions, the Xe^+-etching produces samples with less homogeneous specimen thicknesses, especially in the case of the amorphous oxide layers. Thus, Ar^+ was still employed to thin the $Cap_{300°C\text{-}5h}$ and $Cap_{350°C\text{-}1h}$ samples investigated at the LEO microscope as well as the different capacitor samples analyzed at the VG microscope. Xe^+-etching stages were sometimes combined to the

Ar^+ thinning. In any case, the duration of the Ar^+-etching was strongly reduced in comparison to that employed to prepare the $Cap_{No\text{-}Anneal}$ samples initially investigated at the LEO microscope, and the spectra suspected of Ar contamination were not included in the quantitative analyses. Hence, in the end, the effects of Ar contamination are expected to be insignificant and to contribute only slightly to the stoichiometry inhomogeneities measured between different oxide layers of one and the same capacitor type (VG microscope, see above). In addition, the TEM samples investigated at the LEO microscope were different from those studied at the VG. Nonetheless, in both cases, the C_{Nb}/C_O ratios measured from the oxide layers showed the same trends as a function of the annealing steps (see Fig. 5.2.3 and 5.2.5): no clear distinction could be made between $OL_{No\text{-}Anneal}$ and $OL_{300°C\text{-}5h}$, whereas an increase of the C_{Nb}/C_O ratio is detected after 1 h annealing at 350°C. Thus, it is improbable that the observed trends result from a contamination whose intensity depends on the investigated TEM sample and specimen region.

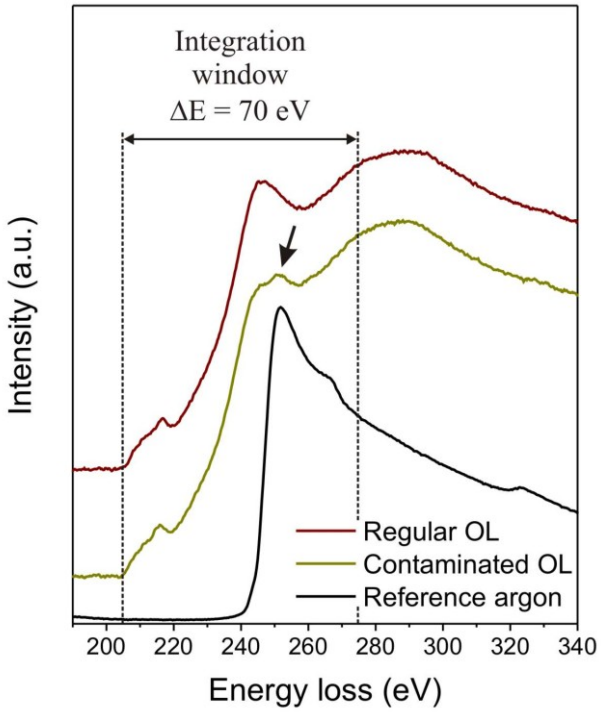

Fig. 5.4.1. EEL spectra taken from a regular oxide layer showing no argon contamination and from a layer contaminated by argon ($Cap_{No\text{-}Anneal}$, LEO microscope), together with an argon reference EEL spectrum (EELS atlas of the Gatan Digital Micrograph software). The two $OL_{No\text{-}Anneal}$ spectra are presented after background subtraction under the under the Nb-$M_{4,5}$ edges and correction for multiple scattering (*Fourier*-ratio deconvolution). The argon reference spectrum shows the background-subtracted Ar-$L_{2,3}$ edges.

5.4.5 Quantitative efficiency vs. homogeneity ranges of the reference materials

The crystalline reference materials were specified as highly stoichiometric by the different suppliers (see section 2.3.1). In addition, their crystal structures were confirmed by SAED or

XRD (See subchapter 4.1). Hence, up to now, the reference oxides were supposed to be purely stoichiometric. However, the investigated crystalline phases may present some non-discrete ranges of homogeneity which cannot be distinguished using SAED or XRD alone. These homogeneity ranges are extremely narrow for NbO, NbO_2 and Nb_2O_5, but the composition deviations with respect to the ideal formulas may be sufficient to affect the efficiency of EELS quantification by means of experimental *k*-factors derived from references. Thus, in order to discuss whether the homogeneity ranges can be neglected in the present study or not, the literature is briefly reviewed below. The widths of the homogeneity ranges can strongly depend on the temperature, the oxygen partial pressure and the gas mixture used to control the partial pressure, and the values found in the literature are sometimes quite confusing if not contradictory.

Homogeneity range of NbO

In the case of the NbO phase, Brauer (1941) indicated that its range of homogeneity is extremely narrow, which was confirmed later on by Elliot (1960) and Pialoux et al. (1982), however without giving values. By measuring the thermal expansion of the lattice parameter of NbO, Pialoux et al. (1982) concluded that the composition of NbO (O/Nb = 1) should not change between 20 and 1500°C but that some substoichiometry (oxygen deficiency) could be possible above 1500°C. Nevertheless, Nowak & Ziolek (1999) reported an existence range extending from $NbO_{0.982}$ to $NbO_{1.008}$. The lower limit corresponds to a C_{Nb}/C_O atomic concentration ratio of 1.018, i.e. to a relative deviation of 1.8% with the ideal composition of stoichiometric NbO (C_{Nb}/C_O = 1.000). The atomic concentration ratio of the upper limit (C_{Nb}/C_O ~ 0.992) corresponds to a relative deviation of 0.8% with that of $NbO_{1.000}$. However Nowak and Ziolek did not give any information on the conditions under which this existence range was determined and other authors measured a less extended range. Hence, according to X-ray studies on a series of samples prepared with the oxygen/niobium ratio changing from 0.5 to 1.5, Hulm et al. (1972) observed that a composition deviation by as little as 0.5 at. % on either side of stoichiometric NbO produces a mixed-phase sample.

Homogeneity range of NbO_2

In the case of NbO_2, Elliott (1960) also indicated that it is characterized by an extremely narrow range of homogeneity and some authors still mention that it has no solubility range of measurable extent (Olszta et al., 2006). Nevertheless, using H_2-O_2 gas mixtures to vary the partial pressure of oxygen, Marucco et al. (1976) determined via thermogravimetric measurements that the homogeneity range of NbO_2 extends from $NbO_{2.0000}$ to $NbO_{2.0032}$ at 1000°C. The relative deviation between the C_{Nb}/C_O ratio of the upper limit (0.4992) and that of stoichiometric NbO_2 (0.5000) amounts to about 0.16%. In addition the authors showed that the homogeneity range becomes larger with increasing temperature, ranging from $NbO_{2.0000}$ (constant lower limit) to about $NbO_{2.0046}$ (relative deviation of 0.23% with stoichiometric NbO_2) at 1050°C and to circa $NbO_{2.0060}$ (relative deviation of 0.30%) at 1100°C. Marucco et al. (1976) also indicated that their results are in contradiction with those of another author who found via a different method a substoichiometric existence range from $NbO_{1.985}$ (relative deviation of about 0.75%) to $NbO_{2.000}$ at 1000°C. Moreover, Janninck & Whitmore (1966)

determined a homogeneous-phase region centered around the stoichiometric compound and extending from about $NbO_{1.9975}$ (about 0.13% relative deviation) to $NbO_{2.0030}$ (0.15% relative deviation) at 1100°C. However, the results of Marucco et al. (1976) are in agreement with those of Schäfer et al. (1969) who measured a wider homogeneity range extending from $NbO_{2.000}$ to $NbO_{2.024}$ (about 1.2% relative deviation) at a higher temperature of 1300°C. In addition, the conclusion of the electron-microscopy and XRD experiments performed by Gannon & Tilley (1977) on niobium oxides with nominal compositions between NbO and $NbO_{2.1}$ was that the NbO_2 phase has a very narrow stoichiometry range at room temperature although this might not be so at higher temperatures.

Implications for the efficiency of EELS quantification, part 1

The relative deviations between the limits of the homogeneity ranges mentioned above for NbO and NbO_2 and the compositions of the corresponding purely stoichiometric compounds are generally lower than 1%. However, in the worst case scenario, a deviation as high as 1.8% was reported. Thus, considering the literature, such a large deviation does not appear particularly probable (especially not at room temperature) but could be possible. A constant deviation between assumed and real composition of a reference oxide would not necessarily affect the precision of the EELS quantification. In addition, a value of 1.8 % is still lower or at least of the same order as the standard deviations (corresponding to the precision) which were generally found in the present work while determining a *k*-factor from several reference spectra (for instance ± 2.6% for the *k*-factor determined from 12 NbO spectra in section 4.3.3, or ± 1.8% for the *k*-factor $k_{NbM4,5\text{-}OK} = 9.39 \pm 0.17$ derived from all the three reference oxides and used in section 5.2.2 to quantify the capacitor oxide layers without deconvolution at the LEO microscope). However it is clear that such a deviation or even a deviation of only 1% between the assumed composition of a reference oxide and the real one could dramatically affect the accuracy of the EELS quantification.

Homogeneity range of Nb_2O_5

Nb_2O_5 may appear substoichiometric but it is generally accepted in the literature that its homogeneity range is very narrow (some authors mentioned the existence of a solid solution-region or a substoichiometric region which may extend from Nb_2O_5 down to $Nb_2O_{4.84}$ or $NbO_{2.4}$ but in the fact it does not correspond to one and the same phase but to a variety of more or less "discrete" compounds including the different metastable phases occurring in this composition range and presented in section 2.1.3 (see e.g. Kimura 1973). The homogeneity range of the high-temperature H-Nb_2O_5 phase extends from $NbO_{2.489}$ (0.44% relative deviation with stoichiometric Nb_2O_5) to $NbO_{2.500}$ (stoichiometric Nb_2O_5) at 1300°C according to Schäfer et al. (1969) who controlled the oxygen pressure by using a H_2-H_2O gas mixture. By using a CO_2-H_2 gas mixture to control the oxygen pressure, Kimura (1973) observed a homogeneity range extending from $NbO_{2.490}$ (0.40% relative deviation) to $NbO_{2.500}$ at 1300 as well as 1400°C. Marucco (1974) found the homogeneity range to extend from $NbO_{2.4905}$ (0.38% relative deviation) to $NbO_{2.5000}$ at 1100°C and from $NbO_{2.4846}$ (0.62% relative deviation) to $NbO_{2.5000}$ at 1000°C in a CO_2-CO gas mixture. Using a CO_2-H_2 gas mixture, Naito et al. (1980) found under some assumption that the limiting composition of oxygen-

deficient Nb_2O_5 is $NbO_{2.484}$ (0.64% relative deviation) at 1060°C (slight disagreement with Marucco (1974) who found less oxygen-deficient limiting compositions $NbO_{2.4875}$ at 1050°C and $NbO_{2.4893}$ at 1075°C).
Thus, the homogeneity range of Nb_2O_5 depends on the temperature and gas mixture used to control the oxygen partial pressure, but in all cases, extremely low partial pressures of oxygen P_{O2} are required to form the limiting substoichiometric oxides. For instance, Kimura (1973) prepared $NbO_{2.490}$ under $P_{O2} \sim 7.8 \cdot 10^{-9}$ atm at 1400°C and $P_{O2} \sim 4.0 \cdot 10^{-10}$ atm at 1300°C. At 1000°C, Marucco (1974) needed a partial pressure P_{O2} of the order of $3 \cdot 10^{-17}$ atm to form $NbO_{2.4846}$. At constant temperature, a further decrease of P_{O2} yields the formation of different metastable oxide phases with compositions in the range of $NbO_{2.4}$ to $NbO_{2.5}$ (see, e.g., Kimura, 1973; Naito et al., 1980; see also section 2.1.3 for more information on these oxide phases), whereas an increase of P_{O2} results in less oxygen-deficient Nb_2O_5 (composition closer to the ideal stoichiometry). Hence, Nb_2O_5 is considered by all the authors as being stoichiometric in the air at 1050°C (Marucco et al., 1976), and in addition, all the niobium oxides turn into the H-Nb_2O_5 modification at high temperature in the air (see section 2.1.3).

Implications for the efficiency of EELS quantification, part 2
Consequently, it appears more complex to produce strongly substoichiometric H-Nb_2O_5 than stoichiometric H-Nb_2O_5. It is particularly improbable that the investigated reference Nb_2O_5 corresponds to the maximum possible deviation from the ideal stoichiometry, and in any case this maximum deviation (~ 0.38%-0.64%, see above) is still of the same order as the best accuracy of 0.4-0.6% assumed up to now after the quantification tests on NbO_2 (see sections 4.3.4 and 4.3.5). Hence the homogeneity range of Nb_2O_5 is negligible in the present work and the investigated reference Nb_2O_5 can be considered as purely stoichiometric.
In this context, two aspects suggest that the investigated NbO and NbO_2 reference materials were also purely stoichiometric, or at least that their eventual composition deviations with respect the ideal stoichiometries have no significant influence on the accuracy of the EELS quantification:
a) The quantitative EELS results obtained at the LEO microscope from Nb_2O_5 (negligible deviation from stoichiometry) are in very good agreement with those from NbO and NbO_2: indeed a low relative deviation (0.6%) was achieved between the mean *k*-factor derived from Nb_2O_5 and that from NbO (using ΔE = 70 eV, see section 4.3.3) and an excellent accuracy (0.4-0.6%) was obtained while quantifying NbO_2 by means of a *k*-factor derived from both NbO and Nb_2O_5 (using the same ΔE = 70 eV, see sections 4.3.4 and 4.3.5).
b) As already discussed in section 5.4.2, the quantitative results obtained from the capacitor structures by using all three reference materials (i.e. inclusive NbO and NbO_2, LEO microscope, see section 5.2.2) are consistent with those derived by means of only Nb_2O_5 as reference (VG microscope, see section 5.2.3, since Nb_2O_5 can be considered as purely stoichiometric, these results are "sure" with respect to the problem of the reference-materials homogeneity range, and they can thus be regarded as a kind of reference). In both cases, similar oxygen deficiencies relative to stoichiometric Nb_2O_5 are observed in the capacitor oxide layers (a slightly less understoichiometric composition is however found for $OL_{350°C\text{-}1h}$ with the LEO microscope than with the VG microscope, but this may be related to the poor

statistics of the LEO measurements on $OL_{350°C\text{-}1h}$), and these oxygen deficiencies appears to be worsened by an annealing step of 1h at 350°C.

Conclusion

Hence, in the present work, the existence under certain conditions of narrow homogeneity ranges for the investigated reference materials appears to have no significant effect on the quantitative EELS results obtained assuming ideal stoichiometries. Thus, these possible homogeneity ranges should not affect the conclusions of the discussions conducted up to now and can be further neglected in the present work.

5.4.6 Nb-based capacitor structures

The results concerning the stoichiometry of the capacitor structures and the corresponding discussion conducted up to now can be summarized in the following observations and statements:

a) The capacitor oxide layers are globally oxygen deficient with respect to stoichiometric Nb_2O_5 (cf. sections 5.2.2, 5.2.3, and 5.4.2)
b) The oxygen deficiency in the capacitor oxide layers is increased by an annealing step of 1h at 350°C (cf. sections 5.2.2, 5.2.3, and 5.4.2).
c) Quantitative EELS does not allow to observe any significant influence of an annealing step of 5h at 300°C on the stoichiometry of the capacitor oxide layers (cf. sections 5.2.2, 5.2.3, and 5.4.2).
d) There appears to be some occasional stoichiometry inhomogeneities between different oxide layers of one and the same capacitor structure (cf. sections 5.2.3 and 5.4.4).
e) No stoichiometry gradients could clearly be detected on a nanometer scale within the capacitor oxide layers (cf. section 5.3.1).
f) The capacitor oxide layers mostly appear homogeneous on a nanometer scale. However, local stoichiometry inhomogeneities (of a few nanometer in size) were apparent in a few oxide layers (cf. section 5.3.1).
g) Some sharp interfaces (≤ 5 nm) between Nb-anodes (An) and oxide layers (OL) were observed in $Cap_{No\text{-}Anneal}$. Such interfaces were not observed in $Cap_{300°C\text{-}5h}$ and $Cap_{350°C\text{-}1h}$ (cf. Fig. 6.3.1 and section 5.3.2.).
h) The width of the An-OL interface region seems to increase (by approximately 3 to 5 nm) owing to annealing steps of 5h at 300°C or 1h at 350°C (resulting in smooth stoichiometry gradients, cf. section 5.3.2)
i) After an annealing step of 1h at 350°C, some small crystallites (of the order of 10 nm in size) having a stoichiometry close to NbO_2 (or at least strongly oxygen deficient with respect to Nb_2O_5) were observed at the An-OL interface. However, the corresponding capacitor structures are not homogeneous: these crystallites were not systematically present at all the An-OL interfaces of $Cap_{350°C\text{-}1h}$ (cf. section 5.3.3).
j) The annealing steps (5h at 300°C, 1h at 350°C) yield an oxygen uptake in the Nb-anodes (cf. sections 5.1.5 and 5.2.2)

Some of these aspects are discussed here with respect to literature data.

Homogeneity of the capacitor structures

Störmer et al. (2006) investigated the microstructural and dielectric qualities of capacitor structures with respect to different processing parameters taking part in the preparation of sintered niobium powder compacts (sintering temperature) and the anodic oxidation of the sintered compacts (electrolyte solution, temperature, formation voltage, time). It was for instance shown that some electrolytes (e.g. HNO_3 or NaOH) do not yield homogeneous oxide layer growth. The formation parameters used to prepare the capacitor structures investigated in the present work (see section 2.3.2) were chosen since they were found to result in highly reproducible oxide layers with respect to layer thickness and homogeneity and do not cause field-induced crystallization (Störmer et al., 2009). However, by means of quantitative EELS investigations, some inhomogeneities were still occasionally detected within one and the same oxide layer or while comparing different oxide layers or An-OL interfaces of one and the same type of capacitor structure (points d, f, and i). This indicates that some parameters/phenomena are still not perfectly defined and/or understood and/or controlled. Nevertheless, this is not surprising owing to the numerous factors involved in the complex procedures applied on an industrial scale to produce the Nb-based capacitors (production of high-purity Nb powder with high specific surface area, pressing and sintering, two-stage anodization process) and on the whole the observed inhomogeneities are not particularly strong or frequent. With respect to the fabrication process, Pozdeev-Freeman & Gladkikh (2003) reported for instance that impurities from materials and tooling used for powder pressing and sintering can strongly affect the quality of the anodic oxide layers.

Stoichiometry gradients (in OL) and An-OL interfaces

If the Nb/Nb_2O_5 system is heat treated in air, a gradient of oxygen deficiency is expected across the oxide layer, with the highest value adjacent to the metal (Qiu et al., 2002; see also section 2.2.3). Furthermore, Störmer et al. (2009) measured an increase of the specific capacitance Q/m_{Anode} after heat treatments at temperatures up to 320°C as shown in Fig. 5.4.2 (see also section 2.3.2 for more information on the definition of the mass-specific charge). To explain this behavior (and also the results of other electrical measurements, see below), the authors proposed the following model schematized in Fig. 5.4.3. After the anodization process (the same process as that employed in the present work and described in section 2.3.2), the Nb-anode is covered by a homogeneous dielectric oxide layer of thickness $d_{Ox} \sim 128$ nm. This oxide Nb_2O_{5-x} is slightly oxygen deficient with respect to stoichiometric Nb_2O_5, but its conductivity is still lower than the value σ_0 (value above which the electrical response is not anymore capacitive, Smyth & Tripp, 1966; see also section 2.2.3), so that it acts as dielectric. Upon annealing, oxygen is extracted by the Nb-anode, which results in the formation of a strongly oxygen deficient intermediate layer with a high conductivity exceeding σ_0. Hence, the electrical response of this intermediate layer of thickness d_{cond} can be considered as purely resistive and no longer as capacitive. As a consequence, the thickness of the oxide layer which effectively acts as a dielectric $d_{Ox,effective}$ decreases, resulting in the observed increase of Q/m_{Anode} ($\propto 1/d$). Hence, based on capacitance measurements performed while applying a DC

bias voltage U_{bias} of 10 V to the capacitor structures (see Fig. 5.4.2), Störmer et al. (2009) estimated that the effective dielectric thickness is reduced by about 30% after an annealing step of 1h at 300°C (this annealing step yielded a strong increase of Q/m_{Anode} of about 44%). This corresponds to d_{cond} ~ 39 nm and $d_{Ox,effective}$ ~ 89 nm. This model is neither confirmed nor invalidated by the results obtained in the present work.

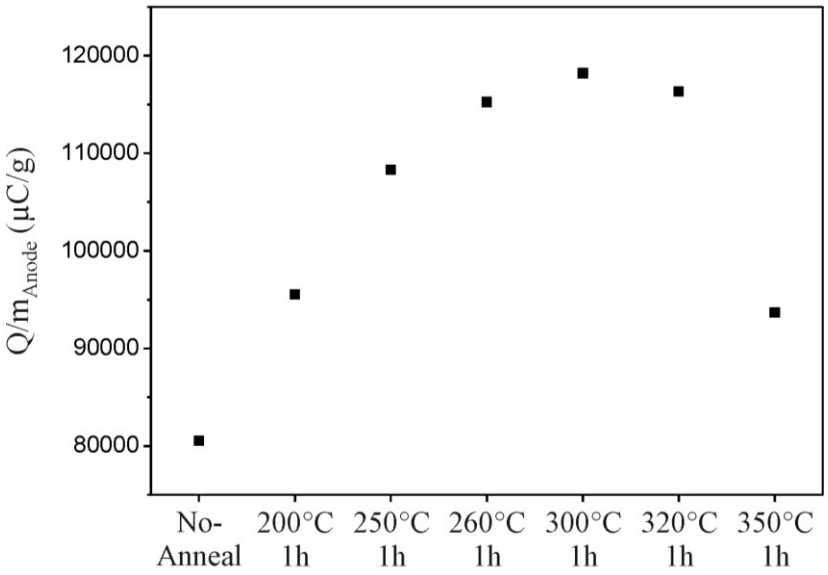

Fig. 5.4.2. Specific capacitances of Nb-based capacitor structures as measured by Störmer et al. (2009) as a function of the preparation-process step. As-anodized (No-Anneal) as well as anodized and annealed capacitor structures were investigated. The anodization conditions were the same as in the present work (1 wt.% H_3PO_4, 65°C, 40 V, 180 min, see section 2.3.2). Annealing steps were performed at temperatures between 200°C and 350°C for 1h in air. The capacitance measurements were carried out at a frequency of 120 Hz with a DC bias voltage U_{bias} = 10 V (for more details, see Störmer et al., 2009).

Indeed, stoichiometry gradients across the oxide layer or large regions with different stoichiometries (intermediate layer and effective dielectric layer with the above mentioned dimensions) were not detected in the present work by investigating $Cap_{300°C\text{-}5h}$ and $Cap_{350°C\text{-}1h}$ (above-mentioned points e and f). However, after an annealing step of 1h at 350°C the increase of Q/m_{Anode} is only of about 16% with respect to as-anodized capacitor structures (Störmer et al., 2009). According to Fischer (2005), an annealing step of 5h at 300°C also leads to a less pronounced increase of Q/m_{Anode} than an annealing step of only 1h at 300°C (the increase can be estimated to approximately 25%). Thus, according to the model of Störmer et al. (2009), the thickness of the intermediate region d_{cond} is expected to be smaller in $Cap_{300°C\text{-}5h}$ and $Cap_{350°C\text{-}1h}$ than after an annealing of 1h at 300°C or 320°C. Nevertheless, it can be calculated that, d_{cond} should still be as large as about 18 nm and 26 nm in the case of $Cap_{300°C\text{-}5h}$ and $Cap_{350°C\text{-}1h}$, respectively. The results of the present work only indicate some possible increase of the width of the An-OL interface region owing to annealing (point h). This effect could contribute to a diminution of the thickness of the effective dielectric layer and thus to the increase of Q/m_{Anode}. However, compared to $Cap_{No\text{-}Anneal}$ this apparent increase

of the An-OL width is limited to approximately 3 to 5 nm for $Cap_{300°C\text{-}5h}$ and $Cap_{350°C\text{-}1h}$. Thus, this effect is clearly not sufficient to explain the above-described variations of Q/m_{Anode}. In the case of $Cap_{350°C\text{-}1h}$ an intermediate region taking the form of NbO_2 crystallites was sometimes observed (point i) which could contribute to the increase of Q/m_{Anode}. But the occurrence of this region is far of being systematic, so that here again this effect is not sufficient to provide a satisfying explanation for the behavior of Q/m_{Anode}. In addition, EELS-linescan analyses on a nanometer scale were also performed at the VG microscope on capacitor structures annealed for 1h at 320°C (however, owing to the use of slightly different experimental parameters, the results were not directly comparable with those presented for $Cap_{No\text{-}Anneal}$, $Cap_{300°C\text{-}5h}$, and $Cap_{350°C\text{-}1h}$ in sections 5.3.1 and 5.3.2 and were not presented there). As for $Cap_{No\text{-}Anneal}$, $Cap_{300°C\text{-}5h}$, and $Cap_{350°C\text{-}1h}$, no stoichiometry gradients or regions differing in stoichiometry could be clearly observed in the oxide layers. Thus, the conclusion of this paragraph is that the model proposed by Störmer et al. (2009) cannot be confirmed within the detection limit of EELS.

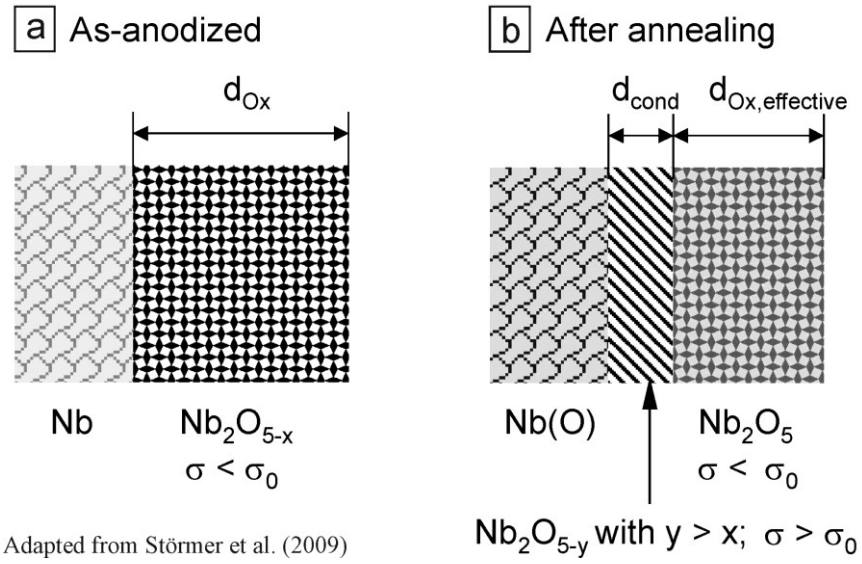

Fig. 5.4.3. Model proposed by Störmer et al. (2009) for the interface region niobium-metal anode / niobium-oxide layer after anodization **(a)** and after subsequent annealing **(b)**. The oxide layer in as-anodized capacitor structures is oxygen deficient, exhibiting the composition Nb_2O_{5-x} (a). Upon annealing in air, an intermediate layer with a conductivity > σ_0 is formed owing to oxygen extraction from the dielectric oxide layer by the Nb-anode (b). It is assumed that this intermediate layer does not consist of a certain fixed composition Nb_2O_{5-y} but contains a steep oxygen gradient. In any case this layer is resistive and contributes no longer to the capacitance. As a result, the effective dielectric oxide layer thickness ($d_{Ox,effective}$) is reduced yielding an increase of the specific capacitance. In addition, an oxygen uptake occurs from the annealing atmosphere (air) into the oxide adjacent to the atmosphere leading to a more stoichiometric niobium pentoxide within the remaining effective dielectric layer.

The sensitivity towards stoichiometry gradients in the oxide layers is of course limited by the experimental detection limit. In the case of the C_{Nb}/C_O measurements performed for the oxide layers at the VG microscope, it was shown in section 5.4.2 that the sensitivity is not necessarily better than 1%. Hence, there is no guarantee that a stoichiometry gradient

corresponding to a total relative composition variation of 1% or less would be clearly detected. However, as reported in section 2.1.3, minimal stoichiometry variations can be sufficient to dramatically affect the electrical properties of niobium pentoxide. For instance, as the composition O/Nb decreases from 2.500 by stoichiometric Nb_2O_5 to 2.480 by $Nb_{25}O_{62}$ - corresponding to a relative composition variation of 0.8% - Schäfer et al. (1969) measured an increase of the conductivity from $3 \cdot 10^{-6}$ S/cm to $5 \cdot 10^{2}$ S/cm (though, it should be noted that these definite values were determined from crystalline phases so that they are not transposable in an absolute manner to anodically grown amorphous oxides - but the trend observed with varying oxygen deficiency is expected to apply qualitatively as well). Thus, a composition variation of less than 1% can yield a conductivity variation over eight orders of magnitude. This could obviously be sufficient to change the electrical response of the oxide from a capacitive to a resistive one. Hence, it can not be excluded that small deviations from stoichiometry and composition gradients are present in the oxide layers that could explain the observed variations of Q/m_{Anode} with annealing in agreement with the model proposed by Störmer et al. (2009). This model cannot be invalidated by the results of the present work.

Olszta & Dickey (2008) also used EELS (stoichiometry quantification and relative chemical shifts of the Nb-M_3 ionization edge) in a scanning transmission electron microscope for the nanoscale investigation of Nb-based capacitor structures consisting like in the present work of oxide layers anodically grown on porous anodes sintered from Nb powders. Nevertheless, they did not study the effects of thermal annealing (investigation of as-anodized capacitor structures without subsequent heat treatment) and it can also be noted that some parameters of the anodization process used to form their capacitor structures differed from those employed in the present work. Except in an about 5 nm wide interface region adjacent to the Nb-metal anode, the authors did not note a particular stoichiometry gradient in the oxide layer (investigated up to a distance of about 30 nm from the anode) which appears quite homogeneous in agreement with the results obtained here (points e and f).
Using secondary ion mass spectroscopy (SIMS) Kovacs et al. (2003) investigated the in-depth composition of oxide layers which were formed on Nb by means of an anodization process close to that employed in the present work (oxidation in 1 wt.% H_3PO_4 at 65°C and with U_{Ox} = 40 V like in the present work, but with different current density and oxidation time). Owing to an annealing step of 1h at 270°C in air, they observed some variations in the measured normalized ion-yield depth profiles that could suggest that the heat treatment resulted in some moderate decomposition of the anodically grown Nb_2O_5 layer, mainly taking place in the neighborhood of the oxide/metal interface. However, the measured normalized ion-yields were not converted into absolute $C_{\mathrm{Nb}}/C_{\mathrm{O}}$ concentration ratios which prevents an assessment of the strength and extension of eventual stoichiometry gradients. In addition, these observations were conducted on oxide layers grown on flat Nb sheets and not directly on convoluted capacitor structures achieved from the oxidation of porous sintered anode bodies.

Olszta & Dickey (2008) measured a stoichiometry gradient of approximately 4-5 nm in extent at the anode/dielectric interface in Nb-based capacitor structures (without annealing, see

above). This is consistent with the observation in $Cap_{No\text{-}Anneal}$ of "sharp" transitions taking place within about 5 nm between anode and oxide layers (point g).
Using scanning electron microscopy (SEM), Fischer (2005) and Störmer et al. (2006; 2009) analyzed the fracture surfaces in capacitor structures between Nb-anode and amorphous oxide after anodization as well as after subsequent annealing for 1h in air at different temperatures. They reported a remarkable change in the fracture behavior after annealing at temperatures exceeding 300°C (frequent fractures along the interface in as-anodized samples and samples heat treated at temperatures below 300°C but no crack propagation along the interface after annealing above 300°C), indicating (microstructural) changes at the interface and/or possibly pronounced oxygen diffusion across the interface during high-temperature annealing. Thus, these observations could be correlated to the fact that "sharp" interfaces were detected in $Cap_{No\text{-}Anneal}$ but not in $Cap_{300°C\text{-}5h}$ and $Cap_{350°C\text{-}1h}$ (point g) and to the apparent widening - in the form of stoichiometry gradient - of the interface region after annealing (point h).

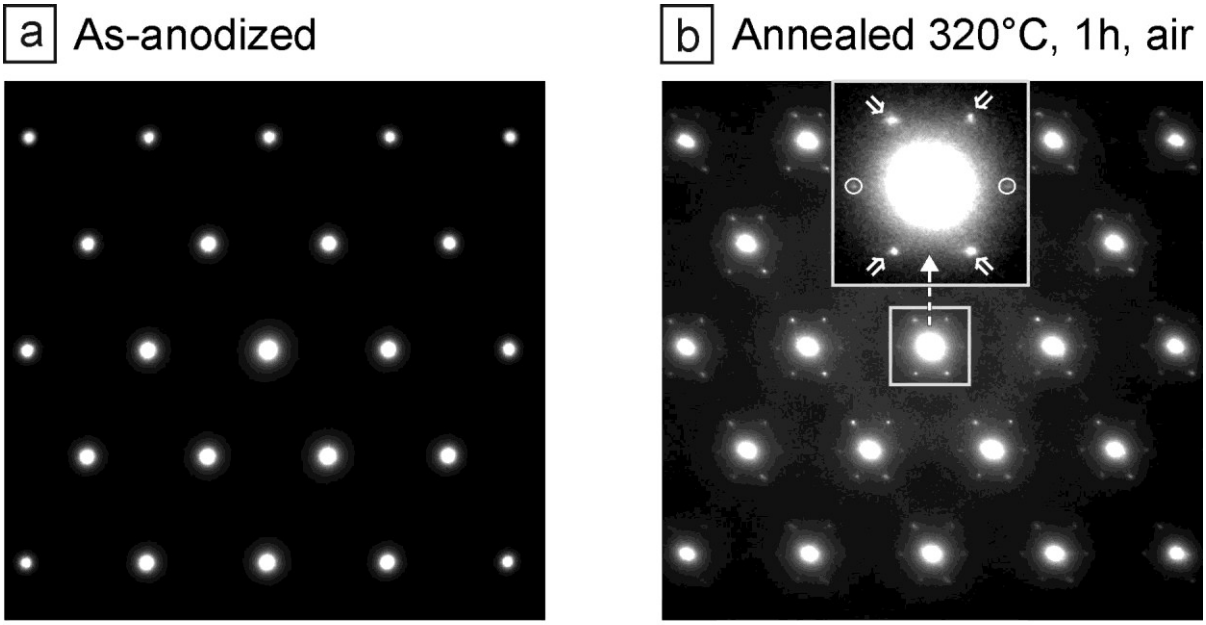

Adapted from Störmer et al. (2009)

Fig. 5.4.4. SAED patterns recorded by Störmer et al. (2009) from anodes of Nb-based capacitor structures after anodization **(a)** and subsequent annealing in air for 1h at 320°C **(b)**. The anodization conditions were the same as in the present work (see section 2.3.2). The SAED pattern of the anode of the as-anodized sample corresponds to niobium with bcc structure along the [111]-zone axis (a). Additional diffraction intensities are observed after annealing at 320°C (b). They can be assigned to an Nb_6O superlattice.

Oxygen uptake in the anode material

SAED investigations performed by Fischer (2005) and Störmer et al. (2006; 2009) showed that oxygen migrates from the niobium-oxide layer into the metallic Nb-anode upon annealing in air at temperatures ≥ 300°C. Indeed, the incorporation of oxygen in Nb-anode is not limited by the solubility limit of oxygen in niobium. Fig. 5.4.4 presents SAED patterns recorded by Störmer et al. (2009) from Nb-anodes after anodization (a) and subsequent annealing in air for

1h at 320°C (b). Without annealing the diffraction pattern correspond to a purely bcc Nb metal structure. After annealing, additional diffraction intensities appear which indicate a quadrupling of the lattice parameter and are attributed the formation of an Nb_6O superstructure in oxygen-oversaturated Nb metal. Such superlattice reflections were not observed after annealing below 300°C. However, Fischer et al. (2005) showed that after 5h annealing at 300°C a majority of the Nb grains in the anode exhibit this superstructure. Thus, these observations are in agreement with the detection via EELS of an oxygen uptake in the Nb-anode owing to annealing (point j). EELS quantification yields an estimation of the C_{Nb}/C_O atomic concentration ratios in the anodes of $Cap_{300°C\text{-}5h}$ and $Cap_{350°C\text{-}1h}$ (cf. section 5.2.2). Whereas Nb_6O (termed NbO_x in section 2.1.2) corresponds to $C_{Nb}/C_O = 6$, even lower ratios near 4 were determined (4.2 for $An_{300°C\text{-}5h}$ and 3.7 for $An_{350°C\text{-}1h}$) which could be consistent with the formation of Nb_4O (termed NbO_y in section 2.1.2). However, these low C_{Nb}/C_O ratios are not incompatible with the observation of Nb_6O superstructures. Firstly, numerous assumptions were made to determine these C_{Nb}/C_O values, so that they have to be considered with caution (cf. sections 4.3.7 and 5.2.2). Secondly, the C_{Nb}/C_O compositions of NbO_x and NbO_y are not precisely determined and these phases only form in definite ranges of temperature and oxygen pressures (Niebuhr, 1966; Gmelin, 1970; see also section 2.1.2). Thus, even if the composition was compatible with Nb_4O, this phase would not form if all the conditions of temperature and pressure were not adequate.

Stoichiometry inside the oxide layer (away from An-OL interface)

Störmer et al. (2009) also used SAED to investigate the amorphous oxide layer in capacitor structures after anodization and after subsequent annealing at 320°C for 1h in air. Diffraction patterns were recorded from large oxide-layer areas with a diameter of 100 nm. From the analysis of the radial intensity distribution of the patterns as a function of the spatial frequency, they determined the nearest-neighbor distances. Within the achievable accuracy of this technique, no influence of annealing could be detected and the results were in all cases found to be compatible with Nb_2O_5.

Considering the error with which EELS quantification was performed by Olszta & Dickey (2008), their measurements inside the oxide layer (without annealing) also appear consistent with stoichiometric Nb_2O_5. However, this error derived from *k*-factor analysis on standards is quite large (± 6.5 % while determining the composition). In addition, the accurate determination of the stoichiometry inside the layer was not the first aim of the authors who did not propose any averaged composition value resulting from a statistical analysis of all their measurements performed in the different investigated oxide layers.

In contrast to the above-mentioned literature data, the good accuracy of the quantification method applied in the present work allows the detection of some oxygen understoichiometry inside the layers with respect to Nb_2O_5 (point a). By averaging the results of the five employed analysis procedures (two at the LEO microscope, three at the VG, see sections 5.2.2 and 5.2.3), a mean value $C_{Nb}/C_O \sim 0.404$ is found for $OL_{No\text{-}Anneal}$, corresponding to $Nb_2O_{4.95}$. Thus, owing to this oxygen deficiency with respect to stoichiometric Nb_2O_5, the oxide is expected to have a n-type semiconducting behavior (see section 2.1.3 and, e.g., Schäfer et al., 1969). This agrees with the conclusions of the electrical characterizations made by Fischer et

al. (2002) and Störmer et al. (2009). The authors observed that the achieved specific capacitance of the anodized Nb-anodes (without annealing) strongly depends on the DC bias voltage U_{bias} applied during the measurements. This bias dependency was found to indicate n-type semiconducting behavior of the anodized oxide layers. Thus, since oxygen-deficient niobium pentoxide phases behave like n-type semiconductors, Störmer et al. (2009) suggested in their model that the anodically formed oxide layers (before annealing) have a composition Nb_2O_{5-x} due to oxygen vacancies compared to stoichiometric Nb_2O_5 (see Fig. 5.4.3a). The results of the present work confirm this composition.

The bias dependency of Q/m_{Anode} is markedly reduced after annealing at temperatures between 260°C and 320°C (air, 1h), indicating a decrease of the oxygen deficiency in the oxide layers, i.e. a composition variation towards stoichiometric Nb_2O_5 (Fischer et al., 2002; Störmer et al., 2009). Thermogravimetric analyses also indicated that annealing in air induces an oxygen uptake in the oxide layers (Störmer et al., 2009). Thus, in their model, Störmer et al. (2009) assume that stoichiometric niobium pentoxide is formed upon annealing due to recombination of the oxygen vacancies with oxygen from the ambient annealing atmosphere (indicated in Fig. 5.4.3b by a composition Nb_2O_5 for the effective dielectric layer achieved after annealing). The decrease of the O-vacancy concentration upon annealing was confirmed by an analysis of the capacitance measurements on the basis of the Mott-Schottky equation which establishes a relationship between capacitance, applied voltage, and donator density for n-type semiconductors (Fischer et al., 2002). This analysis resulted in calculated donor densities ranging from $8 \cdot 10^{18}/cm^3$ after some anodization step to $2 \cdot 10^{18}/cm^3$ after annealing at 320°C (Fischer et al., 2002). However, Fischer (2005) also observed that annealing at temperatures between 260°C and 320°C results in a strong increase of the leakage current. This behavior could be explained by an increase of the conductivity in the effective dielectric oxide layer. Thus, according to Fischer (2005), an increase of the oxygen deficiency could also be expected upon annealing in air, in contradiction to the results of the Mott-Schottky analysis. In the present work, owing to a sensitivity which can be worse than 0.7 % at the LEO microscope (see section 5.4.2), no clear influence of annealing at 300°C could be detected on the stoichiometry inside the oxide layers (mean value $C_{Nb}/C_O \sim 0.404$, point c). In any case, the fact that an oxygen deficiency with respect to Nb_2O_5 is measured in the oxide layers (point a) is qualitatively consistent with a relatively high conductivity and thus with the high leakage currents that are generally reported for Nb-based capacitors (Persico et al., 2001; Fischer, 2005; Li et al., 2006).

In contrast, an annealing step of 1h in air at 350°C resulted in a clear increase of C_{Nb}/C_O inside the capacitor oxide layers (point b). By averaging the results of the five analysis procedures a mean value $C_{Nb}/C_O \sim 0.412$ is found for $OL_{350°C\text{-}1h}$, corresponding to $Nb_2O_{4.86}$. The origin of the increase of Q/m_{Anode} upon annealing at temperatures up to 320°C could not be clarified by the present work. However, the decrease of Q/m_{Anode} with increasing annealing temperature from 300°C to 350°C can be explained by the loss of oxygen in the oxide layers which is certainly accompanied by a deterioration of the dielectric properties (ε_r) resulting in the decrease of the specific capacitance Q/m_{Anode}.

Chapter 6

Summary

A comprehensive electron energy-loss spectroscopy (EELS) study of niobium, stable niobium-oxide phases, and anodically grown niobium-oxide layers was carried out. The near-edge fine structure ("fingerprints") of ionization edges and quantitative EELS data were analyzed in a systematic manner using niobium and stoichiometric Nb-oxides with the different formal oxidation states 0 (Nb), +2 (NbO), +4 (NbO_2) and +5 (Nb_2O_5) as reference materials. Numerous characteristic EELS features were identified which allow the distinction between different Nb-oxidation states. Optimized sensitivity (*k*-)factors were experimentally determined for the Nb-O system which provide a particularly efficient composition-quantification tool with an accuracy of the order of 0.5%. The results of the reference materials were applied for the investigation of solid-electrolyte capacitor structures with Nb as anode material. The composition of the dielectric oxide layer and the interface between anode and oxide layer were characterized on a nanometer scale and discussed in terms of electrical properties of the capacitor and influence of heat treatments. This thesis provides detailed examples of EELS analysis procedures which can be useful for the investigation of other material systems, too.

6.1 Plasmons and ELNES of reference niobium oxides

EELS was performed on the crystalline reference materials (Nb, NbO, NbO_2, Nb_2O_5) to record spectra of the plasmon losses and the Nb-$N_{2,3}$, Nb-$M_{4,5}$, Nb-$M_{2,3}$, Nb-M_1, Nb-$L_{2,3}$, and O-K ionization edges. The plasmons and near-edge structures were analyzed to obtain fingerprints for the distinction of the different formal oxidation states. Niobium and the Nb-oxides can be clearly distinguished by the ELNES of all edges (apart from the Nb-M_1 due to its extremely low intensity) and the characteristics of plasmon excitations. However, the most pronounced signatures are observed for the O-K edges and plasmons in the different materials. The ELNES of the O-K edge can be understood in a first approximation in terms of ligand-field theory.

Chemical shifts of the Nb-$N_{2,3}$, Nb-$M_{4,5}$, Nb-$M_{2,3}$ and Nb-$L_{2,3}$ edges are extracted which amount to about 4 eV as the oxidation state increases from 0 for Nb to +5 for Nb_2O_5. However, it is suggested to use the relative chemical shift between the Nb-$M_{2,3}$ and O-K edge as a criterion for the distinction of the oxides because these two edges shift in opposite energy directions with varying Nb-oxidation state yielding a sensitive criterion. The relative chemical shift measured between NbO and NbO_2 amounts to 1.2 ± 0.3 eV towards higher energies and between NbO and Nb_2O_5 to 2.6 ± 0.4 eV.
The normalized intensity of the Nb-$L_{2,3}$ white-line edge was evaluated and correlated with the niobium 4d-state occupancy in the different reference materials. A sensitive criterion is found for the quantification of the niobium 4d-state occupancy of unknown Nb-oxide phases and thus for the determination of the Nb-oxidation state using the procedure applied in this study to separate the bound-state from the continuum intensity.
Four different microscopes including a 200 keV ZEISS Libra with monochromator were used for spectroscopy covering a wide range of experimental parameters with respect to the primary electron energy (E_0 = 100 keV to 300 keV), convergence (α = 0.4 mrad to 11.2 mrad) and collection (β = 2.3 mrad to 12.3 mrad) semi-angles, as well as energy resolution (dE = 0.3 eV to 2.1 eV). In the range of experimental parameters for E_0, α, β, no dramatic influence on the ELNES of the recorded spectra was observed. The most pronounced effects are attributed to the different energy resolutions and were found a) on the splitting of the different peaks of the O-K edge, b) on the relative height of the first two peaks of the O-K-edge, c) in the low-loss region, d) with respect to resolving double-peak structures of the Nb-$M_{2,3}$ white lines.

6.2 Quantitative EELS analysis of reference niobium oxides

The three stable niobium oxides (NbO, NbO_2, and Nb_2O_5) were analyzed quantitatively by means of EELS. Experimental *k*-factors were derived from the ratio between the intensity under the Nb-$M_{2,3}$ and Nb-$M_{4,5}$ edges, respectively, and the intensity under the O-K edge. The investigation of the three reference oxides allowed a) the investigation and optimization of the precision and accuracy of the resulting quantification tool (*k*-factor), b) the illustration of critical steps in the EELS quantification procedure, and c) the development of some methodological aspects which can be of general interest for the investigation of other material systems (see also subchapter 6.4).
The width of the intensity-integration window ΔE was shown to play a decisive role for the attainable accuracy, since it is correlated with the background-related and ELNES-related systematic errors. Optimum ΔE values (ΔE = 50 eV for the Nb-$M_{2,3}$ edges and ΔE = 70 eV for the Nb-$M_{4,5}$ edges) were determined for the niobium-oxygen system yielding a good compromise between the different systematic errors for quantification. If an optimum ΔE cannot be found for a particular material system, a pragmatic adaptation of the *k*-factor

method is proposed which may improve the obtainable accuracy. The influence of the sample thickness on the measured *k*-factors was also analyzed in detail. Averaging several spectra recorded from specimen regions with different thickness strongly affects the precision. However, it was shown that the use of two different ΔE values to integrate the intensity under two edges of different basic shapes (sawtooth O-K edge and delayed maximum Nb-$M_{4,5}$ edges) can be an alternative to deconvolution techniques to improve the precision of the *k*-factors determined from the corresponding intensity ratio.

The use of experimental *k*-factors derived from Nb-$M_{4,5}$ ($k_{NbM4,5\text{-}OK}$) is generally recommended for highest accuracy and precision as compared to e.g. the *k*-factor derived from the evaluation of the Nb-$M_{2,3}$ ($k_{NbM2,3\text{-}OK}$). In any case, experimental *k*-factors ($k_{NbM4,5\text{-}OK}$ and $k_{NbM2,3\text{-}OK}$) give better results than calculated ratios of the Nb-$M_{4,5}$ to O-K partial ionization cross-sections which were found to lead to a strong underestimation of C_{Nb}/C_O atomic concentration ratios in the order of 40%.

6.3 EELS investigations of Nb-based capacitor structures

Nb-based solid-electrolyte capacitor structures were investigated by means of ELNES and quantitative EELS. They consist of approximately 130 nm thick amorphous niobium-oxide layers anodically grown on Nb anodes. They were studied without annealing after the anodic oxidation (Cap_{No_Anneal}) or with a subsequent annealing step in air for 5 h at 300°C ($Cap_{300°C\text{-}5h}$), 1 h at 320°C ($Cap_{320°C\text{-}1h}$), or for 1h at 350°C ($Cap_{350°C\text{-}1h}$).

EEL spectra of the plasmon losses and the Nb-$N_{2,3}$, Nb-$M_{4,5}$, Nb-$M_{2,3}$, Nb-$L_{2,3}$, and O-K ionization edges were recorded from the oxide layers (OL) and compared to the reference fingerprints. They show close similarities to the plasmon losses and ELNES of reference Nb_2O_5 but some details of the OL spectra are significantly different compared to crystalline Nb_2O_5. These discrepancies are mainly attributed to the fact that the capacitor oxide layers are amorphous whereas the Nb_2O_5 reference material is crystalline. On the whole, the plasmon fingerprints and ELNES results indicate that the niobium oxidation state in the oxide layer is close to +5.

Quantitative EELS was performed on OL_{No_Anneal}, $OL_{300°C\text{-}5h}$, and $OL_{350°C\text{-}1h}$ using five distinct analysis procedures based on the *k*-factors ($k_{NbM4,5\text{-}OK}$) experimentally derived from the reference measurements (LEO 922 Omega and VG HB501UX microscopes). The resulting C_{Nb}/C_O atomic concentration ratios are particularly close to the nominal value for Nb_2O_5 (0.400). For instance, $C_{Nb}/C_O = 0.405 \pm 0.011$ (±2.7%) is found for OL_{No_Anneal} by means of one of the quantification procedures. At first sight, considering the precision of the quantification, the results are still compatible with stoichiometric Nb_2O_5. However, owing to the high accuracy of the applied procedure, the investigations indicate a slight oxygen deficiency with respect to Nb_2O_5. An Oxygen deficiency in the oxide layers is qualitatively consistent with electrical properties reported in the literature for solid-electrolyte capacitors

with Nb as anode material (bias dependency of the specific capacitance, high leakage currents). The mean C_{Nb}/C_O values of the five procedures amount to approximately 0.404 ($Nb_2O_{4.95}$), 0.404 ($Nb_2O_{4.95}$), and 0.412 ($Nb_2O_{4.86}$) for OL_{No_Anneal}, $OL_{300°C\text{-}5h}$, and $OL_{350°C\text{-}1h}$, respectively. Thus, no clear influence of the annealing step of 5h at 300°C can be recognized, whereas 1h annealing at 350°C is found to result in an increase of the oxygen deficiency.
In agreement with SAED literature data, EELS indicates an oxygen uptake in the Nb anode (An) during annealing (5h at 300°C, 1h at 350°C). A stoichiometry of the order of $NbO_{0.25}$ can be determined for $An_{300°C\text{-}5h}$ and $An_{350°C\text{-}1h}$.
By means of a scanning transmission electron microscope (VG HB501UX, electron probe of 0.5 nm in diameter), Cap_{No_Anneal}, $Cap_{300°C\text{-}5h}$, and $Cap_{350°C\text{-}1h}$ were examined by EELS on a nanometer scale. Within the achievable sensitivity of EELS quantification, no stoichiometry gradient could be detected across the oxide layers. However, the typical An-OL interface width appears to increase by about 3 to 5 nm due to annealing. In addition, some small crystallites (of the order of 10 nm in size) were occasionally observed at the An-OL interface of $Cap_{350°C\text{-}1h}$ with a stoichiometry close to NbO_2 (or at least strongly oxygen-deficient with respect to Nb_2O_5). Similar crystallites could not be detected in Cap_{No_Anneal} or $Cap_{300°C\text{-}5h}$, hinting to an effect of the annealing at 350°C.

6.4 General aspects of the applied EELS analysis procedures

The present study is an experimental ELNES and quantitative EELS investigation of one specific material system, namely the niobium-oxygen system. In the first instance, the results are specific to niobium oxides and (particularly for quantitative EELS) to the used experimental parameters (see section 4.4.8). However, the procedures used to identify characteristic ELNES features and to determine the experimental *k*-factors were described in detail since they could be of interest for the investigation of other material systems.
In terms of ELNES, the advantages of relative chemical shifts were examined, as well as the strong influence of the energy resolution on the phase fingerprints. The influence of different crystalline/amorphous structures at nearly constant composition was considered, too.
In terms of quantitative EELS, the different factors that may affect the precision and accuracy of the quantification were discussed extensively, including multiple scattering, background subtraction, ELNES, signal intensity, TEM-sample preparation, crystalline/amorphous structure, and homogeneity range of the reference materials.
Particularly, some aspects of the quantitative reference results should be transferable to materials analyzed by a sawtooth edge in combination with an edge showing a delayed maximum. This condition is fulfilled for other 4d transition-metal oxides with delayed maximum shape of the metal $M_{4,5}$ ionization edges, like, e.g., molybdenum oxides. Obviously, a similar sensitivity of the *k*-factors with respect to the window width for integration and the specimen thickness can be expected as the particular shapes of the

analyzed edges were shown to play an important role (increase of $k_{\text{MetalM4,5-OK}}$ when ΔE increases and t/Λ decreases, see sections 4.4.8 and 4.4.5). For instance, the effects of Fourier-ratio deconvolution on the determined *k*-factor values should be analogous (cf. Fig. 4.3.8a, the LEO Nb-$M_{4,5}$ data in Table 4.3.3, section 4.4.5). Also, as an alternative to deconvolution, the use of two different windows for integrating the O-K and metal-$M_{4,5}$ signals should improve the precision of the EELS quantification when spectra of differently thick regions are analyzed (cf. section 4.4.6, especially Fig. 4.4.3).

More generally, the described method to find an optimum integration window in terms of accuracy could be applied to determine experimental *k*-factors for other binary material systems, too. Usually, for quantifying EEL spectra energy windows between 50 and 100 eV are employed owing to large ELNES-related errors below 50 eV and large background-related errors above 100 eV (Egerton, 1986, Brydson, 2001). However, the results of the present systematic study illustrate that the choice of an appropriate integration window can be particularly crucial (see, e.g., Fig. 4.3.4), but there is only little information in the literature how this choice should be made. Obviously, the use of solely one standard may be insufficient. The procedure applied in the present work firstly consists in the investigation of two standards of extremely different compositions (for the composition range of interest) to search for an optimum window (see section 4.3.3). However, the fact that the *k*-factors determined from two standards are in good agreement does not necessarily imply that they will yield a correspondingly good accuracy for the characterization of all the in-between compositions (see, e.g., in section 4.4.7 the case of the quantification using Nb-$M_{2,3}$ edges). Thus, a third standard having an intermediate composition was measured to characterize the accuracy effectively achieved via the "optimum" window derived from the two first standards (see section 4.3.4). In addition, an alternative quantification formalism is proposed in the case were the classical formalism does not allow to find an optimum window by means of two standards (see section 4.4.7). Here again, a third standard was used to check the accuracy of this modified quantification method. In summary, it is recommended to investigate as much standards as possible. It might be time-consuming but it is the key for controlling and optimizing the quantification accuracy.

References

ADLER, D. (1968). Mechanisms for metal-nonmetal transitions in transition-metal oxides and sulfides. *Rev. Mod. Phys.* **40**, 714-736.

AHN, C.C. & KRIVANEK, O.L. (1983). *EELS Atlas – A reference guide of electron energy loss spectra covering all stable elements*, GATAN Inc.

AHN, C. & REZ, P. (1985). Inner shell edge profiles in electron energy loss spectroscopy. *Ultramicroscopy* **17**, 105-116.

AHN C.C. (Editor) (2004). *Transmission Electron Energy Loss Spectrometry in Materials Science and the EELS Atlas*. New York: Wiley.

ANDERSSON, S. & WADSLEY, A.D. (1966). Crystallographic shear and diffusion paths in certain higher oxides of niobium, tungsten, molybdenum and titanium. *Nature* **211**, 581-583.

ANN MCCONNELL, A., ANDERSON, J.S. & RAO, C.N.R. (1976). Raman spectra of niobium oxides. *Spectrochim. Acta* **32A**, 1067-1076.

ARFAOUI, I., COUSTY, J. & SAFA, H.. (2002). Tilting of a Nb(110) surface with NbO crystals nanosized by the NbO/Nb misfit. *Phys. Rev. B* **65**, 115413(1-8).

AUERHAMMER, J., REZ, P. & HOFER, F. (1989). A comparison of theoretical and experimental L and M cross sections. *Ultramicroscopy* **30**, 365-370.

BACH, D., STÖRMER, H. & GERTHSEN, D. (2004). EELS investigation of different niobium oxide phases. In *Proceedings of the 13th European Microscopy Congress (EMC 2004)*, Antwerp (Belgium)

BACH, D., STÖRMER, H., GERTHSEN, D. & VERBEECK, J. (2005). EELS investigation of different niobium oxide phases. In *Abstracts of the International EELS Workshop "EDGE2005"*, Grundlsee (Austria), p. 114.

BACH, D., STÖRMER, H., SCHNEIDER, R., GERTHSEN, D. & VERBEECK, J. (2006). EELS investigations of different niobium oxide phases. *Microsc. Microanal.* **12**, 416-423.

BACH, D., STÖRMER, H., SCHNEIDER, R., GERTHSEN, D. & SIGLE, W. (2007*a*). EELS investigations of reference niobium oxides and anodically grown niobium oxide layers. *Microsc. Microanal.* **13 (Suppl 2)**, 1274-1275.

BACH, D., STÖRMER, H., SCHNEIDER, R. & GERTHSEN, D. (2007*b*). Quantitative EELS Analysis of Niobium Oxides. *Microsc. Microanal.* **13 (Suppl 3)**, 390-391.

BACH, D., SCHNEIDER, R., GERTHSEN, D., VERBEECK, J. & SIGLE, W. (2009*a*). EELS of niobium and stoichiometric niobium-oxide phases. Part I: Plasmon and near-edges fine structure. *Microsc. Microanal.*, accepted.

BACH, D., SCHNEIDER, R. & GERTHSEN, D. (2009*b*). EELS of niobium and stoichiometric niobium-oxide phases. Part II: Quantification. *Microsc. Microanal.*, accepted.

BAI, X.D., ZHU, D.H. & LIU, B.X.. (1996). Anodic and air oxidation of niobium studied by ion beam analysis with implanted Xe marker. *Nucl. Instrum. Meth. B* **114**, 64-69.

BATCHELOR, A.D., LEONARD, D.N., RUSSELL, P.E., STEVIE, F.A., GRIFFIS, D.P. & MYNENI, G.R. (2007). TEM and SIMS analysis of (100), (110), and (111) single crystal niobium. *AIP Conf. Proc.* **927**, 72-83.

BERTONI, G. & VERBEECK, J. (2008). Accuracy and precision in model based EELS quantification. *Ultramicroscopy* **108**, 782-790.

BLAHA, P., SCHWARZ, K., MADSEN, G.K.H., KVASNICKA, D. & LUITZ, J. (2001). *WIEN2K, An Augmented Plane Wave + Local Orbitals Program for Calculating Crystal Properties*. Karlheinz Schwarz, Tech. Universität Wien, Austria.

BRAUER, G. (1940). Über die Oxyde des Niobs. *Naturwiss.* **28**, 30.

BRAUER, G. (1941). Die Oxyde des Niobs. *Z. anorg. Allg. Chem.* **248**, 1-31.

BRAUER, G., MÜLLER, H. & KÜHNER, G. (1962). Oxide der Tieftemperaturoxydation von Niob und Tantal. *J Less-Common Met* **4**, 533-546.

BRAYNER, R. & BOZON-VERDURAZ, F. (2003). Niobium pentoxide prepared by soft chemical routes: morphology, structure, defects and quantum size effect. *Phys. Chem. Chem. Phys.* **5**, 1457-1466.

BRULEY, J., WILLIAMS, D.B., CUOMO, J.J. & PAPPAS, D.P. (1995). Quantitative near-edge structure analysis of diamond-like carbon in the electron microscope using two-window method. *J. Microsc.* **180**, 22-32.

BRYDSON, R. (1992). Electron energy loss near-edge structure as an analytical tool – the study of minerals. In *Transmission electron energy loss spectroscopy in materials science*, Disko, M.M., Ahn, C.C. & Fultz, B. (Eds), pp. 131-154.Warrendale: The Minerals, Metals & Materials Society.

BRYDSON, R., GARVIE, L.A.J., CRAVEN, A.J., SAUER, H., HOFER, F. & CRESSEY, G. (1993). $L_{2,3}$ edges of tetrahedrally coordinated d^0 transition-metal oxyanions XO_4^{n-}. *J. Phys.: Condens. Matter* **5**, 9379-9392.

BRYDSON, R. (2000). A brief review of quantitative aspects of electron energy loss spectroscopy and imaging. *Mat. Sc. Technol.* **16**, 1187-1198.

BRYDSON, R. (2001). *Electron Energy loss spectroscopy*. Oxford: BIOS Scientific Publishers Ltd.

CAVIGLIASSO, G.E., ESPLANDIU, M.J. & MACAGNO, V.A. (1998). Influence of the forming electrolyte on the electrical properties of tantalum and niobium oxide films: an EIS comparative study. *J. Appl. Electrochem.* **28**, 1213-1219.

CHEETHAM, A.K. & RAO, C.N.R. (1976). A neutron diffraction study of niobium dioxide. *Acta Crystallogr., Sec. B* **32**, 1579-1580.

CHO, N.-H., KANG, H.B. & KIM, Y.H. (1994). Dielectric characteristics and chemical structures of Nb_2O_5 thin films grown by sol-gel techniques. *Ferroelectrics* **152**, 43-48.

CIOVATI, G. (2006). Improved oxygen diffusion model to explain the effect of low-temperature baking on high field losses in niobium superconducting cavities. *Appl. Phys. Lett.* **89**, 022507(1-3).

CLARKE, F. W. (1914). Columbium versus Niobium. *Science* **39**, 139-140.

COX, B. & JOHNSTON, T. (1963). The oxidation and corrosion of Niobium (Columbium). *T. Metall. Soc. AIME* **227**, 36-47.

D'ACAPITO, F., MOBILIO, S., CIKMACS, P., MERLO, V. & DAVOLI, I. (2000). Temperature modification of the Nb oxidation at the Nb/Al interface studied by reflEXAFS. *Surf. Sci.* **468**, 77-84.

DAHMEN, U., ERNI, R., KISIELOWKI, C., RADMILOVIC, V., RAMASSE, Q., SCHMID, A., DUDEN, T., WATANABE, M., MINOR, A. & DENES, P. (2008). An update on the TEAM project – first rsults from the TEAM 0.5 microscope, and its future development. In *Proceedings of the 14th European Microscopy Congress (EMC 2008)*, Aachen (Germany), pp. 3-4.

DEARDO, A.J. (2001). Fundamental metallurgy of niobium in steel. In *Proceedings of the international Symposium Niobium 2001*, Niobium 2001 Ltd, Bridgeville, USA, pp. 427-500.

DE GROOT, F.M.F., GRIONI, M., FUGGLE, J.C., GHIJSEN, J., SAWATZKY, G.A. & PETERSEN, H. (1989). Oxygen 1s x-ray-absorption edges of transition-metal oxides. *Phys Rev B* **40**, 5715-5723.

DELHEUSY, M., STIERLE, A., KASPER, N., KURTA, R. P., VLAD, A., DOSCH, H., ANTOINE, C., RESTA, A., LUNDGREN, E. & ANDERSON, J. (2008). X-ray investigation of subsurface interstitial oxygen at Nb/oxide interfaces. *Appl. Phys. Lett.* **92**, 101911.

DJEBARA, L. & NGUYEN, T.P. (2004). Some investigations concerning the tantalum oxide for electrolytic capacitors: effect of thermal treatment. In *Proceedings of the 18th Passive Components Symposium (CARTS Europe 2004)*, Nice (France), pp. 121-125.

DREWES, E.J. & WALKER, E.F. (2001). Niobium bearing steels in the automotive industry. In *Proceedings of the international Symposium Niobium 2001*, Niobium 2001 Ltd, Bridgeville, USA, pp. 873-888.

ECKERT, J., REICHERT, K., SCHNITTER, C. & SEYEDA, H. (2001). Processing of columbite-tantalite ores and concentrates for niobium and niobium compounds in electronic applications. In *Proceedings of the international Symposium Niobium 2001*, Niobium 2001 Ltd, Bridgeville, USA, pp. 67-87.

EGERTON, R.F. (1978). Formulae for light-element microanalysis by electron energy-loss spectrometry. *Ultramicroscopy* **3**, 243-251.

EGERTON, R.F. (1979). K-shell ionization cross-sections for use in microanalysis. *Ultramicroscopy* **4**, 169-179.

EGERTON, R.F. (1986). *Electron Energy-Loss Spectroscopy in the Electron Microscope*. New York: Plenum Press.

EGERTON, R.F. (2003). New techniques in electron energy-loss spectroscopy and energy-filtered imaging. *Micron* **34**, 127-139.

EGERTON, R.F. (2009). Electron energy-loss spectroscopy in the TEM. *Rep. Prog. Phys.* **72**, 016502(1-25).

EISENBARTH, E., VELTEN, D.& BREME, J. (2007). Biomimetic implant coatings. *Biomolecular Engineering* **24**, 27-32.

EL-MAHDY, G.A. (1997). Formation and dissolution behaviour of niobium oxide in phosphoric acid solutions. *Thin solid films* **307**, 141-147.

ELLIOTT, R.P. (1960). Columbium-oxygen system. *Trans. Am. Soc. Metals* **52**, 990-1014.

ERNI, R. & BROWNING, N.D. (2005). Valence electron energy-loss spectroscopy in monochromated scanning transmission electron microscopy. *Ultramicroscopy* **104**, 176-192

ESSERS, E., MITTMANN, D., MANDLER, T. & BENNER, G. (2008). The MANDOLINE filter and its performance. In *Proceedings of the 14th European Microscopy Congress (EMC 2008)*, Aachen (Germany), pp. 51-52.

FISCHER, V., WEBER, A., KRÜGEL, A., STENZEL, M., ZILLGEN, H. & IVERS-TIFFÉE, E. (2002). Nanoscale anodic oxide layers for new niobium capacitors: electrical and structural properties. In *Proceedings of the 202nd Meeting of the Electrochem. Soc.*, Salt Lake City (UT, USA), pp. 78-87.

FISCHER, V., STÖRMER, H., GERTHSEN, D., STENZEL, M., ZILLGEN, H. & IVERS-TIFFÉE, E. (2003). Niobium as New Material for Electrolyte Capacitors with Nanoscale Dielectric Oxide Layers. In *Proceedings of the 7th International Conference on Properties and Applications of Dielectric Materials (ICPADM 2003)*, Nagoya (Japan), pp. 1134-1137.

FISCHER, V. (2005). *Nanoskalige Nioboxidschichten für den Einsatz in hochkapazitiven Niob-Elektrolytkondensatoren*, PhD Thesis, Universität Karlsruhe (TH), Germany. Aachen, Germany: Verlaghaus Mainz GmbH.

FIX, T., ULHAQ-BOUILLET, C., COLIS, S., DINIA, A., BERTONI, G., VERBEECK, J. & VAN TENDELOO, G. (2007). Nanoscale analysis of interfaces in a metal/oxide/oxide trilayer obtained by pulsed laser deposition. *Appl. Phys. Lett.* **91**, 023106 1-3.

FRANCHY, R., BARTKE, T.U. & GASSMANN, P. (1996). The interaction of oxygen with Nb(110) at 300, 80 and 20 K. *Surf. Sci.* **366**, 60-70.

FRIEDRICHS, O., SANCHEZ-LOPEZ, J.C., LOPEZ-CARTES, C., KLASSEN, T., BORMANN, R. & FERNANDEZ, A. (2006). Nb_2O_5 "pathway effect" on hydrogen sorption in Mg. *J. Phys. Chem. B* **110**, 7845-7850.

FROMM, E. (1966). Zur p-T-c-Darstellung der Systeme Niob-Sauerstoff und Tantal-Sauerstoff. *Z. Metallkde.* **57**, 540-545.

GANNON, J.R. & TILLEY, R.J.D. (1977). The microstructure of slightly substoichiometric NbO_2. *J. Solid State Chem.* **20**, 331-344.

GATEHOUSE, B.M. & WADSLEY, A.D. (1964). The Crystal Structure of the High-Temperature form of Niobium Pentoxide. *Acta Cryst* **17**, 1545-1554.

GHANASHYAM KRISHNA, M. & BHATTACHARYA, A.K. (1999). Thickness and oxygen pressure dependent optical properties of niobium oxide thin films. *Int. J. Mod. Phys. B* **13**, 411-418.

Gmelin Handbuch der Anorganischen Chemie, Niob, Teil B1 (1970). Weinheim: Verlag Chemie GmbH.

GODLEY, R., STAROSVETSKY, D. & GOTMAN, I. (2004). Bonelike apatite formation on niobium metal treated in aqueous NaOH. *J. Mater. Sci.-Mater. M.* **15**, 1073-1077.

GRAETZ, J., AHN, C.C., OUYANG, H., REZ, P. & FULTZ, B. (2004). White lines and d-band occupancy for the 3d transition-metal oxides and lithium transition-metal oxides. *Phys. Rev. B* **69**, 235103-1-6.

GRAHAM, R.A. & SUTHERLIN, R.C. (2001). Niobium and niobium alloys in corrosive applications. In *Proceedings of the international Symposium Niobium 2001*, Niobium 2001 Ltd, Bridgeville, USA, pp. 337-355.

GRIFFITH, W.P. & MORRIS, P.J.T. (2003). Charles Hatchett FRS (1765-1847), chemist and discoverer of Niobium. *Notes Rec. R. Soc. Lond.* **57**, 299-316.

GROSSMAN, E.N., HARVEY, T.E. & REINTSEMA, C.D. (2002). Controlled barrier modification in Nb/NbOx/Ag metal insulator metal tunnel diodes. *J. Appl. Phys.* **91**, 10134-10139.

GRUEHN, R. (1966). Eine weitere neue Modifikation des Niobpentoxids. *J Less-Common Met* **11**, 119-126.

GRUEHN, R. & NORIN, R. (1967). Zur Darstellung und Kristallstruktur von $NbO_{2.483}$. *Z. anorg. Allg. Chem.* **355**, 176-181.

GRUEHN, R. & NORIN, R. (1969). Zur Darstellung und Kristallstruktur von $NbO_{2.464}$. *Z. anorg. Allg. Chem.* **367**, 209-218.

GRUNDNER, M. & HALBRITTER, J. (1980). XPS and AES studies on oxide growth and oxide coatings on niobium. *J. Appl. Phys.* **51**, 397-405.

HALBRITTER, J. (1987). On the oxidation and on the superconductivity of niobium. *Appl. Phys. A* **43**, 1-28.

HANADA, N., ICHIKAWA, T. & FUJII, H. (2006). Catalytic effect of niobium oxide on hydrogen storage properties of mechanically ball milled MgH_2. *Phys. B* **383**, 49-50.

HANADA, N., ICHIKAWA, T. & FUJII, H. (2007). Hydrogen absorption kinetics of the catalyzed MgH_2 by niobium oxide. *J. Alloy. Compd.* **446-447**, 67-71.

HARTEL, P., MÜLLER, H., UHLEMANN, S. & HAIDER, M. (2007). First experimental results with advanced hexapole C_s-correctors. *Microsc. Microanal.* **13 (Suppl. 3)**, 004-005.

HATCHETT, C. (1802*a*). An analysis of a mineral substance from North America, containing a metal hitherto unknown. *Phil. Trans. R. Soc. Lond.* **92**, 49-66.

HATCHETT, C. (1802*b*). Eigenschaften und chemisches Verhalten des von Charles Hatchett endeckten neuen Metalls, Columbium. *Annalen der Physik* **11**, 120-122.

HAYASHI, K., OTSUKA, K. & ITOH, K. (2001). Niobium in heat resisting cast steel auto parts. In *Proceedings of the international Symposium Niobium 2001*, Niobium 2001 Ltd, Bridgeville, USA, pp. 1055-1062.

HEBDA, J. (2001). Niobium alloys and high temperature applications. In *Proceedings of the international Symposium Niobium 2001*, Niobium 2001 Ltd, Bridgeville, USA, pp. 243-259.

HÉBERT, C. (2007). Practical aspects of running the WIEN2k code for electron spectroscopy. *Micron* **38**, 12-28.

HEISTERKAMP, F & CARNEIRO, T. (2001). Niobium: future possibilities - technology and market place. In *Proceedings of the international Symposium Niobium 2001*, Niobium 2001 Ltd, Bridgeville, USA, pp. 1109-1159.

HELALI, S., ABDELGHANI, A., HAFAIEDH, I., MARTELET, C., PRODROMIDIS, M.I., ALBANIS, T. & JAFFREZIC-RENAULT, N. (2008). Functionalization of niobium electrodes for the construction of impedimetric biosensors. *Mat. Sci. Eng. C* **28**, 826-830.

HEURUNG, G. & GRUEHN, R. (1982). Neues zur Struktur und Stabilität von M-Nb_2O_5. *Z. anorg. Allg. Chem.* **491**, 101-112.

HEUSING, S., SUN, D.L., OTERO-ANAYA, J. & AEGERTER, M.A. (2006). Grey, brown and blue coloring sol-gel electrochromic devices. *Thin Solid Films* **502**, 240-245.

HIBST, H. & GRUEHN, R. (1978). Weitere neue Nb_2O_5-Modifikationen, metastabile Oxidationsprodukte von NbO_x-Phasen ($2{,}4 < x < 2{,}5$). *Z. anorg. Allg. Chem.* **442**, 49-78.

HOFER, F. & GOLOB, P. (1988). Quantification of electron energy-loss spectra with K and L shell ionization cross-sections. *Micron Microsc. Acta* **19**, 73-86.

HOFER, F., GOLOB, P. & BRUNEGGER, A. (1988). EELS quantification of the elements Sr to W by means of M_{45} edges. *Ultramicroscopy* **25**, 81-84.

HOFER, F. (1991). Determination of inner-shell cross-sections for EELS-quantification. *Microsc. Microanal. Microstruct.* **2**, 215-230.

HOFER, F. & KOTHLEITNER, G. (1993). Quantitative microanalysis using electron energy-loss spectroscopy: I. Li and Be in oxides. *Microsc. Microanal. Microstruct.* **4**, 539-560.

HOFER, F. & KOTHLEITNER, G. (1996). Quantitative microanalysis using electron energy-loss spectroscopy: II. Compounds with heavier elements. *Microsc. Microanal. Microstruct.* **7**, 265-277.

HOFER, F., KOTHLEITNER, G. & REZ, P. (1996). Ionization cross-sections for the L_{23}-edges of the elements Sr to Mo for quantitative EELS analysis. *Ultramicroscopy* **63**, 239-245.

HULM, J.K., JONES, C.K., HEIN, R.A. & GIBSON, J.W. (1972). Superconductivity in the TiO and NbO systems. *J. Low Temp. Phys.* **7**, 291-307.

HUSSAIN, A., REITZ, B. & GRUEHN, R. (1986). A new NbO_x phase with β-$ZrNb_{24}O_{62}$ structure. *Z. anorg. Allg. Chem.* **535**, 186-194.

HYODO, T., OHOKA, J., SHIMIZU, Y. & EGASHIRA, M. (2006). Design of anodically oxidized Nb_2O_5 films as a diode-type H_2 sensing material. *Sensors and Actuators B* **117**, 359-366.

JANNINCK, R.F. & WHITMORE, D.H. (1966). Electrical conductivity and thermoelectric power of niobium dioxide. *J. Phys. Chem. Solids.* **27**, 1183-1187.

JEGLITSCH, F. (2001). Niobium in tool steels and cemented carbides. In *Proceedings of the international Symposium Niobium 2001*, Niobium 2001 Ltd, Bridgeville, USA, pp. 1001-1039.

JIANG, N. & SPENCE, J.C.H. (2004). Electron energy-loss spectroscopy of the O K edge of NbO_2, MoO_2, and WO_2. *Phys. Rev.* B **70**, 245117-1-7.

KAISER, U., CHUVILIN, A., SCHRÖDER, R.R., HAIDER, M. & ROSE, H. (2008). Sub-Angstrom Low-Voltage Electron Microscopy – future reality for deciphering the structure of beam-sensitive nanoobjects? In *Proceedings of the 14th European Microscopy Congress (EMC 2008)*, Aachen (Germany), pp. 35-36.

KATO, K & TAMURA, S. (1975). Die Kristallstruktur von *T*-Nb_2O_5. *Acta Cryst* B**31**, 673-677.

KATO, K (1976). Structure refinement of *H*-Nb_2O_5. *Acta Cryst* B**32**, 764-767.

KARLINSEY, R.L. (2006). Self-assembled Nb_2O_5 microcones with tailored crystallinity. *J. Mater. Sci.* **41**, 5017-5020.

KEAST, V.J., SCOTT, A.J., BRYDSON, R., WILLIAMS, D.B. & BRULEY, J. (2001). Electron energy-loss near-edge structure – a tool for the investigation of electronic structure on the nanometre scale. *J. Microsc.* **203**, 135-175.

KIM, S.-J., CHO, B.J., YU, M.B., LI, M.-F., XIONG, Y.Z., ZHU, C., CHIN, A. & KWONG, D.-L. (2005). Metal-Insulator-Metal RF bypass capacitor using niobium oxide (Nb_2O_5) with HfO_2/Al_2O_3 barriers. *IEEE Electr. Device L.* **26**, 625-627.

KIMURA, S. (1973). Phase equilibria in the system NbO_2-Nb_2O_5: phase relations at 1300 and 1400°C and related thermodynamic treatment. *J. Solid State Chem.* **6**, 438-449.

KURIOKA, N., WATANABE, D., HANEDA, M., SHIMANOUCHI, T., MIZUSHIMA, T., KAKUTA, N., UENO, A., HANAOKA, T. & SUGI, Y. (2003). Preparation of niobium oxide films as a humidity sensor. *Catal. Today* **16**, 495–501.

KUKLI, K., RITALA, M. & LESKELÄ, M. (2001). Development of dielectric properties of niobium oxide, tantalum oxide, and aluminium oxide based nanolayered materials. *J. Electrochem. Soc.* **148**, F35-F41.

KURATA, H., LEFÈVRE, E., COLLIEX, C. & BRYDSON, R. (1993). Electron-energy-loss near-edge structures in the oxygen K-edge spectra of transition-metal oxides. *Phys Rev* B **47**, 13763-13768.

KURMAEV, E.Z., MOEWES, A., BUREEV, O.G., NEKRASOV, I.A., CHERKASHENKO, V.M., KOROTIN, M.A. & EDERER, D.L. (2002). Electronic structure of niobium oxides. *J. Alloy. Compd.* **347**, 213-218.

KOVÁCS, K., KISS, G., STENZEL, M. & ZILLGEN, H. (2003). Anodic oxidation of niobium sheets and porous bodies – Heat-treatment of the Nb/Nb-oxide system. *J. Electrochem. Soc.* **150**, B361-B366.

KRAUTH, H. (2001). Fabrication and applications of NbTi and Nb_3Sn superconductors. In *Proceedings of the international Symposium Niobium 2001*, Niobium 2001 Ltd, Bridgeville, USA, pp. 207-219.

LAI, F., LI, M., WANG, H., HU, H., WANG, X., HOU, J.G., SONG, Y. & JIANG, Y. (2005). Optical scattering characteristic of annealed niobium oxide films. *Thin Solid Films* **488**, 314-320.

LEAPMAN, R.D., REZ, P. & MAYERS, D.F. (1980). K, L, and M shell generalized oscillator strengths and ionization cross sections for fast electron collisions. *J. Chem. Phys.* **72**, 1232-1243.

LEAPMAN, R.D., GRUNES, L.A. & FEJES, P.L. (1982). Study of the L_{23} edges in the 3d transition metals and their oxides by electron-energy-loss spectroscopy with comparisons to theory. *Phys. Rev. B* **26**, 614-635.

LEITEL, R., STENZEL, O., WILBRANDT, S., GÄBLER, D., JANICKI, V. & KAISER, N. (2006). Optical and non-optical characterization of Nb_2O_5–SiO_2 compositional graded-index layers and rugate structures. *Thin Solid Films* **497**, 135-141.

LI, J., YI, D.-Q., WEN, J.-J., ZHONG, H. & LIU, H.-Q. (2006). Electric properties stability of NbO anode for new electrolytic capacitor. *Trans. Nonferrous Met. Soc. China* **16**, 848-852.

LINDAU, I. & SPICER, W.E. (1974). Oxidation of Nb as studied by the uv-photoemission technique. *J. Appl. Phys.* **45**, 3720-3725.

LING, H.W. & KOLSKI, T.L. (1962). Niobium solid electrolyte capacitors. *J. Electrochem. Soc.* **109**, 69-70.

LIRA-CANTU, M., NORRMAN, K., ANDREASEN, J.W. & KREBS, F.C. (2006). Oxygen release and exchange in niobium oxide MEHPPV hybrid solar cells. *Chem. Mater.* **18**, 5684-5690.

MACEK, M. & OREL, B. (1998). Electrochromism of sol-gel derived niobium oxide films. *Sol. Energy Mater. Sol. cells* **54**, 121-130.

MALIS, T., & TITCHMARSH, J.M. (1986). "k-kactor" approach to EELS analysis. In *Electron Microscopy and Analysis 1985* (Institute of Physics, Bristol, UK), pp. 181-182.

MALIS, T., CHENG, S.C. & EGERTON, R.F. (1988). EELS log-ratio technique for specimen-thickness measurement in the TEM. *J. El. Microsc. Tech.* **8**, 193-200.

MARUCCO, J.F. (1974). Thermodynamic study of the system NbO_2-Nb_2O_5 at high temperature. *J. Solid State Chem.* **10**, 211-218.

MARUCCO, J.F., TETOT, R., GERDANIAN, P. & PICARD, C. (1976). Etude Thermodynamique du dioxyde de niobium à haute temperature. *J. Solid State Chem.* **18**, 97-110.

MASSE, J.-P., SZYMANOWSKI, H., ZABEIDA, O., AMASSIAN, A., KLEMBERG-SAPIEHA, J.E. & MARTINU, L. (2006). Stability and effect of annealing on the optical properties of plasma-deposited Ta_2O_5 and Nb_2O_5 films. *Thin solid films* **515**, 1674-1682.

MATSUI, Y., HIRATANI, M., KIMURA, S. & ASANO, I. (2005). Combining Ta_2O_5 and Nb_2O_5 in bilayered structures and solid solutions for use in MIM Capacitors. *J. Electrochem. Soc.* **152**, F54-F59.

MENON, E.S.K. (2001). Oxidation behaviour of complex niobium based alloys. In *Proceedings of the international Symposium Niobium 2001*, Niobium 2001 Ltd, Bridgeville, USA, pp. 121-145.

MEYER, B. & GRUEHN, R. (1982*a*). Oxydationsprodukte von monoklinem $Nb_{12}O_{29}$ Elektronenoptische Untersuchung. *Z. anorg. Allg. Chem.* **484**, 53-76.

MEYER, B. & GRUEHN, R. (1982*b*). Oxydationsprodukte von orthorhombischem $Nb_{12}O_{29}$ Elektronenoptische Untersuchung. *Z. anorg. Allg. Chem.* **484**, 77-97.

MEYER, B. & GRUEHN, R. (1982*c*). Weitere metastabile Nb_2O_5-Modifikationen, Produkte der langsamen Oxydation von NbO_x-Phasen ($2{,}4 < x < 2{,}5$). *Z. anorg. Allg. Chem.* **484**, 98-123.

MITTERBAUER, C., KOTHLEITNER, G., GROGGER, W., ZANDBERGEN, H., FREITAG, B., TIEMEIJER, P. & HOFER, F. (2003). Electron energy-loss near-edge structures of 3d transition metal oxides recorded at high-energy resolution. *Ultramicroscopy* **96**, 469-480.

MORISHITA, M. & ONOZAWA, M. (2001). Niobium oxide in environmental friendly optical glass. In *Proceedings of the international Symposium Niobium 2001*, Niobium 2001 Ltd, Bridgeville, USA, pp. 311-322.

NAKA, T., NAKANE, T., FURUKAWA, Y., TAKANO, Y., ADSCHIRI, T. & MATSUSHITA, A. (2006). Pressure-induced metal-insulator transition in orthorhombic $Nb_{12}O_{29}$. *Physica B* **378-380**, 337-338.

NAITO, K., KAMEGASHIRA, N. & SASAKI, N. (1980). Phase equilibria in the system between NbO_2 and Nb_2O_5 at high temperatures. *J. Solid State Chem.* **35**, 305-311.

NIEBUHR, J. (1966). Die niederen Oxide des Niobs. *J Less-Common Met* **11**, 191-203.

NORMAN, N. (1962). Metallic oxide phases of niobium and tantalum I. X-ray investigations. *J Less-Common Met* **4**, 52-61.

NOWAK, I. & ZIOLEK, M. (1999). Niobium compounds: preparation, characterization, and application in heterogeneous catalysis. *Chem. Rev.* **99**, 3603-3624.

OKAZ, A.M. & KEESOM, P.H. (1975). Specific heat and magnetization of the superconducting monoxides: NbO and TiO. *Phys. Rev. B* **12**, 4917-4928.

OLSZTA, M.J., WANG, J. & DICKEY, E.C. (2006). Stoichiometry and valence measurements of niobium oxides using electron energy-loss spectroscopy. *J. Microsc.* **224**, 233-241.

OLSZTA, M., SLOPPY, J., LI, J. & DICKEY, E.C. (2007). Field-induced crystallization of anodized Nb and NbO electrolytic capacitors. *Microsc. Microanal.* **13 (Suppl 2)**, 810-811.

OLSZTA, M.J. & E.C. DICKEY (2008). Interface stoichiometry and structure in anodic niobium pentoxide. *Microsc. Microanal.* **14**, 451-458.

OREL, B., MACEK, M., GRDADOLNIK, J. & MEDEN, A. (1998). In situ UV-Vis and ex situ IR spectroelectrochemical investigations of amorphous and crystalline electrochromic Nb_2O_5 films in charged/discharged states. *J. Solid State Electrochem.* **2**, 221-236.

ORGEL, L.E. (1960). *An Introduction to Transition-Metal Chemistry: Ligand-Field Theory*. Methuen & Co Ltd.

PALA, S. (2005). RoHS aspects on aluminium versus NbO capacitors for automotive applications. In *Proceedings of the 19th Passive Components Symposium (CARTS Europe 2005)*, Prague (Czech Republic), pp. 45-49.

PARK, S.-S. & LEE, B.-T. (2004). Anodizing properties of high dielectric oxide films coated on aluminium by sol-gel method. *J. Electroceram.* **13**, 111-116.

PATERSON, J.H. & KRIVANEK, O.L. (1990*a*). ELNES of 3d transition-metal oxides I. Variations across the periodic table. *Ultramicroscopy* **32**, 313-318.

PATERSON, J.H. & KRIVANEK, O.L. (1990*b*). ELNES of 3d transition-metal oxides II. Variations with oxidation state and crystal structure. *Ultramicroscopy* **32**, 319-325.

PEARSON, D.H., FULTZ, B. & AHN, C.-C. (1988). Measurements of the 3d state occupancy in transition metals using electron energy loss spectroscopy. *Appl. Phys. Lett.* **53**, 1405-1407.

PEARSON, D.H., AHN, C.-C. & FULTZ, B. (1993). White lines and d-electron occupancies for the 3d and 4d transition metals. *Phys. Rev. B* **47**, 8471-8478.

PERSICO, D.F., MELODY, B.J., KINARD, T., MANN. L., BEESON, J.J. & NANCE, J. (2001). The use of niobium in capacitor applications. In *Proceedings of the international Symposium Niobium 2001*, Niobium 2001 Ltd, Bridgeville, USA, pp. 323-336.

PETIT, L., CARDINAL, T., VIDEAU, J.J., DURAND, E., CANIONI, L., MARTINES, M., GUYOT, Y. & BOULON, G. (2006). Effect of niobium oxide introduction on erbium luminescence in borophosphate glasses. *Opt. Mater.* **28**, 172-180.

PIALOUX, A., JOYEUX, M.L. & CIZERON, G. (1982). Étude du comportement du niobium sous vide par diffraction des rayons X à haute température. *J Less-Common Met* **87**, 1-19.

POKRANT, S., CHEYNET, M., JULLIAN, S. & PANTEL, R. (2005). Chemical analysis of nanometric dielectric layers using spatially resolved VEELS. *Ultramicroscopy* **104**, 233-243

POZDEEV-FREEMAN, Y. & GLADKIKH, A. (2003). The effects of thermal treatment on the dielectric properties of anodic oxide films on tantalum and niobium: B. Crystallization. In *Proceedings of the 23rd Capacitor And Resistor Technology Symposium (CARTS USA 2003)*, Scottsdale (AZ, USA), pp. 29-36.

PROCH, D., SCHMUESER, P., SINGER, W. & LILJE, L. (2001). Niobium in superconducting rf cavities. In *Proceedings of the international Symposium Niobium 2001*, Niobium 2001 Ltd, Bridgeville, USA, pp. 187-206.

PRYMAK, J.D., STAUBLI, P. & PREVALLET, M. (2004). Derating review of Ta-MnO_2 vs. Ta-polymer vs. Al-polymer vs. NbO-MnO_2. In *Proceedings of the 18th Passive Components Symposium (CARTS Europe 2004)*, Nice (France), pp. 45-48.

QIU, Y., KITCHELL, R., SMYTH, D. & KIMMEL, J. (2001). A novel substrate for solid electrolytic capacitors. In *Proceedings of the 21th Passive Components Symposium (CARTS USA 2001)*, St. Petersburg (FL, USA), pp. 99-103.

QIU, Y., SMYTH, D. & KIMMEL, J. (2002) The stabilization of niobium-based solid electrolyte capacitors, *Active and passive electronic components* **25**, 201-209.

RANDO, N., VERHOEVE, P., VAN DORDRECHT, A., PEACOCK, A., PERRYMAN, M., ANDERSSON, S., VERVEER, J., COLLAUDIN, B., GOLDIE, D.J. & VENN, R. (1996). Detection of optical photons with superconducting tunnel junction detectors. *Nucl. Instrum. Meth. A* **370**, 85-87.

RAEBIGER, H., LANY, S. & ZUNGER, A. (2008). Charge self-regulation upon changing the oxidation state of transition metals in insulators. *Nature* **453**, 763-766.

RAFFERTY, B. & BROWN, L.M. (1998). Direct and indirect transitions in the region of the band gap using electron-energy-loss spectroscopy. *Phys. Rev. B* **58**, 10326-10337.

RAFFERTY, B., PENNYCOOK, S.J. & BROWN, L.M. (2000). Zero loss peak deconvolution for bandgap EEL spectra. *J. Electr. Microsc.* **49**, 517-524.

RAO, C.N.R., WAHNSIEDLER, W.E. & HONIG, J.M. (1970). Plasma resonance in TiO, VO and NbO. *J. Solid State Chem.* **2**, 315-317.

RAYNER-CANHAM, G. & ZHENG, Z. (2008). Naming elements after scientists: an account of a controversy. *Found. Chem.* **10**, 13-18.

RESTA, R. (2008). Charge states in transition. *Nature* **453**, 735.

REZ P. (1982). Cross-sections for energy loss spectrometry. *Ultramicroscopy* **9**, 283-288.

RHO, S., JAHNG, D., LIM, J.H., CHOI, J., CHANG, J.H., LEE, S.C. & KIM, K.J. (2008). Electrochemical DNA biosensors based on thin gold films sputtered on capacitive nanoporous niobium oxide. *Biosens. Bioelectron.* **23**, 852-856.

ROSENFELD, D., SAJINES, R., LEVY, F., BUFFAT, B.A., DEMARNE, V. & GRISEL, A. (1994). Structural and morphological characterization of Nb_2O_5 thin film deposited by reactive sputtering. *J Vac Sci Technol A* **12**, 135-139.

ROYON, A., CANIONI, L., BOUSQUET, B., RODRIGUEZ, V., COUZI, M., RIVERO, C., CARDINAL, T., FARGIN, E., RICHARDSON, M. & RICHARDSON, K. (2007). Strong nuclear contribution to the optical Kerr effect in niobium oxide containing glasses. *Phys. Rev. B* **75**, 104207(1-6).

SASAKI, K., ZHANG, L. & ADZIC, R.R. (2008). Niobium oxide supported platinum ultra-low amount electrocatalysts for oxygen reduction. *Phys. Chem. Chem. Phys.* **10**, 159-167.

SCHÄFER, H., GRUEHN, R. & SCHULTE, F. (1966). Die Modifikationen des Niobpentoxids. *Angew. Chem.* **78**, 28-41.

SCHÄFER, H., BERGNER, D. & GRUEHN, R. (1969). Die thermodynamische Stabilität der sieben zwischen 2,00 and 2,50 O/Nb existierenden Phasen. *Z. anorg. Allg. Chem.* **365**, 31-50.

SCHMID, H.K. & MADER, W. (2006). Oxidation states of Mn and Fe in various compound oxide systems. *Micron* **37**, 426-432.

SCHNEIDER, R. (2003). *Structural and chemical characterization of low-dimensional material systems by transmission electron microscopy*. Habilitationsschrift, Humboldt-Universität, Berlin, Germany.

SCHNITTER, C., MICHAELIS, A. & MERKER, U. (2003). New niobium based materials for solid electrolyte capacitors. In *Proceedings of the 23rd Capacitor And Resistor Technology Symposium (CARTS USA 2003)*, Scottsdale (AZ, USA), pp. 15-20.

SCHULTZE, J.W. & LOHRENGEL, M.M. (2000). Stability, reactivity and breakdown of passive films. Problems of recent and future research. *Electrochim. Acta* **45**, 2499-2513.

SCHWARTZ, N., GRESH, M. & KARLIK, S. (1961). Niobium solid electrolytic capacitors. *J. Electrochem. Soc.* **108**, 750-758.

SCHWARZ, W. & HALBRITTER, J. (1977). On oxygen enrichments in Nb surface layers and their apparent conductivity as observed by the superconducting penetration depth $\Delta\lambda(T,f,B_{ac})$. *J. Appl. Phys.* **48**, 4618-4626.

SEBASTIAN, J.T., SEIDMAN, D.N., YOON, K.E., BAUER, P., REID, T., BOFFO, C. & NOREM, J. (2006). Atom-probe tomography analyses of niobium superconducting RF cavity materials. *Physica C* **441**, 70-74.

SEEBER, B. (1998). *Handbook of applied superconductivity*. Philadelphia: Institute of Physics Publ.

SIGLE, W. (2005). Analytical Transmission Electron Microscopy. *Annu. Rev. Mater. Res.* **35**, 239-314.

SHTASEL, A. & KNIGHT, H.T. (1961). An investigation of columbium as an electrolytic capacitor metal. *J. Electrochem. Soc.* **108**, 343-347.

SMYTH, D.M. & TRIPP, T.B. (1966). The heat-treatment of anodic oxide films on niobium. *J. Electrochem. Soc.* **113**, 1048-1052.

STADELMANN P.A. (1987). EMS – a software package for electron diffraction analysis and HREM image simulation in materials science. *Ultramicroscopy* **21,** 131-145.

STÖRMER, H., IVERS-TIFFÉE, E., SCHNITTER, C. & GERTHSEN, D. (2006). Microstructure and dielectric properties of nanoscale oxide layers on sintered capacitor-grade niobium and V-doped niobium powder compacts. *Int. J. Mat. Res.* **97**, 794-801.

STÖRMER, H., WEBER, A., FISCHER, V., IVERS-TIFFÉE, E. & GERTHSEN, D. (2009). Anodically formed oxide films on niobium: microstructural and electrical properties. *J. Eur. Ceram. Soc.*, **in press**.

SU, D.S., RODDATIS, V., WILLINGER, M., WEINBERG, G., KITZELMANN, E., SCHLÖGL, R. & KNÖZINGER, H. (2001). Tribochemical modification of the microstructure of V_2O_5. *Catal. Lett.* **74**, 169-175.

SUN, D.Z., QU, C.F., YAO, C.H., DU, H., JIN, Q.H. & LIN, S.W. (2001). Relation between the phase transitional behavior and the content of additive niobium oxide in PZT 97/3. *Ferroelectrics* **262**, 281–286.

TANABE, K. (2003). Catalytic application of niobium compounds. *Catal. Today* **78**, 65–77.

TURZHEVSKY, S.A., NOVIKOV, D.L., GUBANOV, V.A. & FREEMAN, A.J. (1994). Electronic structure and crystal chemistry of niobium oxide phases. *Phys. Rev. B* **50**, 3200-3208.

USHIKUBO, T., KOIKE, Y., WADA, K., XIE, L., WANG, D. & GUO, X. (1996). Study of the structure of niobium oxide by X-ray absorption fine structure and surface science techniques. *Catal. Today* **28**, 59–69.

VELTEN, D., EISENBARTH, E., SCHANNE, N. & BREME, J. (2004). Biocompatible Nb_2O_5 thin films prepared by means of the sol-gel process. *J. Mater. Sci.-Mater. M.* **15**, 457-461.

VENKATARAJ, S., DRESE, R., LIESCH, C., KAPPERTZ, O., JAYAVEL, R. & WUTTIG, M. (2002). Temperature stability of sputtered niobium-oxide films. *J. Appl. Phys.* **91**, 4863-4871.

VERBEECK, J. (2002). *Electron energy loss spectroscopy of nanoscale materials*. PhD Thesis, Universiteit Antwerpen, Belgium.

VERBEECK, J. (2004). Personal communication.

VERBEECK, J. & VAN AERT, S. (2004). Model based quantification of EELS spectra. *Ultramicroscopy* **101**, 207-224.

WIESKE, M., SU, D.S., BECKMANN, F. & SCHLÖGL, R. (2002). Electron-beam-induced structural variations of divanadium pentoxide (V_2O_5) at liquid helium temperature. *Catal. Lett.* **81**, 43-47.

WILLIAMS, D.B. & CARTER, C.B. (1996). *Transmission Electron Microscopy*. New York: Plenum Press.

WIMMER, E., SCHWARZ, K., PODLOUCKY, R,. HERZIG, P. & NECKEL, A. (1982). The effect of vacancies on the electronic structure of NbO. *J. Phys. Chem. Solids* **43**, 439-447.

WU, A.T. (2006). Investigation of oxide layer structure on niobium surface using a secondary ion mass spectrometry. *Physica C* **441**, 79-82.

YI, K. (2003). Niobium technology enters capacitor market. *Power Electronics Technology* **29**, 32-36.

YOON, K.E., SEIDMAN, D.N., BAUER, P., BOFFO, C. & ANTOINE, C. (2007). Atomic-scale chemical-analyses of niobium for superconducting radio-frequency cavities. *IEEE Trans. Appl. Supercond.* **17**, 1314-1317.

ZEDNICEK, T., ZEDNICEK, S., SITA, Z., MCCRACKEN, C., MILLMAN, W.A. & GILL, J. (2004). Technology of niobium oxide capacitor. *Advancing Microelectronics* **31**, 6-10.

ZEDNICEK, S., HORACEK, I., ZEDNICEK, T., SITA, Z., MCCRACKEN, C., MILLMAN, W. (2005). Extended range NbO capacitors through technology and materials enhancements. In *Proceedings of the 19th Passive Components Symposium (CARTS Europe 2005)*, Prague (Czech Republic), pp. 57-63.

ZEITLIN, B.A. (2001). The future of low temperature niobium based superconductors. In *Proceedings of the international Symposium Niobium 2001*, Niobium 2001 Ltd, Bridgeville, USA, pp. 221-241.

ZILLGEN, H., STENZEL, M. & LOHWASSER, W. (2002). New Niobium Capacitors with Stable Electrical Parameters. *Active and Passive Electronic Components* **25**, 147-153.

Danksagung

An erster Stelle möchte ich mich sehr herzlich bedanken bei Frau Prof. Dr. Dagmar Gerthsen, dass sie meine Arbeit betreut hat und für das Korrektur lesen. Trotz der anwachsenden Gruppengröße im Bereich Diplomanden und Doktoranden hat Frau Gerthsen für alle Institutsmitglieder ein offenes Ohr und mich während der ganzen Zeit im Laboratorium für Elektronenmikroskopie sehr unterstützt.

Vielen Dank an Frau Prof. Dr. Ute Kaiser (Materialwissenschaftliche Elektronenmikroskopie, Universität Ulm) für die Übernahme meines Korreferats.

Mein ganz besonderer Dank gilt Dr. Reinhard Schneider, der sich über alle Maße engagiert hat und mir in der Verfassung der Dissertation ebenso wie schon beim Experimentieren und Auswerten der Daten ein unersetzlicher Diskussionspartner war. Vielen Dank auch noch für die freundlichen Gespräche während unserer gemeinsamen Mittag- als auch Abendessen!

Vielen Dank an Dr. Heike Störmer für ihre stetige und kompetente Betreuung in der Thematik Nioboxide und niobbasierte Kondensatoren. Sie war außerdem eine sehr angenehme Bürokollegin. Ich werde ihre stetige gute Laune vermissen, genauso wie sie meine immer aufgeklärten Kommentare vermissen wird.

I would like to thank Dr. Jo Verbeeck (EMAT, University of Antwerp), who is an outstanding EELS expert, for initiating me in the basics of EELS as well as for the experiments and fruitful discussions that arose through cooperation. More particularly, I am deeply grateful for his help during the measurements at the JEOL JEM-3000F, which yielded an important contribution to the results of the present work.

Der zweite entscheidende und für die Arbeit unersetzliche Kooperationspartner war Dr. Wilfried Sigle (Max-Planck-Institut für Metallforschung, Stuttgart), wofür ich mich auch sehr bedanken möchte. Er war immer interessiert an meiner Arbeit und hat mir Messungen am ZEISS Libra FE und am VG HB501UX ermöglicht, die mir wichtige Ergebnisse geliefert haben.

Für die Einführung in die Arbeit mit Transmissionselektronenmikroskopen danke ich Herrn Foutouhi, der immer geduldig und hilfsbereit war. Vielen Dank an Dr. Harald Rösner (ehemals am Institut für Nanotechnologie, Forschungszentrum Karlsruhe) für seine Hilfe bei Vorexperimenten.

Ein Dankeschön möchte ich auch an die ehemalige Kollegin Sabine Kalhöfer sagen, die mich sehr unterstützt hat in der Präparation von TEM Proben. Herzlichen Dank auch noch mal für die Dauerleihgabe des Fahrrads!

Mein Dank gilt auch den anderen ehemaligen "Damen der Präparation" Frau Kamilli, Frau Krebs und Frau Spickert.

Vielen Dank an Rita Sauter für die Hilfe bei allen möglichen Formalitäten und ihren großen Beitrag zum Wohlfühlen des Instituts.

Vielen Dank an Dr. Virginie de Pauw für ihre lachende Unterstützung.

Schließlich möchte ich mich ganz herzlich bei allen Lemmingen bedanken für die gute Zusammenarbeit, das angenehme Arbeitsklima und auch die ganzen netten Grillabende und Partys.

Last but not least, vielen Dank an meine Katrin, sie weiß schon warum und es würde diese Dissertation noch mal um 50 Seiten verlängern alles aufzuzählen! Je remercie ma mère et ma sœur pour leur soutien inconditionnel. Merci à mon père.